Study of lipid bilayer behaviour modified by substrate interactions

MILLER, ETHAN,JOSHUA

Study of lipid bilayer behaviour modified by substrate interactions

by

Ethan Joshua Miller

Submitted in partial fulfilment of the requirements for the degree of Doctor of Philosophy

Department of Physics and Astronomy

Durham University

January 2019

Declaration

The following work presented in this thesis was conducted under the supervision of Dr Margarita Staykova and Dr Kislon Voïtchovsky at Durham University. All results, analysis, figures and text of the manuscript is my own, unless stated otherwise. None of the following work in this thesis has been presented for any other degree or qualification.

Acknowledgements

I thank my supervisors, Dr Kislon Voïtchovsky and Dr Margarita Staykova, whose guidance and help allowed me to develop not only my project but myself during my time working under their supervision. I am very grateful to be one of the initial members of each of their fantastic groups, both of which will only grow brighter and more successful in the coming years**.** I also thank my industrial supervisors David Moore, Michael Thompson and Eloise Welfare for their many insightful conference calls and kind encouragement.

Speaking of which, I would like to say a big thank you to all the members of the Voïtchovsky and Staykova groups, past and present, who have not only been excellent colleagues but even better friends. It is quite special to be part of such kind, creative, ingenious, resilient and fun group of people. I tactically omitted lists of names as this sentiment extends out to numerous people working in the physics department at Durham University, who have all made my stay in the quaint little city a fond one with many warm memories. I wish you all best in your futures and hope to cross paths with each of you again.

I would like to give a special thank you to my family: David, Jennifer, Nadine and Danielle, for their continued support and understanding throughout my PhD. A heart-felt thank you goes to my dearest friend Beatrice Fontana, who always listened, and encouraged me. Finally, my ultimate thanks goes to God, who has kept me throughout.

Abstract

Biological membranes rarely exist as free-floating structures but are often confined and supported by various cellular assemblies such as the cytoskeleton and the extracellular matrix. It has already been shown that biological and polymeric substrates can modulate the morphology and response to various stimuli of supported lipid bilayers significantly. The interaction between such structures and the membrane are obviously important yet remain poorly understood even in minimal or synthetic systems.

The work of this thesis utilises a variety of fluorescence microscopy and atomic force microscopy (AFM) techniques to investigate the behaviour and structure of supported lipid bilayers, in particular how interfacial features of their support substrate influence and modulate their morphology and biophysical properties. First, surface modification of polydimethylsiloxane is systematically explored, in particular how the interfacial properties of such a polymer substrate can be modified to create fully and partially plasma-treated interfaces that stably support lipid bilayers. Lipid patch formation on such substrates is then investigated, revealing that the membrane undergoes significant morphological reorganisation after vesicle fusion has completed forming a lipid patch. The underlying mechanisms can be altered by substrate interactions following different pathways for fully and partially plasma-treated PDMS substrates. Furthermore, partially plasma-treated substrates are demonstrated to be capable of specifically depleting cholesterol from supported lipid membranes, while stably supporting the other remaining phospholipid species. Studies of cholesterol depletion of lipid patches possessing liquid-ordered and disordered domains reveal a disruption in domains structure, with the partitioning of fluorescent dyes into regions from which they were previously excluded. This structure perturbation was found to be reversible upon the reinsertion of cholesterol into the bilayer.

Many of the discussed mechanisms are only observed in the presence of a substrate, emphasising the importance of substrate interactions in both functional biomembranes and the development of supported membrane technologies.

Table of Contents

Acknowledgements ..... **ii**

Abstract ..... **iii**

Table of Contents ..... **iv**

List of Abbreviations ..... **viii**

List of Figures ..... **xi**

List of Tables ..... **xv**

Chapter 1: Introduction **1**

1.1 Lipid membrane: Origin and biology 2

1.2 Lipid membranes: A model system 5

1.2.1 Self-assembly of lipid molecules *6*

1.2.2 Membrane phase and fluidity *9*

1.3 Supported lipid membrane: Relevance for biological models 13

1.4 Supported lipid bilayers: Substrate impact 15

1.4.1 Substrate impact on the lateral diffusivity in lipid bilayers *17*

1.4.2 Miscibility, criticality and phase transition effects *19*

1.4.3 Mitigating the substrate influence *21*

1.5 Passively remodelling of supported lipid membranes 22

1.5.1 Chemical surface patterning *23*

1.5.2 Topographical surface patterning *23*

1.6 Dynamically remodelling of supported lipid membranes 25

1.6.1 Supported membranes modulated by fluid shear *26*

1.6.2 Supported membranes modulated by electric fields *26*

1.6.3 Supported membranes modulated by mechanical stress *27*

1.7 Conclusion 29

Chapter 2: Materials and methods **30**

2.1 Lipid preparation 30

2.1.1 Fluorescent label 31
2.2 Buffer solution: 34
2.3 Substrate preparation 35
2.3.1 Glass 35
2.3.2 Mica 35
2.3.3 Polydimethylsiloxane 36
2.4 Forming supported lipid membranes 37
2.4.1 Continuous SLBs using large unilamellar vesicle fusion 37
2.4.2 Distinct SLB patches using giant unilamellar vesicle fusion 38
2.5 Fluorescence microscopy 40
2.5.1 Epifluorescence microscopy 41
2.5.2 Fluorescence recovery after photobleaching 43
2.5.3 Reflection interference microscopy 45
2.5.4 Image acquisition, processing and analysis 47
2.6 Atomic force microscopy 50
2.6.1 Modes of AFM operation 51
2.6.2 Amplitude modulation mode 51
2.6.3 Lateral force microscopy and mapping friction 53
2.6.4 Tip-substrate interaction forces 54
2.6.5 Force spectroscopy and force mapping 57
2.6.6 Tip functionalisation 60
2.7 Wetting measurements 61
2.8 Stretching flexible substrates and surface cracking 63

Chapter 3: Surface modification of polydimethylsiloxane substrates using air plasma treatment 66

3.1 Modifying surface chemistry with plasma treatment 68
3.2 Hydrophobic recovery after plasma treatment 73
3.3 Creating wrinkled topographies 75
3.4 Surface cracking under mechanical stress 77
3.5 Conclusion 79

Chapter 4: Morphological changes in lipid bilayers induced by vesicle fusion to substrates 81

4.1 Morphological changes in supported lipid bilayers induced by vesicle fusion 83
4.2 Morphological changes in cholesterol-containing bilayers induced by vesicle fusion 89
4.3 Transient formation of lipid protrusion after vesicle fusion 91
4.4 Impact of osmotically induced membrane tension on lipid patch morphology after vesicle fusion 94
4.5 Impact of partially plasma-treated PDMS on supported lipid bilayers formed by vesicle fusion 97
4.6 Conclusion 99

Chapter 5: Cholesterol extraction from supported lipid bilayers via substrate interactions 100

5.1 Substrate-induced cholesterol extraction 100
5.2 Nanoscale characterisation of PDMS substrates and PDMS-membrane interactions 106
5.3 Quantifying the change in cholesterol mole fraction 110
5.4 Cholesterol extraction can induce phase changes 117
5.5 Mechanically triggering cholesterol extraction 119
5.6 Conclusion 123

Chapter 6: Disruption of phase domains by cholesterol modulation of supported lipid bilayer patches 125

6.1 Disruption of lipid bilayer domain behaviour by cholesterol addition and depletion 127
6.1.1 Cholesterol addition through the solution (soluble cholesterol) 130
6.1.2 Depletion of cholesterol through the solution (cyclodextrin) 132
6.2 Impact of cholesterol depletion on domain structure and membrane properties 136
6.3 Increased resistance to cholesterol modulation conferred by saturated lipids 142
6.4 Substrate-induced cholesterol depletion disrupts domain behaviour 145
6.5 Reversibility of lipid domain restructuring by cholesterol modulation 147

6.5.1 Preliminary investigations: Identifying sub-optical L_o/L_d domains formed by melting micron scale domain structure in lipid patches 153

6.5.2 Preliminary investigations: Using wrinkled substrates to investigate the influence of curvature on phase separation 156

6.6 Conclusion 158

Chapter 7: Conclusions and Future Outlook 160

7.1 Thesis Summary 160

7.2 Outlook and Further Work 165

Bibliography 170

List of Abbreviations

AC	Alternating current
AFM	Atomic force microscopy
AM-AFM	Amplitude modulation atomic force microscopy
AMP	Antimicrobial peptides
CCD	Charge Coupled Device
Chol-MβCD	Methyl-β-cyclodextrin loaded with cholesterol (soluble cholesterol)
CMOS	Complementary Metal-oxide Semiconductor
DiIC$_{18}$(5)	1,1'-Dioctadecyl-3,3,3',3'-Tetramethylindodicarbocyanine, 4-Chlorobenzenesulfonate Salt
DLPC	1,2-dilauroyl-sn-glycero-3-phosphocholine
DLPG	1,2-dilauroyl-sn-glycero-3-phospho-(1'-rac-glycerol)
DMPC	1,2-dimyristoyl-sn-glycero-3-phosphocholine
DMPG	1,2-dimyristoyl-sn-glycero-3-phospho-(1'-rac-glycerol) (sodium salt)
DOPC	1,2-dioleoyl-sn-glycero-3-phosphocholine
DPPC	1,2-dipalmitoyl-sn-glycero-3phosphatidylcholine
DPPG	1,2-dipalmitoyl-sn-glycero-3-phospho-(1'-rac-glycerol) (sodium salt)
EDL	Electric double layer
Egg-PC	L-α-phosphatidylcholine
FCS	Fluorescence correlation spectroscopy
FI	Fluorescence intensity
FRAP	Fluorescence recovery after photobleaching
FRET	Förster resonance energy transfer
GUV	Giant unilamellar vesicle

ITO	Indium tin oxide
L_d	Liquid-disordered
LFM	Lateral force microscopy
LMWS	Low molecular weight species
L_o	Liquid-ordered
L_β	Gel phase
LUV	Large unilamellar vesicle
MβCD	Methyl-β-cyclodextrin
Mol%	Mole percent
NaP	Naphthopyran
PC	Phosphocholine
PDMS	Polydimethylsiloxane
PEG	Polyethylene glycol
PFS	Perfect focus system
POPC	1-palmitoyl-2-oleoyl-sn-glycero-3-phosphocholine
Rh-DPPE	1,2-dipalmitoyl-sn-glycero-3-phosphoethanolamine-N-(lissamine rhodamine B sulfonyl) (ammonium salt)
RICM	Reflection interference contrast microscopy
RMS	Root mean square
RPM	Rotations per minute
SAM	Self assembled monolayer
SLB	Supported lipid bilayer
STED	Stimulated emission depletion
SUV	Small unilamellar vesicle
TIRF	Total internal reflection fluorescence

TRIS	Tris(hydroxymethyl)aminomethane
UV	Ultraviolet
Vpp	Peak-to-peak voltage

List of Figures

Figure 1.1: Basic schematic of the cellular membrane. 4

Figure 1.2: Diagram of lipid polymorphism. 7

Figure 1.3: Membrane phases in ternary lipid bilayer mixture. 11

Figure 1.4: Schematic of cellular interfaces supporting the plasma membrane. ... 14

Figure 1.5: Langmuir-Blodgett and vesicle deposition methods. 17

Figure 1.6: Schematic of polymeric spacer techniques to mitigate substrate influence. 22

Figure 1.7: Impact of nanotopography on supported lipid bilayers. 24

Figure 2.1: Experimental set up for GUV electroformation. 38

Figure 2.2: Example of segregated and coarsened domain structure in lipid patches 39

Figure 2.3: Schematic of the experimental set up for GUV deposition. 39

Figure 2.4: Schematic representation of the epifluorescence microscopy and fluorescence recovery after photobleaching set-up. 42

Figure 2.5: Formation of out of plane tubular projections. 43

Figure 2.6: Schematic of reflectance interference microscopy. 46

Figure 2.7: Example of the Otsu thresholding method. 49

Figure 2.8: Schematic representation of amplitude modulation-AFM (AM-AFM). . 52

Figure 2.9: Schematic description of lateral force microscopy. 54

Figure 2.10: Illustration representing a force spectroscopy measurement on a point location of a sample. 58

Figure 2.11: Schematic representation of a contact angle measurement. 61

Figure 2.12: Schematic of a biaxial stretching device and PFS system. 64

Figure 3.1: Schematic of plasma oxidation treatment of PDMS. 68

Figure 3.2: Change in physical and chemical surface properties of PDMS after plasma oxidation treatment. 70

Figure 3.3: Force spectroscopy measurements of PDMS-cholesterol interactions. 72

Figure 3.4: Hydrophobic recovery of PDMS. 74

Figure 3.5: A PDMS topography modified by plasma treatment and example topographies. 77

Figure 3.6: Surface cracking in plasma-treated PDMS due to tensile strains. 78

Figure 4.1: Formation of supported lipid patches on hydrophilic surfaces. 84

Figure 4.2: Fusion induced membrane reorganisation on a hydrophilic substrate. 85

Figure 4.3: Fusion induced membrane spreading and homogenisation on hydrophilic substrates. 86

Figure 4.4: Fusion induced membrane spreading and homogenisation on hydrophilic substrates. 88

Figure 4.5: Cholesterol containing membrane reorganisation after vesicle fusion. 90

Figure 4.6: Fluctuations in membrane distance from the substrate immediately after fusion. 92

Figure 4.7: Formation of lipid protrusions during vesicle fusion. 93

Figure 4.8: Impact of osmotic stress in vesicles on the contraction of the resultant lipid patch area. 96

Figure 4.9: Impact of the partially hydrophilic substrate on lipid patch spreading and homogenisation. 98

Figure 5.1: Substrate-induced changes in PDMS-supported lipid bilayers. 101

Figure 5.2: Relative changes in surface area of lipid patches supported on fully plasma-treated PDMS substrate 102

Figure 5.3: Quantifying cholesterol extraction from supported lipid bilayers on PDMS. 104

Figure 5.4: No correlation between lipid patch size and cholesterol depletion rate. 105

Figure 5.5: Force spectroscopy measurements of PDMS–cholesterol interactions. 107

Figure 5.6: Illustration of the semi-automated procedure used to analyse the AFM spectroscopy extraction curves 108

Figure 5.7: Cholesterol condensing effect. 111

Figure 5.8: Fitting of cholesterol depletion model to experimental data. 114

Figure 5.9: Analysis of cholesterol extraction as a function of cholesterol concentration. 116

Figure 5.10: Saturated lipid membranes on PDMS substrates. 118

Figure 5.11: Mechanically triggered the extraction of cholesterol from supported lipid bilayers. 120

Figure 5.12: Change in supported DOPC lipid bilayer area during expansion/compression cycles. 121

Figure 5.13: Evidence of microscale surface cracking on PDMS substrates. 122

Figure 6.1: Depletion of cholesterol from sessile phase separated GUV. 128

Figure 6.2: Doping of cholesterol into phase separated supported lipid bilayers. 131

Figure 6.3: Depletion of cholesterol disrupting fluorophore partitioning for supported lipid membranes. 133

Figure 6.4: Homogenisation and loss of NaP signal during cholesterol depletion. 135

Figure 6.5: Depletion of cholesterol allows Rh-DPPE to penetrate the liquid-ordered phase. 137

Figure 6.6: Change in patch morphology, pore formation, area shrinkage due to cholesterol depletion of phase separated supported bilayers. 140

Figure 6.7: Effects of cholesterol depletion of supported lipid bilayers with a predominantly liquid-ordered phase. 143

Figure 6.8: Disruption of fluorophore partitioning initiated by substrate-induced cholesterol depletion. 146

Figure 6.9: Cycling cholesterol extraction and addition to disrupt and heal phase-separated lipid patches. 148

Figure 6.10: Effects of cholesterol depletion after phase separated lipid patches promoted into a single phase. 151

Figure 6.11: Change in patch morphology during cholesterol depletion. 152

Figure 6.12: Disruption of liquid-ordered and disordered domain structure by heat treatment. 154

Figure 6.13: Image showing the relative positions of scans from Figure 6.12 (b,e). 155

Figure 6.14: Impact of local curvature on gel domain formation. 157

List of Tables

Table 2:1: Name and chemical structure of the fluorophores Rh-DPPE and DiIC$_{18}$(5) and NaP. 33

Table 2:2 Filter cube used with in the epifluorescence microscope setup 43

Table 5.1: Extracted values for accessible cholesterol mole fraction and cholesterol depletion rate constant. 115

Chapter 1: Introduction

One of the primary building blocks of cellular life is a class of molecules called lipids. These molecules are integral to forming the cellular membrane and can be utilised to create minimal model systems in the form of synthetic lipid membranes. Artificial lipid membrane systems are a popularly utilised tool for research and technological innovations [1]. When adhered to a support substrate, these lipid membranes have a favourable geometry for many experimental techniques and improved stability compared to other synthetic lipid systems such as vesicles and black lipid membranes [1]. They have been widely exploited in biological investigations to elucidate various aspects of the cell membrane behaviour, and more specifically how lipids play an integral role in membrane function. However, such systems are often considered restrictive, with substrate interactions being seen as a drawback due to the fact that they influence the membrane properties such as fluidity, morphology and chemical activity [2]. This distortion of membrane properties is sometimes thought to produce behaviours that are not representative of native biological membranes. In fact, substrate interactions are often thought to reduce the biological relevance of such systems. This is a common miscomprehension; instead, biological membranes rarely exist as free-floating structures *in vivo* and are adhered support structures such as the cytoskeleton and extracellular matrix, with substrate interactions being important for successful membrane morphology and function. Even for technological applications, supported lipid membrane interfaces are exploited, for example in healthcare, drug discovery, food safety and environmental monitoring [3].

At the present time, a full understanding of the membrane-substrate interactions and their impact remains elusive and often marginalised, partly due to the inherent complexity of lipid systems and difficult length/time scales of measurement required to help decipher their behaviours.

In this chapter, a review of the role of the lipid in the cell membrane is presented, along with discussions on how the lipids' chemical structure imparts functional properties such as membrane fluidity, phase behaviour, and barrier function even in minimal model supported lipid systems. The influence of a supporting surface on

membrane properties and behaviour are discussed, in both model and biological systems, detailing how substrate surfaces can passively and dynamically alter membrane structure and function.

1.1 Lipid membrane: Origin and biology

Cell membranes are highly complex in composition, containing a precise content of lipids, carbohydrates and proteins that elegantly accomplish a broad range of tasks, most importantly forming the cellular barriers that separate the inside of a living cell from its inanimate surroundings [4,5]. Lipids satisfy three main functions within the cell: energy storage [6,7], signal transduction [8], and the formation of membranes [9]. In the latter role, lipids were initially thought to act as passive two-dimensional structures serving for the encapsulation of the cell content and hosting membrane proteins [10]. Recently, this picture has evolved with the lipids now accepted to be much more active players in the membrane, forming a dynamic and heterogeneous matrix of laterally organised lipids, in which protein species can transiently reorganise. The complexity of the lipid membrane is partly attributed to the diverse array of lipid species present in the membrane, with informatics and computational studies predicting over 100,000 different lipids in the cellular lipidome [11,12]. Over 21,000 biologically relevant lipid structures have already been catalogued in the LIPIDS MAPS Structure Database using experimental techniques such as; nuclear magnetic resonance, liquid chromatography and mass spectrometry [13]. This prompts the question as to why is the cell membrane lipid composition so complex. One reason is that various lipids can be intricately involved in membrane protein assembly and enzyme function. A typical example can be found in the loss of function of the membrane protein lactose permease when reconstituted in the absence of phosphatidylethanolamines [14,15]. Another possible reason is to facilitate the dynamical adjustment of membrane behaviour near critical miscibility points. Near criticality, small changes in composition can dramatically alter the membrane's chemical and mechanical properties, a behaviour that requires fine-tuning through a complex composition of lipids [16–18]. The lipid composition also aids controlling the spatial biomolecular organisation within the membrane by the formation of distinct phase-separated domains of a specific composition. Several studies suggest that

criticality in plasma membranes can explain many of the observations typically connected to the formation of microdomains of lipid and protein [16,17,19], the so-called lipid rafts. The study of lipid delivery to apical and basolateral surfaces in polarised epithelial cells inspired the idea that lipid rafts are used for biological functions. Studies showed that the delivery of selected lipids to regions of the cell membrane led to the lateral and asymmetric separation of sphingolipids and glycerolipids, which in turn coincided with the localisation of membrane proteins through specific lipid-protein interactions [20]. This was then proposed as a method for laterally organising cellular membranes and facilitating cell functions.

The presence of distinct sub-compartments in biological membranes is also relevant for detergent resistance. Experiments demonstrated that cell membranes were not fully solubilised in the detergent Triton X-100 at low temperatures [21]. Instead, the membrane was left with detergent-resistant domains, which were concentrated in cholesterol/sphingolipid [21]. Indications of these microdomains have also been obtained in live cells using multiphoton microscopy approaches, most notably the observation of changes in lipid membrane ordering of whole, live zebrafish embryos [22], and identification of clustered lipid microdomains in the filopodia of macrophages [23,24].

However, the presence of lipid rafts *in-vivo* remains controversial; individual rafts are small and highly dynamic, rendering their direct visualisation difficult and elusive [23,25,26]. Despite these controversies, the intriguing biological implications of the “lipid rafts” concept stimulated a surge in fundamental research about the principles driving local lipid lateral organisation in cellular membranes [11]. The local lipid composition not only impacts lateral membrane organisation [27,28] but also influences phase separation and protein aggregation, membrane signal transduction [8], membrane nanomechanics [29,30] and various biomolecule interactions [31–34]. Studies have shown membrane composition to even play a role in host-pathogen interactions, especially in the case of viral capsid lipid coatings [35–37]

Defective replication of the correct lipid composition in membranes has also been linked with various pathologies [38]. Bullous disease, an ailment that leads to symptoms such as blistering of the skin, is linked to a disruption of plasma membrane composition in keratinocyte cells. A dysfunction in cellular cholesterol

content disrupts lipid membrane lateral structure, proposedly impacting membrane barrier function and contributing to the pathogenesis of the disease [39]. Atherosclerosis is another example of pathology with links to dysfunctional membrane composition leading to plaque development on the inside of arteries. One particular study suggested that membrane microdomains in macrophages could help colocalisation of the platelet-activating factor and CD36 proteins. In doing so, the lipid domains facilitate the complexation of these two proteins, increasing oxidised low-density lipoprotein interaction with macrophages, leading to the development of atherosclerosis [40]. Even neurological disorders such as Alzheimer's disease have proposed origins in disrupted membrane composition. The “seeds” for the amyloid fibril formation central to the pathogenesis [41] are suggested to have origins in intracellular membrane microdomains [42].

All these examples make it obvious that lipids play a deciding role in plasma membrane structure, and consequently, the fate and function of the overall cell.

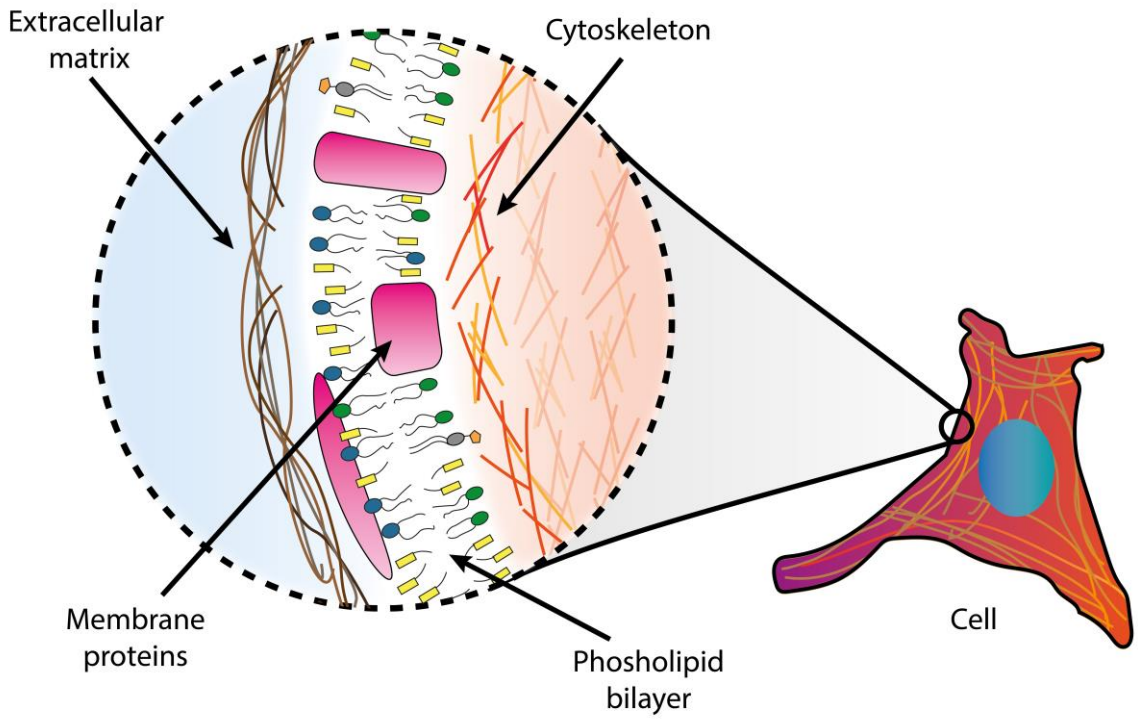

Figure 1.1: Basic schematic of the cellular membrane. The plasma membrane is a complex structure made up of various lipid species as well as different membrane proteins, supported by the cytoskeleton and extracellular matrix. The two lipid leaflets composing the membranes tend to exhibit different lipid composition (so-called leaflet asymmetry).

However, the plasma membrane is not an isolated structure; it is impacted and modulated by surrounding cellular structures such as the cytoskeleton and extracellular matrix (Figure 1.1). For example, condensation of lipid domains in the plasma membrane of T-lymphocytes occurs above actin-rich structures in the cytoskeleton [43]. The reorganisation of these domains could be connected to cytoskeletal restructuring, underpinning a molecular mechanism for cross-talk between the cytoskeleton and plasma membrane. While still hypothetical, this further highlights the complexity of the cell membrane, with countless factors influencing its structure and function. In light of this complexity, a minimal model system can prove useful for studying fundamental aspects of the properties and functions of the lipid species in the cell membrane, as well as the impact of the structures supporting the membrane. The first step, when developing such minimal models, is to understand how different lipid assemblies and chemical structures relate to their role in membrane function.

1.2 Lipid membranes: A model system

Lipids can be loosely defined as a group of hydrophobic or amphiphilic small organic molecules that do not readily dissolve in polar solvents such as water. Such a broad definition reflects the fact that lipids form a broad and complex class of molecules with a substantial structural diversity that encompasses numerous combinations of fatty acid chain lengths and possible headgroups linked together by a glycerol backbone [12]. Lipids are essential constituents for the membrane's function, defining mechanical, biophysical, and functional properties. The investigation of lipid systems has flourished, along with an appreciation of their complexity. The lipid composition of the plasma membrane continually evolves, affecting the membrane local molecular organisation, mechanical properties and lipid-protein interactions in order to support cell structure and function [20]. Lipids can be produced synthetically [44], allowing for full compositional control in the development of minimal model systems. This strategy is invaluable for a "bottom-up" approach: building complex systems through the controlled combination of fundamental elements. This approach can aid the identification and interpretation of the fundamental biophysical

principles underpinning complex biological processes, and is used extensively in the present thesis.

1.2.1 Self-assembly of lipid molecules

Phospholipids are one of the most common classes of lipids and constitute a major building block of the plasma membrane structure. Phospholipids are made of a hydrophilic polar “headgroup” and typically two hydrophobic fatty acid acyl chains known as a “tail-group”. When placed in water, the hydrocarbon tails of the phospholipids disrupt the network of hydrogen bonds formed by water molecules, forcing them to re-order and hence decreasing the system's overall entropy. These hydrophobic interactions drive the tails to group together and reorient to expose only the hydrophilic headgroups which remain in contact with the aqueous phase. This drives the spontaneous self-assembly of lipid structures in water: as phospholipid molecules are progressively added to the aqueous solution, they first self-assemble into micelles once the so-called critical micelle concentration is reached. Phospholipids tend to have extremely low critical micelle concentrations, with examples ranging from 0.01 – 1 mM for several phosphatidylglycerol (PG) lipid species, and as low as 0.5 – 100 nM for several phosphatidylcholine (PC) lipid species [45]. Such low critical micelle concentrations ensure the stability of self-assembled lipid structures even when their bathing medium becomes depleted of lipids [46]. The low critical micelle concentration of phospholipids has been exploited in the design of artificial cells or protocells [4,47–51]. Protocells can encapsulate, compartmentalise and replicate genetic material, such as RNA, and the formation of a semi-permeable membrane could be one of the first evolutionary steps taken by life, likely forming the progenitor of the cell membrane as we know it [5,52].

Various factors influence the structure of the lipid micelles (or aggregates) including temperature, pH, electrolyte concentrations and the molecular structure of the lipids themselves. This plasticity of lipid assemblies is often described as lipid polymorphism: the ability of chemically identical structures to have two or more distinct organisational forms. The packing properties of lipid molecules play a significant role in the favoured structures into which lipids assemble. In its most basic form, the features controlling lipid organisation can be summarised by three

parameters: the optimal molecule area a_0, the volume occupied by the hydrocarbon chain v, and the maximum effective length the chain can assume or the critical chain length l_c. These three parameters can be related by the following equation in order to predict a packing parameter, P:

$$P = \frac{v}{a_0 \, l_c} \qquad \text{Equation 1.2}$$

The packing parameter characterises the molecular arrangement yielding a zero bending stress depending on the intrinsic geometry of the lipids [53] (Figure 1.2). This predicted "spontaneous curvature", is an important parameter that can vary significantly between lipid molecules, impacting morphology, bending rigidity, lipid packing and phase behaviour [54].

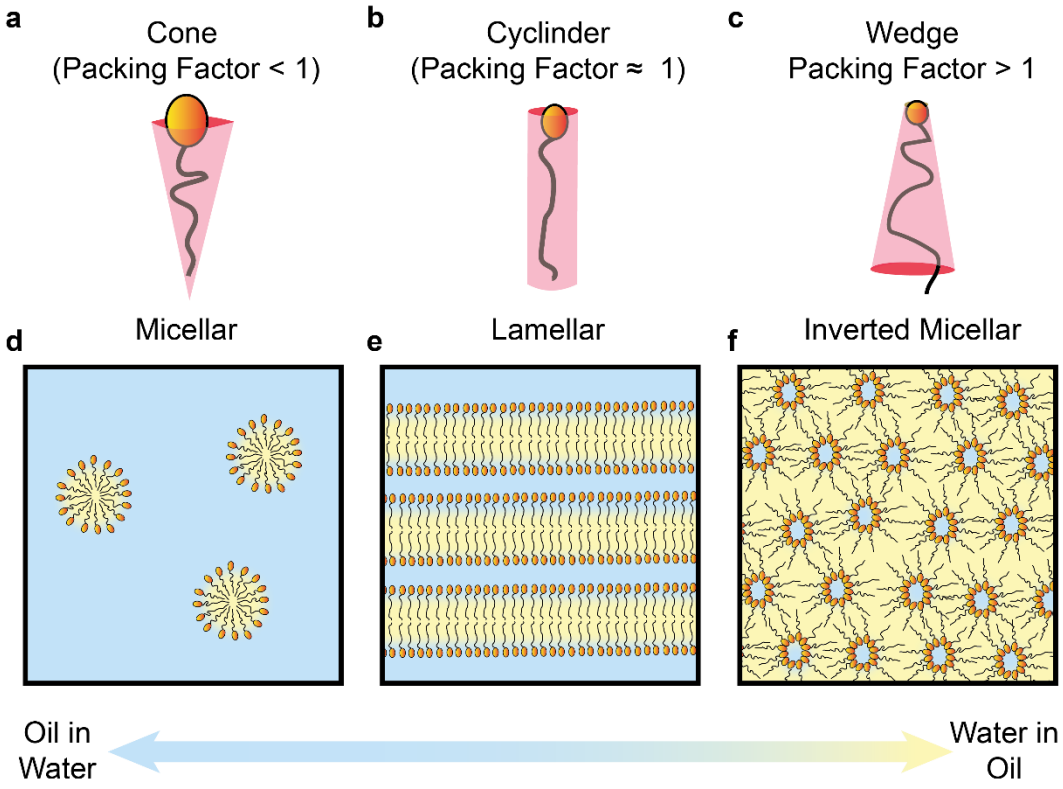

Figure 1.2: Diagram of lipid polymorphism. Example lipid molecules with cone (a), cylinder (b) and wedge shapes(c). When such structures self-assemble in aqueous solution, they have a preference for forming certain structures, with micellar (d), lamellar (e) and inverted micellar (f) structures being given as corresponding example structures

Lipids can exhibit positive or negative spontaneous curvature. For example, such as 1,2-dioleoyl-sn-glycero-3-phosphocholine (DOPC) and cholesterol being negative (with spontaneous curvature values of -0.091 ± 0.008 nm^{-1} and -0.494 ±

0.013 nm^{-1} respectively), and 1,2-dipalmitoyl-sn-glycero-3-phosphocholine (DPPC) being positive (with a spontaneous curvature value of 0.068 ± 0.032 nm^{-1}) [55]. A great variety of structures can be formed, from common micelles (Figure 1.2d) and lamellar structures (Figure 1.2e) to more exotic inverted structures such as the inverted micellar phase (Figure 1.2f). The contribution of molecular-level structure on large scale lipid assemblies demonstrates the influence lipids can play across multiple length scales. The fact the self-assembly of lipid structures does not require strong covalent bonding but are instead held together by weaker interactions such as hydrophobic interactions, hydrogen bonding, weak electrostatic interactions and van der Waals interactions allows lipid structures to be soft and fluid-like [46]. This soft, fluid-like nature allows the lipids in biomembrane to be dynamic and adapt their geometry [56], mechanical properties [57,58] and composition [18,59] to transiently reorganise membrane structure and function. Cells utilise this ability to dynamically remodel lipid structures into different conformations for different uses, from micellular structures to facilitate material transport [60], to membranes going through transformations reminiscent of topologies in inverted phases during budding, fission [61], and endocytosis [62]. Of particular interest to the studies discussed in this thesis are the lamellar structures such as monolayer, bilayer and multilayer membrane structures. Lamellar structures are the conformation utilised by cells to create barriers, having tuneable permeability, bespoke mechanical properties and structural stability [53]. Similarly, lamellar structures provide accessible tools for encapsulation, making them useful in methods of drug delivery[63], cosmetic formulation [64] and flavour encapsulation [65]. Notable examples of lamellar structures are small unilamellar vesicles (SUVs), large unilamellar vesicles (LUVs) and giant unilamellar vesicles (GUVs), which are commonly used in research and industry due to their facile formation (which is discussed in further detail in Chapter 2.4). The transformation of all these structures is linked to membrane composition and fluidity; both intrinsically linked to the overall phase behaviour of the lipid membrane.

Aside from influencing the value of the packing factor, the tail-groups also have a strong influence on overall membrane physiology. The hydrocarbon chains of the tail-groups are attracted to each other via van der Waals interactions and longer tail-groups typically increase the membrane cohesion. Additionally, lipids with fully saturated tail-groups can pack tightly together, further reinforcing attractive van der

Waals interactions between the tails, decreasing the lipids mobility and increasing the melting temperature of the membrane. For example, DPPC bilayers exhibit a melting temperature of 41 – 43 ^{o}C [66,67], compared to DMPC (24 ^{o}C) and 1,2-dilauroyl-sn-glycero-3-phosphocholine (DLPC) (-2 ^{o}C) [66]. Partly unsaturated tail-groups' chains have more conformational freedom, with the associate bonds in the acyl chain able to freely rotate. This tends to disrupt close-packing and lowers the melting temperature for the membrane: DOPC and DPPC have very similar length alkyl tails, but DOPC has a significantly lower melting of -17 ^{o}C [66]. As a result, DOPC bilayers are completely fluid at room temperature.

Cells can alter the amount of saturated and unsaturated lipid tails in their membranes to control the membrane's state at physiological temperatures, for example, to allow protein molecules to diffuse along the membrane [46]. Studies on zebrafish embryos found that the membrane could tune its composition depending on the environmental temperature during the embryo's development. At lower temperatures, cells produced less monounsaturated fatty acid chains and a broader distribution of lipid chain lengths [68]. Such adaptive changes in composition can help maintain the membrane fluidity and ion permeability even at lower temperatures.

1.2.2 Membrane phase and fluidity

The capability of lipid structures to dynamically remodel is intrinsically related to their ability to move within the plane of the membrane. This fluidity allows an inextensible surface such as the lipid membrane [69] to dynamically reorganise and adapt to mechanical stresses and accommodate rapid changes in membrane area [70,71]. Membrane fluidity also enables protein/lipid organisation to be dynamically altered, allowing the formation of distinct phases within a continuous membrane. Lipid phases are commonly categorised as liquid-disordered (L_d), solid gel ($L_ß$), and liquid-ordered (L_o), illustrations of which are shown in Figure 1.3a-c respectively. Solid gel phases have high acyl chain order and low diffusivity; liquid-ordered shows high acyl chain order and high diffusivity while liquid-disordered is characterised by low acyl chain order and high diffusivity. Phase diagrams help illustrate the possible phase states of a membrane in thermodynamic equilibrium, many of which can coexist [72]. Such diagrams, similar to Figure 1.3d, are often deciphered by mapping

extensive experimental results, can be used to highlight compositional regions of criticality and coexistence, aiding researchers to appropriately selected model compositions for their study [18,59,73,74].

The various phases accessible to lipid membranes help create a complex array of behaviours directly linked to the lipid miscibility, segregation and coarsening within and between, the phases. This behaviour can occur at a variety of time and length scales in membranes with domains of a distinct composition having been imaged at the nanoscale [75] and microscopically [59,72]. These domains possess dynamical features and are heavily dependent on temperature and composition [18]. Phase transitions between gel and liquid phases can be induced by heating/cooling lipid systems [76], with possible coexistence of both phases depending on lipid composition in binary systems [59]. The addition of cholesterol adds complexity to this behaviour, being able to induce the coexistence of L_o and L_d phases in ternary lipid compositions. Cholesterol is able to interact with saturated and unsaturated lipids, which possess relatively high and low melting temperatures, respectively. This allows it to disorder the $L_ß$ phase by disrupting the acyl chains, and order the L_d phase by condensing and ordering chain packing [59,77]; overall this enables a L_o phase to coexist with an L_d phase. It should be noted that cholesterol's ability to promote ordering and rigidity of fluid lipid membranes occurs even in single phase liquid-disordered systems, for example in 1,2-dimyristoyl-sn-glycero-3-phosphocholine (DMPC) and cholesterol mixtures as reported from nuclear magnetic resonance and differential scanning calorimetry measurements [78,79].

Although the presence of distinct coexisting microdomains has not been directly visualised in cell membranes [23,25,26], macroscopic phase separation of L_o and L_d phases has been commonly observed in model lipid vesicle systems [19,59,72,80–82]. The coexisting L_o and L_d domains coarsen up to sizes of tens of microns, and even larger, in diameters with smooth circular edges, as shown in Figure 1.3ii, 1.3iii. Lipid domain structure tends to be in registry between the proximal and distal leaflets, with experimental results showing a strong coupling exists between L_o and L_d domains of the inner and outer leaflet for liposomes [83]. Similarly, L_o and L_d domains in supported lipid patches tend to remain in registry at equilibrium [84–86], but deregistration is possible in high shear flows [87].

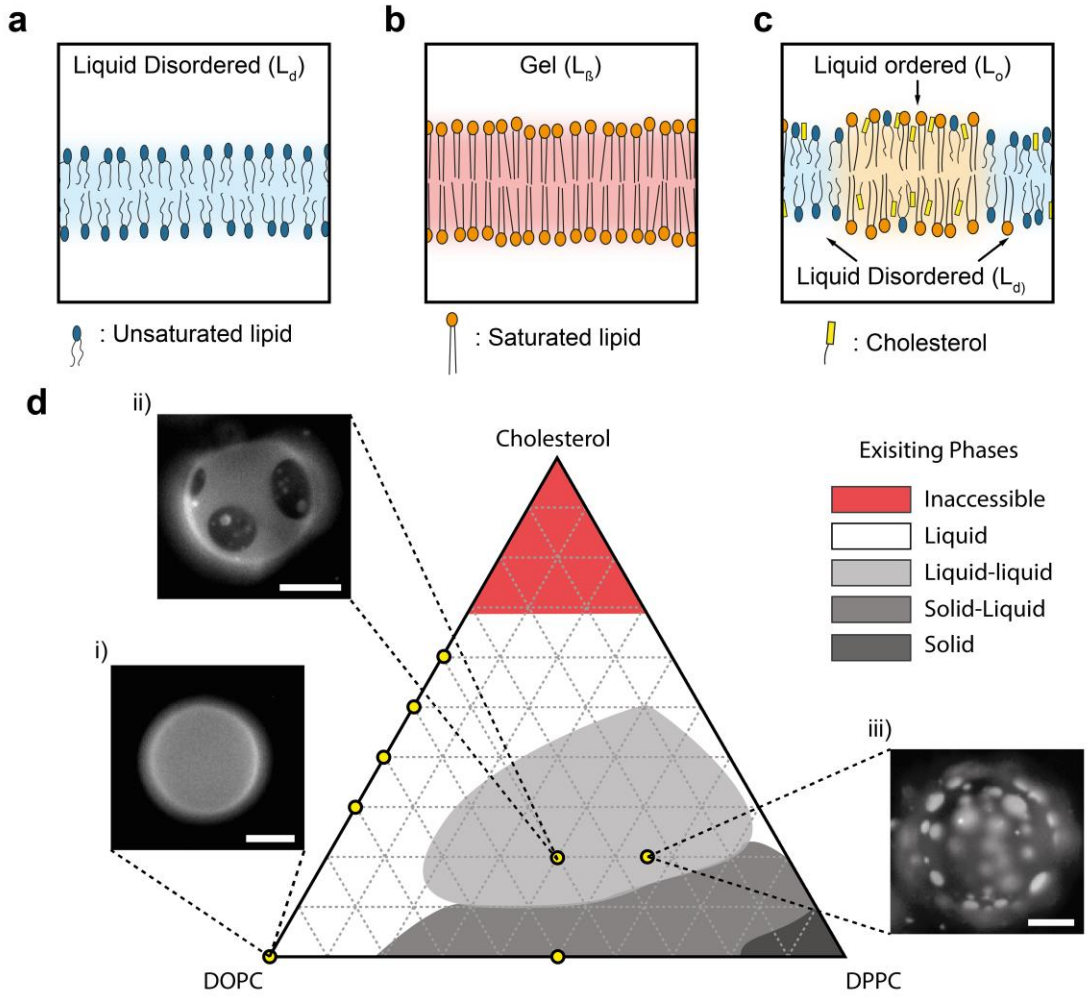

Figure 1.3: Membrane phases in ternary lipid bilayer mixture. Illustration of the lipid bilayer phases liquid-disordered (a), gel phase (b) and liquid-disordered (c) formed from mixtures of unsaturated, saturated lipids and cholesterol. Sketch of existing phases at different compositions of DOPC (unsaturated lipid), DPPC (saturated lipid) and cholesterol (d). Regions of each existing phase are adapted from [59], with permissions from Elsevier. Each point represents the position of compositions tested in the experimental section, with example fluorescent images of giant unilamellar vesicles of composition (i) Pure DOPC (ii) DOPC:DPPC:Cholesterol (40:40:20 molar ratio) and (iii) DOPC:DPPC:Cholesterol (16:64:20 molar ratio). Scale bars are 20 µm.

The main phase transition temperature can be different between proximal and distal leaflets with some decoupling [76,88]. However, this tends not to be the case with domain structure between leaflets, which usually remains in registry despite theoretical studies suggesting that may not be the case for lipid membranes containing cholesterol [89].

The observation of coexisting liquid phases in ternary lipid systems inspired ideas of lateral heterogeneity being present in the cell membrane. The fact lipid membranes can possess coexisting liquid phases allows for the formation of regions

with distinct compositions, melting temperatures and mechanical properties, while maintaining overall membrane fluidity and integrity. This provides a potential mechanism for biological membranes to control the lateral organisation of membrane proteins, initiate membrane signalling and tune various membrane biophysical properties. The proposed microdomains (or lipid rafts) are expected to be in the order of tens of nanometres in cells, based on Förster resonance energy transfer (FRET) and multiphoton measurements [23–26], with diffusivities theorised to be on the order of ~ 0.1 - 1 $\mu m^2 s^{-1}$ [90]. Unfortunately, although widely studied, the various interactions present in between $L_ß/L_o/L_d$ phases is not fully understood, even in the model lipid systems. The corroboration of such investigations is often hindered by several factors, including miscibility interactions being strongly dependent on the lipids used [72], the complexities added by the effects of changing specific lipid components [59] and the overall sensitivity of morphologies to lipid ratio and impurities[16].

All of these factors hamper the derivation of a complete and consistent phase diagram for many ternary lipid systems. This complexity is likely key for many biological systems to remain highly adaptable and robust to internal and external changes.

Aside from lipid composition, another vital component is missing from the picture when trying to model cell membranes. The cell membrane is not an isolated structure but is connected to supporting cellular structures like the cytoskeleton and extracellular matrix. These supporting structures are built up of various proteins with the cytoskeleton being composed of actin filaments, microtubules and intermediate filaments [91]. The extracellular matrix includes a combination of proteins and carbohydrates, such as proteoglycans complexes, fibronectin and collagen fibres [92]. Transmembrane proteins such as integrins mediate a dynamic, two-way link between the cytoskeleton and extracellular matrix, aiding the synchronisation of the two structures [8,93]. These supporting structures, and their synchronisation, play an important role in membrane locomotion, structural stability, and likely their lateral organisation. Supported lipid membranes provide an ideal tool to decipher such elusive yet influential interactions between the substrate and supported lipid membrane.

1.3 Supported lipid membrane: Relevance for biological models

It is well-known that the growth of cells and tissues necessitates a substrate, a supporting surface without which most tissue cells are non-viable in solution [94]. Supporting substrates are therefore vital for tissue development [94], with cells responding differently depending on their environment, whether it is the surrounding tissue matrix, adjacent cells or synthetic substrates. Synthetic substrates are commonly used for in *in-vitro* models, with a compelling example found in the directed differentiation of stem cells via gel matrix elasticity [95]. This necessity of a support is clear when put into the biological context, with structures like the cytoskeleton and extracellular matrix being ubiquitous inside and between tissues [91,92], (Figure 1.4).

The cytoskeleton provides the internal link to the cell's external environment. Through its dynamic assembly, the cytoskeleton also spatially organises cellular content and help the cell move and change shape [91]. Signalling between the extracellular matrix and the cytoskeleton occurs through the lipid membrane. This indicates that the interactions between the membrane and its substrate are crucial to understanding how the cell "feels" and responds to its environment, as well as how it integrates and coordinates these responses between cells and tissues. Although the cytoskeleton is a dynamically assembling and dissembling structure that remodels the cell through coordinated forces, it must remain bound within the plasma membrane. The membrane and the supporting cytoskeleton must therefore be coupled efficiently. One mechanism enabling modulation of the actin cortex by the plasma membrane is the phosphoinositides and GTPases that can modify the actin monomer pool and actin assembly respectively [96,97].

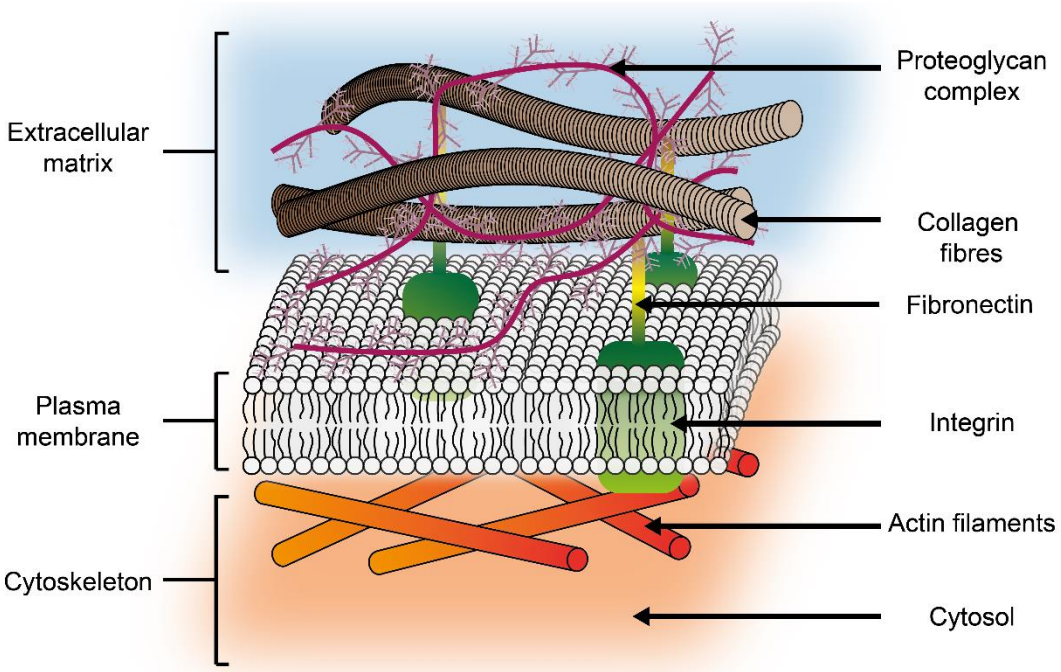

Figure 1.4: Schematic of cellular interfaces supporting the plasma membrane. The extracellular matrix, containing components such as collagen fibres and proteoglycan complexes is anchored by points of focal adhesion structures (e.g. fibronectin and integrin). The plasma membrane is also scaffolded by the cytoskeleton, containing various filaments, e.g. actin filaments, providing support and a means to generate forces to aid cell movement and shape changes. The figure was created based on images publicly available at http://en.wikipedia.org/wiki/Cell_membrane.

Actin networks have also been shown to have an impact on the lateral fluidity of adhered membranes. A study based on fluorescence correlation spectroscopy (FCS) showed that egg-PC lipid membranes displaying a significant decrease in membrane lateral diffusivity when adhered to a minimal actin cortex, dropping from $9.9 \pm 0.6\ \mu m^2 s^{-1}$ to $4.8 \pm 0.4\ \mu m^2 s^{-1}$, and with a clear correlation between reduced membrane mobility and actin density [98]. Other studies found that the presence of an actin meshwork underneath the lipid membrane had consequences on the membrane phase behaviour, with the suppression of large-scale phase separation below the transition temperature [99], and in some cases an altogether absence of phase transition [100]. Interestingly, super-resolution observations indicate that the actin network does not destroy all lateral organisation in the membrane, with L_d domains appearing to align along actin fibres [100]. In fact, actin structures can be utilised to impart lateral membrane organisation: the actin cortex can self-organise into a variety of patterns including bundles, asters and stars [101]. Order in the plasma membrane is increased over asters, but not altered near stars or actin bundles. This behaviour shows how interactions between the actin cortex can be used to modulate

the local membrane environment without perturbing the macroscopic mechanical properties of the cell. Generally, the consequences of an underlying actin network are not limited to the in-plane organisation of the membrane and a model actomyosin cortex has been shown to induce geometrical membrane transformations such as membrane wrinkling when the adhered actomyosin cortex is contracted [102].

Taken together, these studies clearly demonstrate the importance of the role played by the cytoskeleton in the membrane's molecular organisation and behaviour. It is, therefore, necessary to carefully consider the substrate's surface properties when attempting to replicate the fundamental behaviours of biomembranes with minimal model systems. Hereafter, the focus is placed on the influence of the substrate on membrane organisation in model lipid systems.

1.4 Supported lipid bilayers: Substrate impact

Supported lipid bilayers are bidimensional lipid structures formed by two lipid monolayers (leaflets) assembled in a sandwich so as to expose only the headgroups, and existing at the surface of an immersed solid. Although lipid monolayers are also viable supported lipid structures [1], lipid bilayers are preferable to study biologically relevant systems, which they reflect more accurately. They spontaneously self-assemble on hydrophilic surfaces with the ~ 5 nm thick double leaflet structure not directly adhered to the substrate surface but separated by a few molecular layers of water (typically 1 – 2 nm thick) [2]. This nanoconfined layer of water has peculiar properties, such as an increased heat capacity [103] and a viscosity proposed to be 10^2 - 10^6 times higher when compared to bulk water [104,105]. These changes are consistent with the water confined between the bilayer and the substrate adopting a more ordered molecular arrangement that results in a glassy behaviour. This is a consequence of two combined effects: a reduced conformational entropy and a strong interaction between the water molecules and the two confining surfaces. It is important to keep in mind that the water is not "frozen" but allows the lipid bilayer to maintain lateral diffusivity even while adhered

to the substrate surface. This property alone already makes supported lipid bilayers a powerful tool in the exploration of membrane biophysics.

Another advantage of supported lipid bilayers is their easy fabrication. Several methods exist for the formation of supported lipid bilayers, most notably Langmuir-Schaefer/Blodgett [106] and vesicle deposition [107–109]. A schematic representation of both methods shown in Figure 1.5. The vesicle fusion method holds many advantages including easy application to a variety of different surfaces (of varying size and geometry), organic solvent free bilayers, and fabrication of lipid bilayers on substrates with complex topographies. Moreover, vesicle deposition also allows for the continuous measurement of a variety of membrane properties during the transition from free-floating liposomes to adhered bilayer [85,108]; making this method ideal for studying the influence of substrate interactions on membrane properties. It will be used extensively throughout this thesis and in particular in Chapter 4.

Although conceptually relatively simple, the transformation process of colloidally suspended lipid vesicles into supported bilayers is complex. Factors such as the vesicle composition, size, surface charge, coupled with substrate roughness, hydrophobicity and finally the solution pH, ionic strength and the osmotic pressure on vesicles all contribute to the pathway and success of the supported lipid bilayer formation. This renders the vesicle deposition methods slightly esoteric with identical conditions often difficult to reproduce [1]. Even when a supported lipid membrane is successfully formed, a given type of membrane can possess different morphologies depending on the formation history. The importance of the formation history has been evidenced in coarse-grain simulations modelling deposited vesicles forming lipid patches in a “partially” or “fully” disintegrate state, depending on the strength of membrane adhesion to the hydrophilic surface [107]. Other coarse-grain simulations revealed two vesicle fusion pathways, each tuned by the substrate roughness and hydrophilicity [110]. These simulations did not only corroborate previous experimental studies [108,111] but also showed that different fusion pathways result in different redistributions of lipids between the membrane proximal and distal leaflets after fusion. The membrane then undergoes a variety of conformation changes to become a flat, stably supported bilayer, each influenced by the surroundings and hence the interfacial properties of the substrate [107].

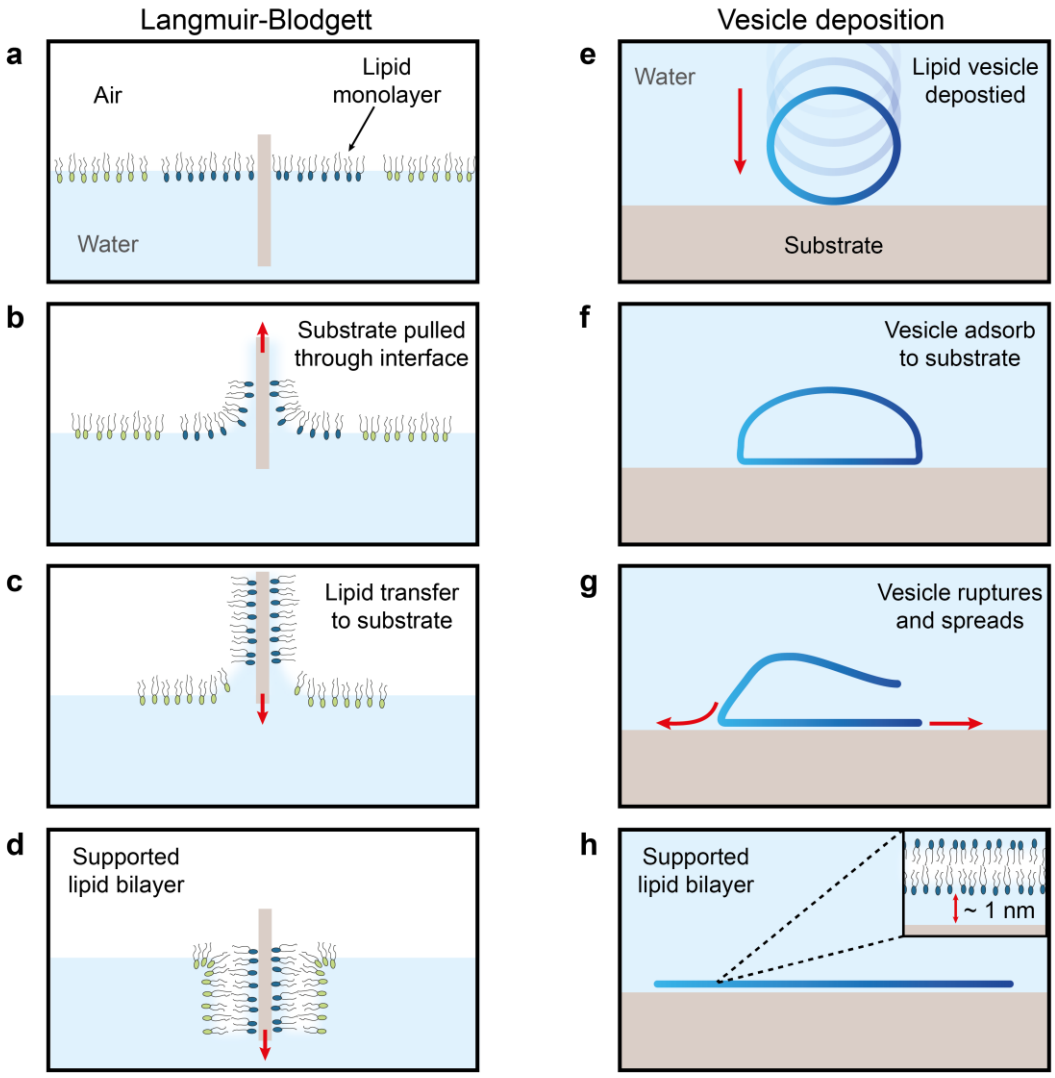

Figure 1.5: Langmuir-Blodgett and vesicle deposition methods. In the Langmuir-Blodgett method (a-d), a hydrophilic substrate surface immersed in a Langmuir trough (a), is pulled through a lipid monolayer at the air-water interface (b), transferring the lipid to the substrate surface (c). Upon re-submerging the substrate, a supported lipid bilayer is formed (d). In vesicle deposition (e-f), lipid vesicles are deposited on a hydrophilic substrate immersed in aqueous solution (e). These vesicles adsorb to the substrate surface (f) and spontaneously rupture and spread (g) in a process of vesicle fusion, subsequently forming a supported lipid bilayer (h).

1.4.1 Substrate impact on the lateral diffusivity in lipid bilayers

One of the most obvious effects of the substrate on the supported bilayers' properties is the impact on lipid diffusivity. The lateral diffusivity is reduced on substrates such as mica and glass when compared to free GUVs [2,112,113] with reports of a reduction of up to 50% [114]. Yet, despite the reduced lateral diffusivity, supported

lipid bilayers exhibit an increased flip-flop rate compared to free liposomes: single particle tracking experiments demonstrated a flip-flop half-time of the order of hours for vesicles but only seconds for supported lipid bilayer [105]. The increased flip-flop rates were attributed primarily to the increased density of packing defects that form when the membrane is cooled down through its main transition temperature [114]. Transient structure defects may also play a role, but they are present in both free-standing and supported membranes [115].

Surface roughness plays a significant role in modulating the membrane diffusivity. Using glass slides that were polished and etched to create controlled surface roughness, Blachon et al. [116] showed that the diffusivity of 1-palmitoyl-2-oleoyl-sn-glycero-3-phosphocholine (POPC) and DMPC membrane decreased from ~1 $\mu m^2 s^{-1}$ to 0.2 $\mu m^2 s^{-1}$ when the substrate roughness was increased from ~0.1 nm to 2 nm root mean square roughness [116]. This drastic loss of fluidity was attributed to local, highly curved regions on nanorough surfaces, causing pinning centres, an increased number of defects and increased local membrane order and packing. Results combining epifluorescence microscopy and fluorescence recovery after photobleaching (FRAP) demonstrated that nano-corrugated surfaces hindered macroscopic L_o domain coarsening when compared to smooth regions on the same substrate [117]. Recently, similar results have also been shown with high-resolution techniques such as atomic force microscopy (AFM) where a defined roughness introduced on mica surfaces could arrest domain coalescence and limit phase separation to molecular accretion [118]. The roughened mica reduced the correlation length of domains to 57 nm, down from 2-3 µm observed on smooth mica surface [118].

Roughness is not the only contributing factor though, with smooth hydrophilic substrates such as mica, still demonstrating reduced lateral diffusivities of 0.49 $\mu m^2 s^{-1}$ for egg-PC supported lipid membrane despite a root mean square roughness of only 0.03 nm [104]. It is also worth noting that many of the diffusive properties observed in lipid bilayers do not follow simple Brownian motion [119]. Anomalous diffusive behaviours can be found in the decoupling upper and lower leaflet diffusivities, as measured with single particle tracking [104] on egg-PC membranes supported on aluminium oxide.

Some of these differences may be linked to the increased order [120–123] and viscosity [104,105] of the interstitial water layer, which in turns leads to a disparity in the friction experienced by the two leaflets, one facing the bulk water and the other the confined water layer [105]. Issues related to diffusivity are further complicated by the introduction of ionic species to the solution, in particular with respect to the confined water layer [124]. The addition of chloride salts of monovalent metal ions demonstrated a significant improvement in the lubricating properties of confined water. This was explained by the ions disrupting the ordered hydrogen bond network of the confined water with an effectiveness following a direct Hofmeister series [124]. Ions present in the confined water layer can also modulate the local membrane stiffness and global lipid diffusivity [125], as revealed by a recent study combining AFM and FRAP. The results suggested that the confined ions can modulate the interaction between lipids which in turn affected the lateral diffusivity in the membrane. It is not difficult to see how such effects could extend to natural biomembranes in aqueous environments when supported.

1.4.2 Miscibility, criticality and phase transition effects

The presence of a substrate also has consequences on other vital biophysical properties of the membrane, including its thermodynamic state and stability. The phase behaviour of the lipid membrane is of particular importance because local composition differences in membranes are thought to be responsible for much of lateral organisation, and the precept of the controversial lipid rafts.

Supported lipid membranes have a markedly increased main phase transition temperature when supported on mica and glass substrates [76,87,88]. This change in the main transition temperature is not always uniform across both leaflets, with a decoupling observed for bilayers formed on mica [76]. Parameters such as incubation temperature, the type and concentration of the ionic species present also modulate this substrate effect [76]. These parameters influence the membrane-substrate interactions which in turn create an asymmetry in the phase transition of the upper and lower leaflets.

Membrane-substrate interactions are thought to stabilise phase separated lipid domains. The presence of a substrate effectively fixes the lateral organisation [85],

hence inhibiting domain coarsening and restricting macroscopic phase separation [118]. Cellular substrates such as the cytoskeleton and extracellular matrix may fulfil similar functions for the plasma membrane, although this remains to be clearly demonstrated.

Substrates have been shown to maintain the diffusion coefficients of individual molecules within the L_o/L_d domains, but the diffusion of these domains themselves is drastically altered [19]. Studies have shown that when fused to a substrate surface, L_o domains previously capable of traversing the L_d phase become fixed in position and large-scale domain coarsening is inhibited [85]. Interestingly, recent studies have demonstrated that previously L_o/L_d domains macroscopically separated (Figure 1.3d) no longer coarsen and segregated once the supported bilayers is heated and cooled through its main phase transition [86]. This has been linked to substrate interactions such as drag force of the underlying water layer, impeding large scale coarsening to below a resolvable length scale. These results could explain why large-scale coarsening is never seen in vivo, where the membrane is adhered to a cytoskeleton, possibly obstructing large scale phase separation close to critical temperatures. Questions surrounding these behaviours are further discussed in the investigations presented in Chapter 6.

At the molecular level, the consequences of the altered of L_o/L_d domains dynamical behaviour can be seen near criticality. Critical points occur at particular combinations of composition and temperature in the phase diagram, where tie-lines merge into a single point and multiple compositions can coexist[19]. Critical compositions are often considered as prime candidates for the formation of raft-like structures, with model GUV systems exhibiting transient fluctuations in domain size and structure. This behaviour can be replicated with giant plasma membrane vesicles (GPMVs) that have the exact lipid compositions of native membranes [126]. The presence of a substrate surface increases the main transition temperature of the membrane and shifts its point of criticality, and also alters the dynamics of domain formation at these regions in the phase diagram [18]. Studies with supported lipid membranes have revealed that several behaviours of lipid bilayer systems are only observable once the bilayer adheres to a supporting substrate.

1.4.3 Mitigating the substrate influence

In all the cases discussed so far, the model membrane is closely adhered to the substrate surface, only separated by a ~0.5 - 2 nm water layer from the substrate [2]. While the separation is large enough to allow for membrane self-healing and lateral diffusion, it is not sufficient to fully mitigate the influence of the substrate. In the presence of transmembrane proteins, such a small interstitial space may result in proteins being denatured due to direct contact with the substrate [127]. Denaturing of proteins can be avoided using a hydrophilic polymer interlayer which sufficiently increases the space between the membrane and the substrate to negate many of the substrate effects, maintain lateral diffusivity, and allow for membrane proteins to be incorporated into the bilayer. The two most common strategies utilising polymer interlayers are polymer cushions, and polymer tethers [128]. Polymer cushions rely on depositing polymeric materials at the interface between the bilayer and underlying hard substrate. Direct contact of proteins can be avoided by using "cushions" made from various materials such as polyacrylamide brushes [129] and Polyethylene glycol (PEG) [130] hydrogels [131] or biological materials such as cellulose [132] (Figure 1.6a). These cushions are thought to mimic the extracellular matrix and the cell-surface glycocalyx [128], and can be as thin as ~ 10 nm while successfully supporting the membrane [132]. Alternatively, polymer tethers and spacers can be utilised to distance the membrane and reduce substrate interactions, as shown in Figure 1.6b below. Lipopolymers are commonly utilised as they can be heavily tailored to have different surface couplings groups, lengths and side functionalities [133]. Lipopolymers offers advantages in tuning membrane-substrate distance as well as viscosity, both of which are polymer layer dependent. A caveat of these spacers is that the mismatch between the lipid anchor and polymer tethers can render such systems unsuitable for preparations involving direct self-assembly of the lipid bilayer [128]. Polymers can also become untethered, bind to the membrane and hence distort the membrane behaviour, for example causing anomalous diffusion[134]. For both polymer cushions and tethers, balancing the attractive and repulsive interactions must be tuned precisely to ensure the lipid system does not collapse and remains a continuous bilayer with mobile lipids [128].

Soft, flexible, polymeric substrates can not only be utilised as cushions and tether but can act as a robust surface for direct lipid bilayer self-assembly [135,136]. Polymeric substrates have the advantage of being much more deformable, and easier to mould. Also, being a filamentous network makes them a better mimic in terms of simulating the mechanical properties found in the natural support structures of the cell, especially when compared to hard substrates such as glass.

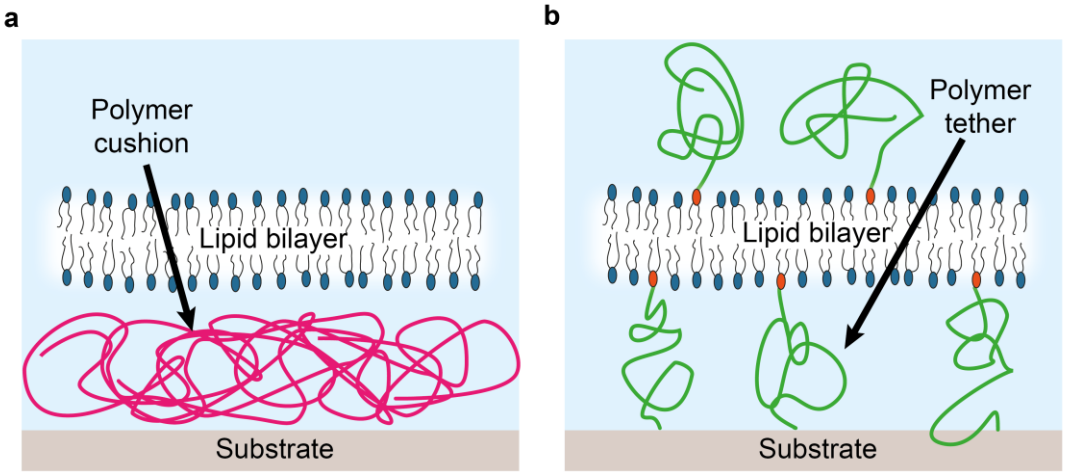

Figure 1.6: Schematic of polymeric spacer techniques to mitigate substrate influence. Images depict a polymeric cushion (a), and polymeric tether (b) used as spacers for supported lipid bilayer on substrate.

While often desirable, negating the influence of the substrate leaves a wealth of membrane behaviours that depend on interactions with a support unexploited. This is to be taken in conjunction with the development of nanomaterials, where the control of a substrates interfacial properties can be tuned on a nanoscale level. Designer nanomaterials are already being employed in a variety of technologies, but there is still a lack of understanding of their toxicity [137] and how they enter, interact, and penetrate the cellular interface [138]. In this respect, supported lipid bilayers provide an ideal system for investigating the influence of nano-interfacial effects on the membrane structure, morphology, and composition.

1.5 Passively remodelling of supported lipid membranes

Understanding membrane-substrate interactions facilitates the development of predictive associations between interfacial properties and the resultant membrane behaviour. This exploration will not only help unravel the mysteries of the cellular

interface but can also be exploited for future biomimetic surfaces and devices. Technologies in advanced drug delivery and targeting [139], lab-on chip[140] and organ-on-chip devices [141] would all significantly benefit from such knowledge.

1.5.1 Chemical surface patterning

Surface patterning has long been used to modify and control lipid bilayer organisation on substrate surfaces. The first designs used simple mechanical barriers to inhibit membrane spreading, creating 2D corrals of fluid, but distinct membrane patches [142,143]. Micro-contact blotting has also been heavily utilised to create surface patterning [135] and has more recently been extended to create phase segregated supported lipid bilayers of bespoke composition through stencilling [144]. More interestingly, chemical patterning of a substrate surface can be used to promote the spontaneous self-assembly of lipids into designed patterns across a substrate. Grid-like diffusive barriers can be created via chemical patterning of the substrate's surface [145]. These techniques can be used to create both hydrophilic and hydrophobic regions on the substrate, causing the adhered lipids to self-assemble into spatially controlled arrays of lipid monolayers and bilayers respectively [146]. Although initially limited in resolution, many patterning techniques are approaching nanometre resolutions. For example, Dip-pen nanolithography has been utilised with lipids as ink, to create nanoscale features on self-assembled monolayer (SAM) surfaces [147]. Such a control over the lipid organisation represents an extraordinary opportunity for biotechnological devices, that could be exploited to create systems analogous to the surface patterning used by biological interfaces to modify the shape and function of membranes.

1.5.2 Topographical surface patterning

Micron-scale scale mechanical barriers have also been effectively used for surface patterning to inhibit lateral lipid diffusion [142]. Although manually made surface scratches may seem an obvious tool to prohibit lipid spreading, the impact of such topographical features becomes more nuanced when shrunk to the nanoscale. Nanotextured surfaces can control the sorting and partitioning of L_o/L_d domains, using topographic features to create and disrupt domain structure in supported

model membranes [117]. Individual molecular species can also be affected differently, with fluorescently labelled lipids showing curvature induced slowing and aggregation with a magnitude dependent on the fluorescent label attached to the lipid [148,149].

Here, nanoroughness is to be understood as a root mean square roughness on the order of nanometres. Nanorough surfaces can significantly impact membrane diffusion, without damaging membrane integrity [116]. Nanoroughness tends to decrease the lateral diffusivity of lipids, in some case up to 5-fold [116]. Such changes in diffusivity originate from increased lipid trajectories, lipid confinement, hidden areas, increased number of defects, altered surface adhesion, and local curvature. When all these factors are disentangled, it is high local curvatures (radius of curvature between 10 and 40 nm) that most significantly lowers the membrane diffusivity [116]. This is likely due to a curvature-induced increase in lipid order, packing, and bending rigidity, acting together to reduce the membrane fluidity[150]. Curvature effects are further discussed in Chapter 6.5.2.

The effects of surface curvature are not just limited to changes in lipid mobility but can also induce morphological changes. Topographic features in the order of 1 - 22 nm can cause a loss of membrane integrity and the formation of pores [151], as shown in Figure 1.7. Outside of this range, the membrane can flow over the features, following the underlying topography. This can be exploited in technology to create nanopores that host single molecules [152].

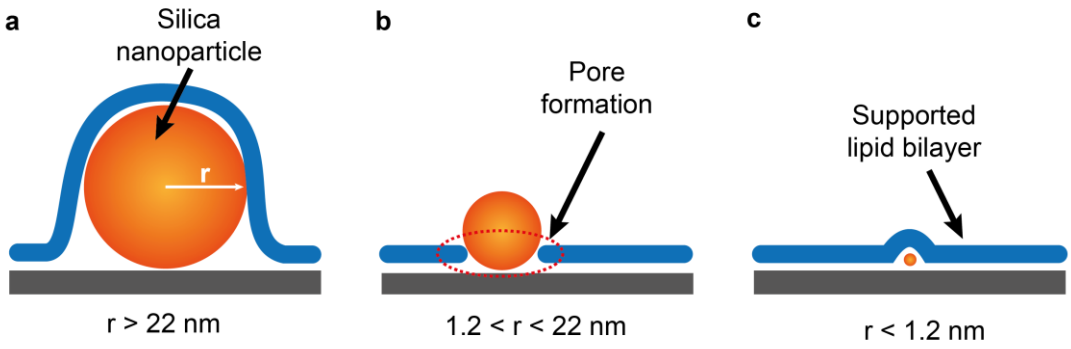

Figure 1.7: Impact of nanotopography on supported lipid bilayers. Nanoparticles below 1.2nm allow the bilayer to form on top (a), features above 1.2 nm cause the formation of pores in the membrane (b) until a size of 22 nm where membrane follows contours of particles once again. Figure adapted from reference [151], with permission from Langmuir. Copyright 2009 American Chemical Society.

While curved surfaces pose an increased difficulty for self-assembly of continuous lipid bilayers on the micron-scale, these difficulties are often overcome by modulating the lipid charge or the ionic composition of the aqueous solution [153]. Hence, such curved substrates have been used to model biological processes in membranes such as membrane budding and exocytosis [61]. Patterned substrates can also help reproduce molecular mechanisms that involve curvature-associated proteins and raft activity in membranes [154]. This is the case for endocytic vesicle scission and the self-assembly of dynamin [61]. Many of these mechanisms can also be applied to the partitioning and purification of active membrane species [155]. This has already been demonstrated with lipid migration and sorting in curved architectures [156], enabling liquid-ordered domains to preferentially distribute in regions of lower curvature. Similarly, in the work of Steinem et al. [157–159], pore-spanning lipid membranes were utilised to control lipid species segregation, showing that the domain formation in pore-spanning membranes depends on the geometric properties of the porous array: the rims of curved pore are unfavourable regions for L_o domains formation due to their larger bending modulus [158]. The size of the pores could hence be used to tune the size of the L_o domains confined in the pore-spanning membrane.

1.6 Dynamically remodelling of supported lipid membranes

Many of the previously described behaviours involve the passive manipulation of membrane properties by static substrate features. However, cells are dynamical structures, changing their shape and composition in response to a variety of mechanical [94,160–162] and chemical stimuli [58,163,164]. During these transformations, the membrane often remains coupled to the underlying cytoskeleton, which also must respond to these changing stimulations. Indeed, studies have demonstrated that the cytoskeleton plays a key role in actively manipulating and maintaining plasma membranes in response to internal and external stimuli [58,91,93,96,165]. The interplay between the plasma membranes' dynamical response to external stimuli and the coupling to their support is not yet fully understood. Extending this understanding would aid the development of novel methods to actively control and manipulate the membrane's behaviour.

1.6.1 Supported membranes modulated by fluid shear

The active remodelling of the cytoskeleton requires the membrane to maintain its integrity under varying stress and strain rates. One of the main aspects to consider is the frictional force experienced by the membrane when its support evolves. Studies have shown that when using a hydrodynamic driving force, the frictional resistance experienced by the membrane under shear flow is not always uniform amongst membrane-bound species [166]. Both the sliding friction of the species within the membrane and the membrane-substrate lateral friction plays a significant role in modulating the species mobility [166]. Other studies have shown that under high enough shear rates, supported lipid bilayers can deregister their upper and lower leaflets, causing novel effects such as the formation of asymmetric membranes and the disappearance of previously phase-separated domains [87]. In all cases, the influence of the substrate is key to the observed behaviours, highlighting the intricate links between the apparent membrane behaviour and the substrate's interfacial properties.

1.6.2 Supported membranes modulated by electric fields

Electric fields can be used to control cell membranes and alter the membrane's properties. Exposure to high electric fields can cause a rapid and substantial increase in the conductivity and permeability of biological membranes. This change can be reversible or irreversible and has been demonstrated on cells and planar lipid bilayers [167,168]. Recent studies have shown that exotic lipid morphologies can be formed during the electroformation of lipids using external electric fields. Electroformation is traditionally used in the formation of GUVs. In GUV electroformation, alternating current (AC) electric fields are used to induce gentle hydrodynamic flows in a fluid cell containing an electrode coated with dried lipids (see Chapter 2: Materials and Methods for further details). These gentle hydrodynamic flows rehydrate and agitate the dried lipid layers in a fashion which creates unilamellar vesicles [169,170]. Although commonly done with flat plates or a cylindrical needle, exotic electrode geometries such as co-planer interdigitated electrodes can result in the formation of lipid nanotubes [171]. Lipid nanotubes can

then be used as a template for silica mineralisation, and the basis of new nanomaterials.

The use of electric fields is not only limited to controlling the membrane morphology; they can be used to the modulate the membrane's composition and lateral organisation. Lower voltages have been utilised to perform electrophoresis of molecular species tethered to solid-supported lipid membranes, controllably altering the local composition of lipids. This has been demonstrated with the separation and purification of charged fluorescent dyes [172], and the dynamical reorganisation of more complex lipid compositions that are capable of raft formation [173].

1.6.3 Supported membranes modulated by mechanical stress

The cell must respond to mechanical stimulation through various life processes, including cytosis, growth, replication and locomotion. Many of the forces experienced, induced, and interpreted by the cell are operated through the cytoskeletal network to which the membrane adheres. Various techniques have been employed to investigate the behaviour of membranes under mechanical stress including micropipette aspiration, magnetic/optical tweezers, cytoindenters, atomic force microscopy and microplate manipulation [174]. A caveat of this broad toolset is that each technique tends to elicit a different mechanical response from the system investigated.

Recently, flexible substrates have been used to study the response of adhered membranes to mechanical stretching. Studies have shown that bilayers confined to a substrate can passively regulate their shape and stress by adopting different conformations such as creating tubes, adsorbing adhered vesicles, and generating or resealing pores [56]. This behaviour illustrates some of the innate mechanisms available to lipid membranes in order to control their area while remaining attached to the supporting substrate. Most interestingly, membrane-substrate interactions are key to controlling many of these behaviours [175]. Depending on the substrate properties, different membrane behaviour such as sliding across hydrophilic surfaces, or sticking and tubulating on more hydrophobic interfaces [175] can occur under mechanical strain. Even on the nanoscopic length scales, differences in the membrane-substrate interactions can change the membrane mechanical response:

AFM results revealed that ions can modulate the membrane response at the nanometre level, leading to the nanotexturing of fluid supported lipid bilayers when placed under stress by the AFM tip [125]. This localised gel-like solidification of the membrane strongly depends on the ion species present in the solution [125].

This overview of recent results emphasises the ability and importance of local membrane-substrate interactions to modulate the biophysical response of supported lipid membranes. While still underexplored, the underlying mechanisms could be vital to the proper function of the cellular interface.

1.7 Conclusion

The ability of membrane-substrate interactions to induce specific cell responses is becoming well recognised in the scientific community, already gaining ground in organ-on-chip research [176]. This suggests that the development of future biotechnological interfaces may lie with solid-supported membranes first because of their easy fabrication, lower cost, robustness and second due to the many behaviours and mechanism that they can elicit from their interaction with the substrate. While the field is arguably still in its infancy, further research will not only allow for substrate-induced membrane responses to be predictable, but also controllable, opening the door to a variety of biotechnological innovations. With that in mind, this thesis will detail investigations into the influence of the substrates' properties on the behaviour of supported membranes. This includes the question as to how such effects can be controlled and exploited.

Chapter 2 will discuss the materials and methods utilised to measure the structure and properties of lipid bilayers across a variety of length scales and investigate the effect of the substrate on the behaviour of the system.

Chapter 3 discusses the mechanisms allowing functionalised substrates such as polydimethylsiloxane (PDMS) substrates to achieve the desired surface chemistries and topographies for later investigations.

Chapter 4 examines the deposition and fusion of vesicles onto a substrate, in particular, the mechanics of membrane reorganisation during vesicle fusion and its dependence on interfacial properties.

Chapter 5 discusses novel membrane-substrate interactions that enable the specific extraction of cholesterol from membranes supported on partially hydrophilic substrates.

Chapter 6 investigates the effect cholesterol depletion on the structure of phase domains and the disruption of fluorophores partitioning in ternary lipid compositions that exhibit L_o/L_d coexistence.

Finally, chapter 7 provides a brief summary and future outlooks regarding the work presented in this thesis.

Chapter 2: Materials and methods

With supported lipid bilayers as a minimal model system, investigations were conducted mainly using microscopy techniques to image the changes in membrane morphology and properties under the influence of substrate interactions. To study the membrane behaviour on a wide range of length scales multiple microscopy techniques were utilised. The macroscopic morphological changes (both in and out of the plane to the bilayer) are captured with fluorescence microscopy techniques which offer a global, non-invasive view. Many changes in the lipid organisation, composition and local structure such as lipid diffusivity and inferences to lipid packing changes can be also characterised with fluorescence techniques. The nanoscale properties of the membrane, supporting substrate and membrane-substrate interactions can be characterised with atomic force microscopy. These techniques can be further complemented by reflectance interference contrast microscopy and simple contact angle measurements to allow a full investigation of the substrate's influence on the membrane behaviour, including the possible exploitation of these effects to manipulate membrane processes, morphology, and composition.

In this chapter, each of the techniques utilised in the thesis is described, starting with a review of the protocols used for lipid preparation and supported bilayer formation.

2.1 Lipid preparation

The lipid species used in this thesis are 1,2-dioleoyl-sn-glycero-3-phosphocholine (DOPC), 1,2-dipalmitoyl-sn-glycero-3-phosphatidylcholine (DPPC) and cholesterol. All the lipids were obtained from Avanti Polar Lipids (Alabaster, AL). The saturated lipid (DPPC) and sterol (cholesterol) were obtained in powder form. Unsaturated lipids are susceptible to air oxidation during preparation [72,177,178], and hence DOPC was purchased in chloroform solution so as to limit oxidation due to air exposure during the sample preparation.

DOPC is a naturally occurring phospholipid that is used in many investigations; it is proven to successfully create supported lipid bilayers that can be probed by a variety of methods. Due to its low melting transition temperature of -17 ^{o}C [66], DOPC bilayers remain fluid and stable in an L_d phase at room temperature. Thus, DOPC lipid bilayers usually maintain a high degree of lateral diffusivity, facilitating membrane reorganisation due to substrate influences. DPPC is also naturally occurring and commonly used, but unlike DOPC, it has a relatively high main transition temperature of 41 – 43 ^{o}C [66,67], making DPPC predominantly gel-phase at room temperature. DPPC possesses the unusual feature of being able to exist in a so-called ripple phase. Unlike with the well-known fluid and gel phase membranes, ripple phase membranes present an asymmetric, saw-toothed rippled surface that can be identified with multiple techniques such as scanning differential calorimetry [88,179], X-ray diffraction [180] and AFM [181]. The ripple phase typically occurs at a temperature slightly above the main phase transition. It can exist in a stable or metastable state, depending upon whether the system is being heated up from the gel phase or cooled down from the liquid crystalline phase [180].

Combinations of these three lipids allow access to a wide range of phase behaviours, with different, lateral diffusivity, mechanical properties, miscibility and transition temperature (to name a few properties). This is true for a myriad of lipid combinations, but the wealth of literature available for DOPC/DPPC/Cholesterol mixtures makes them a reference system with foundational studies mapping the full phase diagram (work of Veatch and Keller) [59,72,81,82]. This phase diagram (see Figure 1.3) can be split into several distinct regions: a single liquid phase, a phase with coexisting liquid-liquid, coexisting solid-liquid phase and a single solid phase. Additionally, there is an inaccessible region above 66 mol% cholesterol, the solubility limit for cholesterol in phosphocholine bilayers [182,183].

2.1.1 Fluorescent label

The fluorophore or fluorescently labelled agent is a key component to many of the lipid mixtures being measured with fluorescence microscopy. These fluorescent labels allow the investigation of the formed lipid membranes using, in the present case, epifluorescence imaging and fluorescence recovery after photo-bleaching

(see Chapter 2.5.2 for further details). There is a wide library of fluorophores available, covering most of the visible range of excitation/emission wavelengths. However, choosing a suitable fluorophore is not straightforward because differences in their chemical structure can have a significant impact on their position within the lipid membrane, as well as the molecular organisation of the surrounding membrane. For the work presented in this thesis, three different fluorescent labels were used: 1,2-dipalmitoyl-sn-glycero-3-phosphoethanolamine-N-(lissamine rhodamine B sulfonyl) (ammonium salt) (Rh-DPPE) obtained from Avanti Polar Lipids (Alabaster, AL), 1,1'-Dioctadecyl-3,3,3',3'-Tetramethylindodicarbocyanine Perchlorate ($DiIC_{18}(5)$) obtained from Invitrogen® (ThermoFisher) and Naptho[2,3-a]pyrene (NaP) obtained from Santa Cruz Biotechnology (Heidelberg, Germany).

Many fluorescent probes have been demonstrated to alter membrane behaviour including mechanical properties [184], fusion pathways[108], lipid diffusivity [185] and miscibility temperature [81]. Repeating measurements using fluorescent probes with different structures and partitioning properties helped distinguish observed effects from specific fluorophore related artefacts. Rh-DPPE is a lipophilic fluorophore with the rhodamine molecule being attached to the phosphoethanolamine head group.

Rh-DPPE was used as the primary fluorescent label in most experiments; mainly due to its availability, widespread use and facile incorporation into the lipid membrane. Its strong fluorescent signal and resistance to bleaching allow for measurements over long timescales (order of hours) without the worry of a total loss of signal. In the present work, Rh-DPPE samples maintained strong fluorescent signals over hours, whereas NaP samples lost significant fluorescence over imaging periods of minutes.

$DiIC_{18}(5)$, another popularly used fluorescent label, resides amongst the acyl chains unlike Rhodamine and is known to impact membrane behaviour differently [148], making it a useful control. Both molecules still have a strong preference for the liquid-disordered phase and have similar excitation/emission spectra. This is known to cause signal crosstalk or “bleed-through”, where the emission from one fluorophore is detected across filter combinations dedicated for a different fluorophore [186]. Hence the simultaneous use of Rh-DPPE and $DiIC_{18}(5)$ in a single membrane is often counterproductive.

NaP is a fluorescent probe with dissimilar excitation/emission wavelengths to Rh-DPPE and has a strong preference for the L_o phase [187–189]. Simultaneous labelling of lipid patches with Rh-DPPE and NaP allows the L_o and L_d domains to be easily and complementarily distinguished. This property is used for the investigations carried out in Chapter 6 where the partitioning behaviour of fluorophores between L_o/L_d domains is examined under external constraints.

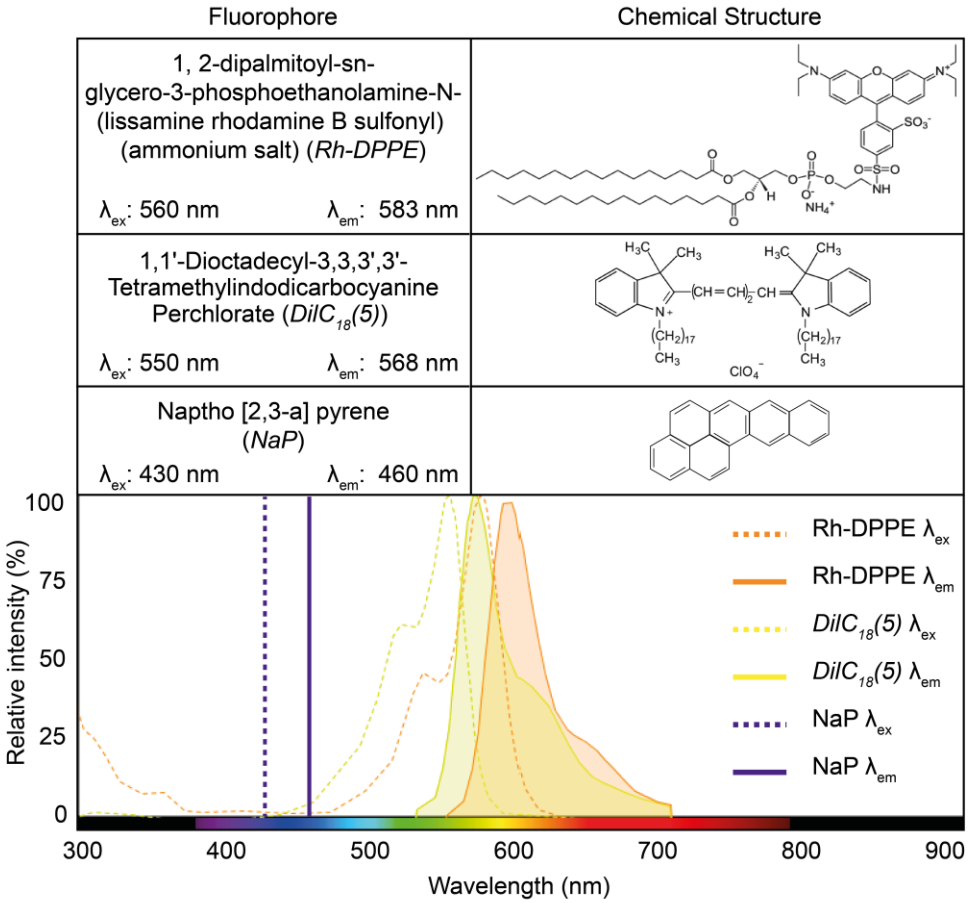

Table 2:1: Name and chemical structure of the fluorophores Rh-DPPE and $DiIC_{18}(5)$ and NaP. The nomenclature also states wavelengths corresponding to the maximum of absorption/emission for each fluorophore. The full absorption/emission spectra are also given for the fluorophores in aqueous solution (taken from reference [188,190] and adapted from ThermoFisher scientific © SpectraViewer, link https://www.thermofisher.com/uk/en/home/life-science/cell-analysis/labeling-chemistry/fluorescence-spectraviewer.html).

In all cases, even minimal amounts of fluorescent probes still have an impact on the membrane behaviour [81,185]. To mitigate this issue, concentrations of 0.1, 0.5 and 3 mol% were utilised when doping membranes with Rh-DPPE, $DiIC_{18}(5)$ and NaP respectively. This achieves a reasonable signal-to-noise ratio for the fluorescence

measurements while minimising the concentration of fluorophores used to label the membranes.

2.2 Buffer solution:

All experiments were performed in aqueous solution, using ultrapure water (18.2 MΩ, 0.5 ppm organics) obtained from a Merck Direct-Q® 3UV-R dispensing unit (Merck Millipore, Watford, UK). Sodium chloride and calcium chloride salts as well as the buffering agent tris(hydroxymethyl)aminomethane (TRIS) were purchased from Sigma-Aldrich (UK). The buffer solution composition used was 10 mM TRIS, 150 mM sodium chloride and 2 mM calcium chloride. The buffer was adjusted to pH 7.5 with the addition of concentrated hydrochloric acid. The addition of the salts facilitated the successful formation of supported lipid bilayer via vesicle deposition method,[85,191–193] screening long-range electrostatics by reducing the Debye length to < 1 nm. Sodium chloride also bolstered buffer salinity to a similar level as physiological saline but allowed the buffer to be a more biologically relevant medium than ultrapure water. Ions and buffer salts have a subtle but significant impact on the membrane-substrate, and lipid-lipid interactions; they affect the local hydration structure enough to modify the membrane behaviour [194]. The same buffer solution was used in all experiments, thus standardising the impact of the electrolyte solution on the membrane properties and enabling comparative studies disentangling the changes due to ions from substrate effects.

The osmolarity of all aqueous solutions was tested using an Osmomat 3000, freezing point osmometer (Gonotec®, Berling, Germany). Firstly, the osmometer was calibrated with ultrapure water (50 µL in an Eppendorf tube) followed by 50 µL measurement of the aqueous solution of interest in a clean Eppendorf tube. This process was repeated five times per solution to acquire a statistically meaningful value of the solution's osmolarity, resulting in an error of less than ± 5 mOsmol/L.

2.3 Substrate preparation

Correct and consistent preparation of the substrates is vital for all investigations. Each substrate was kept as clean as possible to ensure that generic contamination did not impact subsequent surface functionalisation or adhered sample properties.

2.3.1 Glass

All glassware (cover glasses, cover slides) were purchased from VWR (Leicestershire, UK). All glassware was first sonicated for 10 minutes in isopropanol followed by 10 minutes in ultrapure water in order to remove residual organics and contaminants. The clean glass was then dried with a gentle nitrogen flow. Glass substrates were subsequently exposed to low-pressure air plasma-treatment (also referred to as plasma oxidation) at a pressure of 1 mbar and power of 300 Watts (VacuLAB Plasma Treater, Tantec) for 30 seconds, pyrolysing any remaining contaminants. The cleanliness of the glass substrates after the protocol was completed, was controlled by placing a 1 µL droplet of water on the edge of the glass slides and observing full wetting (contact angle ~0 degrees).

As glass is transparent, relatively flat, and smooth [195], it is routinely used to support fluid lipid bilayers. Here, glass was used as a control substrate to offer a comparison point with other substrates of interest, in particular with how they modulated the bilayer behaviour.

2.3.2 Mica

Muscovite mica (SPI supplies, West Chester, USA) was used as a hydrophilic and atomically flat substrate, ideal for AFM investigations on lipid bilayers. Mica is partially transparent and can be used in both AFM and fluorescence measurements. The low roughness of the mica surface can be exploited as a control substrate to disentangle the effects of surface topography on the behaviour of fusing bilayer (results and discussions of chapter 4). To prepare mica substrates, a single mica disc was affixed to a clean glass slide using epoxy glue (SPI supplies, West Chester, USA). After the epoxy was fully cured the mica disc was cleaved by firmly pressing

adhesive tape onto the substrate, and then smoothly peeling it off 2 – 3 times. This left the exposed mica substrate mirror-smooth to the eye and ready for sample application.

2.3.3 Polydimethylsiloxane

Polydimethylsiloxane (PDMS) was used as a polymeric substrate to investigate the effects of nanoscale surface chemistry and topography on the properties of supported lipid membranes. PDMS is widely used in biotechnology due to its transparency, low cost, inertness, biocompatibility and easy mouldability. Such properties have popularised its use in the field of microfluidics and biomedical devices and its application continues to grow [196]. Another advantage of PDMS substrates is that their surface topography can be easily modified, both topographically and chemically, using plasma oxidation. This makes PDMS an ideal substrate to investigate the impact of substrate properties on that of the supported lipid bilayer. PDMS is extensively used in later investigations.

A detailed discussion of the PDMS surface modification and characterisation is left to chapter 3; here only the PDMS preparation is given. A 10:1 ratio of elastomer to curing agent from the Sylgard 184 Silicone Elastomer Kit (Dow Corning Corp., Michigan, USA) was thoroughly mixed and degassed for 30 minutes in a vacuum chamber. Then, ~2 mL of the degassed PDMS was then spin-coated onto cleaned glass slides at 500 rotations per minute (RPM) for 10 seconds, followed by 1000 RPM for 5 minutes. This produced a uniform ~100 μm thick coating of PDMS, comparable to reports found in the literature for similar protocols [197]. The thickness of the PDMS substrate was verified using optical microscopy by varying the focus height between the object plane of the glass surface and the PDMS surface. The slides were then baked at 60 °C overnight to ensure full curing.

In various cases, the PDMS substrate was bonded to a glass substrate. To achieve this, both the PDMS and the glass were plasma-oxidised for 30 seconds while exposing their adhering surface and then held together for several minutes. This induced non-reversible covalent adhesion of the PDMS to the glass [198].

2.4 Forming supported lipid membranes

Supported lipid bilayers were created using the vesicle fusion method, as briefly described in Chapter 1.4. The interfacial properties of the substrate surface are of importance to ensure successful vesicle fusion (more details in chapter 4). The following protocols describe the strategy used to form continuous supported lipid membranes using a LUV suspension, or distinct lipid patches using a GUV suspension.

2.4.1 Continuous SLBs using large unilamellar vesicle fusion

A suspension of LUVs was first made by decanting 2 mg of desired lipid mixture dissolved in chloroform into a cleaned glass vial. The chloroform was then removed by blow drying with nitrogen followed by desiccation under vacuum for several hours to remove any residual chloroform. This resulted in a dried lipid film which was then rehydrated with 2 mL of buffer solution (see Chapter 2.2) while gently agitating to produce a turbid suspension of multilamellar vesicles (MLVs). The MLV suspension was then sonicated with a tip sonicator (130-Watt Ultrasonic processor 44347, Cole-Parmer, UK) for 5 minutes at 40% amplitude, resulting in a cloudy suspension of unilamellar vesicles. The size distribution of these vesicles was measured with dynamic light scattering (zetasizer Nano ZS, Malvern Instruments, UK) to confirm the presence of LUVs (normal size distribution of with 170 ± 50 nm diameter).

Continuous and uniform SLBs were then created from the LUV suspension using the following protocol: an acrylic ring, with a thickness of 20 mm and diameter of 30 mm, was attached to the substrate's supporting plate using vacuum grease, and filled with 1 mL of buffer, thus creating a small well to which 200 µL of 0.1 mg/mL LUV suspension was added. The sample was then incubated for 30 minutes. This allowed sufficient time for spontaneous absorption, rupture and fusion of the LUVs on the solid interface. The sample was then gently washed 5 times with 1 mL of buffer to remove any excess vesicles and fluorescent aggregates from the suspension and reduce background fluorescent signal during imaging.

2.4.2 Distinct SLB patches using giant unilamellar vesicle fusion

Giant unilamellar vesicles (GUVs) were created using a protocol adapted from the electroformation procedure pioneered by Dimitrov [169]. Desired lipid mixtures were dissolved in chloroform to create 2 mg/mL lipid stock solutions. 40 µL of this stock solution was then evenly spread on the conductive side of an indium tin oxide (ITO) plate, dried with nitrogen and subsequently desiccated for several hours to remove any residual chloroform. A Teflon spacer (30 mm by 20 mm by 2 mm) was then placed on the sample and capped with an additional ITO plate so as to create an electroformation chamber (see Figure 2.1). The chamber was filled with a 300 mM sucrose solution using a disposable syringe, sealed with vacuum grease, and secured with bull clips. The sucrose solution was made from sucrose powder (grade of 99.5% sucrose, Sigma-Aldrich, UK), and deionised water. The sucrose solution helps increase contrast over GUV in optical microscopy imaging and reduces osmotic imbalances between the inside of the GUVs and the surrounding buffer solutions in subsequent experiments.

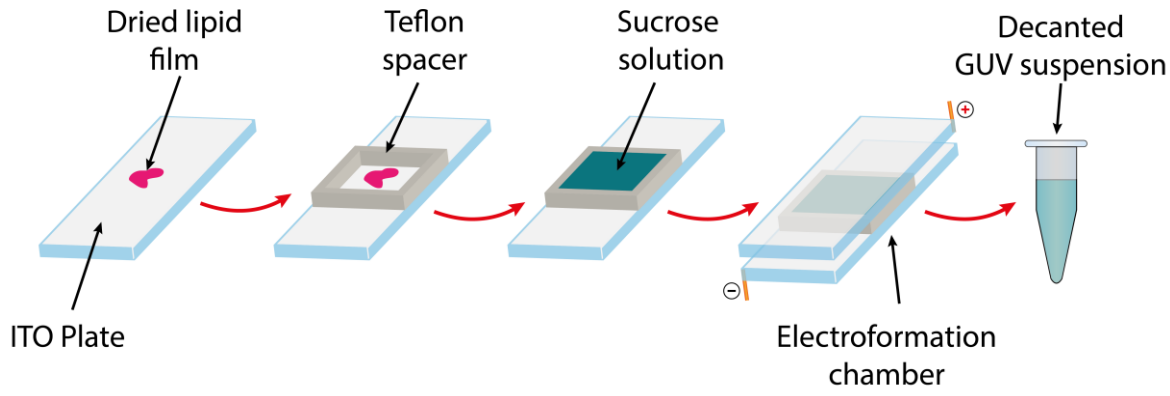

Figure 2.1: Experimental set up for GUV electroformation.

The electroformation chamber was then connected to a signal generator, and a sinusoidal voltage signal with a frequency of 3 Hz and an amplitude of 1.5 volts peak to peak (Vpp) was applied overnight between the ITO electrodes. During electroformation the samples were placed in an oven at 60 ^{o}C to ensure that lipids were fully fluidised. The rehydration of the dried lipid film, coupled with the gentle hydrodynamic oscillations set up by the external electric field stimulates electroformation of a colloidal suspension of GUVs with sizes ranging from 10-100 µm. This GUV suspension was left at room temperature for 30 minutes, allowing it

to thermally equilibrate. To quench GUV samples with coexisting L_o/L_d domains, the GUVs were placed in the fridge at 4 ^oC for 30 minutes. This procedure effectively reduced domain ripening, favouring the formation of a segregated domain structure over larger, more coarsened domains, as shown in Figure 2.2.

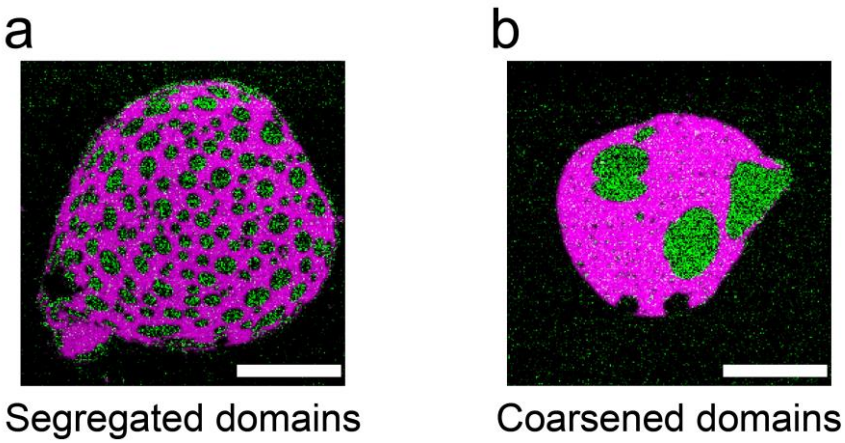

Figure 2.2: Example of segregated and coarsened domain structure in lipid patches Fluorescence micrographs of lipid bilayer patches composed of DOPC:DPPC:Cholesterol (40:40:20 mol%) doped with 0.1mol% Rh-DPPE (purple) and 3 mol% NaP (green) on a hydrophilic glass substrate. Scale bars 50 µm.

SLBs were formed from the GUV suspensions using the following protocol: an acrylic ring, with a thickness of 20 mm and diameter of 30 mm, was attached to the substrate using vacuum grease and filled with 1 mL of buffer followed by 0.5-2 µL of the GUV suspension (Figure 2.3). This allowed the vesicle fusion process to be imaged. Samples were washed gently five times with 1 mL of buffer within 2 minutes to remove any excess vesicle.

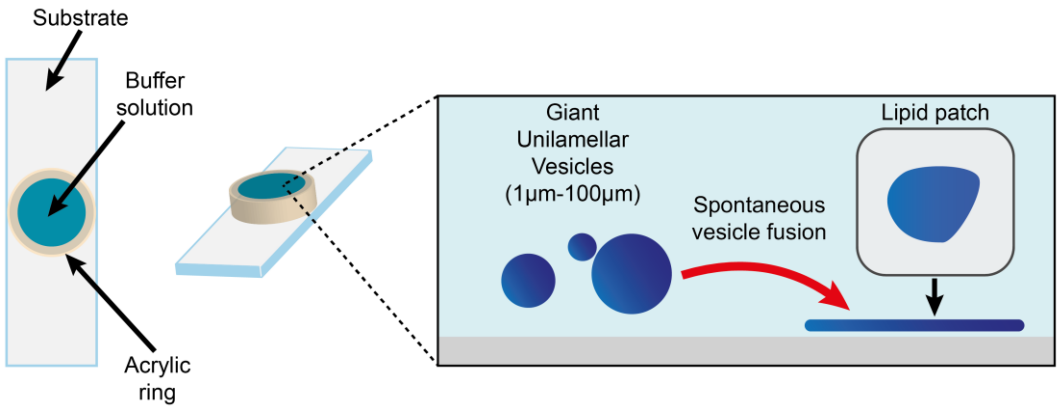

Figure 2.3: Schematic of the experimental set up for GUV deposition.

This method forms distinct lipid patches which are useful for imaging of changes in patch area, fluorescence properties, and even out of plane morphologies such as

tubes formation during vesicle fusion. The protocol also enables continued imaging of the samples during the infusion of chemical agents. This is utilised in Chapter 6 to quantify the effect of methyl-β-cyclodextrin (MβCD) on cholesterol depletion from lipid patches.

The following protocols for these measurements were adapted from the literature [60,199]. For cholesterol depletion experiments, lipid patches were formed on substrates using protocols described earlier. Then 500 mL of buffer solution was removed from the acrylic well, depicted in Figure 2.3, and replaced with 500mL of 2 mM MβCD dissolved in buffer. This resulted in the dilution of the in the MβCD solution, leaving lipid patches being exposed to a roughly uniform concentration ~1 mM MβCD solution. The convection flows caused by adding an equal volume of MβCD solution to the buffer solution in the acrylic well was assumed to fully mix with the liquids present in the well over a short time. For cholesterol infusion, a solution of 8 mg/mL soluble cholesterol (Chol- MβCD) dissolved in buffer was added to the well instead, leaving the lipid patches exposed to a 4 mg/mL Chol-MβCD solution.

2.5 Fluorescence microscopy

Optical microscopy is a heavily utilised tool in the biological sciences. It is a non-invasive, yet highly informative, technique for understanding biochemical and biophysical processes on a wide range of length scales. Although in bright field microscopy, differences in material optical properties create sample contrast [59], fluorescence microscopy requires the sample to be labelled with fluorescent molecules or fluorophores. Fluorophores absorb light at a particular wavelength, resulting in one of its electrons being transferred into an excited state. After a short period, the electron relaxes back into its ground state by emitting a photon with a characteristic fluorescence wavelength. Some of the excited electrons energy is dissipated through non-radiative processes, making the fluorescent photon less energetic than the excitation photon, and hence characterised by a longer wavelength. The difference between the adsorption (excitation) and emission (fluorescence) wavelengths is called the Stokes Shift. The time needed for an

excited fluorophore to relax and fluoresce is called the decay lifetime and is a characteristic of a given fluorophore [200,201].

Labelling biological samples with fluorophores allows for tracking of specific components or features both temporally and spatially. This technique is often utilised with unilamellar SLBs systems which are only ~ 5 nm thick and would hence not provide any contrast in standard optical microscopy. In contrast, fluorescently labelled bilayers (usually chemically attached to lipid, fatty acid or sterol derivatives that can incorporate into the membrane) can easily be observed with fluorescence microscopy.

High-resolution techniques such as stochastic optical reconstruction microscopy (STORM) and photo-activated localisation microscopy (PALM) can surpass the diffraction limit of light, enabling spatial resolutions below tens of nanometres [202]. This renders possible the direct imaging of nanoscale structures and processes such as the dynamic clustering of membrane proteins like hemagglutinin [203] and GPI proteins [204] in living cell membranes despite these structures being only ~ 40 nm and ~ 20 nm in size respectively.

Epifluorescence microscopy does not offer such high resolution but this is counterbalanced by its wide availability and ease of use.

2.5.1 Epifluorescence microscopy

In epifluorescence microscopy, the wavelength of the illumination light is selected to match the absorption wavelength of the fluorophore. The optical set-up reduces the amount of illumination light arriving at the detector, resulting in it being more selective to the emission signal. The high ratio of emission light to illumination light means small amounts of fluorescent molecules can be imaged clearly. The set-up utilised in this thesis (data presented in Chapters 4,5, and 6) comprises an inverted Nikon Ti microscope coupled with an arc discharge lamp used to provide a source of white light. The desired illumination wavelength is then selected by passing the white light through a filter cube (details in Table 2.2). The light is then focused onto the sample by the objective lens, resulting in a cone of light exciting the fluorophores present in the sample, as depicted in Figure 2.4. The resulting fluorescent emission of light is collected by the objective lens and redirected on a Complementary Metal-

oxide Semiconductor (CMOS) camera via the filter cube. Although both the excitation and emission light pass through the same objective, they are separated using a dichroic mirror in the filter cube to allow accurate measurement of the emission photon intensity.

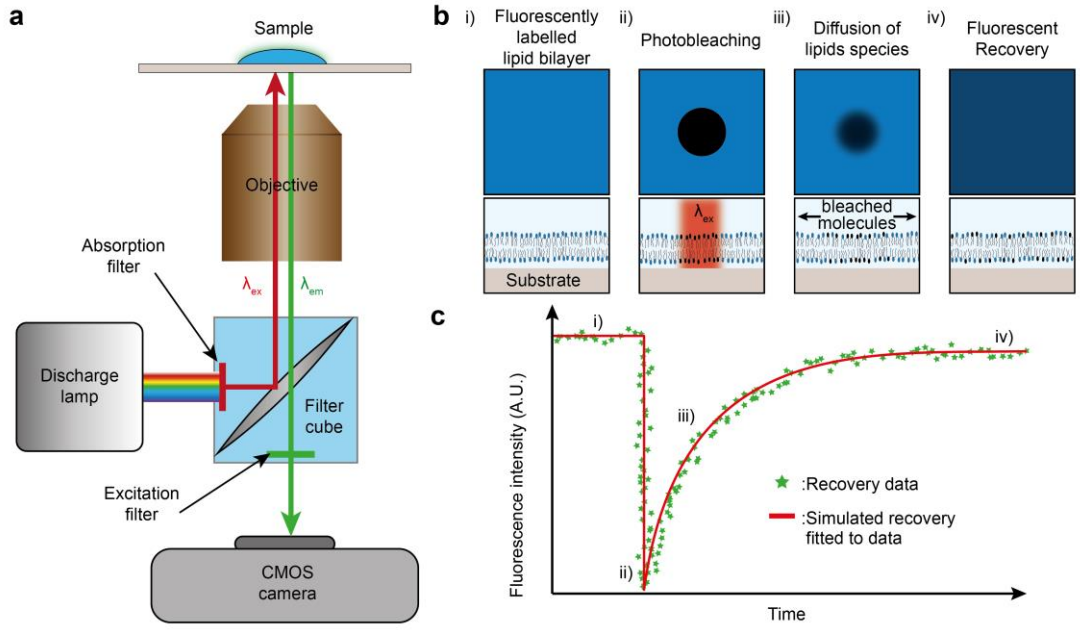

Figure 2.4: Schematic representation of the epifluorescence microscopy and fluorescence recovery after photobleaching set-up. Inverted epifluorescence microscope (a) and fluorescence recovery after photobleaching (FRAP), with depiction of a recovery curve (c). The initial supported lipid membrane with a uniform distribution of fluorescently labelled lipids (b*i*), until exposed to intense excitation light photobleaches a spot of fluorescent molecules (b*ii*), creating a bleachspot which then recovers by diffusion of unbleached lipid molecules (b*iii*) until full recovery of the fluorescence (b*iv*). A typical shape fluorescence recovery curve for a lipid bilayer (c), can be then used to extract values for lateral diffusivity by fitting simulated recovery curve to experimental data. Data and curves in Figure 2.4c are purely for illustrative purposes and do not represent real data.

Epifluorescence facilitates the imaging of specific components of a system, allowing easy distinction from other system components. When applied to model SLBs, epifluorescence can quantify changes in membrane morphology, including out of plane structures. Figure 2.5b gives an example of out of plane structures with tubular protrusions emerging from an SLB. Indeed, such epifluorescence measurements were used to investigate the response of SLBs to mechanical stress [56,70,175], where changes in patch area and the nucleation of protrusions were linked to the membrane passively regulating its shape under stress. Information about

Fluorophore	**Excitation**, nm	**Dichroic Mirror**, nm	**Emission**, nm
Rh-DPPE	540/25	565	605/55
$DiIC_{18}(5)$	535/40	565	590/40
NaP	375/28	415	460/60

Table 2:2 Filter cube used with in the epifluorescence microscope setup

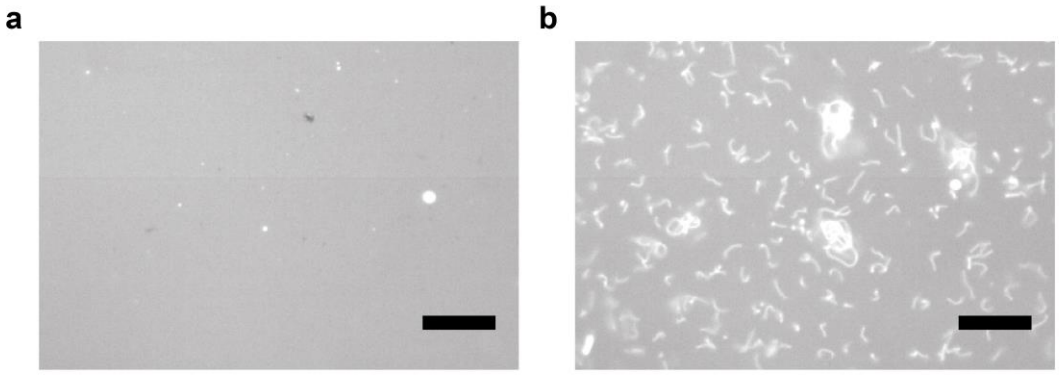

Figure 2.5: Formation of out of plane tubular projections. A fluorescence image of a uniformly flat supported DOPC lipid membrane with 0.1 mol% Rh-DPPE (a), and a similar membrane with out of plane tubular projections (b). The scale bar in both images is 20 µm.

fluctuations in the local lipid composition and density can also be inferred [205]. Chapter 5 relies extensively on such observations to investigate the substrate-induced modification of membrane composition.

2.5.2 Fluorescence recovery after photobleaching

The technique of fluorescence recovery after photobleaching (FRAP) is widely utilised in the biophysical community to characterise the fluidity of membranes and quantify the local molecular diffusivity (see also chapter 1.2.2). The technique can be applied to a wide range of membranes species including membrane proteins [206], and the lipids themselves [207,208]. The basic principle of the technique relies on photobleaching fluorescent molecules in a well-defined region by exposing them to a short period of intense illumination, as depicted in Figure 2.4b. The photobleaching causes a photochemical alteration in the fluorophore molecules, permanently preventing them to fluoresce and reducing the fluorescence intensity over the bleached area to the background noise. However, the bleached molecules can still diffuse normally within the membrane. As unbleached molecules

progressively diffuse into the bleached area, the fluorescence intensity recovers. Measurements of this recovery over time (fluorescence recovery curve, see Figure 2.4c) are used to extrapolate a quantitative value for the average lateral diffusivity of lipid molecules within the membrane. Practically, this task was performed using the image processing freeware FIJI [209], a package of the ImageJ analysis platform. A specific plugin called SIMFRAP [210] was used to quantitatively track the evolution of the fluorescence intensity across the bleaching area, a user-defined square region. The experimental data were then fitted with equation 2.1 to extract a lateral diffusion coefficient, D_c. Equation 2.1 models the fluorescence recovery on the assumption of an unbiased diffusion of the fluorescent probes (2D random walk), using the first post-bleach image from the FRAP dataset as a starting point (further details about the model used are presented in reference [210]):

$$I_t = I_\infty\left(1 - \sqrt{\left(w^2(w^2 + 4\pi D_c t)\right)^{-1}}\right) \qquad \text{Equation 2.1}$$

In Equation 2.1, I_t is the fluorescence intensity as a function of time, I_∞ is the intensity as time goes to infinity (equilibrated fluorescence), w is the width of the bleach spot and t is time.

The main source of error comes from the stochastic character of the diffusion process with each set of data producing slightly different recovery curves, as well as deviations in data fitting due to equation 2.1 ignoring measurement noise [210]. To mitigate these issues, FRAP measurements were typically taken from at least 3 different samples, and 3 different regions on each sample to obtain an averaged and representative measure of lateral diffusivity from the lipid samples.

Another practical problem came from the setup used for acquiring most of the fluorescence images, the Nikon Ti microscope. The Nikon Ti cannot achieve an illumination intense enough to bleach SLBs in less than minutes, rendering recovery measurement imprecise. FRAP measurements were therefore taken using an EZ-C1 Nikon Confocal Microscope (Nikon UK Limited, Kingston, UK) capable of bleaching micron-sized regions supported lipid membrane in 10.4 seconds.

The technique of confocal microscopy utilises a pinhole to block any fluorescence light emitted by fluorophores located out-of-plane of the focal region. The light captured through the pinhole behaves as a point illumination, enabling rasterising

the light across the sample to achieve optical sections of different depth with high spatial resolution. These sections are then assembled into a two-dimensional, or three-dimensional image as the whole sample is scanned. This approach is commonly utilised to image thin sections of thick samples, such as cells and tissues.

For FRAP experiments conducted in this thesis, the bleached area was formed by ten consecutive raster scanning of a point illumination. Each scan lasted 1.040 seconds. The recovery of the 10 by 10 µm bleach area was subsequently imaged by tracking a larger a 500 by 500 µm region with the bleached area in the centre. The specific protocols for FRAP measurements described in chapters 4, 5 and 6 were modified from references [125] and [210].

It should be noted that the EZ-C1 Nikon Confocal Microscope does not have an acoustic optical modulator (AOM), hence the laser intensity cannot be modulated on a sub-millisecond timescale [211]. This limits the temporal resolution of FRAP measurements with the bleaching period and the timescale of lipid diffusion being comparable for the measurements on liquid-disordered membranes in Chapters 4, 5 and 6. This issue is directly visible in the fluorescence images where the edges of the bleached area appear blurred already in the first post-bleach image. This is a clear indication that significant amounts of diffusion have occurred before the recovery imaging could start. The diffusion coefficients provided are hence to be understood as estimates of an average lateral diffusivity. The diffusion coefficients are not quantitatively correct, but still accurate enough to identify differences in lateral diffusivity between gel, liquid-ordered, and liquid disordered phases. Qualitatively, FRAP measurements also aided in verifying that continuous SLBs have been formed (rather than a discontinuous layer of adhered vesicles).

2.5.3 Reflection interference microscopy

Reflection interference contrast microscopy (RICM) is a widely used technique extensively applied in the field of biomembrane and cell imaging [212]. RICM allows measuring the distances between a planar transparent substrate and the sample its support, without requiring any sample labelling to generate a contrast image.

The set-up for RICM utilises a light source and an inverted microscope coupled with a CCD camera. A pre-filter (here green 436 ± 17 nm) is placed within the optical

pathway, together with a field diaphragm, aperture diaphragm, and a polariser. The pre-filter and the polariser produce linearly polarised monochromatic light, and the diaphragms allow for control of the incident illumination. The incident light passes through a quarter-wave plate, resulting in the light being circularly polarised. When shone onto the sample, the reflected light beam passes once again through the quarter wave plate, resulting in a 90^{o} change in polarisation when compared to the incident light. This offset in orientation allows incident and reflected light to be distinguishable. The interaction between the incident and transmitted light beams induces constructive and destructive interference (Figure 2.6). This is due to the substrate, the surrounding medium, and the sample itself having different refractive indexes which all lead to the transmitted light experiencing an altered light path. The intensity of the resulting interference image is hence strongly dependent on the separation of the substrate and the sample.

Here, an inverted optical microscope (Axio Observer, Zeiss Germany) was used with a standard antiflex oil objective x63; 1.25NA (Zeiss, Germany) that included a built-in quarter wave plate located in front of the lens. A metal Halide lamp (X-cite 120, Excelitas Technologies, USA) acted as a light source. Images were recorded with an EM-CCD camera (iXon, Andor, Belfast).

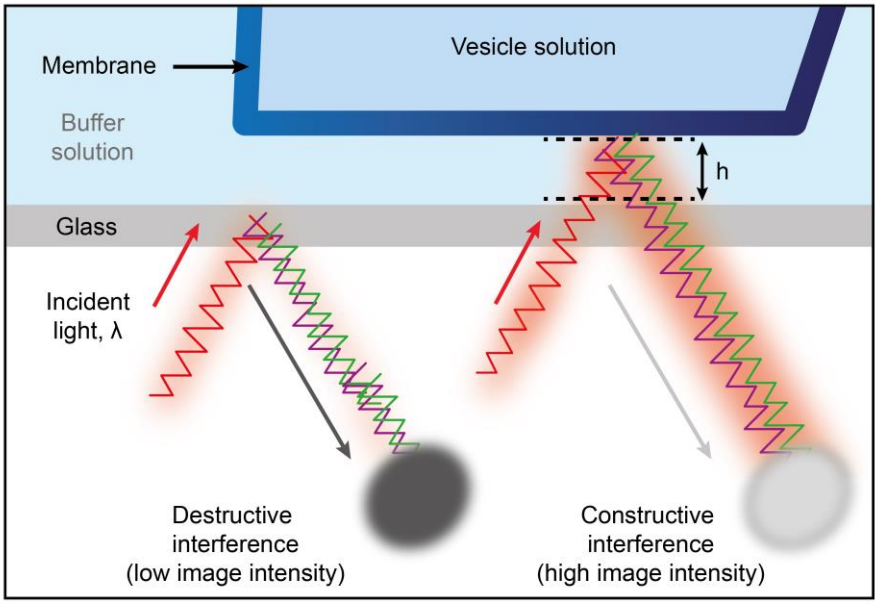

Figure 2.6: Schematic of reflectance interference microscopy. Incident light is reflected off the sample, creating interference patterns related to the sample distance, h, from the substrate surface. The figure was created based on images publicly available at (https://en.wikipedia.org/wiki/Interference_reflection_microscopy).

RICM is used in chapter 4 to investigate the equilibration of SLB patches formed from vesicle fusion. The change in membrane height immediately after the fusion process could be measured.

2.5.4 Image acquisition, processing and analysis

Image acquisition, processing and analysis is a central part of most microscopy, including fluorescence microscopy. Intuitively, images allow rapid "visual" inspection and interpretation of the data, but significant processing is still necessary both to produce a rendered image and quantitatively analyse it.

In fluorescence microscopy, the image reflects the spatial distribution of the fluorescence intensity: after having passed through the microscope set-up, the fluorescence signal reaches the detector. The detector is typically a CCD or CMOS device composed of a two-dimensional array of equally sized pixel detectors. Each pixel detector has a surface area of typically a few square micrometres and can detect incident photons with a high quantum efficiency. The fluorescence intensity measured by a given pixel detector is correlated to the number of photons detected by that pixel [186], and the position of the pixel in the array is correlated to the area of the sample emitting the light. A spatially resolved image of the fluorescence intensity emitted by the sample can then be obtained by measuring simultaneously the light intensity on each pixel detector: in fluorescence microscopy the pixel intensity is related to the number of emitting fluorophores present in the corresponding area on the sample.

For non-super resolution techniques, the size of the pixel detectors is a limiting factor for spatial resolution. However, even modest image acquisitions systems can achieve sub-second temporal resolution due to a high detector efficiency. This makes fluorescence microscopy well suited to measuring macroscale changes in supported lipid membrane morphology, as described in the subsequent chapters.

After the images are captured, great care must be taken to conduct image processing and analysis; small errors can easily skew the data and lead to misrepresentations or erroneous information. Part of the problem comes for the fact that the range of pixel intensity values accessible to the detector extends far beyond information that can be visually displayed: the levels of 65536 grey accessible to a

standard 16-bit camera become only 256 levels on a typical computer monitor, with only ~100 levels perceivable by the human eye [213]. To overcome this issue, a technique called “contrast stretching” is almost ubiquitously employed: only a set range of the possible 16-bit values is displayed to help identify important features. Colour-coded contrast is also often employed, where grey values are displayed according to a set map of colours in order to highlight small variations in intensity [213]. Both contrast stretching and colour-coded contrast have been extensively used in this thesis, to enhance the presentation of fluorescence images and emphasise the visual features of importance. In doing so there are always associated risks, with the human eye being more sensitive to particular colours and contrasts, possibly creating a bias in the interpretation [213]. However, by using such modifications appropriately and presenting them together with quantitative analysis, a clear and honest representation of the results can be achieved.

Importantly all the quantitative measurements performed on image data use 16-bit TIFF images, a format that preserves the linear relationship between photons and image intensity values [186]. Various methods enable and facilitate the acquisition of such quantitative information from visual data, most notably the approach of image segmentation via thresholding where pixels can be classified into groups. Doing so allows the easy identification of particular image features and properties such as size, shape, and average intensity. It should be noted that although the human eye has evolved to instinctively make such classifications, doing so with an automated image analysis process is more complex.

Automated thresholding of images can be conducted through various methods. A given method typically run an algorithm to convert a distribution of grey values within a raw data image into a binary image. One popular algorithm is the so-called Otsu method: from a histogram of light intensity over the whole image, the algorithm splits the data into two classes, background and foreground. The foreground is generally associated with the class of pixels exhibiting a higher intensity. The algorithm then defines the “optimal” threshold value as the value which minimises the variance of the two classes [214]. This allows a binary image to be formed where black pixels represent features of the samples, and white pixels become the background of the image (see example in Figure 2.7b). Otsu’s method is fast, requires little computational cost, and can often find an effective threshold in a few iterations. Like

many other segmentation methods, the Otsu's method relies on some basic assumptions, such as uniform illumination and bimodal images. These are reasonable assumptions for fluorescence images of SLBs and the method was hence deemed suitable for automated thresholding of images. From the binary images, the area of lipid patches could be readily quantifies using the "*Analyze particles"* feature of ImageJ. This routine counts the pixels of a binary image and is able to function with a defined region of interest occupied by the thresholded objects, as shown by the yellow line in Figure 2.7b. This region of interest can then be applied back to unmanipulated images, as shown in Figure 2.7c, allowing the accurate extraction of pixel intensity values and information.

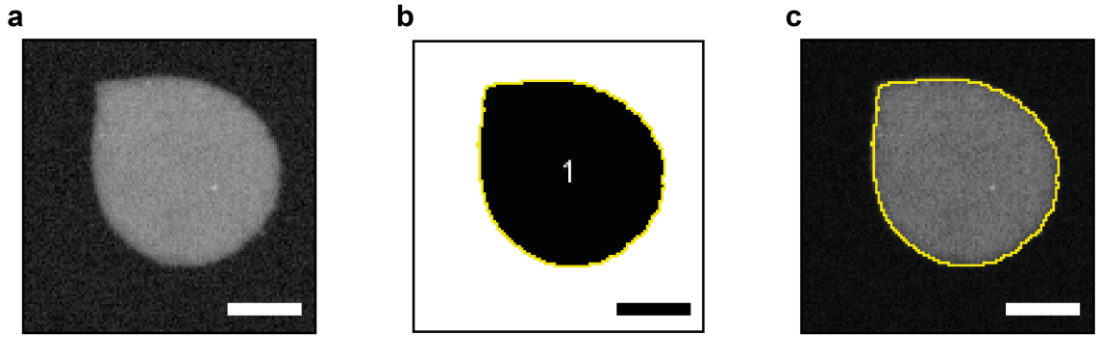

Figure 2.7: Example of the Otsu thresholding method. The original image (a), becomes binarised using the Otsu thresholding (b). A region of interested generated using thresholded image can be overlaid back onto the original image (c). Scale bars in (a-c) are 20 µm.

In typical experiments with SLBs (Chapters 4, 5 and 6), out of focus free floating vesicles can disrupt the automated thresholding. A visual inspection of the final region interest obtained via automated thresholding is hence necessary. Visual representations and quantifiable data are also presented together wherever possible to present an honest and reliable description of data.

Although powerful, the fluorescence microscopy techniques employed in this thesis are subject to the standard diffraction limit and hence not capable of broaching the nanometre spatial resolutions required to characterise the nanoscale properties of the substrate investigated. This can in principle be overcome by the many super-resolution fluorescence microscopy techniques that already exist. Alternatively, here AFM was chosen as a complementary technique due to its practical availability and its ability to also measure molecular forces. This becomes particularly

beneficial when investigating the influence of the substrate on the properties of SLBs.

2.6 Atomic force microscopy

Since its development, more than three decades ago [215], AFM has become a technique of choice for nanoscale science in numerous fields including electrochemistry [216–218], polymeric materials [219], and biological molecules and interfaces [220–224]. Part of this success comes from the fact that AFM can operate in various environmental conditions, such as gas [225,226], vacuum [227] and liquid [228,229] environments with no specific requirements for the sample. In particular, the ability to operate in liquid environments has opened up the possibility of biological studies under more representative aqueous conditions [220–224] when compared to, for example, electron microscopy.

The technique of AFM is based on the local sensing of a surface or an interface with a nano-sharp tip mounted on a flexible cantilever. The attractive or repulsive interactions experienced by the tip induce a vertical deflection of the cantilever which can be accurately measured using a reflected laser.

To function, AFM requires the precise control of the tip position and distance from the sample's surface. This is achieved with a piezoelectric actuator, providing Ångstrom-level positioning precision of the tip holder in the lateral (X and Y) and vertical (Z) directions. A laser beam reflected on the back end of the cantilever amplifies its deflection on a distant photodetector, enabling accurate measurement of the cantilever's deflection down to the sub-Ångstrom level. The photodetector is typically composed of four independent quadrants so that differential signal between the top and bottom directly quantifies the cantilever deflection, after suitable calibration. By knowing the spring constant of the cantilevers, the deflection can be converted into a force between the tip and the sample substrate. This is done on the assumption of a linear deformation (Hooke's law) valid for small deflections (typically < 100 nm). The spring constant of the cantilever must be selected appropriately to ensure a suitable sensitivity [230,231], and minimise tip-wear and sample damage.

2.6.1 Modes of AFM operation

AFM is a high versatility technique with many possible operational modes. Depending on the sample and the investigation, the technique can acquire topographical information through a range of different feedback mechanism and derive further information about the sample, often simultaneously to the topographic measurement.

2.6.2 Amplitude modulation mode

When the AFM is operated dynamically, the cantilever is driven to oscillate at a certain frequency using an external drive. As the vibrating tip approaches the surface of the sample its oscillation characteristics such as amplitude, phase and frequency change due to tip-sample interactions. It is possible to use the amplitude of the cantilever as a feedback channel while the tip raster scans the surface of the sample. This mode of operation is called amplitude modulation AFM (AM-AFM), or "tapping mode". The cantilever is typically driven to vibrate near its fundamental flexural resonance frequency to enhance the oscillation amplitude and the measurement sensitivity. Changes in the cantilever's amplitude and phase are quantified with a lock-in amplifier locked on the driving signal. The feedback keeps the working amplitude constant while scanning across the sample. The working amplitude is smaller than the amplitude of the tip far away from the surface due to tip-surface interactions [225,232]. In its simplest form, the motion of the tip can be approximated by a driven-damped simple harmonic oscillator [233]. The harmonic oscillator also quantifies the damping experienced by the vibrating mass, suggesting that AM-AFM can provide more than only topographic information. Practically, this information is available in the phase of the tip vibration which is allowed to vary freely. From images of the phase it is possible to quantify changes in the sample's viscoelastic properties including quantities such the local adhesion, stiffness and frictional forces [225].

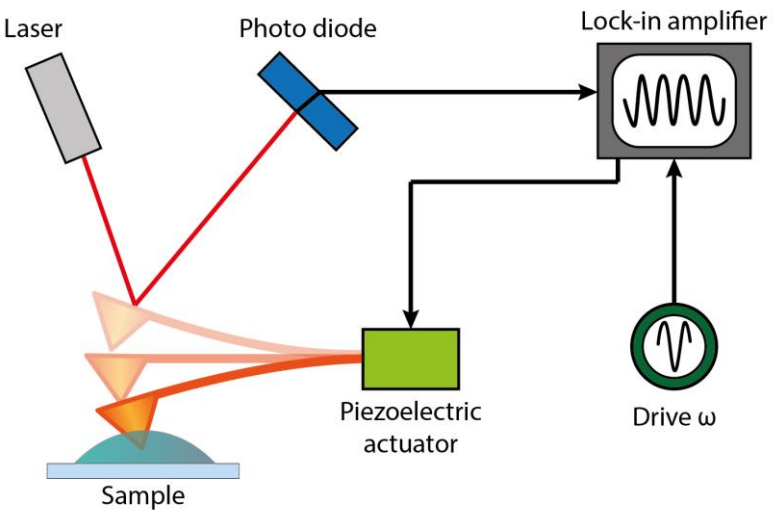

Figure 2.8: Schematic representation of amplitude modulation-AFM (AM-AFM). The cantilever is externally driven to oscillate at frequency ω, close to cantilever resonance. A laser reflected on the back of the cantilever (shown in orange) is directed onto a photodiode which detects changes in the cantilever deflection. In AM-AFM these changes are periodic and can be accurately quantified with a lock-in amplifier. A feedback loop constantly adjusts the distance between the base of the cantilever and the sample so as to maintain a set amplitude of vibration. Adapted from reference [234]

Generally, dynamic AFM modes such as AM-AFM have the advantage of reducing large frictional forces between the tip and substrate, hence preserving both the tip and sample by reducing damage and wear during imaging. Soft AFM cantilevers must also be used to preserve soft biological samples. Although more susceptible to perturbation by thermal noise, a low spring constant makes the cantilever easily deformable, hence less destructive of soft samples such as adhered lipid membranes. In this work, imaging in AFM tapping mode was achieved a silicon nitride RC800PSA (Olympus, Tokyo, Japan). The RC800PSA chips come with a set of 4 different AFM cantilevers, each exhibiting a different nominal spring constant. For all the experiments described in later chapters, the 3rd cantilever of the set, with a nominal cantilever spring constant 0.76 N/m, was used.

In work presented in this thesis, AFM is operated in liquid, allowing measurement and characterisation of membrane-substrate interactions in an aqueous environment. Water plays an influential role in the bilayer's properties at the interface with a substrate. The ability to image in such liquid environments is hence advantageous to derive meaningful results. Operating AFM in liquid environments is, however, challenging due to the liquid environments altering the cantilever dynamics [235] and the tip-substrate interactions [236,237]. When AM-AFM is used

appropriately, these phenomena can be exploited to enhance imaging resolution [237,238] compared to similar measurements in ambient conditions [239]. Details of effective protocols for using AM-AFM in liquid are detailed in earlier published work [240].

2.6.3 Lateral force microscopy and mapping friction

In the most basic AFM operation mode (contact mode), the feedback mechanism is based on keeping constant the vertical deflection of the cantilever. If the sample is scanned perpendicularly to the axis of the cantilever, the frictional force between the tip and the sample can cause the cantilever to twist. This twisting or lateral torsion of the cantilever can also be measured by comparing the difference in the intensity recorded by the left and right sides of the AFM four quadrant photodetector. This mode of operation, often called lateral force microscopy (LFM), simultaneously measure the sample's topography (Figure 2.9a-b) and variations in the tip-sample friction as the tip travels across the sample's surface (Figure 2.9c-f). This friction itself depends on the local surface and tip topographies, physical and chemical properties, and the direction of the travelling tip.

The respective contributions to friction from topography and variations in tip-sample interactions can be distinguished, as visible in Figure 2.9d-f: topographic features produce only a transient signal change when the tip travels over an edge. Additionally, variations in tip-sample interactions induce LFM measurements that are inverted between the forward and backward scan direction (section 1-4 of Figure 2.9e,f). This is in contrast to topographic LFM measurements which are relatively independent of the scan direction.

Here LFM can be used to reveal changes in tip-substrate friction across DOPC:DPPC (40:60 mol% ratio) multi-phase SLBs (Figure 2.9g-h). LFM images of the SLBs on PDMS substrate show lateral friction variations between the more solid-like DPPC rich gel domains (green arrows) and the fluid DOPC regions. The coexistence of gel and fluid domains is expected for such bilayers at room temperature [73]. Interestingly, no significant differences between the domains are visible in topographic images, highlighting the power of the technique where nanoscale interfacial properties cannot easily be detected in topographic alone [241].

LFM is further discussed in Chapter 6.5.2 where it is used to investigate the impact of curved substrates on the molecular organisation of SLBs.

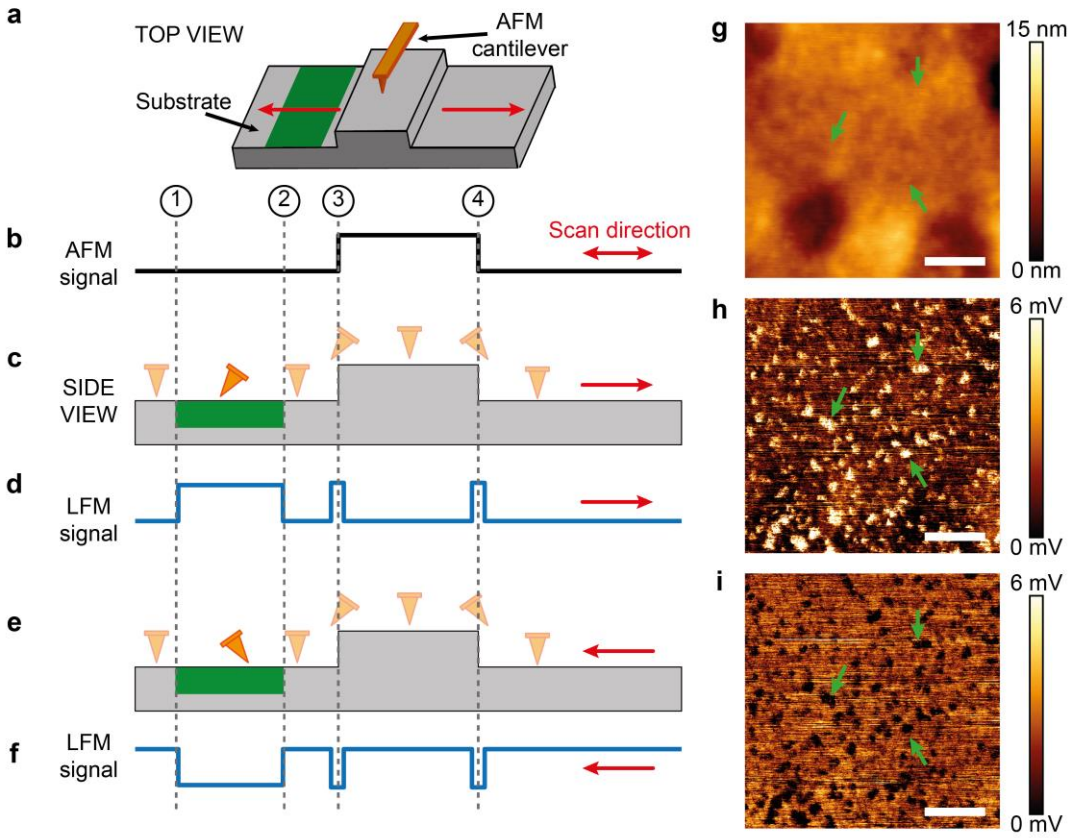

Figure 2.9: Schematic description of lateral force microscopy. Illustration representing of the AFM cantilever scanning across a surface (a) with topographic features (steps) and a region of higher friction represented in green. Topographic information is obtained as AFM tip scans across the surface (b). When the tip moves forward (c), the lateral or LFM measurement senses changes in topography and friction (d). The process is reversed when the tip moves backward (e-f). Example LFM imaging of a 40:60 DOPC:DPPC SLB on a PDMS substrate (g-i): topographic (g) forward LFM (h) and backward LFM (i) information is obtained simultaneously. The scale bars in (g-h) are 200 nm. Images (a-f) adapted from images available online [242].

2.6.4 Tip-substrate interaction forces

AFM is sensitive to the tip-sample interaction forces which play a central role in any type of AFM-based measurement. In most applications, knowledge of the nature and origin of these interactions is not essential. However, understanding the properties of the interactions at play can considerably help with both optimising the measurement, resolution and the interpretation of the data. There are always

multiple types of interactions simultaneously acting between the tip and the sample, but it is often sufficient to understand which is the dominating contribution to improve data acquisition and interpretation.

Hereafter is a short review of some of the main interactions present between the tip and the sample for the measurements conducted in this thesis.

2.6.4.1 van der Waals forces

The van der Waals forces are ubiquitous but usually short-ranged and relatively weak. They are induced by the interactions between the electric dipoles of the interacting molecules. These can be permanent or transient dipoles induced by thermal or quantum mechanical fluctuations. The resulting interaction energy is the product of the two dipoles multiplied by parameters related to the specific nature of the system and temperature. These parameters are usually addressed by the so-called Hamaker constant which depends on a materials atomic polarisability and density [46]. Summing each pair interaction between the macroscopic objects involved (the AFM tip and local sample), the total van der Waals interaction energy can be calculated and hence the total force at work. Van der Waals interactions are always attractive between like surfaces in a medium, but different materials can induce attractive or repulsive interactions depending on both the material properties and properties of the media they are immersed in reference [46]. The relatively short range of the interactions, ~ 0.5 nm, means such forces only become significant once surfaces come into very close contact.

2.6.4.2 Electrostatic double layer

When operating in aqueous environments most solid interfaces can become charged. The ionic species dissolved in the aqueous phase accumulate close to the surface of the immersed solids to ensure electro-neutrality resulting in an electrical double layer (EDL) of counterions. The precise spatial organisation of these charged species at the interface is non-trivial but is often described by the average density of counterions at a given distance from the surface of the solid. The EDL comprises of a Stern layer of tightly bound counterions at the solid-liquid interface and a more loosely bound diffuse layer of ions vanishing exponentially in the solution. When the EDL of two solids overlaps, the density of ions in the overlapping region increases considerably, resulting in a net repulsive force of

entropic origin: the double layer force. The distance at which two such layers begin to interact as two solid surfaces approach each other in a solvent can be characterised by the so-called Debye length. Notably, the Debye length depends solely on the properties of the solution. The type and concentration of electrolytes present in the solution, the solution's dielectric constant and temperature determine the interaction range. Adding salt to the solution reduces the Debye length. Here, the standard buffer solution used results in a Debye length < 1 nm, effectively screening all long-range electrostatic interactions between the tip and the substrate: 2 mM $CaCl_2$ creates a Debye screening length of ~ 4 nm, and 150 mM NaCl a length of ~ 0.8 nm [46], with both types of ions working together in the present imaging buffer. In practice, screening long-range interactions experienced by the tip can allow local interactions at the sample-liquid-tip interface to be better measured. Additionally, the salts added aids SLB formation via vesicle deposition for the same reasons, reducing long-range electrostatic interactions effectively achieving attractive vesicle-substrate interactions [243].

2.6.4.3 Solvation forces

Solvation forces arise from the confinement of a solvent by two surfaces. The confinement induces more order in the solvent molecules adjacent to the surface by local solid-liquid interactions and by restricting the configurational entropy. This often has the net effect of increasing the local liquid density to create a semi-ordered liquid medium near the surfaces. This "interfacial liquid" has dissimilar properties to the disordered bulk liquid, with typically increased density and order, and reduced mobility [46,238]. When the confined interfacial liquid is progressively squeezed out, the configurational entropy and increased pressure and result in solvation forces. Solvation forces can be repulsive or oscillatory due to the layering of the confined liquid parallel to the confining surfaces. Changes in the liquid ordering as the approaching surface squeezes out each layer results in alternating repulsive and attractive interaction depending on the separation distance between the surfaces.

Importantly, the onset of solvation forces from confined liquids do not require specific liquid-solid interactions, or even liquid-liquid interactions, given the entropic origin [46]. Partly for this reason solvation forces in water remain poorly understood, with many unusual interactions existing between hydrated surfaces. To aid distinguishing these interactions, solvation forces are often be categorised as either

primary or secondary hydration forces. Primary hydration results from the enthalpic adsorption or "binding" of water layers to the solid, effectively reducing the adhered layers entropy. This hydrated layer at the interface is typically ~0.2 to 0.4 nm thick, making such interactions relatively short range [244]. Secondary hydration forces are associated with weaker interactions, often with larger decay lengths on the order of up to ~ 10 nm [244]. The decay length is related to the solute distribution in the solution and the solute's ability to perturb the local hydration. If the solute acts as a counterion in an aqueous solution, the Debye length describes the decay length of secondary hydration forces [244]. Changing the liquid-liquid and liquid-surface interaction has an impact on the nature of the hydration force, with hydrophilic or hydrophobic surfaces often inducing repulsive or attractive solvation forces respectively: the liquid-surface attraction characterising hydrophilic surfaces leads to a denser packing of water molecules to the interface. This in turn increases local density and produces a repulsive short-range oscillatory force. Conversely, hydrophobic surfaces create a weaker liquid-surface interaction than the liquid-liquid interaction, resulting in an oscillatory force that tends to be more attractive [46]. The exact origin of these attractive hydrophobic interactions remains controversial, but ideas such as local water structure creating pockets of reduced density provide a possible explanation [46].

In general, the hydrophilicity or hydrophobicity of a surface can significantly impact the local structuring of water which, in turn, affects the forces experienced by two approaching surfaces in aqueous solution. While of short range, such interactions are important for the investigations conducted in Chapter 5 where they locally modulate the adhesion forces between chemically modified surfaces and the AFM tip.

2.6.5 Force spectroscopy and force mapping

The various interactions described in the previous section all contribute in some way to the tip-sample forces underpinning AFM measurement. Changes in the overall tip-sample force can be directly described as function of the separation between the two at any location of the sample's surface. This is called force mapping. Practically, this is achieved by monitoring the deflection of the cantilever as it

performs a controlled descent over a given location of the sample. Plotting the deflection and hence the force experienced by the cantilever as a function of the distance travelled towards the sample produces a so-called force-distance curve. An example of a typical force curve as depicted in detail in Figure 2.10.

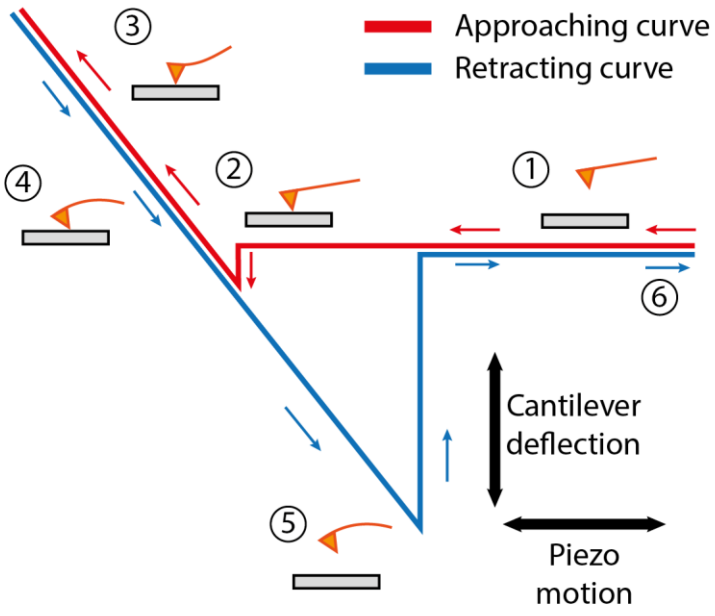

Figure 2.10: Illustration representing a force spectroscopy measurement on a point location of a sample. When the tip is far from the surface (step 1) no deflection is measured. As the tip approaches the surface (step 2), it starts interacting with the sample and experience a vertical force (here attractive) translated by a deflection of the cantilever. If the gradient of the force is larger than the cantilever stiffness, this triggers a sudden "snap-in" deflection. The base of the cantilever can be moved further down with the actuating piezo, compressing the tip on the surface (step 3). If the surface is much stiffer than the cantilever, all the deformation occurs in the cantilever which experiences a linear deflection as the piezo moves down. Upon retraction, the cantilever needs to overcome any adhesion force, creating a hysteresis in the deflection (step 4). When the bending force of the cantilever overcomes the adhesion force, the tip snaps out of contact (step 5), and the cantilever returns to its original null deflection (step 6). This figure was adapted from [245], with permissions from Elsevier.

In a typical force curve, the base of the cantilever is moved down towards the surface of the sample using the AFM piezo actuator. When the tip is beyond the range of the tip-sample interactions, the cantilever deflection is zero (Figure 2.10, step 1). As the tip approaches the surface, the tip-sample interactions become significant, resulting in a cantilever deflection. If the gradient of the interaction force is larger than the cantilever's stiffness, the tip will uncontrollably jump into contact with the surface in the case of an attractive interaction (step 2). Attractive forces

such as the capillary or depletion forces tend to become significant at short range causing the tip to jump to the surface in air. If the base of the cantilever is moved further down towards the surface, the cantilever starts to bend in order to compensate for the fact that the tip cannot move down freely. If the sample is much stiffer than the cantilever, almost all the deformation is carried by the cantilever, resulting in a linear, relationship between the vertical displacement of the piezo and the cantilever deflection (step 3). This is often used to calibrate the magnitude of the deflection. Upon withdrawal of the piezo, the cantilever reduces its bending (step 4) to subsequently jump out of contact from the surface. This occurs when the adhesion force experienced by the tip is exactly balanced by the negative bending of the withdrawing cantilever (step 5). Eventually, the cantilever returns to its initial state with no deflection (step 6). By scanning across the sample surface, a map of measured forces can be acquired, the process commonly termed “force mapping”.

This technique is not limited to the study of tip-substrate interactions but is routinely applied in biological systems to characterise the mechanical properties of lipid membranes [246–249], and the forces required to break protein-ligand complexes [250].

Here, all force mapping measurements were performed in buffer solution, with each force map representing an array of 32 by 32 (1024 force curves) over a 1 μm^2 area. A constant ramp rate of 0.25 Hz , a cantilever extension speed of 0.1 μms^{-1}, and a dwell time of 1 second to allow for tip-sample interactions to equilibrate. The influence of the solvent’s viscosity on the measurement was assumed minimal with only minor effects observed for trials in fluids ~ 40 times more viscosity than water [251].

2.6.5.1 Chemical force mapping

Chemical force mapping is effectively an extension of force mapping, conducted in conditions where the nature of the chemical interactions is more defined. This makes it possible to characterise the chemical signatures of an interface. The idea is to conduct a force mapping of a sample using a tip functionalised with specific chemical groups. By measuring changes in local adhesion forces between the functionalised tip and the sample, the local chemical properties of the substrate can be inferred if the chemically targeted interaction is responsible for the tip adhesion. This technique has successfully been used to map changes in surface

hydrophobicity on crystalline [252,253] and polymeric [254] substrates by coating the probe with hydrophobic chemical groups: when conducted in aqueous solution, a stronger adhesion is expected between the tip and hydrophobic regions of the sample due to hydrophobic forces. This approach is utilised in Chapter 3 to characterise the local hydrophobicity surface of plasma-oxidised PDMS. Obviously, the methods rely heavily on a suitable functionalisation of the AFM tip, a topic covered in the next section.

2.6.6 Tip functionalisation

There are two popular methods for functionalisation of AFM tips: the first methods uses silane chemistry and the second thiol chemistry to form a self-assembled monolayer (SAM) on the tip's surface. Each method differs by its ease of implementation and its compatibility with the tip material. For silicon nitride or oxide tips, silane chemistry is generally used, whereas thiol chemistry tends to be favoured when gold-coated tips are available. In the case of silane chemistry, the terminated group reacts with the tip's surface silanol groups to create a covalent Si-O-Si bond. For thiol chemistry, covalent bonds are made between the gold surface and the terminated thiol group.

In the present work gold AFM tips have been used (experiments in Chapter 3). The functionalisation protocol is detailed below:

Gold coated tips (TR400PB, nominal spring constant of 0.09 N/m, Olympus, Tokyo) were used. The tips are fully coated with a ~40 nm thick gold layer and hence suitable for functionalisation using thiol chemistry. The tips were first bathed in acetone for 20 minutes and placed in a glass petri dish to allow residual acetone to dry off. The tips were then placed in a custom-made UV light box with two Wemlite 18W UV lamps or ozone cleaning: the UV light decomposes the air oxygen into ozone, which pyrolyses residual organic contaminants from the AFM tip. After 20 minutes of treatment, the tips were immersed into an ethanol solution containing 5 mM of either hexanethiol ($C_6H_{14}S$) or thiocholesterol ($C_{27}H_{46}S$). After 24 hours in the thiol solution, the tips were removed, washed with ethanol and then briefly with water (Milli-Q) before measurement. A new functionalised tip was used for each

experiment. The hexanethiol, thiocholesterol, and ethanol were purchased from Sigma-Aldrich (UK).

By forming SAMs with different chemical groups, different surface interactions can be investigated. Here, hexanethiol exposes a hydrophobic hexane group and was used to investigate the nanoscale distribution of hydrophobic regions at the surface of plasma-treated PDMS substrates (see Chapter 3). Thiocholesterol was used to probe surface interactions between cholesterol and partially plasma-treated PDMS substrates (see Chapter 5).

2.7 Wetting measurements

The nanoscale hydrophobic properties of a substrate surface can have macroscopic consequences on the wetting behaviour of the material. The macroscopic wetting properties of a material are easily accessible and can provide useful information about the behaviour of water at its surface. Measurements on samples previously nano-characterised with AFM or chemical mapping also provide a link between the molecular-level and macroscopic properties.

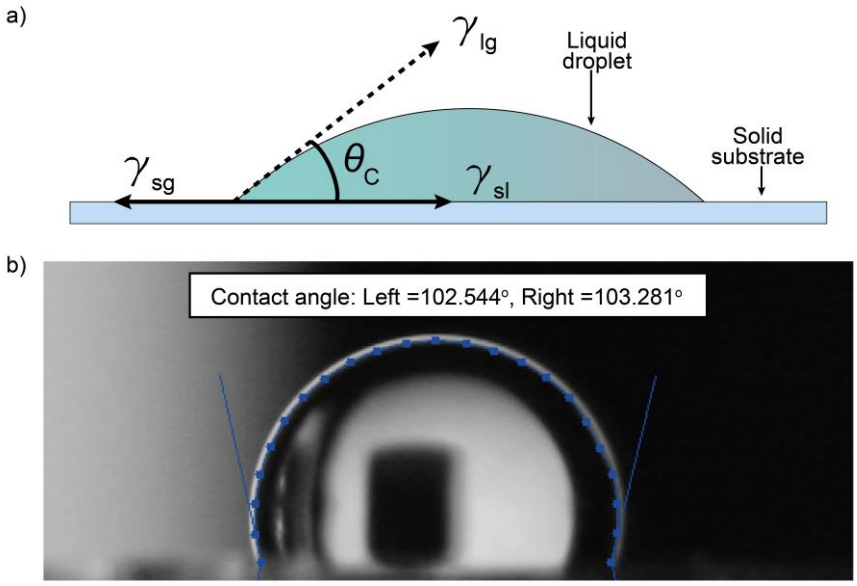

Figure 2.11: Schematic representation of a contact angle measurement. Illustration of a liquid sessile drop on a solid substrate illustrating the contact angle formed by the liquid, solid and gas triple interface (a). Example measurement on a water droplet placed on PDMS substrate (b), with the contact angle, measured using the ImageJ plug-in Dropsnake.

Practically the macroscopic wetting properties of a surface are characterised with the contact angle, θ_C, formed by a small sessile droplet of liquid deposited on the surface (Figure 2.11). From this droplet, the balance of forces at the three phase lines can be used to derive the Young-Dupré equation: [255]:

$$\gamma_{lg} \cos\theta_C = \gamma_{sg} - \gamma_{sl} \qquad \text{Equation 2.3}$$

Where γ_{lg}, γ_{sg} and γ_{sl} are the surface tensions of liquid gas, solid-gas and solid-liquid interfaces respectively. Generally, surface with contact angles < 90^o are classified as hydrophilic, and those above 90^o classified as hydrophobic [46]. Equation 2.3 assumes an idealised interface with a perfectly smooth, chemically homogenous solid surface, similar to the cartoon depiction in Figure 2.11a. Contributions from the surface chemistry and topography can create a convoluted impact on the apparent contact angle [255]. The impact of geometrical roughness on the measurement can be compensated by applying the Wenzel equation that characterises the apparent contact angle rough surfaces [255]:

$$\cos\theta_C = r\cos\theta_W \qquad \text{Equation 2.4}$$

where r, is the roughness parameter defined by the ratio of the actual and projected area of the substrate surface, and θ_W is the contact angle corrected for roughness. Similarly, the Cassie equation can be applied characterise the apparent contact angle on chemically patterned surfaces with two different materials [255]:.

$$\cos\theta_C = \lambda\cos\theta_{Y1} + (1-\lambda)\cos\theta_{Y2} \qquad \text{Equation 2.5}$$

where θ_{Y1} and θ_{Y2} are the contact angles of two materials, and λ is the area fraction of material 1 on the surface.

Based on these concepts, measurements of the wetting properties (static contact angle) of a sample were carried out by depositing a 5 µL droplets of water (Milli-Q) on the sample and subsequently and imaging it with an SLR camera (Canon 1000D). The images were analysed using the ImageJ plug-in DropSnake [256] (Figure 2.11b) that can automatically and objectively identify the contact angles of the

droplet. Roughness was taken into account based on values measured from AFM images of the sample's surface (1 μm^2 areas, average of 5 areas).

The Cassie equation was not needed here due to the fact that the samples were either chemically homogenous or the area fraction of mixed materials was impossible to obtain (see Chapter 3).

2.8 Stretching flexible substrates and surface cracking

The fact that SLBs adhere to a substrate makes it possible to impose and manipulate the mechanical stress experienced by the membranes simply by stretching or compressing the substrate. This requires a flexible substrate material such as PDMS which has been successfully used in numerous studies to infer a controlled mechanical stress on lipid membranes [56,70]. Previous work, most notably in the experiments presented in reference [175], have shown that the substrate properties play a significant role in modulating the response of the membrane to mechanical stress.

In this thesis (Chapter 5), the flexibility of PDMS substrates is exploited to induce a biaxial extension of a substrate supporting an SLB and investigate the effect on the membrane's behaviour. When sufficiently extended, PDMS substrates can undergo surface cracks that modify the substrate's interfacial properties (Chapter 3). The mechanical measurements are achieved with biaxial strain device described in detail elsewhere [70,175] and summarised here:

A microfluidic channel sealed on a glass microscope slide was connected to a ~ 1 mm diameter circular inlet and outlet (Figure 2.12a). A thin, flexible sheet of PDMS, ~ 25 µm thick, was formed from spin coating 2 mL of uncured PDMS in a petri dish, at 500 RPM for 10 seconds, and 2000 RPM for 2 minutes. The sheet was then sealed onto the outlet using the same protocols for bonding PDMS to glass (see Chapter 2.3). The inlet was connected to a Standard Infuse/Withdraw PHD ULTRA syringe pump (Harvard PhD apparatus). Positive air pressures were applied to the microfluidic channel via the syringe resulting in the PDMS sheets expansion from a flat to hemispherical cap geometry. Membranes adhered to the bulging PDMS sheet were then subjected to biaxial area stress (Figure 2.12c).

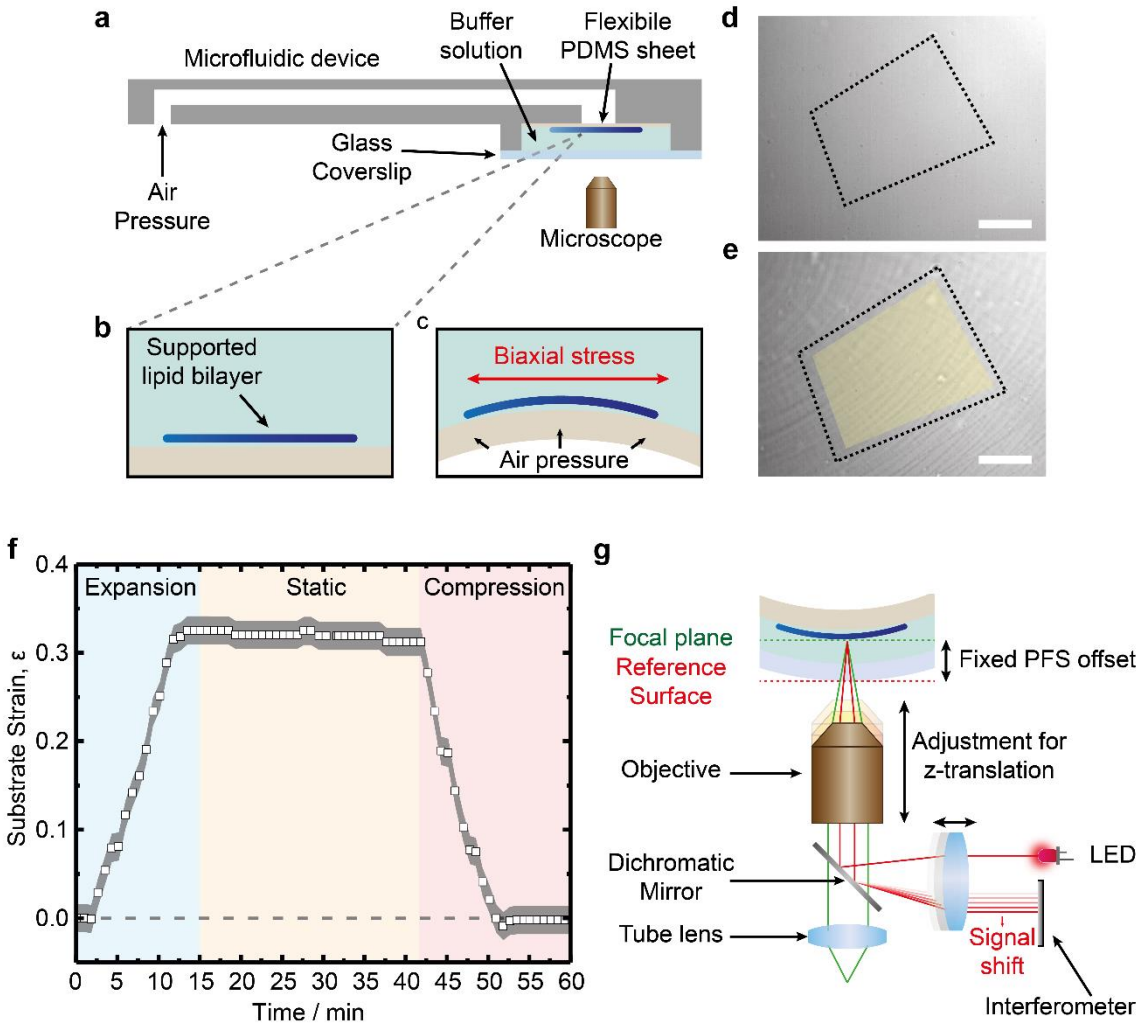

Figure 2.12: Schematic of a biaxial stretching device and PFS system. Schematic of PDMS biaxial stretch device (a), with an illustration of the supported lipid bilayer on a flexible PDMS sheet (b) and the sheet being stretched by air pressure through the microfluidic device, inducing biaxial stress on the supported lipid membrane (c). The resulting bright field image of the flexible PDMS substrate (d), with an area defined by four defects shown by a dotted line. The same substrate under strain (e), and the new position of 4 defects, with the original area highlighted in yellow. Graph showing an example substrate strain cycle with the stretching device (f). Schematic of the PFS system for the Nikon Ti utilised to track z-translation (g), adapted from reference [257]. Scale bars in (d,e) represent 50 µm.

Changes in the position of defects present in the flexible PDMS sheet allows the quantification of the substrate's deformation during stretching (Figure 2.12d-e) and hence the quantification of applied strains for each imaging experiment (Figure 2.12f). By tracking these defects, it was found that an infusion and withdrawal rate of 3 µL/s typically corresponded to a strain rate of ~0.0005% s^{-1} in the biaxial strain devices. Due to the "inflating-bubble" geometry of the stretching device, the biaxial

straining of the substrate is accompanied by a significant z-translation, as the PDMS sheet deforms into a hemispherical cap (Figure 2.12c). These z-translations were tracked and the focus adjusted during the experiments using the Nikon Ti Perfect Focus Systems (PFS), shown schematically in Figure 2.12g. This system offers a feedback on the focus position using a near-infrared LED reflected off a reference surface, such as the bottom of coverslip on which the sample is mounted. The reflected signal is then passed through an offset lens onto an interferometer that quantifies any variation in the distance between the reference sample's surface. This strategy effectively corrects for vibrations, thermal drift and z-translations.

Aside from the stretching device described above, a flexible PDMS sheet identical to that used in the device could be used to cover a ~1 mm diameter hole in a block of PDMS with a length and width of 10 mm and thickness of 5 mm. This simple device created a flexible PDMS sheet over an air pocket, which could be used to form wrinkled substrate topographies (Chapter 3.3).

AFM was used to characterise the topography of surface cracked PDMS after exposure to mechanical stress (later discussed in chapter 3.4). Substrate measurements under tensile strains were conducted with the MFP-3D Infinity AFM using the NanoRack sample stretching stage (Asylum Research, Santa Barbara, USA). The imaging was carried out using standard protocols (described in Chapter 2.4).

Chapter 3: Surface modification of polydimethylsiloxane substrates using air plasma treatment

Polydimethylsiloxane (PDMS) is a widely utilised polymeric support due to its many useful properties such as: transparency, biocompatibility, flexibility, easily modified shape, mechanical properties, surface chemistry and low cost [258]. Such characteristics have made it a popular substrate for the development of lab-on-chip [140], organ-on-chip [141,176], and flexible bio-electronic devices [259]. The biocompatibility of PDMS has led to it being prevalently used as a synthetic substrate to stably support live support cells [260]. The versatility of PDMS has been utilised in various studies to investigate the role of substrate stiffness [261], topography [262] and surface chemistry [263] on cell adhesion and proliferation. For example, a study using Caco-2 cells observed that cell adhesion to physisorbed fibronectin on PDMS substrate could be tuned by altering the PDMS's surface chemistry and topography via oxygen plasma treatment [263]. It was proposed that the synergistic effect of increased surface hydrophilicity and altered topography may facilitate the exposure of physisorbed fibronectin towards Caco-2 cell integrins and consequently enhancing cell adhesion and proliferation on the functionalised surfaces [263].

However, there are limitations to the use of PDMS; one being its innate hydrophobicity. Moreover, even after the PDMS surface has been modified to be more hydrophilic, the material can often recover its hydrophobicity [264]. The literature reports the loss of small hydrophobic molecules from the incubation solutions into the connected PDMS matrix [265]. In addition, the literature describes the absorption of small biomolecules by silicone polymers [266], and even the permeation of oligomers from PDMS bulk into surrounding tissues [267,268]. Although few, there have been documented cases where the transfer of small biomolecules into the PDMS substrate have a significant impact on the materials' mechanical properties [268,269]. Such caveats not only have negative implications for PDMS's application to new biomedical devices but highlight the particular issue for its application to current lab-

on-chip and biomimetic devices where changes in ambient solution composition could possibly impact the outcome of experimental investigations. Regardless, the application of PDMS substrates in this field steadily grows [270–274], due to its ease of use and familiarity within the biotechnology community. To overcome its disadvantages, surface passivation techniques are being actively developed and improved [275]. Popular techniques such as plasma oxidation treatment not only passivate the surface, but can be applied to induce different membrane responses to external stress [175]. Such developments present the first steps towards novel functional synthetic biointerfaces to modify adhered membrane properties controllably. However, a deeper understanding of the interplay between nanoscale interfacial properties and macroscale membrane responses is required to push such technologies further.

The discussions in this chapter set out to explore how controlled air plasma treatment can be used to modify PDMS substrates chemical, topographical, and mechanical properties. This is useful to investigate the interplay between surface modification techniques and controlled alteration of the membrane. For example, it is possible to modify the strength of a membrane's coupling to a flexible PDMS substrate by altering the PDMS surface hydrophilicity [175]. In a recent study, longer plasma treatments lead to a more hydrophilic PDMS surface, inducing a weaker coupling of the adhered lipid patches. This allowed them to "slide" across the substrates interface when subjected to strain deformations rather than stick and form pore defects, as was the case with a more hydrophobic PDMS surface [175]. Further examples of how PDMS surface modifications can be used to alter membrane behaviour during vesicle fusion, and even induce changes in adhered membrane composition are demonstrated and discussed in Chapters 4 and 5, respectively. These investigations offer insights into how such PDMS surface modifications can be utilised as simple and useful techniques to manipulate the behaviour of adhered membranes and can be readily exploited in the field of functional biointerfaces.

3.1 Modifying surface chemistry with plasma treatment

As PDMS is natively hydrophobic, its surface requires chemical modification to become sufficiently hydrophilic to favour the formation of lipid bilayers. This can be achieved through a variety of techniques including the incorporation of amphiphilic molecules to the PDMS bulk [276], deposition of hydrophilic coatings [277], or adhering polyanions and polycations [278]. A well-established approach is plasma treatment; an effective technique used to modify the substrate's surface chemistry and make it hydrophilic [198,258,279,280] with the added advantages of being low cost, simple to apply, and requiring no additional reagents [198]. As described in the protocols of Chapter 2.3, the technique can be used to modify PDMS surface hydrophobicity. Initially, native PDMS substrates have an RMS roughness of 0.309 ± 0.008 nm and a contact angle of 97 ± 4 °. The exposure of PDMS substrates to air plasma alters their chemical structure by removing the hydrophobic methyl side chains ($-CH_3$) present on the PDMS polymeric chains and promoting the formation of polar hydroxyl groups (-OH) at the substrate surface [281].

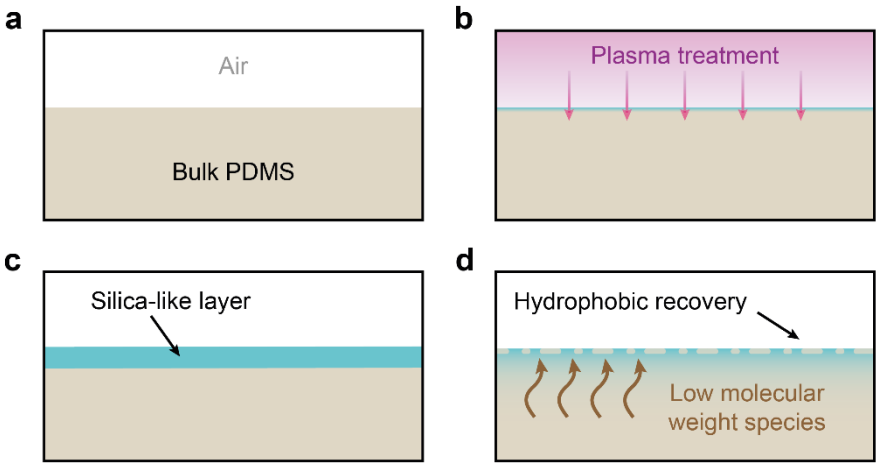

Figure 3.1: Schematic of plasma oxidation treatment of PDMS. The native bulk PDMS in air (a) which is then exposed to air plasma treatment (b), generating a thin silica-like layer on the substrate surface (c), which after some time experiences hydrophobic recovery (d).

This significantly alters the chemical structure of the PDMS surface, making it smoother and more hydrophilic, with a final RMS roughness of 0.203 ± 0.010 nm (measured using AFM), and a contact angle of 0 ± 2 °. These experimental results agree with ideas presented in the literature, whereby the PDMS surface is depicted

as being converted to a thin, brittle silica-like surface layer when exposed to plasma treatment (Figure 3.1c). Studies using techniques such as neutron reflectometry, scanning electron microscopy and X-ray photoelectron spectroscopy, have verified that plasma treatment converts the polymer structures at the PDMS surface into an inorganic SiO_x-rich layer that is thin and smooth [282–285]. Because this layer is so thin (~ 10 - 100 nm thick according to literature [254,282,286]), the underlying bulk PDMS (> 100 µm in thickness), retains its innate hydrophobicity [286–288]. The underlying PDMS bulk also retains its flexibility even after plasma treatment and hence remains a useful deformable substrate for imposing strains on adhered membranes [56,175] and building cell stretching devices [141,161,176].

This modification of surface properties can be demonstrated by changes to the PDMS's macroscale wettability, as well as the alteration to its nanoscale topography, as shown in Figure 3.2. Although subtle, textural differences in the substrate surface are visible in topographic images (Figure 3.2a-c). Shorter plasma oxidation exposure times (3 seconds) resulted in a rougher surface, whereas longer plasma oxidations (30 seconds) created a smoother surface (Figure 3.2d). Conversely, the surface wettability only decreased with increasing plasma treatment exposure, with 3-second plasma treatment creating a partially wetting PDMS surface, and the 30-second treatment resulting in PDMS becoming completely wetting to water. Seeing that all PDMS samples exhibit a roughness comparable to that of cleaned silica glass substrates (< 0.5 nm [195]), the drastic differences in wettability were used to classify PDMS samples. A PDMS sample exposed to 30 second plasma treatment was defined as "fully plasma-treated PDMS", while a PDMS exposed to the shorter 3 second treatment defined as "partially plasma-treated PDMS". Such fully plasma-treated PDMS substrates induced bilayer responses similar to those observed on a glass substrate (both being smooth hydrophilic silica-based interfaces) and will be further discussed in Chapter 4. Partially plasma-treated PDMS substrates, although capable of stably supporting lipid bilayers, induced different membrane-substrate interactions, as discussed in Chapter 5. Although the exposure parameters described above are unique to the experimental setup and plasma generator, they reproducibly produced the substrates with the characteristics described above, making the technique a viable means of substrate modification for later experiments.

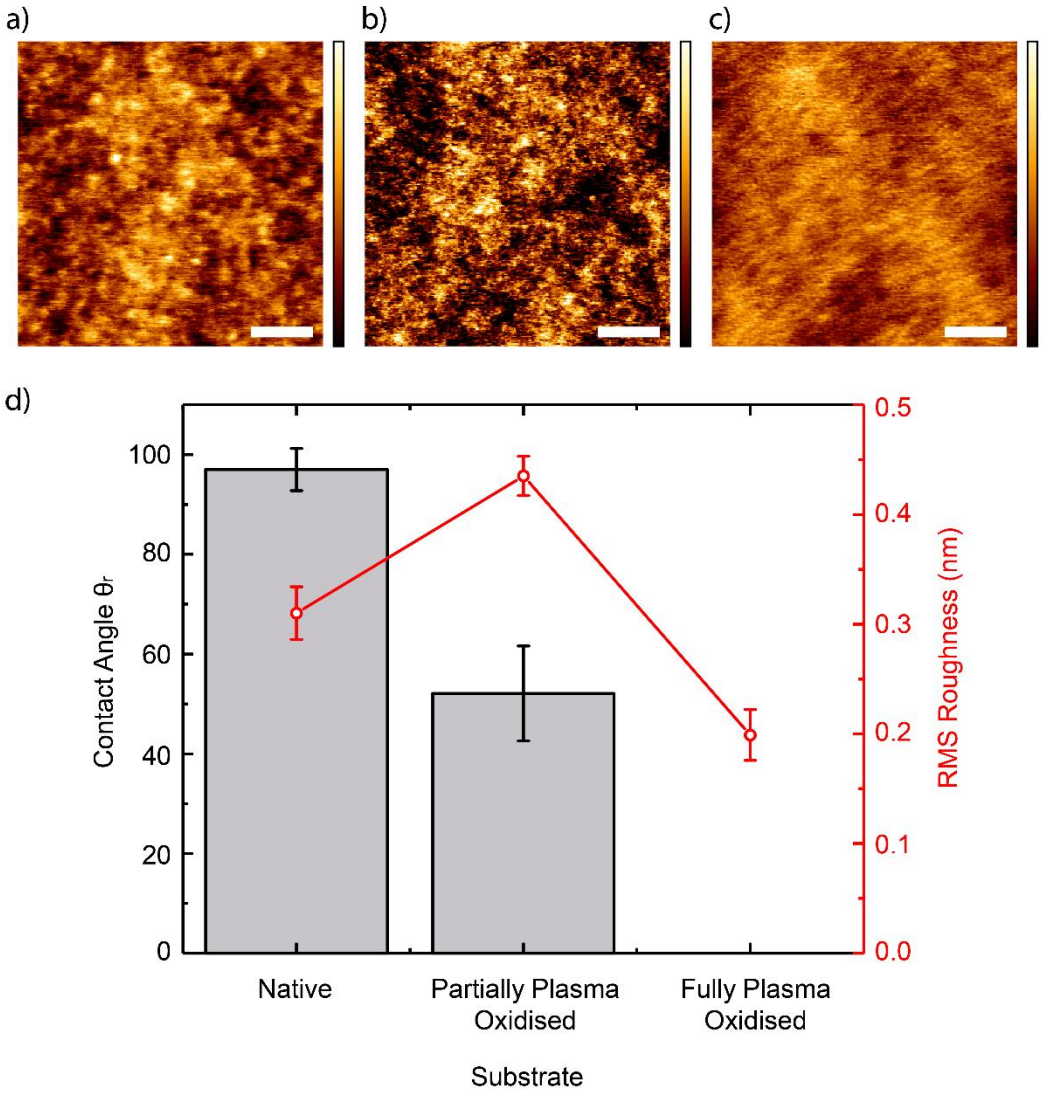

Figure 3.2: Change in physical and chemical surface properties of PDMS after plasma oxidation treatment. AFM topographic images of (a) native PDMS (0 seconds exposure), and (b) partially (3 seconds exposure) and (c) fully (30 seconds exposure) plasma-oxidised PDMS. Graph showing a change in wettability, in terms of apparent contact angle, and root mean square (RMS) roughness of native, partially and fully plasma-oxidised PDMS samples (d). Scale bars and colour bars in (a-c) represent 200 nm and a range of 2 nm, respectively; and error bars in (d) represent the standard error.

The thin silica-like surface layer of fully plasma-oxidised PDMS substrates has similar interfacial properties to glass; both contain inorganic SiO_x species, both are hydrophilic, and both possess a low RMS roughness of ~ 0.2 nm (with reported values from literature ranging from 0.1 - 0.3 nm [2,118,195,289]). Partially plasma-oxidised PDMS, on the other hand, has an RMS roughness of 0.435 ± 0.006 nm. Partial plasma treatment appeared to create a slightly rougher surface with "partial" hydrophilicity, demonstrating a contact angle of 52 ± 9 °.

One possible explanation for this partial hydrophilicity and increased roughness could be that the partial plasma treatment creates an incomplete silica-like layer on the PDMS surface, resulting in an interface of hydrophilic and hydrophobic domains of nanoscale size. Such nanoscale textured surfaces of oxidised and unoxidised PDMS could produce lower contact angles (Cassie equation, Chapter 2), and increased surface roughness (Figure 3.2d). This interpretation is supported by similar studies using advancing and receding contact angles on partially plasma-treated PDMS, that reveal an adhesion hysteresis of up to ~ 15 ^{o}, suggesting a degree of chemical or topographical heterogeneity on partially plasma-treated PDMS's surfaces [290].

To verify experimentally the presence of nanoscale hydrophobic and hydrophilic domains on the surface of partially plasma-oxidised PDMS, chemical force mapping was employed. Chemical force mapping can provide molecular-level insights into the interfacial behaviour of samples and allows characterisation of the differences in hydrophilic/hydrophobic structures present on fully and partially oxidised PDMS substrates when immersed in aqueous solutions. By systematically measuring the adhesion force between a hydrophobised hexanethiol-coated AFM tip and the substrate immersed in an aqueous solution, the lateral distribution of hydrophobic regions on the PDMS surface could be analysed (see Chapter 2.6.4 for further details). The results are presented in Figure 3.3a-b. Each pixel represents a domain of ~ 30 nm by 30 nm, resulting in a 32 by 32 pixels force map. This resolution offered a reasonable compromise between acquisition time (~2 hours for each force map) and experimental limitations such as the radius of the AFM tip (~ 30 nm according to manufacturer specifications). Using such adhesion maps, the lateral distributions of hydrophobic domains on the surface of fully and partially plasma-treated PDMS can be compared. The adhesion map of Figure 3.3a shows that uniformly low adhesion forces are obtained across the fully plasma-oxidised sample. However, the data appears positively skewed compared to the Gaussian distribution (with a mean value of 0.05 nN and a median value of 0.04 nN), likely due to the presence of adhesion values at the lower end of the AFM's force detection limit. Regardless, the measurements corroborate the data shown in Figure 3.2, in which full air plasma oxidation of the PDMS generated a uniformly smooth hydrophilic surface, attributed to the formation of a thin silica-like layer.

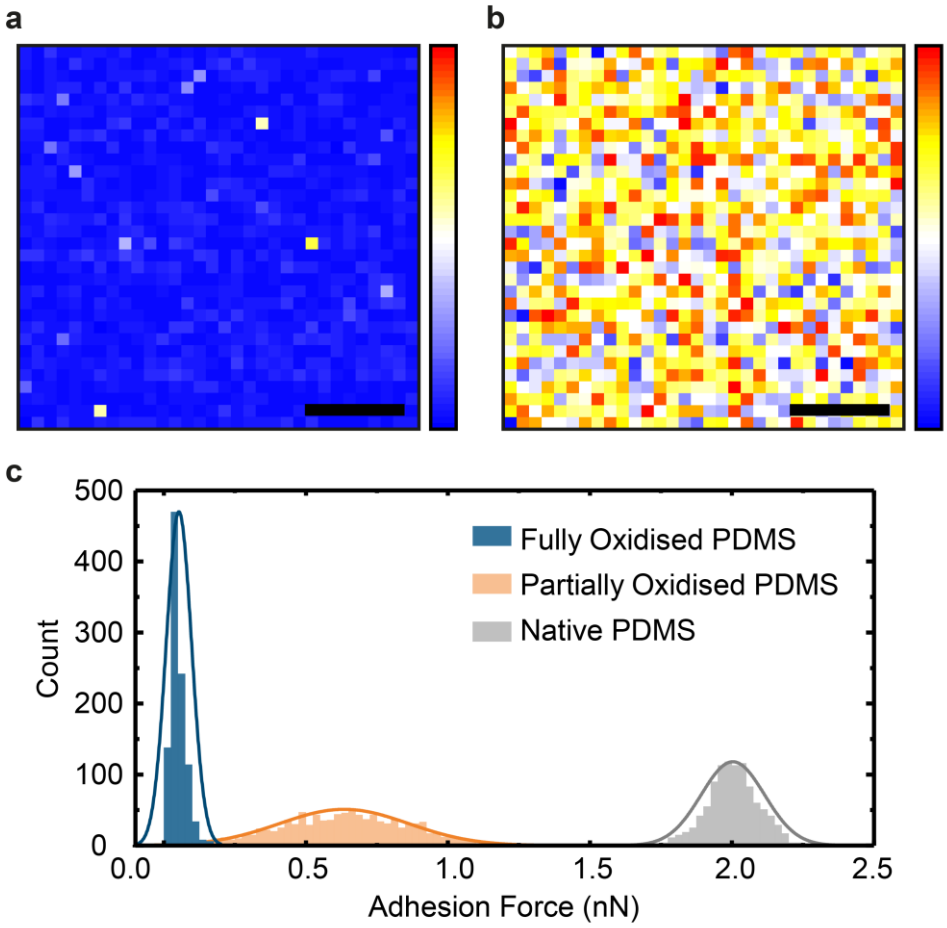

Figure 3.3: Force spectroscopy measurements of PDMS-cholesterol interactions. Adhesion force maps using hydrophobic AFM tips on fully (a) and partially (b) plasma-oxidised PDMS reveal differences in hydrophobicity at the nanoscale. The image is 32 x 32 pixels, and each pixel represents 31.25 nm by 31.25 nm. A histogram of the measured adhesion forces (c) taken over n = 1024 force curves (for each population) indicates means and standard deviation of 0.05 ± 0.04 nN for fully plasma-oxidised PDMS, 0.63 ± 0.23 nN for partially plasma-oxidised PDMS, and 2.00 ± 0.11 nN for native PDMS. Gaussian fitting applied using OriginPro 2017 fitting tool, with two fitting parameters and a bin size of 0.025 nN. Scale bar and colour bars in (a-b) represent 250 nm and a range from 0 - 1 nN, respectively.

The adhesion force map acquired over partially oxidised PDMS (Figure 3.3b) indicates a high degree of lateral heterogeneity across the surface when compared to the result on fully oxidised PDMS. However, no clear domain structure is visible in the adhesion force map, suggesting that either discrete hydrophobic/hydrophilic domains are of a scale smaller than the 30 nm pixel resolution of the force map or that the hypothesis of small domains is incorrect.

Histograms of the measured adhesion forces (Figure 3.3c) showed that partially oxidised PDMS has a higher average and a wider distribution of adhesion forces than for fully oxidised PDMS. This shows partially oxidised PDMS to be distinctly

more hydrophobic and heterogeneous, with small regions that possessed adhesion forces as low as ≤ 0.1 nN, corresponding to strongly hydrophilic areas. The latter appear absent from native PDMS. Notably, the adhesion force histogram for the partially plasma-treated PDMS in Figure 3.3c did not appear bimodal, as would be expected for adhesion forces measured on a surface with discrete hydrophobic and hydrophilic domains. Although it is possible that the domains are less than 30 nm in size and hence not resolved in the force maps, it is also possible that rather than discrete domains, the plasma treatment could result in a gradual conversion of the polymer structure into a glass-like silica-layer; creating a gradual chemical variation rather than a discrete, patchy surface.

The present results do not allow for a definitive conclusion about the existence of small heterogenous hydrophilic/hydrophobic domains, but regardless of the correct interpretation, the partially plasma-treated PDMS substrates exhibit an "intermediate" state of hydrophilicity compared to native, and fully plasma-treated PDMS. Surface functionalisation techniques have long demonstrated that chemically distinct regions on a single surface can be used to organise the lipid membrane. Such patterning is often employed on the micron scale to create 2D structures of lipid bilayers and monolayers [142,144]. The effects of such hydrophilic/hydrophobic regions when shrunk down to the nanoscale or molecular-scale are less explored and can have novel effects, as later discussed in detail in Chapter 5.

3.2 Hydrophobic recovery after plasma treatment

Although plasma oxidation is facile and effective, there is an ongoing struggle to make such modifications permanent, mainly due to the innate property of PDMS hydrophilicity reverting over time, (Figure 3.1d). Several mechanisms are reported to be responsible for PDMS's hydrophobic recovery, including the reorientation of polar chemical groups into the bulk due to conformational changes of the polymer chains, degradation of the polar groups, and diffusion of low molecular weight species (LMWS) from the bulk to the surface layer after treatment [264,267,281,291,292].

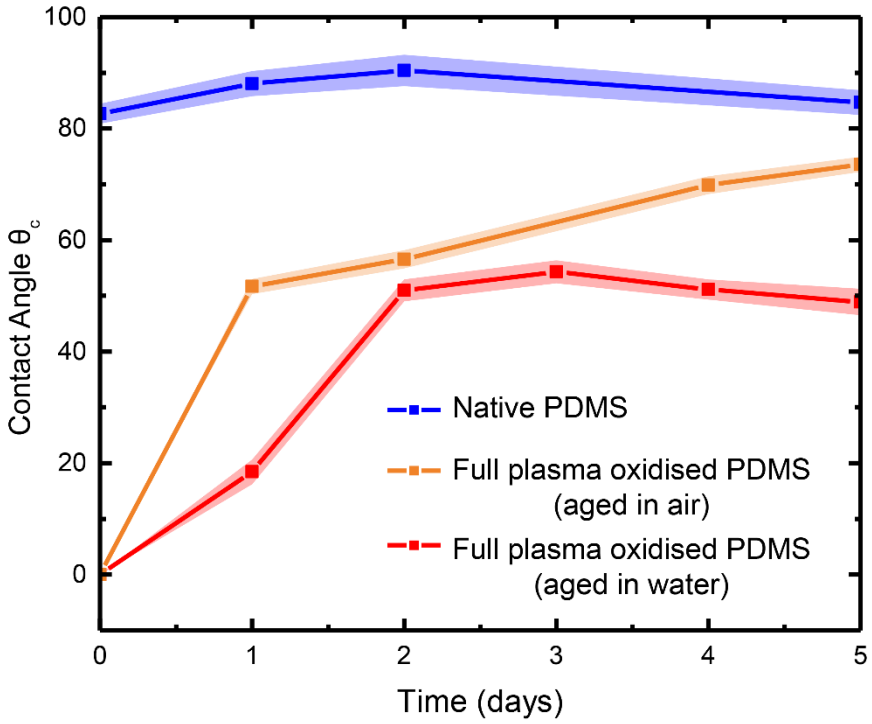

Figure 3.4: Hydrophobic recovery of PDMS. Contact angle measurements conducted over several days on PDMS samples change in wettability due to hydrophobic recovery under different storage conditions.

The migration of LMWS not only induces hydrophobic recovery but could propagate from the PDMS into surrounding adhered samples [267,268]. These LMWS can be formed from scission fragments created during oxidation or from uncured oligomers present after curing [264,281]. Although the Young's modulus of PDMS can be easily modulated by altering the elastomer:curing ratio, this can lead to excess uncured oligomers in the PDMS matrix, and such oligomers may contribute to hydrophobic recovery [293]. The fact that oxidation techniques are widely exploited to modify PDMS stiffness for cell-substrate studies is noteworthy [294], and the presence of such LMWS interfering with measurements is not widely discussed. Although the contribution to uncured oligomers can be reduced by correct fabrication and thermal ageing [293], LMWS formed from scission fragment and polymer reorientation can still significantly contribute to hydrophobic recovery, and loss of surface hydrophilicity after treatment [264,282,288].

Hydrophobic recovery can be sufficiently retarded when the PDMS is stored under proper conditions. Storing the PDMS in polar liquids, like water, can effectively suppress, and even inhibit complete hydrophobic recovery back to wetting

behaviour of native PDMS [295]. Figure 3.4 demonstrates the hydrophobic recovery of fully oxidised PDMS samples, prepared following the protocols described in Chapter 2.3, when stored in air or water. The native PDMS displayed a contact angle of 83 ± 3°, representative of hydrophobic surfaces. Initially, fully oxidised PDMS displayed contact angles of 0 ± 2°, being fully wetting and representative of a perfectly hydrophilic surface. This property degraded with time, with the plasma-treated PDMS regaining a degree of hydrophobicity and contact angles of 74 ± 2° when stored in air. More importantly, although both samples recovered, this behaviour was significantly hindered for plasma-treated PDMS samples stored in water, and seemingly halted after 2 days. With contact angles measuring 53 ± 3° after 5 days, these samples remained significantly wetting and reasonably hydrophilic. As all experiments were conducted in aqueous buffer, this reduction of hydrophobic recovery was also present in all further investigations. Additionally, by freshly preparing PDMS samples for each experiment, hydrophobic recovery could be limited enough to be considered stable for the timescales measured in the experiments described in later chapters.

3.3 Creating wrinkled topographies

Although plasma oxidation only marginally altered surface topography for the bulk PDMS by creating a thin silica layer, it can be used to create more complex topographies under certain conditions. This relies on the fact that the thin silica layer created by plasma oxidation has different mechanical properties than the bulk PDMS with an elastic modulus of 1.5 GPa compared to 0.3 GPa of bulk PDMS [286,287]. As the two directly adhere, this can result in mechanical buckling [296], and therefore has been effectively applied to PDMS substrates to create wrinkled and folded topographies [297–301], even on length scales < 100 nm [300]. Such methods provide a useful and straightforward technique for the study of nanoscale curvature of membrane systems [149,153,302–304]. Although often relying on the precise and controlled application of strains to the substrate through bespoke tensile devices, such structures can be reproduced with thin films of PDMS adhered over a small air pocket, as described in Chapter 2.8. In such devices, a thin film of PDMS is sealed over a 1 mm diameter hole in a 10 by 10 by 5 mm block of PDMS using plasma

treatment. This creates a flexible PDMS sheet suspended above a pocket of air (Figure 3.5a). Such a set-up, when exposed to the low pressures required for air-plasma treatment, induces biaxial stress on the PDMS film as the air pocket expands, imposing a positive air pressure on the flexible PDMS film (Figure 3.5b). During plasma treatment, a thin, brittle silica layer is formed (Figure 3.5c). After ambient pressure is restored, the air pocket is deflated, putting the PDMS film under compressive stress. Unlike the bulk PDMS, the silica layer has reduced elasticity, so the build-up of in-plane compressive stress results in a buckling failure, where out of plane projections such as wrinkles are formed (Figure 3.5d). Such wrinkled topographies reduce in-plane compressive stresses without delaminating the adhered stiff layer from the thicker underlying soft elastic substrate, thereby releasing elastic energy [301]. The formation of such structures has been extensively investigated [299–301], with the iconic chevron pattern (Figure 3.5f) being linked to the presence of circular biaxial stresses. In this case, the geometry was generated by the suspension of the PDMS film across a circular shape. When looking at the resulting wrinkling pattern, folded regions also appear on the substrate surface, indicated by white arrows in Figure 3.5f. Folded features are commonly developed in buckling systems, acting as an additional mechanism for releasing in-plane compressive stresses due to the coupling of the brittle silica to the flexible bulk PDMS [301,305]. These differences in local curvatures can be effectively exploited to see how membranes organise differently in response to substrate curvature. This is utilised and briefly discussed further in Chapter 6.5.2, to show how such local curvature influences the behaviour of supported lipid bilayers with coexisting liquid phases. Although the wrinkled substrate presented in Figure 3.5 data is not novel, the approach to their formation provides a quick, easy and simple method for forming nanoscale curved topography, using limited techniques and materials. Such topographies are highly useful in deciphering the role of local curvature on supported biomembrane function and organisation [149,153,302–304], and publishing of such protocols will aid their broader use in membrane substrate investigations.

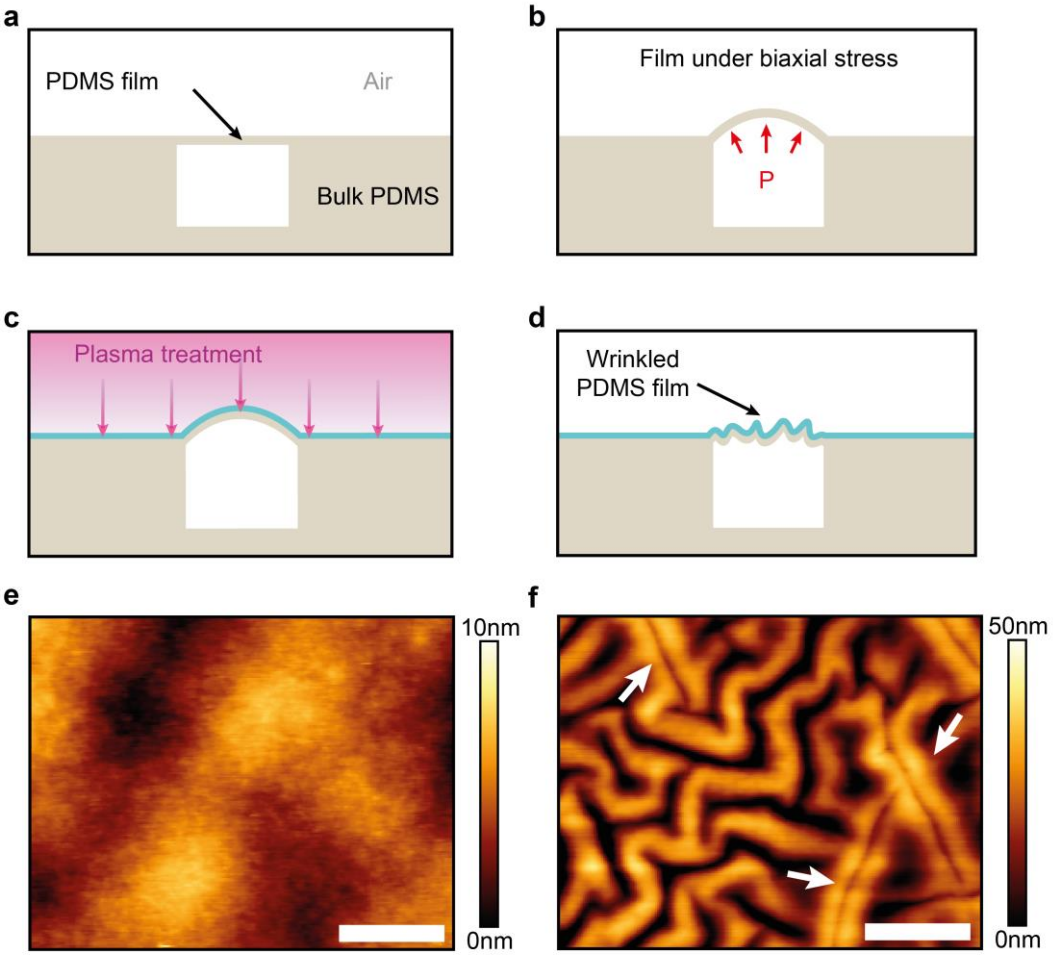

Figure 3.5: A PDMS topography modified by plasma treatment and example topographies. A suspended flexible PDMS film above a trapped air pocket (a), which when exposed to low pressure expands due to trapped air (b) and exerts biaxial stress on the PDMS film. The strained film is exposed to air plasma oxidation, creating a thin, brittle silica layer on the surface (c), and then upon returning to ambient room pressure buckles (d) due to differences in stiffness with the underlying bulk PDMS. AFM images of flat bulk PDMS (e) and wrinkled PDMS film (f), both exposed to 5 seconds of plasma oxidation. The location of folded regions in (f) are shown by white arrows. Scale bars in (e-f) represent 500 nm.

3.4 Surface cracking under mechanical stress

One of the major advantages of PDMS is its flexibility. The elastomeric properties of PDMS have been extensively put to use to investigate the influences of external mechanical properties on adhered biomembranes [56,71,175], and cellular samples [306]. As shown in Figure 2.10 of the previous chapter, the flexibility of a plasma-oxidised PDMS film allows it to be elastically stretched to over 30% strain. These strains could be held static on the timescale of minutes, making such measurements useful

for the controlled application of tensile strains to adhered membranes. Although the PDMS bulk is flexible, the silica-like layer generated during plasma treatment is less so, being relatively brittle and prone to cracking under mechanical stress [288]. To evaluate the surface cracking of PDMS substrate after plasma oxidation, controlled tensile stresses were applied to fully plasma-oxidised PDMS samples and imaged with AFM (see Chapter 2.8 for further details on protocols). In these experiments, fully-oxidised PDMS was used, as this was the most prolonged plasma treatment exposure used to make samples for subsequent measurements presented in this thesis, and samples formed with this treatment would have the thickest and most brittle silica-layer present, and therefore most likely prone to cracking.

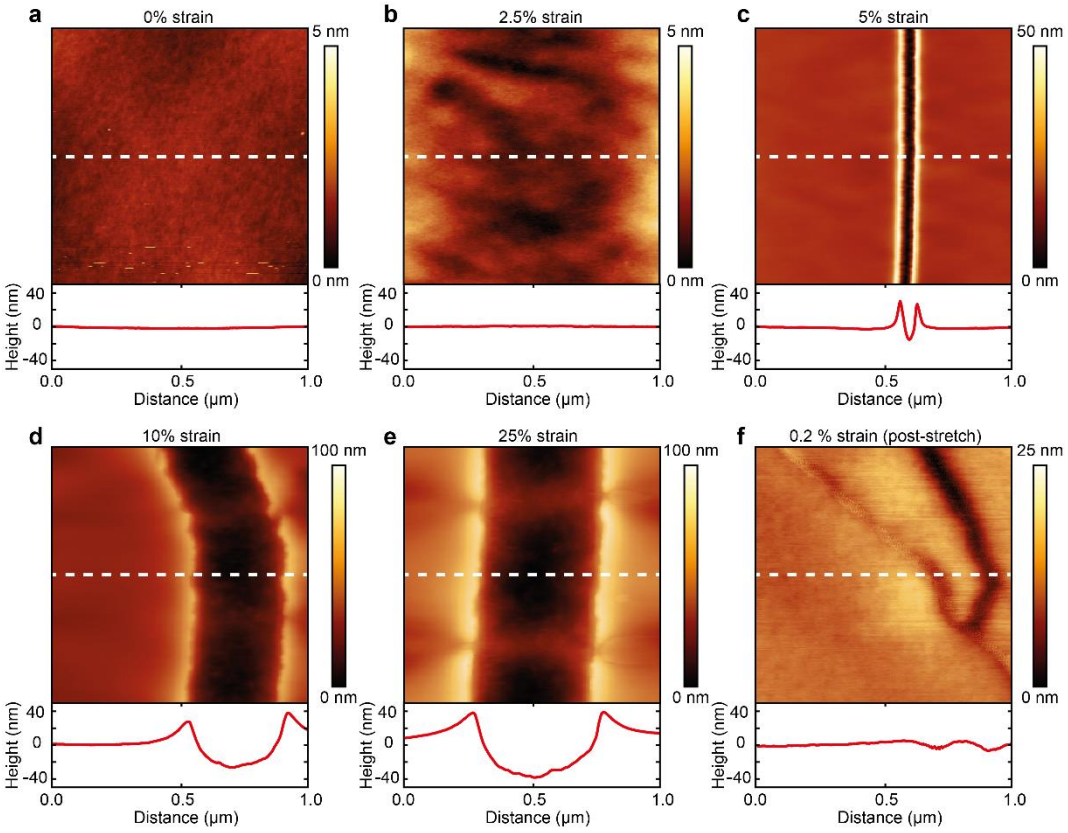

Figure 3.6: Surface cracking in plasma-treated PDMS due to tensile strains. AFM scans of fully plasma-treated PDMS substrate exposed to a tensile strain cycle from 0% (a), 2.5% (b), 5% (c), 15% (d), 25% (e) and returned back to 0.2% (f). Corresponding line profiles from the dotted white line are shown below the scans.

The application of small strains deformed the uniformly flat PDMS surface (Figure 3.6a) to form minor, but visible texturing in Figure 3.6b. At 5% strains, evidence of surface cracking was revealed (Figure 3.6c) with a clear fissure in the substrate

surface. When larger strains were applied (Figure 3.6d-e), the surface cracks widened, revealing what was assumed to be the underlying untreated bulk PDMS substrate, with the silica-like layer being ~ 40 nm thick. This cracking process formed a lip due to stress relaxation processes as the brittle silica snaps [307], which upon the removal of the applied strain left a fissure in the cracks' previous location (Figure 3.6f). The thinness of the silica-layer likely reduced its tendency to form cracks without the application of stress, aiding the formation of uniformly smooth hydrophilic surfaces using such protocols, as seen in examples of Figure 3.2a and Figure 3.6a. Such cracks aid hydrophobic recovery, as they create openings in the diffusive barrier formed by the silica-like layer, allowing LMWS to more easily propagate to the substrate surface [288,295]. However, in static measurements, the PDMS was often bonded to a glass substrate, using protocols described in Chapter 2.3, to provide structural support and aid handling. With this additional support, the PDMS could not easily warp and undergo large enough strains to induce cracking. Hence, it can be satisfactorily concluded that the fully plasma oxidised samples in subsequent investigations were mostly uniform, smooth and devoid of major defects such as cracks, except when undergoing tensile strain measurements. Although often seen as a nuisance, such nanoscale cracking can be a useful modification of the PDMS surface. With the controlled application of tensile stress, the surface of plasma oxidised PDMS samples can be patterned with nanocracks to functionalise interfaces [307–310]. An example of this is demonstrated in Chapter 5, where PDMS nanocracks are used to alter the composition of adhered lipid membranes.

3.5 Conclusion

This chapter describes how PDMS surface hydrophilicity, topography and chemistry can be altered using air plasma oxidation. Furthermore, using described protocols, it was demonstrated that nanoscale features such as surface wrinkles and cracks could be generated on PDMS substrates using air plasma oxidation in conjunction with the application of strain. These more exotic nanoscale surface features could be utilised for investigations into the impact of local curvature and substrate composition on adhered membrane behaviour. Overall, the various means of modifying the PDMS substrate with air plasma oxidation alone demonstrates the

versatility of the system. Such versatility is highly useful in the investigation of the influence of a substrate on adhered bilayers, with plasma oxidation being used to controllably modify membrane properties. These surface modifications are employed in the preliminary investigations of Chapters 6 and exemplify how such techniques can be further exploited to favour the formation of gel domains in specific regions on the substrate. Next, in Chapter 4, the process of supported bilayer formation on PDMS substrates is discussed, including how some of the substrate properties such as hydrophobicity can significantly perturb membrane behaviour, even in the first moments after fusion.

Chapter 4: Morphological changes in lipid bilayers induced by vesicle fusion to substrates

In this chapter, lipid vesicles are fused to glass and PDMS substrates to investigate the after-effects of the fusion process on membrane morphology. Lipid patches are isolated regions of supported lipid bilayer with mostly smooth, rounded edges, and are formed by fusing giant lipid vesicles to a supporting substrate [311]. Even though isolated, lipid patches still represent a large area of continuous supported bilayer, so can be easily scrutinised by high-resolution techniques such as TIRF and AFM [311]. Moreover, lipid patches are large enough to allow simultaneous assessment of changes in their surface area and in/out of plane morphological organisation (tubes, buds, pores) using epifluorescence microscopy. In a study by Bhatia et al. it was demonstrated that macroscale L_o and L_d domains in lipid membranes could be fixated by the fusion of phase separated GUVs to glass [85]. Interestingly, although lateral diffusivity was maintained in the bilayer, L_o and L_d domains were immobile. Using lipid patches, the presence of sub-optical domain structures in L_o/L_d domains were identified with AFM; detailing nanoscale artefacts difficult to observe in free GUVs.

Another benefit of lipid patches is that they represent a supported lipid bilayer system with a stable edge. Persistent free edges are rarely observed in bilayer systems at equilibrium, with edges often eliminated by the self-assembly of lamellar sheets or formation of closed-shell vesicles [312]. In the case of a lipid patch, it is still unfavourable for the hydrophobic core to be exposed to the surrounding aqueous solution at the edge of the membrane. To reduce this hydrophobic penalty the bilayer edge forms a hemi-micellar arrangement [313]. Hence, lipid patches provide a unique SLB system for studying lipid behaviour at the membrane boundary. Indeed, the presence of a persistent bilayer edge is a fascinating property of lipid patches that can be exploited. AFM studies on smaller lipid patches have shown a preference for antimicrobial peptides (AMPs) to adsorb at the patches edge [314–316]. Their adsorption to the edge reduces membrane line tension and increases patch

area and perimeter, as similarly observed with detergent molecules [317]. With increasing AMPs concentration the bilayer is eventually destabilised by the peptide's insertion, transforming the membrane into worm-like micelles and creating more edges, facilitating further peptide insertion and membrane disruption. This mechanism likely facilitates the peptides antimicrobial function.

Lipid patches represent a useful alternative membrane model system, combining the advantages of GUVs and continuous SLB systems [318,319]. The formation of lipid patches by coupling lipid membranes to substrates suppresses membrane fluctuations and equalises membrane tension, making lipid patches a useful system for quantitative analysis of the membrane surface changes [311]. Membrane fusion is a vital cellular function, but remains poorly understood due to its high degree of complexity. GUVs are particularly useful for understanding fusion processes due to them being easily observable with optical microscopy [108,111]. For example, it has been shown that the fusion of GUVs is preceded by the formation of a pore in the adherent vesicle [108,110,111]. This pore quickly expands, initiating the expulsion of the vesicles inner contents, causing the vesicle to rupture and spread across the substrate surface. These processes occur at sub-second timescales, completing in ~ 10 - 20 ms [108]. The majority of current studies focus on capturing these drastic morphological changes of vesicle rupture with high-speed imaging, ignoring the first few seconds following vesicle fusion. It is in these subsequent seconds that the after effects of the fusion process are demonstrated. As the membrane rapidly transitions to a planar geometry, it spreads and confines a newly formed interstitial water layer during vesicle rupture. This process likely imposes hydrodynamic [87], mechanical [175], and osmotic [319–321] stresses on the membrane, all of which can significantly reorganise membrane structure, often within the timescale of seconds to minutes. The literature is lacking in observations of the effects of the vesicle fusion process on resultant lipid patch structure, and how such membranes reorganise due to mechanical stresses of vesicle rupture.

The aim of this chapter is to identify the reorganisation of the lipid bilayer resulting from vesicle fusion, and to observe changes in the lipid patch area and fluorescence homogeneity. The lipid patch area was measured to characterise behaviours such as membrane contraction and spreading across the substrate surface after vesicle

rupture. Additionally, variations in fluorescence intensity were used as an indicator of changes in lipid packing and aggregation of fluorescent molecules in the membrane. By observing the fusion process in cholesterol-containing vesicles, the formation of transient lipid protrusions after vesicle rupture was identified. Lastly, observations between fully and partially hydrophilic substrates were compared to investigate the impact of substrate hydrophobicity on such relaxation processes.

4.1 Morphological changes in supported lipid bilayers induced by vesicle fusion

In the following investigations, lipid patches of DOPC were fused onto different smooth hydrophilic surfaces, namely: mica, glass, and fully plasma-treated PDMS. The lipid patches retained their lateral diffusivities, as shown in Figure 4.1, with magnitudes similar to those found in literature [125].

Although all patches were fluid, the magnitude of diffusivity between the substrates was measurably different, suggesting the kinetics of supported lipid bilayers are substrate dependent, even between materials possessing smooth hydrophilic interfaces. The literature on other PC lipid systems has demonstrated that the diffusion coefficient on mica is significantly lower than on silicon oxide due to micas being atomically flat and having a higher zeta potential than glass, which favours a stronger bilayer-substrate interaction reducing membrane lateral diffusivity [112,113]. This corroborates with the data presented in Figure 4.1, where mica shows the lowest diffusivities, while glass and plasma-treated PDMS samples show slightly higher lateral diffusivities.

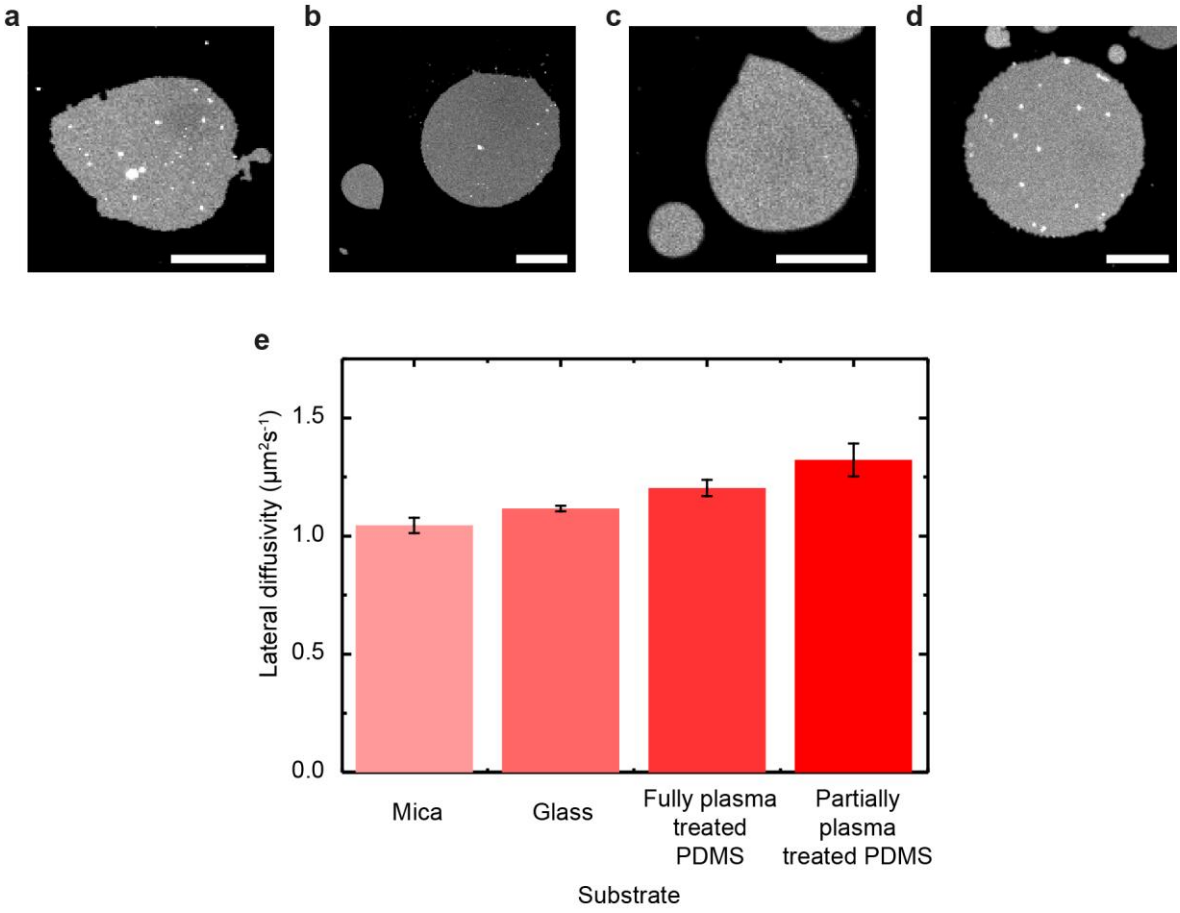

Figure 4.1: Formation of supported lipid patches on hydrophilic surfaces. Changes in the fluidity of liquid disordered membranes on hydrophilic substrates. Fluorescence micrographs of lipid bilayer patches composed of DOPC doped with 0.1 mol% Rh-DPPE supported on mica (a), glass (b), fully plasma-treated PDMS (c), and partially plasma-treated PDMS (d) substrates, 2 minutes after initial fusion. Graph showing average lateral diffusivity of DOPC membranes (e), doped with 0.1 mol% Rh-DPPE, on each of the substrates. The scale bars in (a-d) represent 50 μm.

The lateral diffusivities were calculated from FRAP measurements on fused GUV patches, as it was difficult to form continuous lipid bilayers with LUVs on partially plasma-treated PDMS and gain a comparison for all mica, glass, and fully/partially plasma-treated PDMS substrates. Although this approach is not ideal for FRAP, which requires a relatively infinite reservoir of unbleached fluorophores (as is the case with continuously supported lipid bilayers), reasonable estimations of relative lateral diffusivities could be acquired using lipid patches. Additionally, this benefitted the comparison of the lateral diffusivities' impact on GUV patch formation and homogenisation, as diffusivities were acquired directly from patch systems.

Although in all cases lipid patches spontaneously fused to create supported lipid bilayers as shown in Figure 4.1a-d, visual inhomogeneities within the lipid patch could be detected in the first few seconds after fusion.

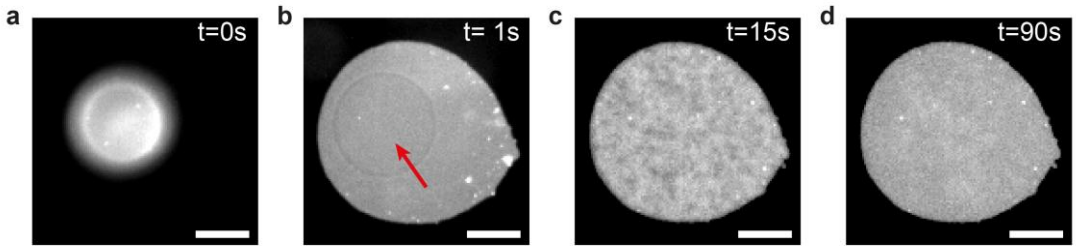

Figure 4.2: Fusion induced membrane reorganisation on a hydrophilic substrate. Fluorescence micrographs of lipid bilayer patches composed of DOPC doped with 0.1 mol% Rh-DPPE fused on a glass substrate (a-d). The red arrow indicates the transient adhesion spot present after vesicle rupture. The scale bars in (a-d) represent 20 μm.

An example of such inhomogeneities is given in Figure 4.2a-d. A deposited vesicle adheres to the substrate surface (Figure 4.2a), ruptures and spreads into a supported lipid patch (Figure 4.2b). The resultant lipid patch shows evidence of the initial adhesion region, where the vesicle initially forms contact with the substrate. This is indicated by a red arrow within the circular area in Figure 4.2b. The adhesion spot quickly dissipates, confirming the lipid patch has retained a significant degree of lateral diffusivity, thereby allowing the bilayer to reorganise. Although the rupturing process itself had completed, evidence of further membrane reorganisation can be seen in Figure 4.2c. Inhomogeneities in the patch fluorescence intensity become visible within a few seconds after the vesicles rupture (Figure 4.2c), before coarsening and disappearing to leave a visually homogenous lipid patch (Figure 4.2d).

The transient mottling of the lipid patches after fusion (Figure 4.2c) indicates macroscale fluctuations in the bilayer structure. These changes in bilayer structure could be related to fluctuations in local fluorophore surface density within the membrane. This could possibly be in response to variations in local membrane tension and lipid packing density, set up by the rapid transition from a spherical membrane geometry to a flat geometry during vesicle fusion. Alternatively, the mottling pattern could be due to the coarsening of wrinkles in the lipid patch, as the bilayer “flattens out” after vesicle fusion. To better quantify this behaviour, changes

in the fused lipid patch area and standard deviation in fluorescence intensity across the patch were measured as a function of time. Changes in patch area indicate how lipid bilayer morphology changes in time, while deviation in fluorescence intensity provides a means of quantifying changes in the mottling pattern and tracking homogenisation of the lipid structure across the patch.

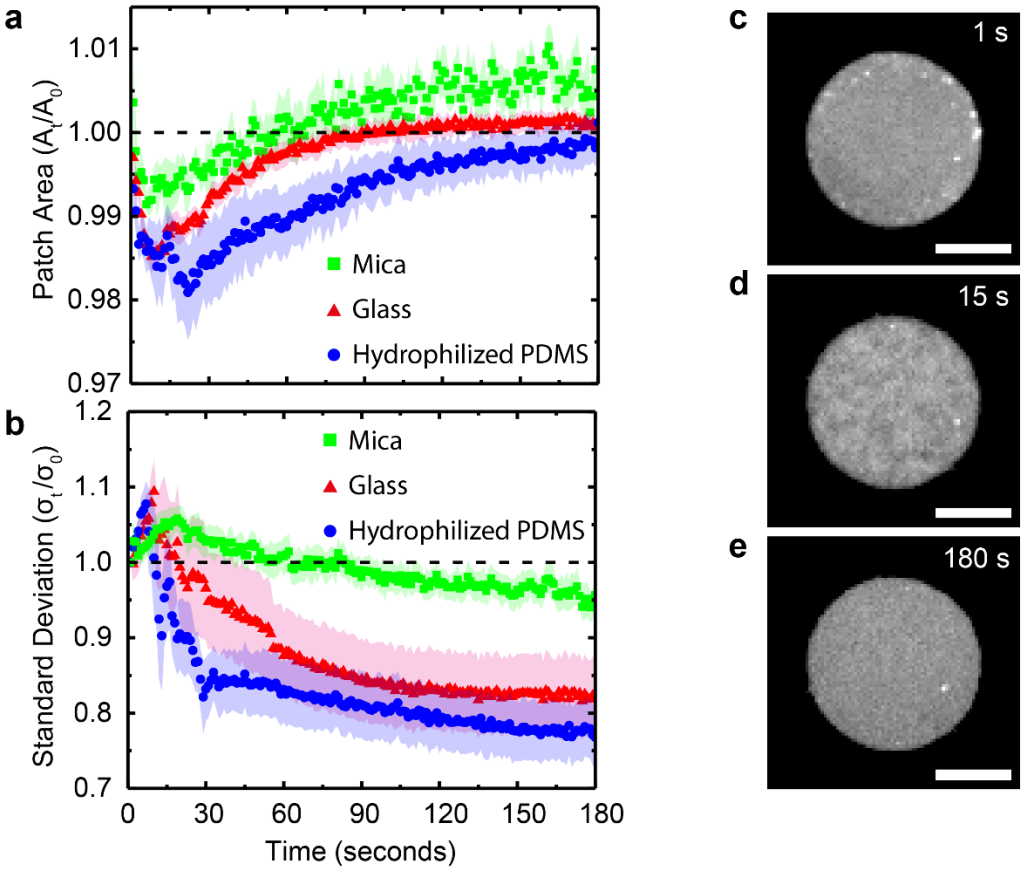

Figure 4.3: Fusion induced membrane spreading and homogenisation on hydrophilic substrates. Relative changes in the patch area (a) and standard deviation between pixels as a function of time (b) for lipid patches fused on mica, glass and hydrophilised PDMS substrates. Data from n = 6, 10, and 7 independent lipid patch samples for mica, glass and hydrophilised PDMS, respectively. Fluorescence micrographs of lipid bilayer patches composed of DOPC doped with 0.1 mol% Rh-DPPE fused on hydrophilic PDMS (c-e). The scale bars in (c-e) represent 20 µm.

Figure 4.3a quantifies the change in patch area immediately after fusion has completed. On hydrophilic substrates, an initial decrease in patch area of 1 - 2% was detected in the first few seconds after vesicle rupture. This was followed by spreading of the patch to recover its initial area. The standard deviation of fluorescence across the patch peaks in the first few seconds, before decreasing over a timescale of the order of 10 s (Figure 4.3b). This initial increase in the standard deviation of fluorescence intensity indicates that the fluorescence of the

patch is inhomogeneous in the few seconds following the fusion process, before becoming more uniform across the patch at around 90 seconds. Notably, the standard deviation of fluorescence intensity within the patch goes below unity, suggesting that the fluorescence signal of the patch is more homogenous after several minutes than immediately after the fusion. Furthermore, the changes in patch area and fluorescence intensity appear to coincide, both being simultaneously observed in ~ 30 % of analysed lipid patches. The fluctuation from unity in both, being maximal around the 10 - 30 second timescale, suggests a correlation between the two processes.

It is here proposed that the observed membrane instabilities may be caused by some membrane tension remaining in the lipid patch after its formation; due to the rapid nature of the vesicle fusion. The relaxation of this remaining membrane tension could possibly induce fluctuations in local lipid density (observed as the mottling pattern), before dissipating as the membrane homogenises and spreads across the substrate to leave a more uniform supported lipid. But, as the membrane tension was never directly measured in the investigations of this thesis, this explanation remains conjectural, and the causes for the lipid patches area and fluorescence instabilities after fusion remains currently unresolved.

To further verify that the observed mottling pattern was not an artefact resulting from the type of fluorescent label used (Rh-DPPE), but was indeed due to fluctuations in the lipid density, similar experiments were conducted using an alternative dye, $DilC_{18}(5)$. Unlike Rh-DPPE, which is tethered to a lipid molecule that is integral to the membrane, $DilC_{18}(5)$ is sequestered in between the lipid tails, thus is more shielded from substrate interactions such as frictional and hydrodynamic forces. Comparable effects were also seen when $DilC_{18}(5)$ was used, albeit at a smaller magnitude (Figure 4.4) .

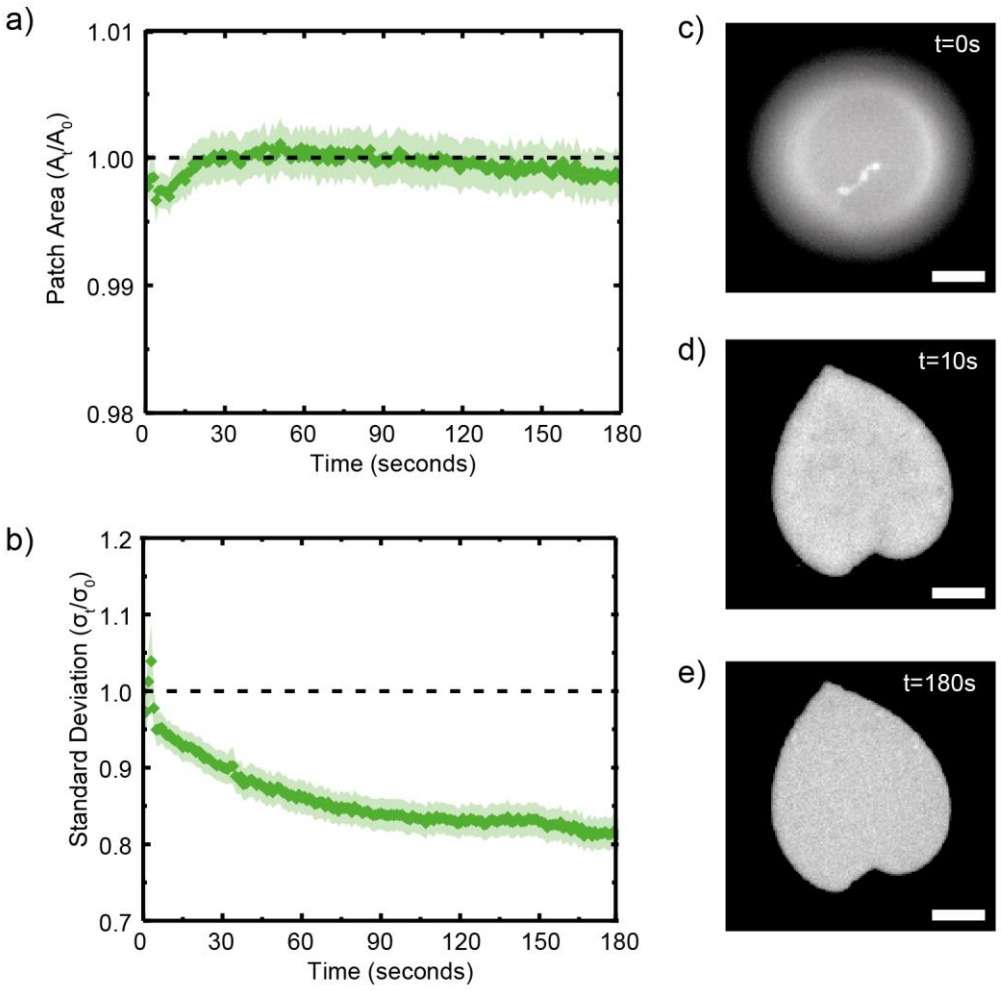

Figure 4.4: Fusion induced membrane spreading and homogenisation on hydrophilic substrates. Relative changes in the patch area (a) and standard deviation between pixels (b) for lipid patches fused on a glass substrate. Fluorescence micrographs of lipid bilayer patches composed of DOPC doped with 0.5 mol% $DiIC_{18}(5)$ (c-e) fused on hydrophilic PDMS. The scale bars in (c-e) represent 20 µm.

The difference in magnitude of the behaviours was likely related to $DiIC_{18}(5)$'s differing diffusive behaviour. $DiIC_{18}(5)$ was found to induce much slower lateral diffusivities in lipid membranes (~ six times lower than Rh-DPPE in a POPC membrane), in addition to possessing anomalous diffusivity behaviour; such as the two populations of diffusers when measured in single-lipid tracking experiments [148]. This suggests that the behaviours of transient fluorescent inhomogeneities are not an artefact caused by the presence of the bulky Rh-DPPE label, but are related to the innate membrane properties; such as lateral diffusivity.

Although mica, glass and fully plasma-treated PDMS are all hydrophilic and smooth, they induce slight differences in lateral diffusivity of adhered membranes [112,113](Figure 4.1e). The lipid patches formed on mica produced the smallest area contraction (Figure 4.3a) and showed longer timescale of fluorescence homogenisation (Figure 4.3b). The lipid patches supported on mica also exhibited the lowest measured lateral diffusivities, with values of 1.05 ± 0.03 $\mu m^2 s^{-1}$ (Figure 4.1e). The opposite was observed for fully plasma-treated PDMS and glass, which had higher lateral diffusivities of 1.20 ± 0.03 $\mu m^2 s^{-1}$ and 1.12 ± 0.01 $\mu m^2 s^{-1}$ respectively. Such magnitudes of lateral diffusivities could possibly explain why the effects in area change and fluorescence were subtle and short-lived, with the tested DOPC membranes possessing a high degree of lateral fluidity. These results, although subtle, demonstrate that the membrane undergoes significant reorganisation even after vesicle fusion has completed. Even if the impact appears minimal in DOPC fluid systems, the effect is likely to be more prominent in less diffusive systems; such as those containing cholesterol.

4.2 Morphological changes in cholesterol-containing bilayers induced by vesicle fusion

Cholesterol is a crucial component in the animal cell membrane and is popularly used in model membranes to modify lateral diffusivity [322,323]. The addition of cholesterol to DOPC systems leads to a significant decrease in lateral diffusivity (Figure 4.5f). This reduction in the fluidity of the lipid membrane hinders lipid movement and often lengthens the timescale over which lipid reorganisation occurs, suggesting the effects described in the previous Chapter 4.1 to be more distinct and easier to detect.

Indeed, the addition of 60 mol% cholesterol drastically lowered the lateral diffusivity in the membrane patches by an order of magnitude, extenuating the timescale over which the lipid patches spread and homogenise (Figure 4.5a-c). The mottled pattern is easily observable in the cholesterol doped DOPC patches supported on hydrophilic glass and remained visible up to five minutes after the fusion (Figure 4.5b). Furthermore, the time over which the mottled features disappear and leave

a homogenous lipid patch was significantly longer. (Figure 4.5c). Separately, the addition of cholesterol to the membrane induced an increase in the final area measured for the lipid patch following vesicle rupture. Subsequent membrane spreading after fusion resulted in a ~ 1% increase in lipid patch area after it fully homogenised.

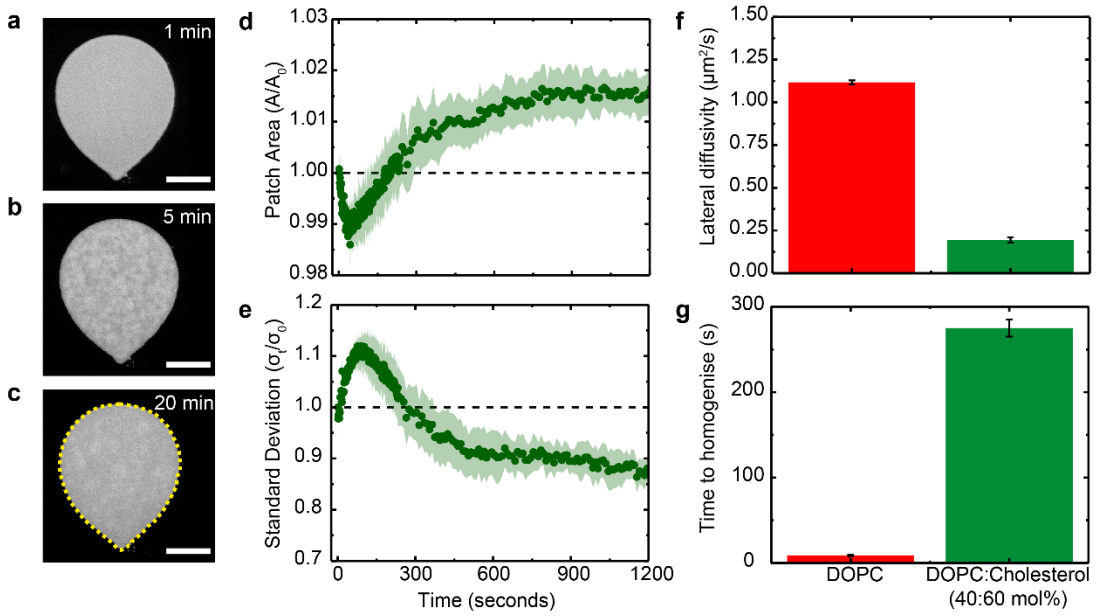

Figure 4.5: Cholesterol containing membrane reorganisation after vesicle fusion. Fluorescence micrographs of lipid bilayer patches composed of DOPC:Cholesterol (40:60 mol%) doped with 0.1mol% Rh-DPPE fused on glass (a-c). Outline of the original patch area shown by the yellow dotted line in c). Relative changes in the patch area and standard deviation between pixels as a function of time for lipid patches fused on glass (d-e). Comparison of membrane lateral diffusivity (f) and time for lipid patch to fluorescently homogenise (g) for lipid patches composed of DOPC and DOPC:Cholesterol (40:60 mol%) fused on a glass substrate. The scale bars in (a-c) represent 50 μm.

As the bilayer is capable of elastically stretching by several percent [324], it is plausible that this slight expansion in patch area after fusion is due to the lipid patch spreading and stretching across the interface as it wets the substrate surface. Overall these morphological changes relatively match the trends shown in Figure 4.3. As demonstrated earlier, samples with a lower membrane fluidity (patches formed on mica substrates), exhibit a smaller patch area contraction and a greater degree of membrane spreading at later times. Compared to pure DOPC membranes, the inclusion of cholesterol significantly decreased the lateral diffusivity, increased patch spreading (Figure 4.5f), and concurrently extended the time for fluorescence homogenisation by 250 times (Figure 4.5g). The doping of the membrane with cholesterol did indeed make the morphological changes present in lipid patches,

immediately after fusion, more distinct and easier to detect. An additional benefit was the extended timescale over which the process completed; with this, more observations could be conducted to validate the hypothesis that these behaviours were induced by membrane wrinkling, which in turn form the mottled pattern.

4.3 Transient formation of lipid protrusion after vesicle fusion

The membrane possesses many mechanisms to passively regulate its area while remaining confined to the substrate surface [56]. Many of these mechanisms rely on the formation of out of plane projections to release in-plane compressive stresses, such as the formation of tubes [56,71,175], vacuole-like dilations [319–321] and buckles/wrinkles [325]. Here, in Chapter 4.3, it is shown that membrane compression following vesicle fusion may also lead to the formation of fluorescence inhomogeneities, as observed on lipid patches that shrink immediately after the fusion process. In the following section, examinations are conducted to determine whether the observed fluorescent inhomogeneities are caused by out of plane membrane texturing. Small out-of-plane texturing would be often difficult to detect and analyse with conventional epifluorescence microscopy, therefore reflection interference contrast microscopy (RICM), previously described in Chapter 2.5.3, has been used.

Measurements from RICM rely on the interference of light reflected from different interfaces. The intensity at a given position depends on the separation between the different interfaces; in this case, the substrate and supported lipid bilayer. This particular set up could achieve z-resolutions of ~ 5 - 10 nm, which should be more than adequate to further characterise the micron-scale mottling behaviour seen with epifluorescence microscopy.

Due to the poor contrast of the fused lipid patches, they had to be located using epifluorescence microscopy, before switching to RICM. Therefore, the fusion process itself could not be imaged. Furthermore, to collect more images of the instabilities following vesicle fusion, DOPC:Cholesterol (40:60 mol%) vesicles were used, in which the mottling effect lasted longer. The RICM images of lipid patches showed a weak contrast, with little observable macroscale variation in intensity

across the patch (Figure 4.6). The intensity variations were correlated to the relative difference in height between the substrate and adhered bilayer using Equation 4.1 [167]:

$$\frac{2I-(I_{max}+I_{min})}{I_{max}-I_{min}} = \cos\left(\frac{4\pi nh}{\lambda}\right) \qquad \text{Equation 4.1}$$

where I represents the intensity of the interfered light, I_{max} and I_{min} represents the maximum and minimum sample intensity respectively, n represents the refractive index of the buffer solution, λ the wavelength of incident light, and h the distance between the sample and the substrate. With this equation, the measured intensity could be converted into a height map, representing the distance of the supported lipid membrane relative to the substrate surface (Figure 4.6i-l) (see Chapter 2.5.3 for further details).

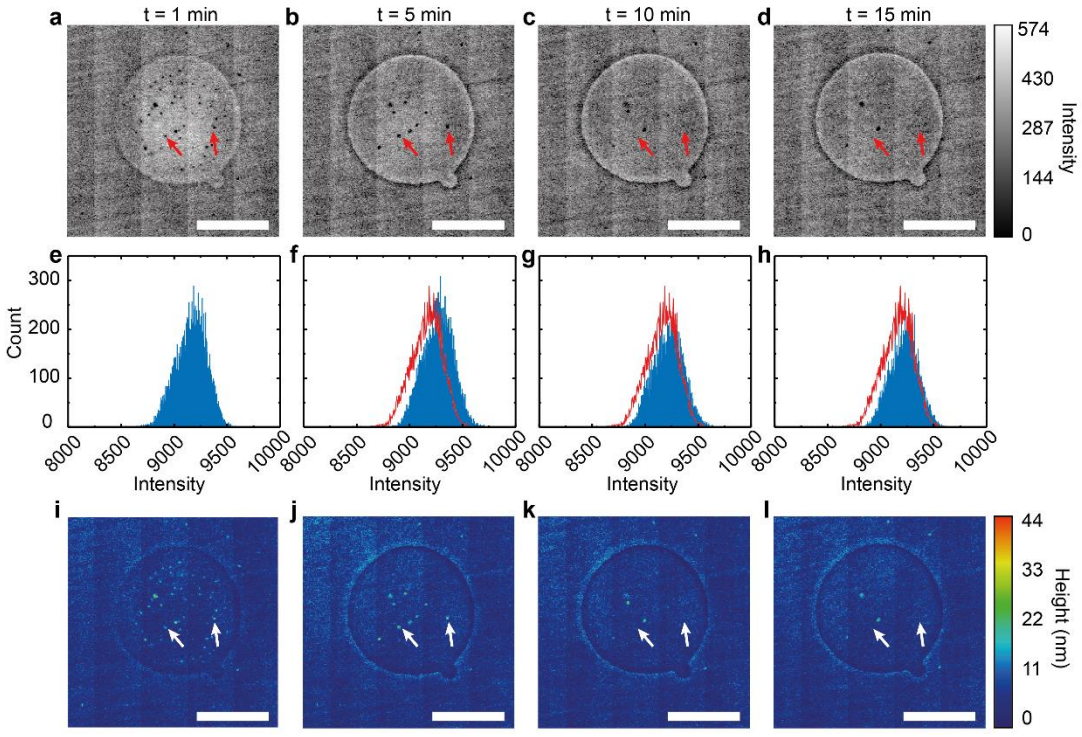

Figure 4.6: Fluctuations in membrane distance from the substrate immediately after fusion. Reflection interference contrast images from DOPC:Cholesterol (40:60 mol%) membrane doped with 0.1 mol% Rh-DPPE after fusion onto glass substrate (a-d). Heightmaps of the same lipid patches (e-h). Regions indicated by red arrows in (a-d) and white arrows in (i-l) suggest the presence of transient lipid protrusion. Histograms of pixel intensity corresponding to the reflection interference contrast images above (e-h). The red line trace indicates the outline of the initial histogram in (e) for comparison. The scale bars in (a-d, i-l) represent 10 µm.

The height maps confirmed that there were no apparent membrane wrinkles greater than 10 nm in height across the patch. It could, therefore, be concluded that the fluorescence inhomogeneities were not due to macroscopic wrinkles. Instead, it is proposed that they are caused by perturbations of local lipid density, causing a change in local fluorophore concentration within the membrane, while the overall membrane remains relatively flat. A possible reason for this might be the uneven interaction of the membrane with the substrate during vesicle fusion, which could cause variations in the lipid flow across the lipid patch during its formation.

While macroscopic wrinkles were absent, other out of plane projections were identified in contrast imaging; specifically, the presence of membrane protrusion, seen as dark spots in the raw contrast images, indicated by red arrows in Figure 4.6a-d.

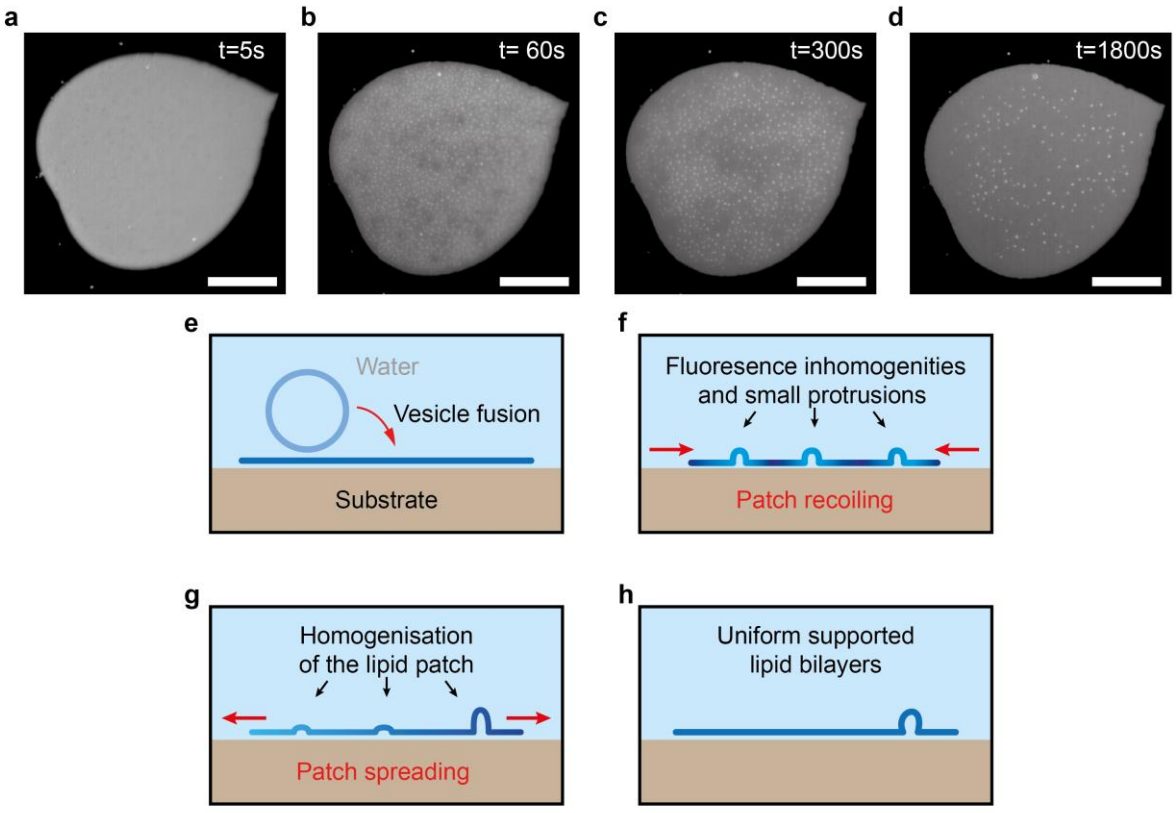

Figure 4.7: Formation of lipid protrusions during vesicle fusion. Fluorescence micrographs of lipid bilayer patches composed of DOPC:Cholesterol (40:60 mol%) doped with 0.1 mol% Rh-DPPE (a-d) fused on a glass substrate. The accompanying cartoons demonstrate the possible mechanisms resultant from initial vesicle fusion (e), leading to the patches area contraction, formation of small protrusions and fluorescence inhomogeneities (f), which relax and homogenise (g), leaving a uniform, stably supported lipid patch (h). The scale bars in (a-d) represent 20 µm.

These spots developed shortly after the initial fusion of the lipid patch and increased in height to ~20 nm (Figure 4.6i-l, white arrows). The majority of protrusions dissipated as the patch homogenises, seemingly being reabsorbed into the membrane; but some persisted even after the homogenisation of the patch fluorescence.

Such persisting protrusions explain the small positive shift in the pixel intensity distribution, as seen in Figure 4.6f-h. The coarsening and homogenisation of the protrusions could also be resolved with high magnification (60x lens) epifluorescence microscopy (Figure 4.7a-d).

The appearance of these protrusions corroborates with the hypothesis; some membrane tension remains in the bilayer after vesicle fusion causing initial lipid patch contraction, lipid density inhomogeneities detected by the fluorescence inhomogeneity and the formation of lipid protrusions, as depicted in Figure 4.6e-h. Indeed, the release of compressive stress in the adhered membrane through tubulation has already been demonstrated experimentally [56] and theoretically [326]. The protrusions reabsorb as the patch equilibrates and spreads (Figure 4.7d) simultaneously with the homogenisation of the fluorescence signal, leaving a uniformly supported lipid bilayer (Figure 4.7h), with a few remnant protrusions.

It should be noted that these protrusions are most prevalent and identifiable in cholesterol-containing patches. One reason for this might be the short period over which protrusions in pure DOPC patches likely exist, making imaging them difficult. However, cholesterol also changes the mechanical and structural properties of the lipid membrane, such as bilayer thickness [77,327], bending modulus [57,328], and interfacial elasticity [329] and therefore may favour the formation of stable protrusions.

4.4 Impact of osmotically induced membrane tension on lipid patch morphology after vesicle fusion

Although the transient mottling pattern in lipid patches formed by vesicle fusion was clearly observable (Figure 4.2c), the cause of this effect remained unclear. To check whether the initial tension in the lipid vesicles had an effect on the instabilities

following vesicle fusion, the vesicles were subject to varying osmotic shocks (Figure 4.8) [243,330,331]. DOPC vesicles were subjected to osmotic stress by using fusion buffer solutions with osmolarities between ~ 200 - 400 mOsmol/L (see Chapter 2.2 for further details). The osmolarities of the fusion buffer were altered by varying the amount of NaCl added to the buffer composition to achieve the desired osmolarities, as it was already present in excess in the fusion buffer solution; compared to the other salts such as TRIS and $CaCl_2$. Additionally, the ion permeability coefficients of Na^+ and Cl^- are in the order of 10^{-10} μms^{-1} and 10^{-7} μms^{-1} respectively, so their concentrations across the vesicle membrane could be assumed constant over the experimental time period [330,332].

Figure 4.8b shows a graph of the relative change in patch area as a function of the osmolarity of the fusion buffer. As expected, lipid patches formed in isotonic fusion buffer of 297 ± 1 mOsmol/L demonstrated the same trends in the changes to the patch area observed previously in Figure 4.3a; with an initial decrease in patch area of 1.66 ± 0.31%, before the original patch area was recovered. Interestingly the minimum patch area for lipid patches formed in hypoosmotic fusion had a lower magnitude, with a decrease of 0.51 ± 0.23% for patches formed in 201 ± 4 mOsmol/L fusion buffers. Conversely, lipid patches formed in hyperosmotic solutions such as 333 ± 1 mOsmol/L showed minimal patch areas, with the largest magnitude being 2.60 ± 0.52%.

In Figure 4.8c, a plot of minimum patch area against relative osmolarity is presented, with a high range of hyperosmotic fusion buffers. Relative osmolarity is defined as the difference in osmolarity of the internal vesicle solution (~300 mOsmol/L) and the fusion buffer. Although initially there appears to be an increase in magnitude of the minimum area of fused lipid patches from hypoosmotic to hyperosmotic fusion buffers, this seems to break down for tests using fusion buffers 340 ± 1 mOsmol/L and 402 ± 2 mOsmol/L. The reason for this remains unclear.

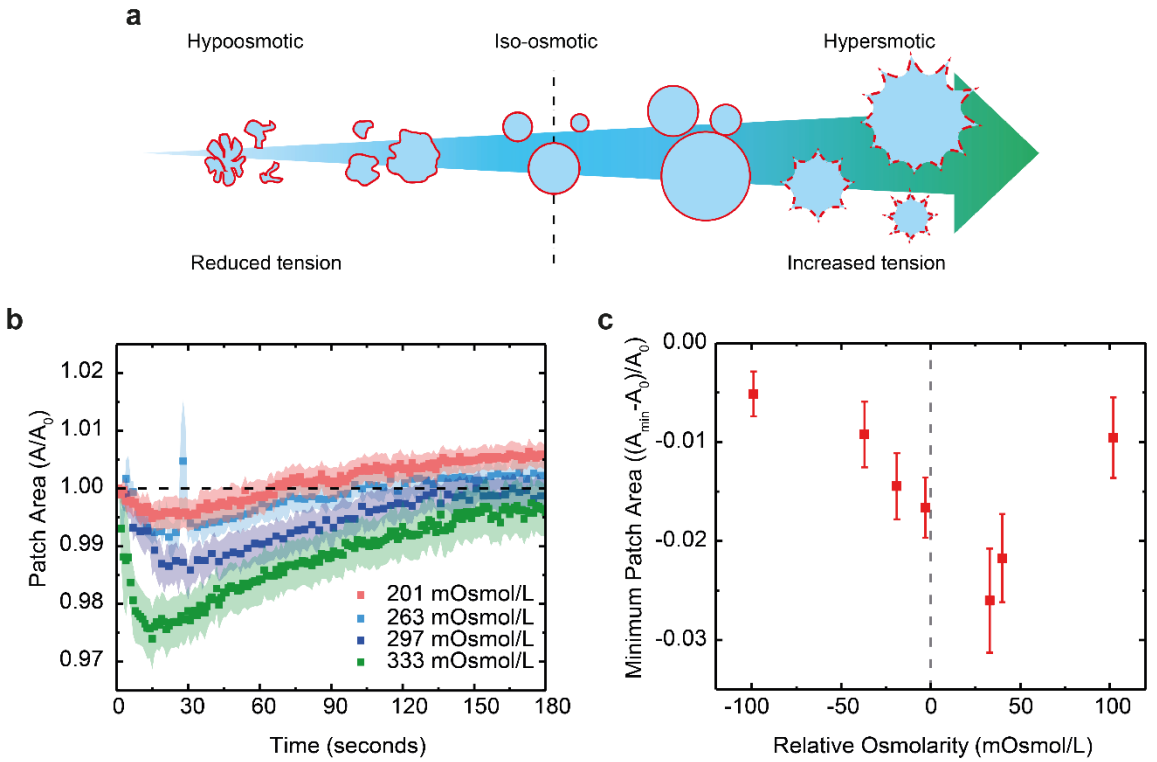

Figure 4.8: Impact of osmotic stress in vesicles on the contraction of the resultant lipid patch area. Illustration depicting the effects of hypoosmotic, iso-osmotic and hyperosmotic stress on membrane tension in liposomes (a), causing them to lyse, exist stably or rupture. Relative changes in the patch area (b) for DOPC lipid patches fused on glass in a buffer solution with osmolarities of 201 ± 4, 263 ± 1, 297 ± 1 and 333 ± 1 mOsmol/L. Changes in minimum patch area with relative osmolarity (c), for DOPC lipid patches formed by vesicle fusion on a glass substrate. Relative osmolarity defines the difference in osmolarity between the solution encapsulated by the vesicles and surrounding buffer solution.

Although these results indicated that there might be a link to changing membrane tension (manipulated through osmotic stressing) and fluctuations in the lipid patch area after fusion, the trend appeared weak and only existed over a limited range of values. Additionally, the impact of varying ionic strength was not accounted for in the described experiments, although it likely plays a role in observed mechanisms. For example, altering the NaCl concentration influences the Debye screening length (as discussed in Chapter 2.6.4.2), and possibly impacts the overall membrane-substrate interaction and resulting strength of vesicle adhesion to the substrate. As demonstrated using optical microscopy, quartz crystal microbalance and surface force apparatus; ionic strength conditions can have significant impacts on the adhesion of zwitterionic vesicles to substrates, even over ranges with a difference in magnitude of only 0 – 80 mM of NaCl [142,243,333]. The results in this chapter are

preliminary and further experiments are required before more detailed conclusions can be drawn.

4.5 Impact of partially plasma-treated PDMS on supported lipid bilayers formed by vesicle fusion

To further investigate the morphological changes in lipid patches immediately after vesicle fusion, the measurements described in Chapter 4.1 were repeated using partially plasma-treated PDMS substrates. As described in Chapter 3.1, these substrates possess a partially hydrophilic interface, but remain capable of stably supporting phospholipid bilayers. Experimental literature suggests that the presence of hydrophobic regions on partially plasma-treated PDMS hinders membrane spreading due to substrate pinning, even when placed under external mechanical strains [175]. Upon fusing DOPC vesicles to the partially hydrophilic PDMS surfaces, differences in the fusion process were notable. An immediately apparent difference between the fully and partially hydrophilic substrates is the persistence of the GUV in its adhered state. This has also been observed on substrates modified with SAMs, where GUVs achieved stable contact angles from ~ 28^{o} to 54^{o} [334].

Lipid vesicles in contact with partially plasma-treated PDMS (Figure 4.9a) experienced interactions only just sufficient to promote vesicle fusion (Figure 4.9b). Indeed, compared to other substrates whereby the membrane-interaction is weak, such as titanium oxide [335], spontaneous vesicle fusion is much less likely, and often requires tuning of other experimental factors such as pH to acquire similar levels of patch formation [290]. When successfully formed, lipid patches on partially plasma-oxidised PDMS retained a significant degree of lateral diffusivity (Figure 4.1e). Interestingly, the patches on partially hydrophilic PDMS exhibit a darker circular region in the first ~ 10 - 20 seconds following GUV fusion, which coincides with the vesicle adhesion contact prior to fusion. As the adhered region of the membrane was in the focal plane of illumination for a more extended time than the surrounding membrane, it is likely that partial bleaching occurred during fusion; explaining why it can be seen long after the GUV rupture event (Figure 4.9b, c). This bleaching

mechanism was also suggested by Hamai et al. [108], where similar effects were seen using epifluorescence microscopy of GUVs fusing to glass. Adhesion spots can also be seen on hydrophilic substrates (Figure 4.2b); however their average lifetime is significantly shorter; completely dissipating after ~ 1 second. The exact cause of this difference in membrane response remains currently unresolved.

In addition, the subtle mottling effect observed on hydrophilic substrates is absent in patches on partially hydrophilic PDMS. One possibility is that it is washed out by the diffusion of bleached molecules. This is also demonstrated in Figure 4.9f, where no characteristic increase in standard deviation is detected, as previously seen in Figure 4.3b. In terms of area changes, the partially hydrophilic PDMS still undergoes the initial 1% decrease in patch area after fusion (Figure 4.9e), but the subsequent spreading process observed on hydrophilic substrates appears inhibited.

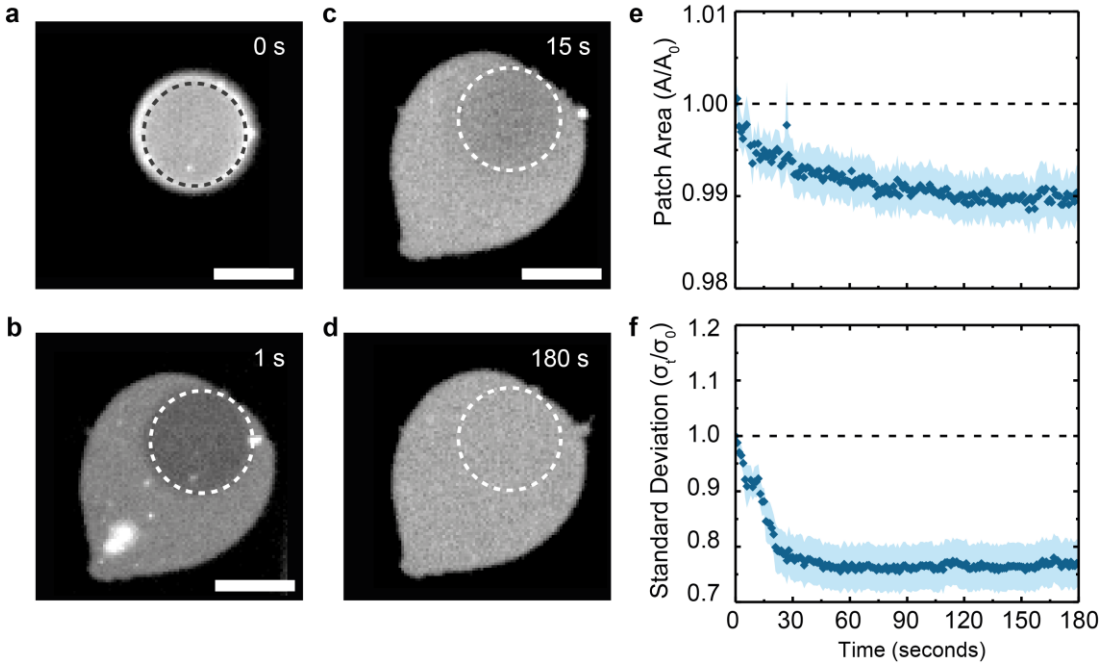

Figure 4.9: Impact of the partially hydrophilic substrate on lipid patch spreading and homogenisation. Fluorescence micrographs of lipid bilayer patches composed of DOPC doped with 0.1mol% Rh-DPPE (a-d) fused on partially hydrophilic PDMS. Relative changes in the average patch area (e) and standard deviation between pixels for lipid patches fused on hydrophilic PDMS (f). The scale bars in (a-d) represent 20 µm.

Membrane pinning by nanoscale hydrophobic regions can be used to explain the reduction in membrane spreading to increase its area, but conflicts with the bilayers retaining the ability to contract across the surface to reduce its area. It is possible

that patch contraction is still viable due to disconnected lipid islands being left behind as the membrane periphery recedes.

4.6 Conclusion

The results in this section, although preliminary, show that supported lipid patches formed from vesicle fusion are not immediately stable or equilibrated. Instead, they undergo significant morphological changes that can exist for extended periods depending on lipid composition and substrate properties.

The most striking observation of vesicles fused on hydrophilic substrates, is the initial patch area shrinking followed by relaxation. The reasons for this area fluctuation remain unknown. However, the accompanying morphological changes in the bilayer can be related to previous observations in the literature. For example, the fluorescence mottling may arise from differences in lipid-substrate friction during patch formation inducing inhomogeneities in lipid density [336,337], whereas the formation of lipid protrusions follows from the incompressibility of the lipid bilayer [56].

Although preliminary, the experiments in this chapter exemplify how substrate properties can be used to modulate membrane behaviours. This is further explored in the next, in Chapter 5, whereby partially plasma treated PDMS is utilised to induce the selective depletion of cholesterol molecules from an adhered lipid bilayer.

Chapter 5: Cholesterol extraction from supported lipid bilayers via substrate interactions

The substrate's influence on biomembranes can be broadly understood to induce physical alterations in the membrane; changing membrane fluidity, tension, shape and morphology [113,134,338,339]. These physical changes activate subsequent biochemical cascades in cells that determine the resultant response and adaptation. Although an active field of study, many of these interactions remain poorly understood. The following chapter uses partially plasma-treated PDMS to demonstrate that substrate interactions can modify not only the physical properties of the adhered membrane, but the chemical composition through passive interactions. Most interestingly, there are no specific chemical interactions at play, meaning the physical criteria required to induce the effect could reasonably exist in other systems.

5.1 Substrate-induced cholesterol extraction

As detailed in Chapter 4.1, lipid patches formed via vesicle deposition on fully hydrophilic PDMS substrates eventually equilibrate to leave uniform stably supported lipid patches for at least ~ 60 hours, as recently demonstrated in reference by Faysal et al. [340]. After 30 minutes, lipid patches formed on fully plasma-treated PDMS are visually homogenous and undergo little subsequent morphological changes, even with cholesterol-containing compositions (Figure 5.1a-b). In contrast, the same lipid membranes behave very differently when coupled to partially plasma-treated PDMS substrates, with the effects seemingly linked to the cholesterol content. Although partially hydrophilic PDMS substrates stably support pure DOPC membranes (Figure 5.1c), cholesterol-containing lipid patches undergo drastic morphological changes, with considerable patch shrinkage,

the formation of microscopic pores, and an increase in patch fluorescence intensity (Figure 5.1e).

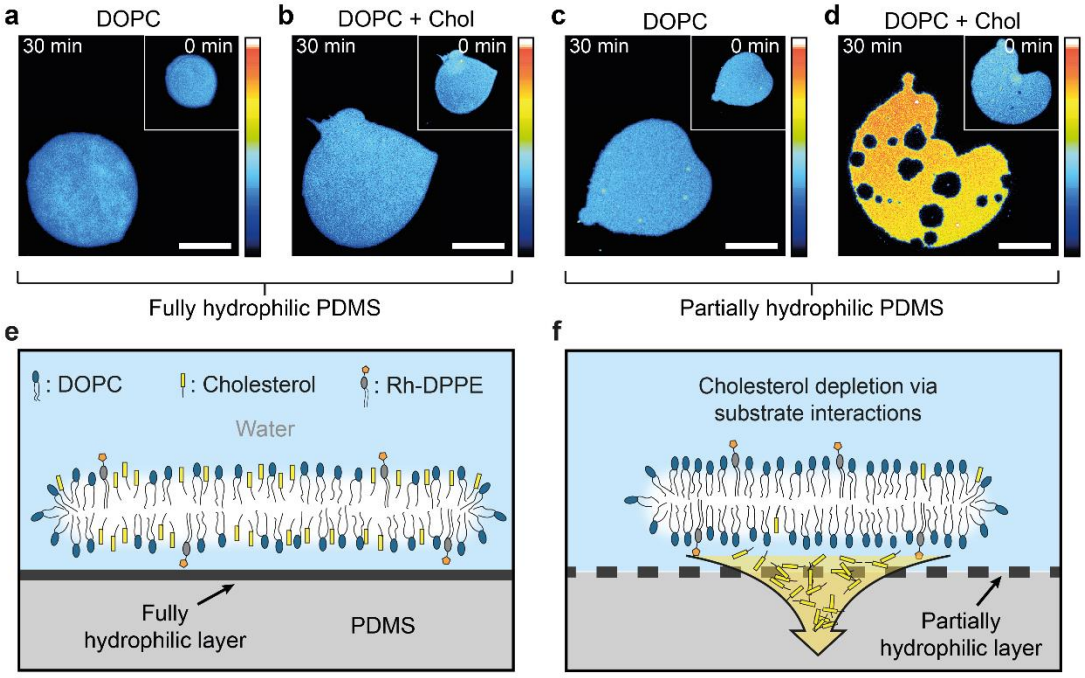

Figure 5.1: Substrate-induced changes in PDMS-supported lipid bilayers. Fluorescence images of lipid bilayer patches composed of pure DOPC (a) and DOPC:Cholesterol (40:60 mol%) (b), supported on fully hydrophilic PDMS. The patches are stably supported. On partially hydrophilic PDMS, DOPC patches remain stable (c), but DOPC:Cholesterol (40:60 mol%) patches undergo changes (b, d). This is due to the extraction of cholesterol by the substrate, as demonstrated in below schematic where cholesterol-containing bilayer (e), undergoes morphological changes due to cholesterol extraction (f). All patches were labelled with 0.1 mol% Rh-DPPE. The scale bar in (a-d) are 50 µm for both inset (taken at 0 min), and main image (taken 30 min after formation). The colour scale represents the fluorescence intensity (arbitrary units).

As this effect was only observed with cholesterol-containing lipid membranes on partially plasma-treated PDMS substrates, it was hypothesised that the phenomenon was due to the substrate interactions inducing cholesterol depletion from the adhered lipid patch. This hypothesis would explain the changes in the area, as a significant loss of cholesterol content from cholesterol-rich lipid patches is known to create defects such as pores and area shrinkage [199]. The specificity of the extraction (only leaching cholesterol) was assumed based on the observed change in fluorescence intensity. If cholesterol were preferentially extracted, the remaining DOPC and fluorescent label Rh-DPPE would concentrate (that is the molar ratio of Rh-DPPE to DOPC would increase as cholesterol is lost), increasing the fluorophores' surface density in the bilayer, and causing an increase in mean fluorescence intensity. Such an effect can be seen in Figure 5.1d, with the patch

becoming relatively brighter compared to its initial state and to other stably supported lipid patches with the same level of fluorescent doping (Figure 5.1a-c).

Fully plasma-treated PDMS is passivated against such a depletion effect by the formation of a thin silica-like layer (Figure 5.1e) as discussed in Chapter 3.1. This allows the formation of stably supported lipid membranes, similarly to when lipid patches are formed on glass substrates. In line with these results, fluorescently-labelled DOPC bilayers; either pure or cholesterol-containing, remain unaffected on fully plasma-treated PDMS, showing no apparent change in fluorescence intensity and no change in patch area or morphology (Figure 5.2). The only minor change observed was a slight, albeit not significant, increase in the patch area due to spreading of the lipid membrane after fusion, similar to results discussed in Chapter 4.2 with cholesterol-containing membranes fused on a glass.

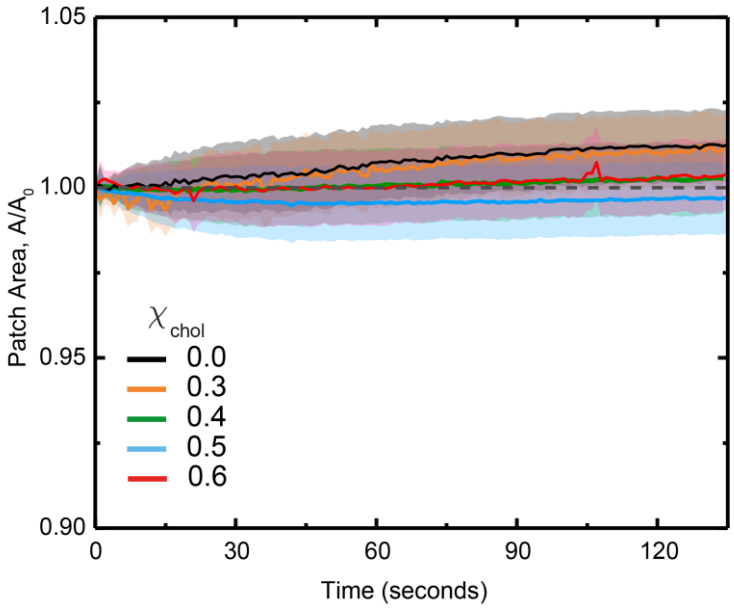

Figure 5.2: Relative changes in surface area of lipid patches supported on fully plasma-treated PDMS substrate Area plotted against time, for selected cholesterol mole fractions, χ_{chol} = 0.6, 0.5, 0.4, 0.3 and 0.0. The data was statistical averaged from n = 20, 15, 15, 16, 26 different patches for cholesterol mole fractions, χ_{chol} = 0.6, 0.5, 0.4, 0.3, and 0.0 respectively, and the error boundaries made from standard errors.

On the other hand, partially plasma-treated PDMS induced the specific depletion of cholesterol (Figure 5.1f). This is likely due to interactions with the partially hydrophilic substrate surface and incomplete/partial formation of a silica-like layer during plasma treatment, as described in Chapter 3.1. As cholesterol is a small, hydrophobic molecule, it is possible that it will interact with the more hydrophobic

regions on the substrate surface, become extracted from the membrane and deplete into the PDMS matrix. Indeed, PDMS is known to absorb small hydrophobic molecules from solution [265], but upon reviewing the existing literature, this appears to be the first documented case of such membrane-substrate interactions altering the composition of adhered biomembranes. This has significant consequences on the impact and influence of PDMS materials on bioassays and cell culture studies, as not only the incubation fluid, but the composition of adhered biomembranes could be directly altered by the PDMS interface.

To further characterise and quantify these effects, the measurements of changes in lipid patch area and fluorescence intensity were repeated with DOPC lipid patches of increasing cholesterol content. As shown in Figure 5.3, the extent of cholesterol depletion determines the degree of the morphological changes observed in the lipid patch. Patches containing a 0.3 cholesterol mole fraction retain more than 90% of their lipids and experience only minor shrinking (Figure 5.3a). Patches with larger initial a cholesterol mole fraction, such as a 0.6 cholesterol mole fraction (Figure 5.3c), lose a greater portion of their lipids, and as a result, typically shrink and form large pores simultaneously. Figure 5.3d shows a graph of relative area loss for lipid patches supported on partially plasma-treated PDMS at different cholesterol mole fractions. Lipid patches containing a 0.6 cholesterol mole fraction lost ~ 25% of their surface area after about 1 minute, whereas lipid patches containing a 0.3 cholesterol mole fraction only lost ~ 3% of their surface area over the same period.

Lipid patches containing no cholesterol showed no significant change in area or fluorescence intensity. As hypothesised, the changes in the membrane lipid composition induced by the substrate can be independently verified by monitoring the relative increase in fluorescence intensity of the shrinking bilayers (Figure 5.3c). This is consistent with the idea that membrane shrinking on partially plasma-treated PDMS is induced by specific depletion of the non-fluorescent cholesterol (Figure 5.3e), thereby concentrating both the DOPC and the Rh-DPPE fluorescent label within the remaining bilayer.

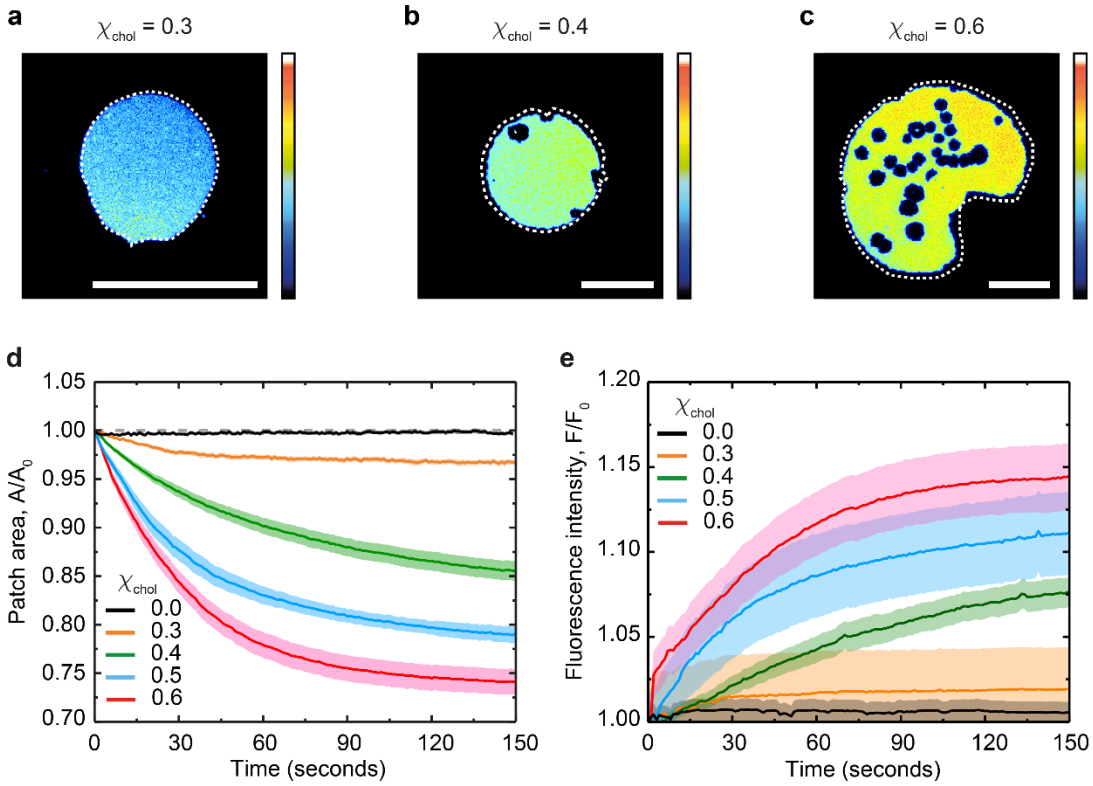

Figure 5.3: Quantifying cholesterol extraction from supported lipid bilayers on PDMS. Fluorescence images of DOPC:Cholesterol lipid patches containing 0.3 (a), 0.4 (b) and 0.6 (c) mole fraction of cholesterol; 150 seconds after deposition on partially plasma-oxidised PDMS. The original patch perimeter is shown as a dotted white line on each image to mark the extent of patch shrinking. Relative changes in (d) the surface area and (e) the fluorescence intensity of the lipid patches supported on partially oxidised PDMS substrate as a function of time, for selected cholesterol mole fractions, χ_{chol} = 0.6, 0.5, 0.4, 0.3 and 0.0. The data was statistical averaged from n = 20, 15, 15, 16, 26 different patches for cholesterol mole fractions, χ_{chol} = 0.6, 0.5, 0.4, 0.3, and 0.0 respectively, and the error boundaries made from standard errors. The scale bars in (a-c) represent 50 µm, and the colour scale of the fluorescence intensity is in arbitrary units.

It should be noted that self-quenching fluorescence has been documented to exist in Rhodamine labelled PC lipid membranes; following a linear relationship with probe concentration between 0 and 10 mol% [341–343]. For example, cholesterol free Egg-PC vesicles show a ~10% decrease in residual fluorescence when containing 2 mol% Rhodamine. If the majority of cholesterol is depleted from DOPC:Cholesterol membranes with a 0.6 cholesterol mole fraction (Figure 5.1c), then the Rh-DPPE concentration could increase from 0.1 mol% to 0.25 mol%, in turn increasing rhodamine self-quenching. However, the change in cholesterol content in the lipid patch has additional effects on rhodamine self-quenching. A previous study using spectrofluorometry has shown that cholesterol enhances self-quenching in PC lipid membranes. Egg-PC vesicles containing a cholesterol mole

fraction of 0.5 demonstrated an exponential decrease in residual fluorescence with increasing rhodamine concentration, compared to a linear one in the absence of cholesterol [341]. Hence the loss of cholesterol from adhered lipid bilayers could facilitate a reduction in self-quenching. These findings suggest that it would be difficult to obtain quantitative information regarding the extent of cholesterol depletion from the changes in the fluorescence intensity of the patches, where a combination of cholesterol depletion and a reduction in rhodamine self-quenching due to a decrease in cholesterol mole fraction may be present.

In the above-described experiments, it is likely that cholesterol is being pulled from only the lower leaflet of the lipid patch, which is in closest proximity to the substrate interface. The transbilayer motion of cholesterol between the proximal and distal leaflets, termed cholesterol flip-flop, occurs in the order of ~ 0.001 - 1 milliseconds in fluid PC lipid membranes [344–346]. This period is at least an order of magnitude faster than the timescale of the substrate-induced cholesterol depletion described here. If unhindered, this facilitates cholesterol's redistribution between the leaflets during the timescale of the depletion experiments. If cholesterol flip-flop was hindered, then the depletion of cholesterol between the two leaflets would have to proceed by edge diffusion, and would vary with lipid patch size. As seen in Figure 5.4, there was no clear visual evidence of asymmetric distribution of cholesterol between leaflets; hence cholesterol depletion was assumed to occur homogeneously across the patch during the depletion process.

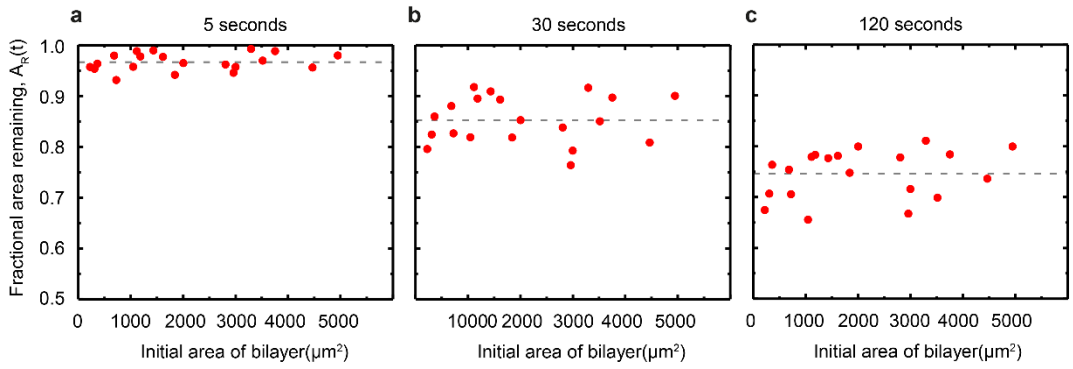

Figure 5.4: No correlation between lipid patch size and cholesterol depletion rate. Change in the fractional area remaining, $A_R(t)$, against initial patch area for n = 20 independent DOPC:Cholesterol (40:60mol%) patches supported on partially plasma-oxidised PDMS for 5 seconds (a), 30 seconds (b) and 120 seconds (c).

5.2 Nanoscale characterisation of PDMS substrates and PDMS-membrane interactions

While the quantitative measurements of changes in lipid patch area and fluorescence intensity unequivocally indicate that partially hydrophilic PDMS specifically depletes cholesterol from the adhered lipid membrane, the molecular mechanisms behind the depletion process was not obvious. For substrate induced extraction to be verified, it must be shown that cholesterol-substrate interactions are at least equally as strong as the cohesive interactions between a cholesterol molecule and its surrounding lipids within the membrane. To do this, chemical force mapping techniques were employed (see chapter 2.6.5 for further details) to measure the extraction forces required to remove cholesterol molecules from DOPC membranes.

The specific removal of single cholesterol-like molecules from lipid bilayers was enabled by the use of thiocholesterol. This cholesterol analogue possesses an exposed thiol group at one extremity, which can bind covalently to Au-coated AFM tips [347]. Upon the retraction of the AFM tip from the membrane, any tethered cholesterol molecules are extracted and the associated forces simultaneously recorded (Figure 5.5a). In general, multiple step-like events were present in the extraction curves (red arrows, Figure 5.5b) due to multiple binding events and extraction of more than one cholesterol molecule from the bilayer.

A semi-automated procedure for extracting quantitative values from force curves (Figure 5.6) was conducted with the help of Dr Kislon Voïtchovsky, who encoded the described algorithm. To objectively analyse a curve exhibiting steps (Figure 5.6a), a smoothing derivation is first applied by sliding a rod along the whole curve and plotting its slope (Figure 5.6b). Practically, the length of the rod is taken to be insensitive to the force fluctuations of the curve's baseline (in this case, 8 points long) and a linear fit of the curve is done for a sliding interval corresponding to the rod's length. A thresholding procedure is then applied to the derivative whereby only parts of the curve above a threshold of two standard deviations of its average value are retained (Figure 5.6c).

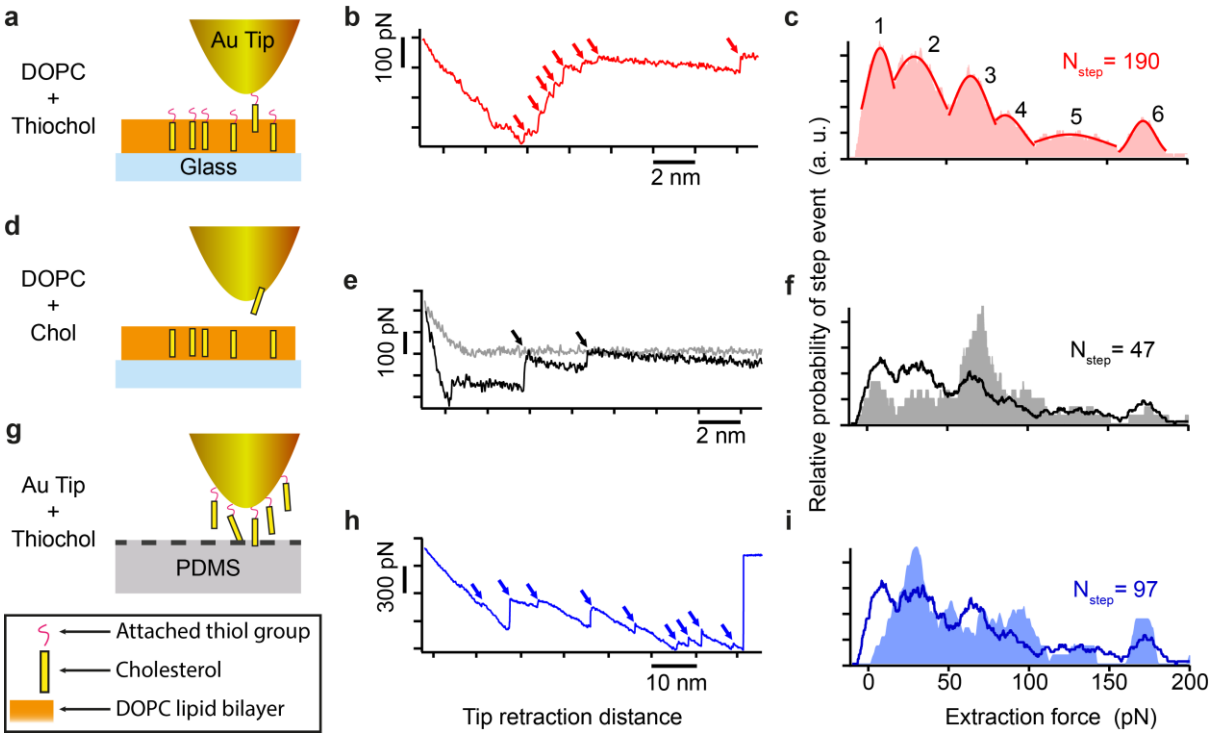

Figure 5.5: Force spectroscopy measurements of PDMS–cholesterol interactions. Au-coated AFM tips bind specifically to the thiocholesterol in DOPC:Thiocholesterol (40:60 mol%) bilayers supported on a glass substrate (a). A typical extraction curve with multiple adhesion events (red arrows) (b). The resulting statistical histogram of measured extraction forces (c) which reveals distinct peaks (labelled 1-6), located at: $F_1 = 9 \pm 6$ pN, $F_2 = 30 \pm 12$ pN, $F_3 = 65 \pm 8$ pN, $F_4 = 87 \pm 8$ pN, $F_5 = 127 \pm 17$ pN, and $F_6 = 172 \pm 17$ pN (Gaussian fitting). Au-coated AFM tips on DOPC:Cholesterol (40:60 mol%) bilayers supported on glass (d). Force curve reveals far fewer extraction events due to a lack of specific tip-cholesterol binding (e). The histogram analysis of the data (f), shown in grey, shows a similar distribution to (c), replicated by the black curve for comparison. Force spectroscopy on partially plasma-oxidised PDMS with thiocholesterol directly tethered to Au-coated AFM tip (g). The extraction curves exhibit multiple steps (blue arrows) (h). The statistical histogram of thiocholesterol extraction forces on PDMS (i) shown in blue with (c) superimposed as a solid curve for comparison. Histograms (c, f, i) have been normalised so that their total area equals 1. The extraction probability (fraction of curves exhibiting steps) is ~ 0.3 for (a-c), and 0.03 for (d-f), each evaluated from n = 1000 curves selected randomly.

The results of the step identification process can be visualised in Figure 5.6d. While the above parameters were used for the vast majority of curves, the outcome of each analysis was controlled visually, and the parameters finely adjusted if necessary. With each step (in this case, 11 steps) the associated force change is calculated by comparing the force at both extremes of the step interval. Taking relatively large intervals (Figure 5.6c,d) allows minimisation of potentially erroneous force measurements at the step itself due to force spikes or instabilities. The results are then compiled into a histogram (Figure 5.6e) where the bin width represents two standard deviations of the force detection baseline in the absence of any step (15 pN).

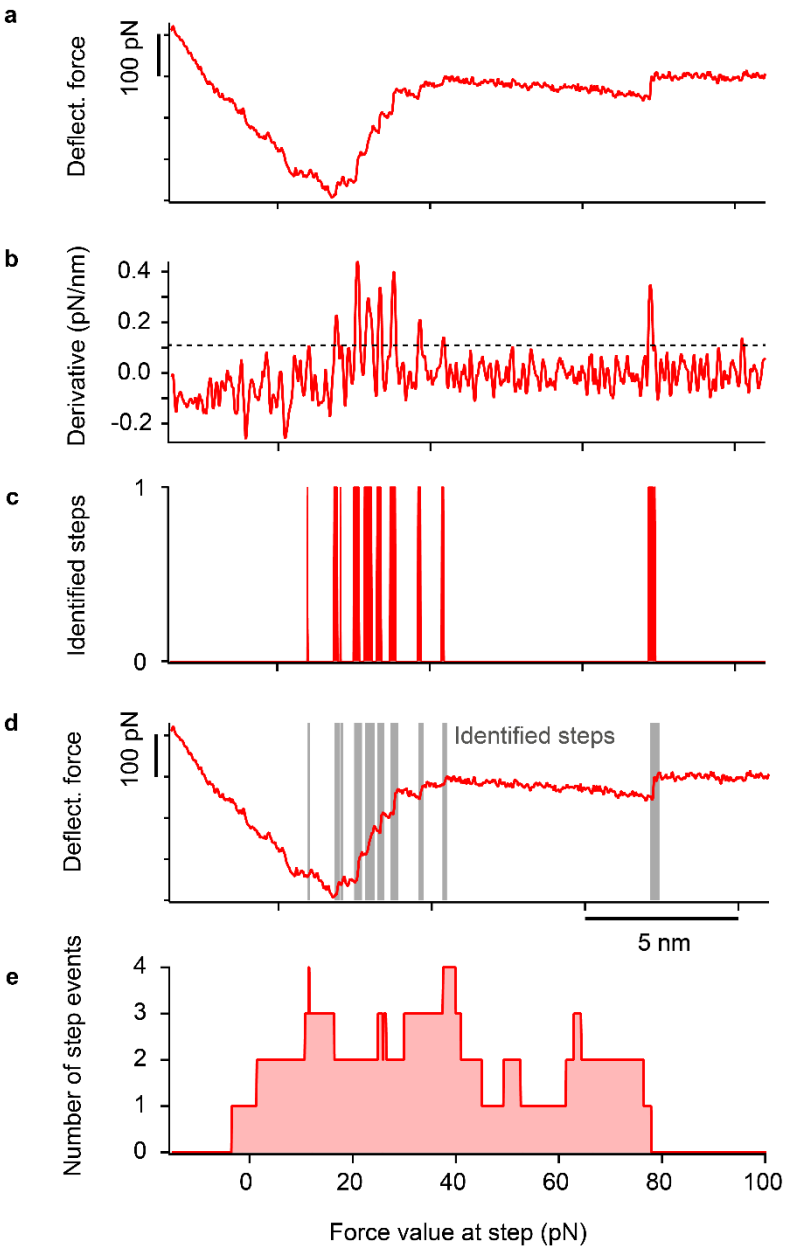

Figure 5.6: Illustration of the semi-automated procedure used to analyse the AFM spectroscopy extraction curves

The histogram may hence give a non-zero probability to negative forces if the step reported is within 15 pN of zero. The histograms for each curve analysed are subsequently combined in a complete histogram, such as those presented in Figure 5.5 c, f, i.

With this procedure, a statistical analysis could be conducted over a large number (>1000) of extraction curves, revealing distinct extraction force populations, as illustrated in a histogram (Figure 5.5c). A clear interpretation of the different force maxima is not immediately apparent, however complementary information can be

obtained by repeating the experiment in different configurations. By measuring the non-specific extraction of lipids from the membrane (Figure 5.5d-f) and the direct adhesion between cholesterol molecules and partially plasma-treated PDMS (Figure 5.5g-i), an interpretation of the molecular interactions could be deciphered. By comparing the results from the initial thiocholesterol force spectroscopy experiments with those from the complementary experiments, similarities and differences between the prevalent extraction forces were revealed.

The first force maximum (F_1 = 9 ± 6 pN) and the third maximum (F_3 = 65 ± 8 pN) are only observed in extraction measurements carried out on fully formed DOPC bilayers (Figure 5.5a-f). These maxima are thus characterised as the extraction forces required to remove cholesterol molecules from the DOPC membrane. Notably, these values are also in agreement with previous reports using similar techniques [348].

The F_1 peak is the dominant event in the DOPC/thiocholesterol system (Figure 5.5d-f) where the bond between the present thiol groups and gold-coated AFM tip creates a specific preference for the extraction of the cholesterol analogue. Coupled with the comparatively small magnitude force at F_1, this peak is identified as the force required to extract single cholesterol molecules. The F_1 peak is also visible in the DOPC:Cholesterol system (Figure 5.5d-f) where non-specific binding occurs. However, the uncoated AFM tip is likely to be capable of removing both cholesterol and DOPC molecules, and hence the F_3 maximum becomes the most common event observed; albeit with a much lower probability than when specific binding is present. A similar interpretation can be made for peak F_6, but the relatively large force suggests that more lipid molecules are involved. Most interestingly, the second maximum at F_2 is present in all three situations (Figure 5.4g-i), where the tethered thiocholesterol molecules directly adhere to the partially plasma-treated PDMS. This demonstrates a significant interaction force between cholesterol and silica-like substrates, such as the plasma-oxidised components of the partially plasma-treated PDMS surface. Cholesterol is known to form hydrogen bonds, which can couple with silanol groups [79,349]. Single hydrogen bonds are documented to have bond strengths ranging between ~ 5 – 950 pN (assuming a bond length of ~ 0.3 nm) [350]; hence, the presence of hydrogen bonding could explain the origin of the attractive interactions indicated in Figure 5.4I, with the measured extraction

forces being of the order ~ 10 – 100 pN. These forces are sufficiently high enough to compete with membrane interactions between cholesterol molecules and the surrounding lipid bilayer. The discovery of the F_2 type maxima present when the bilayer is formed on glass (also a silica-based substrate) suggests substrate-cholesterol interactions are present in all cases measured. These spectroscopy measurements demonstrate that the forces measured between single cholesterol molecules and silica (present on both glass and plasma-oxidised PDMS) are comparable to the cholesterol-lipid interactions within the bilayer. Indeed, this points to the presence of surface interactions providing a molecular mechanism for substrate-induced cholesterol extraction. Unlike the dense silica layer formed on fully plasma-treated PDMS, the partially plasma-treated PDMS interface appears susceptible to penetration by small molecules. Hence, species like cholesterol could be depleted into the porous interior of the bulk PDMS which could act as a sink for hydrophobic molecules.

Similar effects have been exhibited when PDMS substrates are bathed in solutions containing hydrophobic molecules [265] and even with bioimplants exposed to interstitial fluid [266,268]. Thus, once cholesterol molecules are in close proximity to hydrophobic regions, they can be extracted from the lipid membrane and partitioned into the PDMS matrix. The existence of different peaks in the measured extraction forces and the dependence of the extraction force on the cholesterols' environment indicate the importance of the surrounding lipids in the overall membrane stability, and possibly the efficiency at which cholesterol can be extracted. To investigate this further, the exact mole fraction of cholesterol extracted from DOPC bilayers during the depletion process was quantified, and explicitly related to how total cholesterol loss influenced lipid patch area.

5.3 Quantifying the change in cholesterol mole fraction

Provided that cholesterol is being specifically extracted from the bilayer in systems described above (Figure 5.5), it is possible to directly correlate the relative changes in the lipid patch area to the changes in the membrane cholesterol mole fraction. Such calculations have been previously utilised in the study of cyclodextrin-

mediated cholesterol extraction [199], and enrichment [60]. Both studies utilised a model for the change in the average area per molecule, a_{avg}, with cholesterol mole fraction, χ_{Chol}, for DOPC:Cholesterol membranes, shown in Equation 5.1. This was devised by Litz et al. [199] through the aggregation of published data on average area per molecule from x-ray diffraction and neutron scattering experiments. Using this data, an analytical expression for average area per molecule as a function of mole fraction was developed:

$$a_{avg}(\chi_{Chol}) \approx p_1 + p_2 e^{-p_3 \chi_c} \qquad \text{Equation 5.1}$$

where p_1 = 36.5 Å, p_2 = 31.1 Å, p_3 = 2.2 for DOPC bilayers. Although the parameters nor the relationship are assigned any physical meaning, this analytical form provides an approximation of average area per molecule, which facilitates further analysis. Importantly the well-known effects of cholesterol condensing [77,327,351] are accounted for in Equation 5.1.

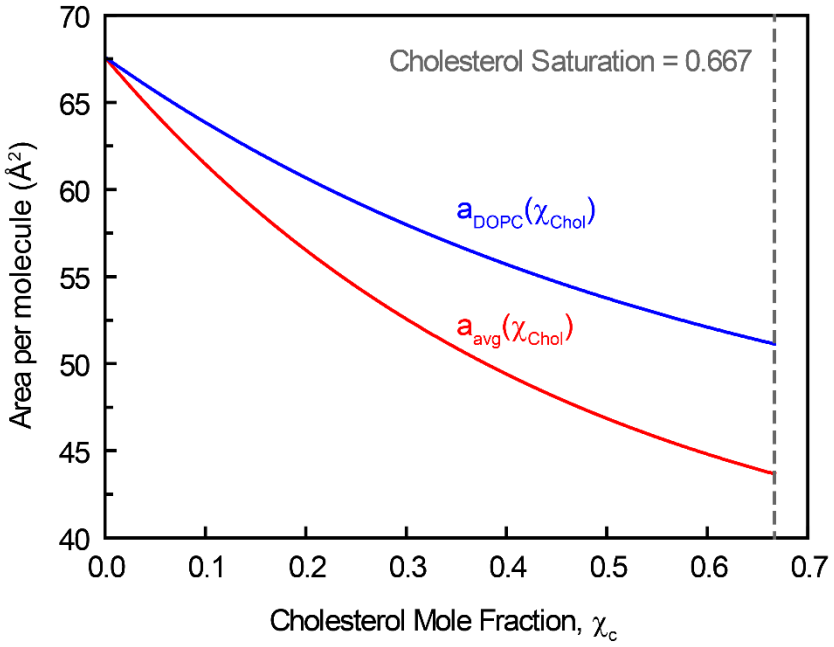

Figure 5.7: Cholesterol condensing effect. Graph showing change in average area per molecule in a DOPC:Cholesterol bilayer, $a_{avg}(\chi_{Chol})$, and change in average area per molecule of the DOPC molecules, $a_{DOPC}(\chi_{Chol})$, up to mole fraction of cholesterol saturation. This figure was adapted from reference [60], with permission from Elsevier.

As shown in Figure 5.7 (adapted from the supplementary information of reference [60]), increasing the cholesterol mole fraction results in a reduction in the average area

per lipid (red line in Figure 5.7, plotted using Equation 5.1). This is not solely due to the decrease in the area caused by the relatively smaller cholesterol molecules taking up a more significant proportion of the bilayer composition. A reduction in the average area per molecule with increasing cholesterol content of the DOPC molecule themselves can also be predicted (blue line in Figure 5.7). The blue curve of Figure 5.7 was formed by combining Equation 5.1 with Equation 5.2, shown below, as described by Rahimi et al. in the supplementary information of reference [60].

$$a_{avg}(\chi_{Chol}) = (1 - \chi_{Chol})a_{DOPC}(\chi_{Chol}) + a_{Chol}(\chi_{Chol}) \quad \text{Equation 5.2}$$

Where $a_{DOPC}(\chi_{Chol})$ and $a_{Chol}(\chi_{Chol})$ are the average area per DOPC and cholesterol molecules, respectively, at cholesterol mole fraction χ_{Chol}. Cholesterol is heavily involved in membrane behaviour and has been postulated to form molecular complexes between sterols and phospholipids, with condensation being one of many effects on the membrane properties [323]. Using Equation 5.1, the relationship between the relative patch area, $A_r(t)$, and the time-dependent cholesterol mole fraction $\chi_{Chol}(t)$ can be evaluated. The following equations are based on similar formulations devised by Litz et al.[199], and could appropriately be applied to the system of substrate-induced cholesterol as described below. Firstly, a change in the relative patch area is related to changes in the average area per molecule:

$$A_r(t) = \frac{A(t)}{A(t_0)} \quad \text{Equation 5.3}$$

$$A_r(t) = \left(\frac{n_P + n_C(t)}{n_P + n_C(t_0)}\right) \frac{a_{avg}(\chi_{Chol}(t))}{a_{avg}(\chi_{Chol}(t_0))} \quad \text{Equation 5.4}$$

Where n_P and n_C are the number of DOPC lipids and cholesterol lipids respectively. These quantities can be related to the cholesterol mole fraction with the following equation:

$$\chi_{Chol}(t_0) = \frac{n_C(t)}{n_P + n_C(t_0)} \quad \text{Equation 5.5}$$

And thus

$$A_r(t) = \left(1 - \chi_{Chol}(t_0) + \frac{n_C(t)}{n_P + n_C(t_0)}\right) \frac{a_{avg}(\chi_{Chol}(t))}{a_{avg}(\chi_{Chol}(t_0))} \quad \text{Equation 5.6}$$

where $1 - \chi_{\mathrm{Chol}}(\mathrm{t}_0)$ represents the constant DOPC mole fraction. To determine the variation in $\chi_{\mathrm{Chol}}(\mathrm{t})$ with time, two assumptions are made. Firstly, it is assumed that the PDMS substrate acts as an infinitely large cholesterol sink, so the kinetics of cholesterol extraction can be modelled as a first-order rate equation. Secondly, it is assumed that there are two populations of membrane cholesterol; one more accessible for removal than the other, in line with previous studies on cholesterol extraction [199,352]. Based on these assumptions, we can write:

$$n_C(t) = n_{acc}(0)e^{-k_f t} + n_{inacc}(0)e^{-k_s t} \qquad \text{Equation 5.7}$$

Where $n_{acc}(0)$ and $n_{inacc}(0)$ represent the number of accessible and inaccessible cholesterol molecules at t_0, respectively; and k_f and k_s represent the associated depletion constants. Hence:

$$\mathrm{A_r(t)} = \left(1 - \chi_{\mathrm{Chol}}(\mathrm{t}_0) + \frac{n_{acc}(\mathrm{t}_0)e^{-k_f t}}{n_P + n_C(\mathrm{t}_0 0)} + \frac{n_{inacc}(\mathrm{t}_0)e^{-k_s t}}{n_P + n_C(\mathrm{t}_0)}\right)\frac{\mathrm{a_{avg}}(\chi_{\mathrm{Chol}}(\mathrm{t}))}{\mathrm{a_{avg}}(\chi_{\mathrm{Chol}}(\mathrm{t}_0))}$$

Equation 5.8

Using the relation described by Equation 5.5, this can be simplified to:

$$\mathrm{A_r(t)} = \left(1 - \chi_{\mathrm{Chol}}(\mathrm{t}_0) + \chi_{\mathrm{acc}}(\mathrm{t}_0)e^{-k_f t} + \chi_{\mathrm{inacc}}(\mathrm{t}_0)e^{-k_s t}\right)\frac{\mathrm{a_{avg}}(\chi_{\mathrm{Chol}}(\mathrm{t}))}{\mathrm{a_{avg}}(\chi_{\mathrm{Chol}}(\mathrm{t}_0))}$$

Equation 5.9

where $\chi_{\mathrm{acc}}(\mathrm{t}_0)$ is the mole fraction of cholesterol accessible to substrate extraction, χ_{inacc} is the mole fraction of cholesterol inaccessible to substrate extraction. Assuming the levels of inaccessible cholesterol remain stable on the timescales of the measurement, (as values of k_s were documented as two orders of magnitude slower than values for k_f in DOPC membranes by Litz et al. [199]) then:

$$\chi_{\mathrm{inacc}}(\mathrm{t}_0)e^{-k_s t} \approx \chi_{\mathrm{inacc}}(\mathrm{t}_0) \qquad \text{Equation 5.10}$$

$$\chi_{\mathrm{Chol}}(t) = \chi_{\mathrm{acc}}(\mathrm{t}_0) + \chi_{\mathrm{inacc}} \qquad \text{Equation 5.11}$$

Substituting into Equation 5.9:

$$\mathrm{A_r(t)} = \left(1 - \chi_{\mathrm{Chol}}(\mathrm{t}_0) + \chi_{\mathrm{acc}}(\mathrm{t}_0)e^{-k_f t} + \chi_{\mathrm{Chol}}(\mathrm{t}_0) - \chi_{\mathrm{acc}}(\mathrm{t}_0)\right)\frac{\mathrm{a_{avg}}(\chi_{\mathrm{Chol}}(\mathrm{t}))}{\mathrm{a_{avg}}(\chi_{\mathrm{Chol}}(\mathrm{t}_0))}$$

Equation 5.12

$$A_r(t) = \left(1 - \chi_{acc}(t_0) + \chi_{acc}(t_0)e^{-k_f t}\right)\frac{a_{avg}(\chi_{Chol}(t))}{a_{avg}(\chi_{Chol}(t_0))} \qquad \text{Equation 5.13}$$

Here, similarly to studies with cyclodextrin,[60,199] we neglect any asymmetry of cholesterol distribution between the bilayer leaflets, due to reasons discussed in Chapter 5.1.

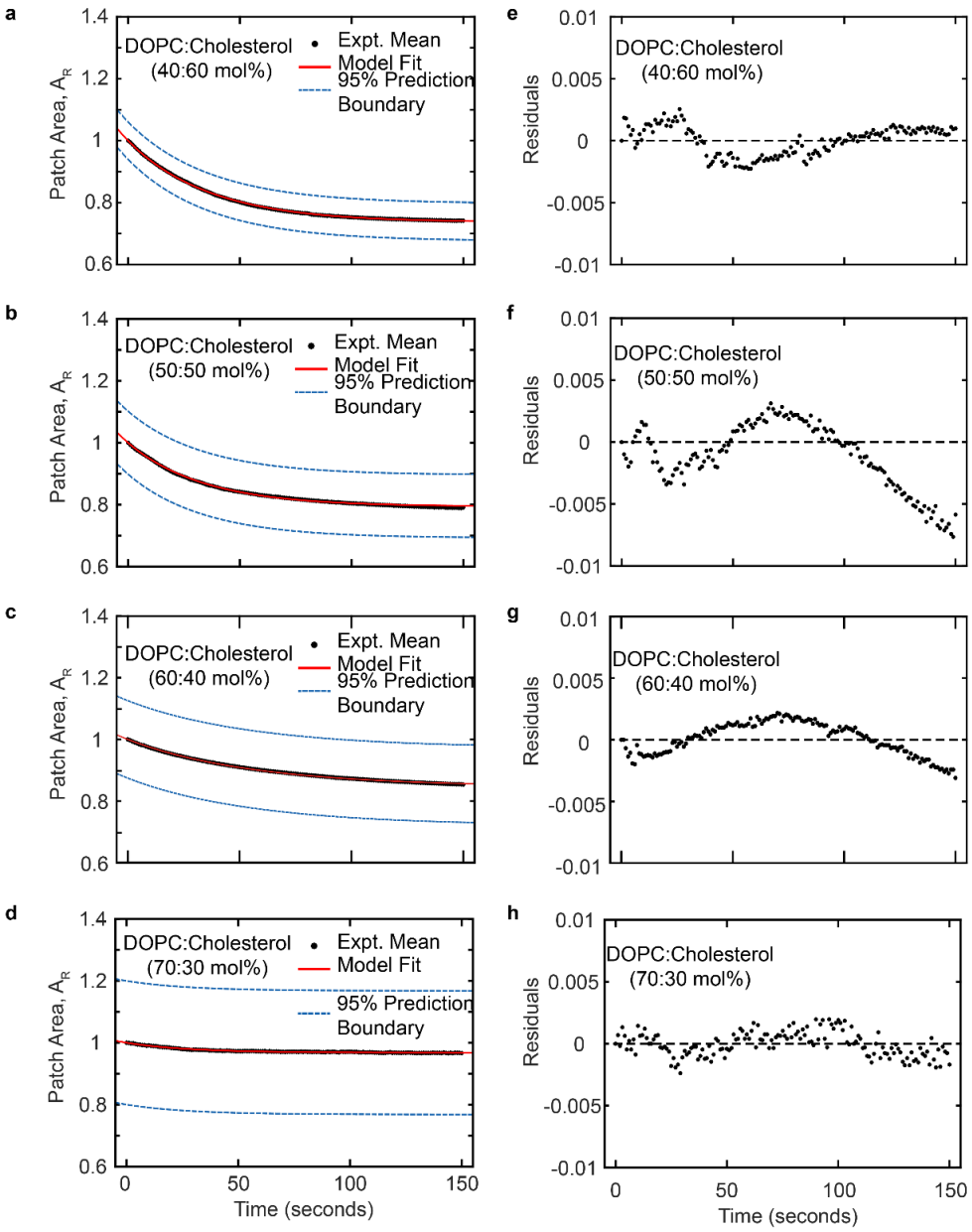

Figure 5.8: Fitting of cholesterol depletion model to experimental data. Curve fitting of experimental data for relative change in area for 0.6 (a), 0.5 (b), 0.4 (b) and 0.3 (d) cholesterol mole fractions, with 95% confidence bounds. The experimental mean of these data sets was fitted to the model presented in Equation 5.13, and weights used to fit the model were derived from the standard deviation within each cholesterol mole fraction data sets. Adjacent graphs show the measured residuals for each model fitting to 0.6 (e), 0.5 (f), 0.4 (g) and 0.3 (h) cholesterol mole fraction data set.

From these equations, a model relating relative patch changes to changes in cholesterol mole fraction was fitted to the data with MATLABs curve fitting tool, using a weighted least-square fitting with two fitting parameters. Equation 5.13 fits the experimental data monitoring the changes of patch area remarkably well (Figure 5.8a-d), producing reasonable residuals (Figure 5.8e-h). This also confirmed the assumption that inaccessible cholesterol remained stable on the timescales was reasonably appropriate for this system.

The 95% prediction bounds became much broader at lower cholesterol mole fractions of 0.3, as seen in Figure 5.8d. This is concurrent with the experimental difficulties encountered at lower mole fractions, as the low cholesterol regime (< 0.3 mol fraction) had weak signal-to-noise in measured results. Due to the exponential changes in the average area per molecule with cholesterol mole fraction, relatively large changes in χ_c at the low cholesterol regime resulted in minimal observable changes in the overall lipid patch area. In other words, the loss of area due to cholesterol depletion was likely counteracted by the reversal of the condensation effect.

Mole Fraction, χ_{Chol}	**Accessible cholesterol mole fraction**, χ_{acc}	**Depletion rate constant**, k_f (s^{-1})
0.3	0.099 ± 0.005	0.0360 ± 0.0006
0.4	0.350 ± 0.012	0.0191 ± 0.0001
0.5	0.387 ± 0.007	0.0314 ± 0.0002
0.6	0.429 ± 0.004	0.0292 ± 0.0001

Table 5.1: Extracted values for accessible cholesterol mole fraction and cholesterol depletion rate constant. The weights used to fit the model were derived from the standard deviations of data sets. Initial cholesterol mole fractions were extracted using the model fits for the accessible cholesterol mole fraction, $\boldsymbol{\chi_{acc}}$, at t=0, and the depletion rate constant $\boldsymbol{k}$ for DOPC:Cholesterol lipid patches with 0.3, 0.4, 0.5 and 0.6.

This could explain the wider prediction bounds for 0.3 cholesterol mole fractions, as the depletion model begins to break down. Using other suitably fit data; values for χ_{acc}, and k could be extracted for each cholesterol mole fractions, with comparable error values to those acquired in investigations by Litz et al [199], from which used models were devised (Table 5.1). Cholesterol extraction occurred very quickly, with a characteristic time varying between 25 - 30 seconds for the various membrane

preparations (Figure 5.9a). Interestingly the amount of extracted cholesterol does not increase monotonically with the initial mole fraction (Figure 5.9b). The relative cholesterol loss is significantly lower for membranes with an initial 30% cholesterol content. This is consistent with current ideas in the literature regarding critical cholesterol mole fractions, at which cholesterol molecules are distributed differently among the surrounding lipids, consequently becoming less accessible for depletion [351,353,354]. There is significant research available that shows that the physical properties of membranes deviate at specific mole fractions such as 0.33 [355]. Bilayer thickness of DOPC membranes initially increases with the addition of cholesterol up to 0.35 mol%, but begins to decrease at 0.4 mol% according to molecular dynamics simulations [77], and is confirmed by X-ray diffraction studies measuring changes in the headgroup spacing of DOPC:Cholesterol compositions [327]. Other X-ray diffraction studies have also demonstrated that the bending modulus of DOPC membranes remains constant with increasing cholesterol mole fraction up until a 0.4 mol%, after which it begins increasing [57].

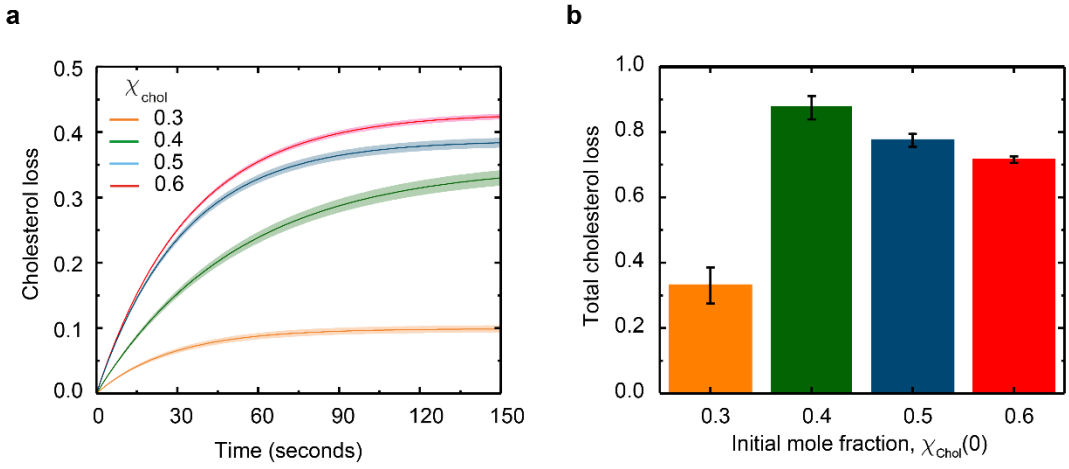

Figure 5.9: Analysis of cholesterol extraction as a function of cholesterol concentration. Time-dependent cholesterol loss defined as $(\chi_{chol}(t_0) - \chi_{chol}(t))$, in DOPC:Cholesterol lipid bilayers supported on partially plasma-oxidised PDMS (a). Total percentage of cholesterol loss, $(1 - \chi_{chol}(t_{end})/\chi_{chol}(t_0))$, as a function of the initial cholesterol mole fraction (b). Errors in (a-b) are estimated using the 95% confidence bounds from the fits.

Conversely, the change in the chain ordering parameter, S_{Xray}, of DOPC membranes rapidly increased with cholesterol mole fraction until 0.4 mol% at which it reaches a plateau until saturation at 0.66 mol% [57]. This could indicate that above a 0.4 cholesterol mole fraction the membrane "switches", having drastically altered behaviours in a high cholesterol regime.

These changes in membrane properties at specific cholesterol mole fractions have been hypothesised to be due to the non-random organisation of cholesterol in membranes. At specific stoichiometries, molecular complexes between sterols and phospholipids are formed and become regularly distributed throughout the membrane, altering the chemical activity of sterols such as cholesterol [351,356]. Sharp jumps in cholesterols ability to escape the membrane have been identified as thermodynamic signatures for changes in the regular distribution of cholesterol within membranes [351]. Thus, the jump in extractable cholesterol identified in Figure 5.9b, could indicate that the complexation and distribution of cholesterol changes between 0.3 and 0.4 cholesterol mole fraction to make membrane cholesterol more accessible to extraction. The idea of complexed cholesterol existing within the membrane is becoming more commonly accepted, with experimental studies [57,327,351] and computer simulations [77] correlating such critical mole fractions to observed “switches” in membrane thickness, cholesterol solubility, bending rigidity and chemical potential [57,323,351]. The identification of such results in systems utilising substrate-induced cholesterol depletion has interesting implications on how biological membrane modulate their cholesterol content. Such passive mechanisms could be utilised to tune and modulate membrane behaviour, utilising the non-monotonic influence of cholesterol on membrane properties.

Interestingly, the stronger interaction of cholesterol with saturated lipids compared to unsaturated lipids renders bilayers more resistant to typical means of cholesterol extraction [323,348,357]. To extend these studies the investigations were expanded to test systems with saturated lipids, which are known to have a higher affinity with cholesterol than the unsaturated counterparts, as described in various experimental studies [329,358–363], and summarised in a review by Ohvo-Rekilä et al. [323].

5.4 Cholesterol extraction can induce phase changes

To examine whether the partially plasma-oxidised PDMS substrates are capable of extracting cholesterol from saturated lipid bilayers, lipid patches composed of DPPC:Cholesterol (60:40 mol%) were used (Figure 5.10). Pure DPPC membranes exist in a gel phase at room temperature, possessing little to no lateral fluidity.

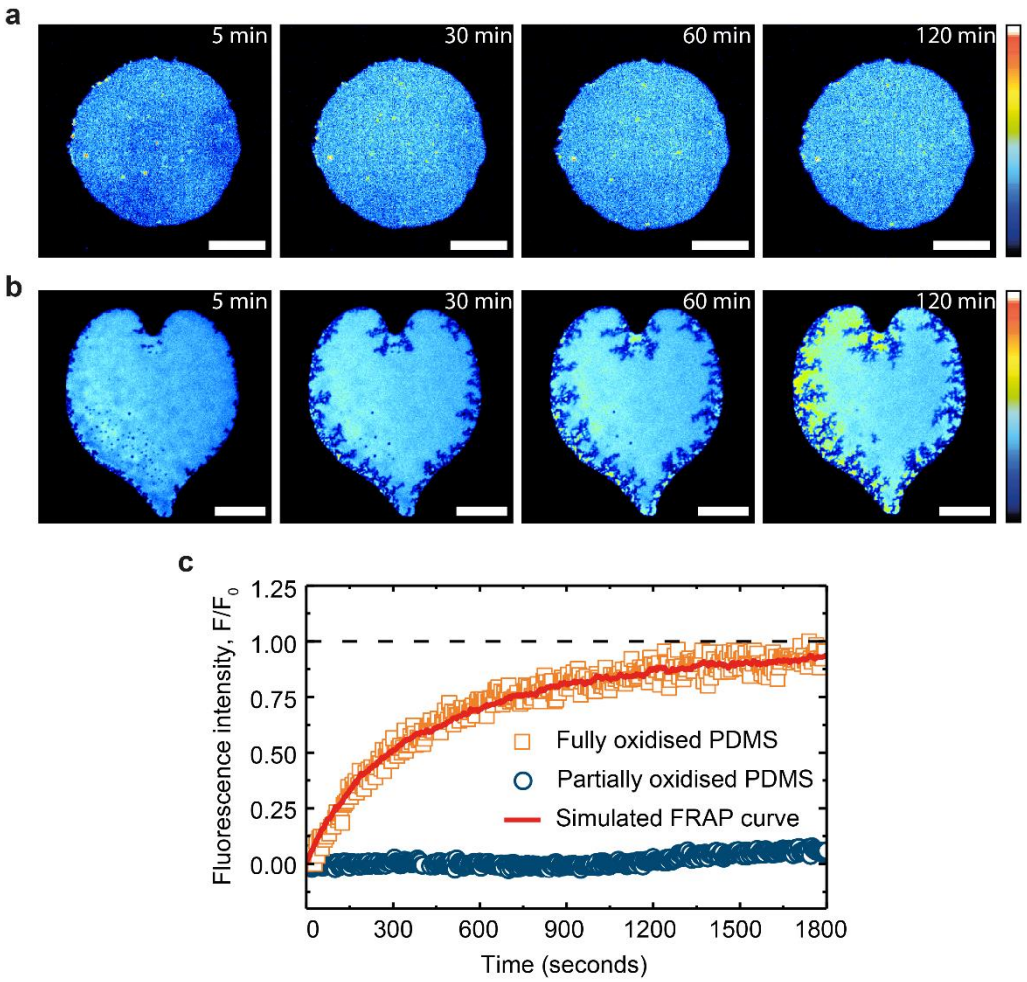

Figure 5.10: Saturated lipid membranes on PDMS substrates. Fluorescence images of DPPC:Cholesterol lipid bilayers (60:40 mol%) on fully (a) and partially (b) plasma-oxidised PDMS substrates 125 min after deposition on the substrate. Lipid bilayers were labelled with 0.1 mol% Rh-DPPE. The scale bars represent 50 µm, and the colour scale of the fluorescence intensity is in arbitrary units. Typical FRAP recovery curves for DPPC:Cholesterol (60:40 mol%) lipid bilayers supported on fully and partially plasma-oxidised PDMS (c). Simulated FRAP curve (see Methods) fitted to our data (red curve) returns the lateral lipid diffusivity.

Upon the addition of cholesterol, the tightly packed acyl chains of the DPPC bilayer are disrupted, reducing chain packing and fluidising the membrane. This is the case for the composition of DPPC:Cholesterol (60:40 mol%), which has sufficient cholesterol present to exist in a fully stable liquid-ordered phase, free of solid domains at room temperature [59,364,365].

As shown in Figure 5.10a, DPPC:Cholesterol (60:40 mol%) membrane patches showed little change in morphology when formed on fully plasma-treated PDMS, and remained stable for at least two hours, similarly to the results described in Figure 5.1a,b. However, when in contact with a partially plasma-treated PDMS surface,

the patches lost a significant portion of their area, while simultaneously increasing their fluorescence intensity (Figure 5.10b). These observations confirm that PDMS can extract cholesterol from saturated lipid membranes, undergoing similar changes described for DOPC:Cholesterol systems (Figure 5.1c,d), albeit at a rate 180 times slower compared to unsaturated lipid membranes.

A notable difference in the cholesterol extraction from the DPPC membranes was that it appeared to induce cracks at the patch's edges (Figure 5.10b), contrasting with the round pores and the smooth edges characteristic of shrinking fluid DOPC membranes [175] (Figure 5.1d). Cracks have been previously observed in supported lipid bilayers and have been suggested to indicate that lipid bilayers have undergone a phase transition from a liquid-ordered phase to a more gel-like phase [325,366]. Using FRAP measurements, the initial fluidity of DPPC:Cholesterol (60:40 mol%) patches on hydrophilic PDMS was found to be 0.060 ± 0.004 $\mu m^2 s^{-1}$, which is in good agreement with the literature [365] (see Chapter 2.5 for further experimental details of FRAP measurements). In contrast, after cholesterol extraction on a partially plasma-treated PDMS substrate, the saturated membranes exhibit little to no recovery after bleaching, as depicted in Figure 5.10c. The drastic reduction in the lipid mobility confirms that the DPPC:Cholesterol patches had indeed solidified due to substrate-induced depletion of cholesterol. These results demonstrate that partially plasma-treated PDMS can induce physical changes via compositional alteration in adhered lipid membranes, manifested here by lipid phase change.

5.5 Mechanically triggering cholesterol extraction

In all of the preceding experiments, the extraction of cholesterol starts as soon as the lipid patch fuses to the substrate. Admittedly, this limits the degree of control over the extraction process and hence its potential for practical applications. Interestingly, the substrate induced cholesterol extraction from adhered lipid bilayers can be controllably initiated using flexible fully plasma-treated PDMS substrates. Previous studies show that when plasma-treated PDMS substrates are subject to tensile strains, the brittle silica-like surface layer forms nanoscale cracks,

partially exposing the underlying hydrophobic bulk PDMS [308,310], as detailed in Chapter 3.4.

To test whether the extraction of cholesterol can be mechanically triggered, a stretching device was used to apply a biaxial strain on the substrate (see Chapter 2.8 for further details). During the initial stretching phase, the lipid patches exhibit negligible changes in their surface area (Figure 5.9a). The applied strain can reach values of up to 15%; an order of magnitude larger than the critical rupture strain for lipid bilayers [69]. Lipid patches can maintain their integrity during such strains via several mechanisms of area regulation, including the formation of tubes, pores and absorbing adhered lipid aggregates [70,71,175].

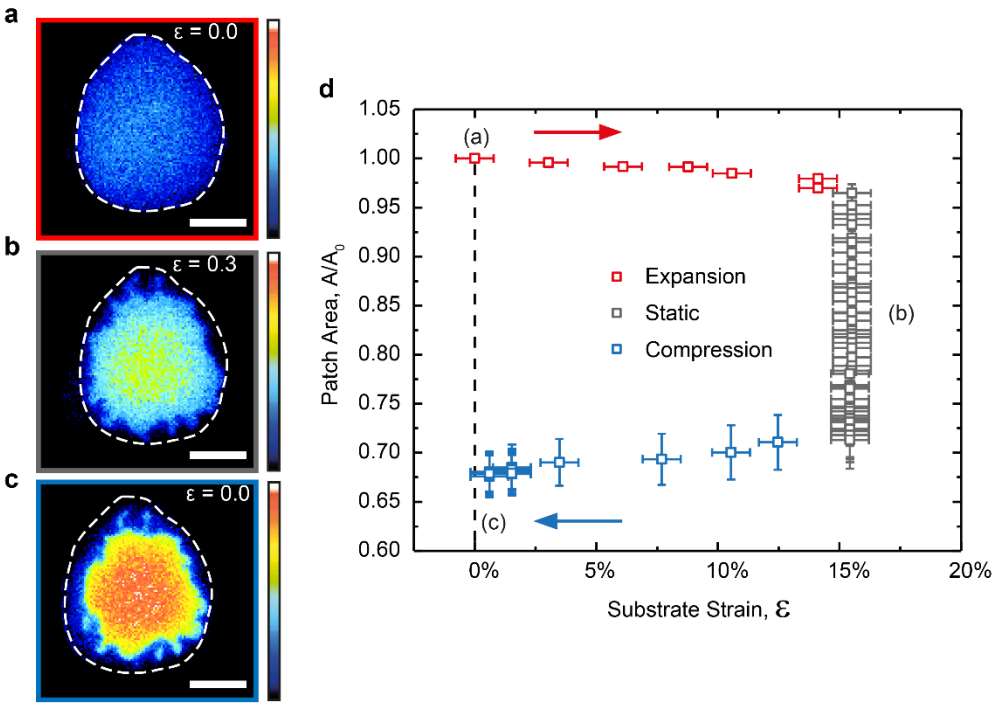

Figure 5.11: Mechanically triggered the extraction of cholesterol from supported lipid bilayers. Fluorescence images of a DOPC:Cholesterol (40:60 mol%) lipid patch, adhered to fully plasma-oxidised PDMS: before expansion (a), while stretched (b), and after compression (c). To highlight the surface area changes in the patch, the initial patch perimeter is highlighted with a dashed white line. The normalised average surface area of n = 7 independent lipid patches with respective standard errors as a function of the substrate strain (d). The location of the images (a-c) within the strain cycle is indicated by labels in (d). The red data points correspond to the stretch phase from 0 to 15%, the grey ones are taken while the substrate is held stretched, and the blue indicates compression from 15% to 0%. Lipid patches were labelled with 0.1 mol% Rh-DPPE. Scale bars represent 20 µm, and colour scale is in arbitrary fluorescence units (a-c).

As described in the work of Stubbington et al. [175], supported lipid bilayers are also able to decouple and slide over sufficiently hydrophilic surfaces, such as fully

plasma-treated PDMS substrates. The sliding allows the membrane to preserve its area and alleviate the elastic stress imposed by the substrate. This behaviour was demonstrated using flexible sheets of fully plasma-treated PDMS that were strained to ~10% at a rate of 0.05% s^{-1} [175]. The results shown in Figure 5.11 are similar to that of Stubbington et al., albeit performed at a significantly smaller strain rate of 0.0005% s^{-1}. For substrate strains up to 10% the lipid patches showed minimal variation in their area (Figure 5.11d) due to their ability to slide over the expanding substrate.

However, once the substrate is sufficiently stretched and held in position, a rapid area loss in the patch can be observed, with an associated increase in the fluorescence intensity (Figure 5.11b); both indicative of cholesterol loss. AFM scans of a PDMS substrate subject to 15% tensile strain verify the existence of surface nano-cracks in the otherwise hydrophilic silica layer, as shown earlier in Figure 3.7. Upon relaxing the substrate to its original dimensions, the patches appear stable again, but much smaller and brighter than they initially were (Figure 5.11c). This simple experiment demonstrates that it is possible to initiate cholesterol extraction in a controlled manner from otherwise stably supported membranes. By subjecting the PDMS substrate to tensile strain, the hydrophilic silica layer is sufficiently cracked to induce substrate-led cholesterol extraction which continues until all the accessible cholesterol has been depleted from the membrane.

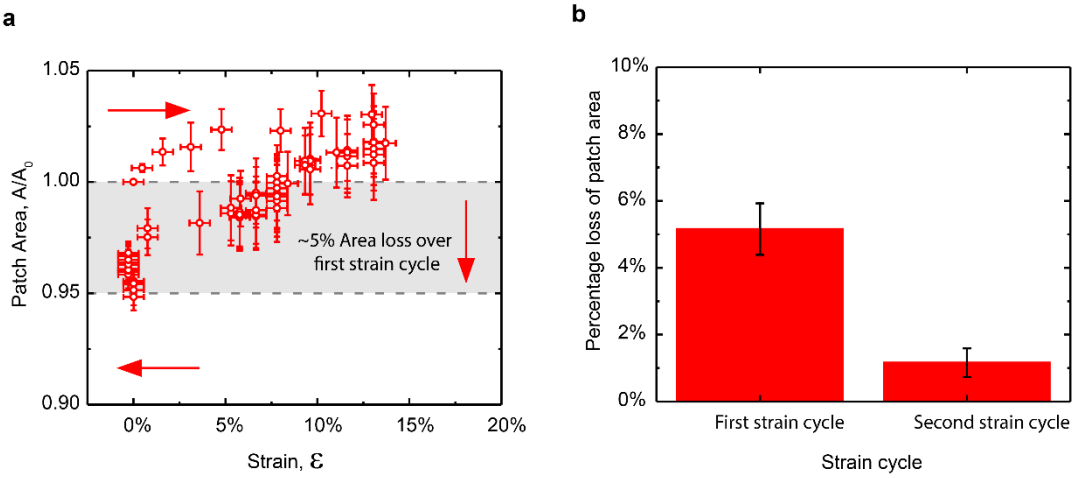

Figure 5.12: Change in supported DOPC lipid bilayer area during expansion/compression cycles. Graph showing typical area changes in DOPC lipid patch during a single substrate strain cycle, ε, (a). A bar chart of percentage loss of patch for DOPC lipid patches after the first and second applications of substrate strain cycles (b).

During the strain cycle shown in Figure 5.11d, the lipid patches lose on average 2 - 5% more area than when statically supported on partially plasma-oxidised PDMS (Figure 5.3d). The reason for this is not entirely clear. Control experiments show that pure DOPC bilayers also lose 5.2 ± 0.8% of their surface area during a strain cycle of similar amplitude (Figure 5.12a). This indicates that the stretching may not only affect the cholesterol population in the bilayer, but further, the depletion of other membrane components cannot be fully excluded. Indeed, when larger micron-scale cracks were formed in the PDMS substrate following mechanical stretching, such non-specific depletion of lipid species was witnessed, as shown in Figure 5.13. These larger cracks were able to extract Rh-DPPE fluorophores, and likely the smaller DOPC and cholesterol molecules. Non-specific lipid extraction is likely to play a role at very large strain magnitudes (> 35%) where the formation of micron-scale fissures in the PDMS surface were occasionally observed.

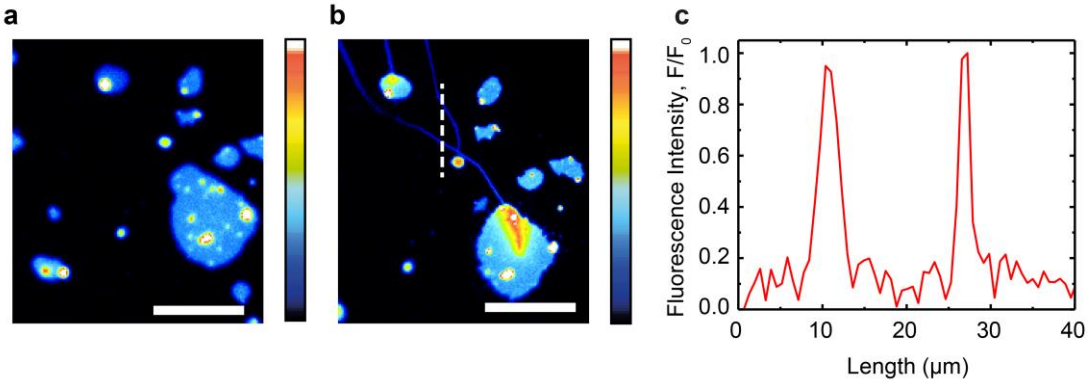

Figure 5.13: Evidence of microscale surface cracking on PDMS substrates. Fluorescent images (a,b) of DOPC:Chol lipid patches (40:60 mol% doped with 0.1mol% Rh-DPPE) on PDMS stretching device. Images show substrate before (a) and after (b) a 35% tensile is applied, and micron-scale surface cracking is evident. The cracks become fluorescent as Rh-DPPE can invade the fissure. A line profile (c) taken from image (b) shows cracks have a diameter of ~ 5 μm. Scale bars represent 20μm and colour scale in arbitrary units for (a,b).

Fortunately, such features could be distinguished as they rapidly fill up with fluorescent membrane and significantly disrupted lipid patches on contact (Figure 5.13b). Such disruptions allowed for the cracks to be quickly visualised and verified to be ~ 5 μm size (Figure 5.13c). Although such results provided a reasonable explanation for discrepancies between the static and dynamic cases for substrate-led cholesterol extractions, there remains slight indications for other possible mechanisms to contribute to the difference. Cholesterol free DOPC membranes exhibited a ~ 2 – 5 % area loss during the initial strain cycle; but upon subsequent

strain cycles, the area of the same DOPC patches remained reasonably unaffected (Figure 5.12b). It is here speculated that the mechanical stress imposed on the lipid patches during the initial strain cycle caused them to decouple and slide across the substrate surface, slightly contracting as they released membrane tension present in lipid patches after vesicle fusion (previously discussed in Chapter 4) and leaving the lipid patch in a more relaxed state. Due to restrictions in time this speculation could not be further investigated. Regardless, even if loss of patch area was due to the minor loss of PC-lipids, although undesired, this is not uncommon even when using conventional cholesterol extraction agents such as cyclodextrin; also known to leach PC lipids from membranes [367,368]. In summary, this technique of cholesterol depletion has comparable flaws to current methods, but does not require the addition of chemical agents to the system.

5.6 Conclusion

Cholesterol is a highly dynamic membrane constituent, often contributing up to 50% of the lipid content in mammalian plasma membranes [354]. Not only is it an essential regulator of membrane fluidity [369], lateral phase organisation [177,370], and bending rigidity [57], but it also influences membrane interactions with the cytoskeleton [371,372]. Cholesterol levels need to be finely controlled both in living cells and in artificial membrane systems; a task previously thought only to be controlled by molecular transporters, such as biological lipoproteins or artificial cyclodextrins [367]. In this chapter, it is shown that plasma-treated PDMS substrates can specifically extract cholesterol directly from the adjacent supported lipid bilayer through simple physical contact. From reviewing the available literature, it is believed that this is the first documented case of a substrate-induced change in the molecular composition of the membrane. The partially hydrophilic surface at PDMS interface plays an important role in the specific extraction of cholesterol, while leaving the remaining bilayer components stably supported. Although the presented results do not provide a definitive answer regarding the detailed extraction mechanism, it is likely driven by direct interactions of cholesterol with the hydrophobic regions at the PDMS substrate surface, with the hydrophilic regions stabilising the support of the remaining bilayer. An interesting parallel can be drawn with the well-known MβCD

extraction method, in which MβCD exhibits a hydrophilic surface and a sub-nanoscale hydrophobic cavity can selectively remove cholesterol from bilayers to the solution [373]. It should be pointed out that the exact mechanism of cholesterol extraction via cyclodextrin is also unclear [367], and these results suggest that the presence of nanoscale hydrophobic and hydrophilic regions on the molecule may be of crucial importance. Still, while the presence and close proximity of nanoscale hydrophobic and hydrophilic regions on the same surface is possibly key to specific cholesterol extraction, the exact features mediating the effect remain unknown.

Although the detailed mechanisms behind substrate-induced cholesterol depletion remain elusive, the results presented in Chapter 5 corroborate with the work of Litz et al. [199], albeit using totally different methods for cholesterol depletion. The observed impacts of cholesterol depletion on lipid patch morphology could be adequately explained by the model derived in the work of Litz et al. [199], in which the complexation of membrane cholesterol leads to two populations of cholesterol in the membrane; one being more accessible to cholesterol depletion than the other. Additionally, a jump in extractable cholesterol was identified for samples with a cholesterol mole fraction higher than 0.4 mol% (Figure 5.9b). Sharp changes in the physical properties of lipid membranes at critical cholesterol mole fraction have often been thought to indicate the formation of specific cholesterol-phospholipid complexes at key cholesterol mole fractions such as 0.2, 0.33 and 0.5 [355]. Thus, the identification of a sharp jump in extractable cholesterol at ~ 0.4 mol% (discussed in Chapter 5.3) further supports the growing body of literature proposing the presence of critical cholesterol mole fractions, and that cholesterol exists in an organised, complexed state within lipid membranes.

Overall, the observations presented in Chapter 5 exemplify how substrate interaction can be utilised to controllably modify the biophysical properties of a simple bilayer system. To further investigate such biological implications, the next chapter will discuss the impact of such substrates on the domain structure of membrane possessing liquid coexistence. The chapter will continue to discuss how the described L_o/L_d systems respond differently to cholesterol depletion when adhered to the substrate surface; most interestingly, impacting the partitioning behaviour of fluorophores.

Chapter 6: Disruption of phase domains by cholesterol modulation of supported lipid bilayer patches

Ternary lipid compositions that combine high and low melting temperature lipids with sterols are widely used as model biomembrane systems as they have the ability to display coexisting liquid phases. Such liquid-liquid coexistence is absent in binary lipid mixtures; for example, DOPC:DPPC liposomes only demonstrate a coexistence of liquid and gel phases at room temperature when experimentally observed with fluorescence depolarisation measurements [374] and theoretically investigated [375]. The addition of sterols, such as cholesterol, facilitates interactions between the lipids with disparate melting temperatures (like DOPC and DPPC), preventing an abrupt gel-fluid transition and allowing the formation of a liquid phase with more ordered hydrocarbon chains; the L_o phase. This change in the system behaviour relies on the nature of many sterols being able to act as both a homogeniser and solvent, when present in sufficient amounts. Hence, sterol addition to lipid mixtures generates a more complex phase diagram with L_d, L_o and $L_ß$ often being able to coexist simultaneously, dependent on the lipid composition. Indeed, the coexistence and segregation of immiscible fluid lipid phases has been proposed as a means to control dynamic lateral organisation in the plasma membrane [376] and membrane signalling [377], respectively. Other studies have even suggested that $L_ß$ phases coexisting with fluid phases could also play a role in organising lateral membrane structure, by forming solid nanoclusters that can stably "dock" membrane proteins [378].

In research, model phase separated systems are often formed on substrates to facilitate the investigation. However, substrate interaction can significantly impact the domain's behaviour within the membrane. The liquid-liquid phase transition temperature has been demonstrated to increase when lipid bilayers are supported on substrates such as glass [86]. Furthermore, although lipids maintain their local lateral diffusivity when supported on substrates, coexisting L_o and L_d domains (that are mobile in free-floating membranes) become fixated and lose the ability to

coalesce [85]. The interaction between the supported lipids and the substrate likely introduces a drag effect on the usually mobile L_o/L_d domains, arising from frictional and pinning effects between the lipid species and the substrate. A recent high-resolution AFM study on SLBs containing L_o/L_d domains demonstrated that L_o domain growth could be limited down to tens of nanometres on roughened mica substrates compared to the typical domain sizes of several microns observed on smooth mica substrates [118]. This behaviour was related to the altered substrate roughness creating more pinning points and inhibiting domain growth. Other studies using fluorescence microscopy have similarly shown macroscopic L_o domain coarsening for supported lipid bilayers is inhibited on artificially roughened surfaces [117]. This behaviour of impeded domain movement has been demonstrated to be strong enough to induce leaflet decoupling in supported lipid membranes subjected to shear flows [87]. In the context of this thesis, these effects pose an obvious question: How will such domain fixation impact membrane restructuring during cholesterol addition and depletion? Cholesterol is well-known to play a key role in stabilising the L_o and L_d domains. Various studies using different phase characterisation techniques have demonstrated that L_o and L_d domains only coexist in compositions containing more than ~ 8% cholesterol for DOPC:DPPC:Cholesterol lipid mixtures at room temperature [59,378,379]. With domain coalescence inhibited, can the membrane form a coexisting gel and liquid-disordered phase upon the depletion of cholesterol below this threshold, as observed in vesicle systems [59]?

In Chapter 5, experiments were focused on single phase systems, with no lateral organisation, and the effect cholesterol depletion had on membrane structure and morphology. The work in this chapter seeks to understand how supported lipid membranes possessing micron-scale L_o/L_d domain structures reorganise under cholesterol addition and depletion. To gain a more comprehensive picture, the reversibility of cholesterol addition and depletion was investigated. Cholesterol content is restored in depleted membranes using a previously established approach of exposing the lipid patches to cholesterol-loaded cyclodextrin (Chol-MβCD), commonly known as soluble cholesterol [60]. Such investigations will aid in understanding how substrate structures play a role in membrane lateral

organisation; whether stabilising or disrupting membrane structures during compositional changes.

6.1 Disruption of lipid bilayer domain behaviour by cholesterol addition and depletion

The substrates' presence significantly impacts the phase properties of supported lipid bilayers, and has been shown to increase their main phase transition temperature [112], miscibility temperature [86] and lower lateral diffusion [113]. Notably, the presence of the substrate has been demonstrated to hinder movement and coalescence of L_o/L_d [85,380]. Phase behaviour in lipid membranes is also altered by compositional changes, such as the depletion of cholesterol, which can be used to cross miscibility boundaries even at constant temperatures. As shown in Figure 6.1, GUVs that possess L_o/L_d domains and are able to freely move and coalesce (Figure 6.1a-c). This leads to the formation of aggregated dark regions in a continuous (presumably L_d) phase upon the extraction of membrane cholesterol through exposure to MβCD. These aggregated domains exclude Rh-DPPE (which has a strong preference for the L_d phase), are no longer able to coalesce, have limited movement, and they are presented with rough non-circular edges, indicating that they are L_β domains. Indeed, previous studies have shown that a depletion of cholesterol from GUVs possessing coexisting L_o/L_d domains causes a disruption of the liquid-liquid coexistence and eventual formation of an a L_β phase in a continuous L_d phase [85,380]; showing similar properties to those seen in Figure 6.1e,f. It should be noted that the bright spots and over exposed regions in Figure 6.1a-f are fluorescent aggregates that adhered to the sessile vesicles and should not to be mistaken for budding vesicle domains. When looking at the phase diagram for DOPC:DPPC:Cholesterol (Figure 6.1g) these changes in phase behaviour can be expected. The composition in Figure 6.1a (represented by the yellow dot) falls from a region of coexisting L_o/L_d phases to a region of coexisting L_d/L_β, with sufficient cholesterol depletion. Notably, the formation of an aggregated gel phase in a continuous L_d phase appears to often rely on domain mobility, as demonstrated in several fluorescence microscopy studies using phase separated GUVs [59,72,80]. Therefore, to investigate how the substrate presence impacts the spatial distribution

of L_o/L_d domains during cholesterol addition and extraction, phase separated lipid patches were exposed to cyclodextrin.

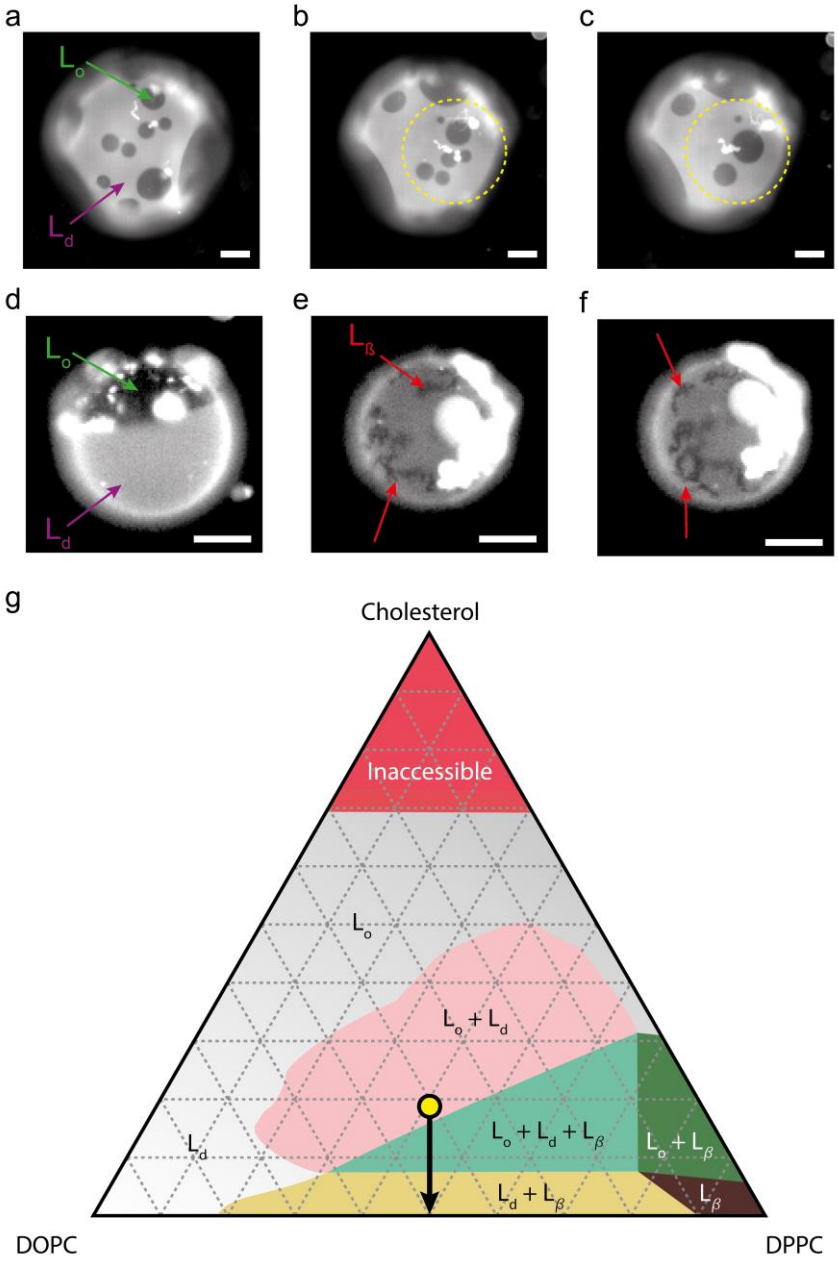

Figure 6.1: Depletion of cholesterol from sessile phase separated GUV. Fluorescence micrographs of lipid bilayer patches composed of DOPC:DPPC:Cholesterol (40:40:20 mol%) doped with 0.1 mol% Rh-DPPE, sessile on a BSA passivated glass slide (a-f). A sessile GUV (a) demonstrates liquid-liquid coalescences, and circular domains can be seen coalescing (b,c) in the yellow dotted region. A similar GUV with fully ripened domains is shown in (d). After 25 minutes incubation with 8 mM methyl-β-cyclodextrin, (e,f), the GUV is depleted of cholesterol forming gel domains, indicated by red arrows. The bright spots in (a-f) are fluorescent aggregates that adhered to the vesicle. Sketch of existing phases at different compositions of DOPC, DPPC and cholesterol (g), with regions of each existing phase adapted from references [59,378,379], with permission from Elsevier. The yellow dot indicates a transition in composition likely occurring in (d-f) as cholesterol is depleted. Scale bars in (a-f) represent 20 µm.

Lipid patches with coexisting L_o/L_d domains were successfully formed using GUV fusion of vesicles with a composition of DOPC:DPPC:Cholesterol (40:40:20 mol%) (Figure 6.2a). This composition is known to produce micron scale domains of L_o/L_d phases, easily observable with fluorescence microscopy [82]. Also, this ternary mixture possessed a relatively high miscibility temperature of ~ 32 ^oC [59], making the resultant phase-separated lipid patches formed from vesicle fusion stable to minor thermal fluctuations of room temperature. The thermal stability of the supported lipid patches was also increased by their fusion onto a glass substrate; with an increased miscibility temperature of ~ 5 ^oC compared to vesicles of the same composition[86]. This meant that the resultant patch's miscibility temperature was significantly above room temperature and could be considered robust against minor fluctuations in ambient temperature.

Two fluorophores were utilised to distinguish the L_o/L_d phases in lipid patches: Rh-DPPE for the L_d phase (Figure 6.2a-d), and NaP for the L_o phase (Figure 6.1e-h). Rh-DPPE has a strong preference for L_d phases; commonly reported to be strongly excluded from coexisting L_o and gel domains, making it useful for distinguishing the two [126,188,381]. The exclusion of Rh-DPPE from the L_o phase has been previously attributed to the bulky nature of the fluorophore, causing unfavourable steric interactions that hinder its partitioning into the L_o phase [187]. However, more recently the fluorophore hydrophilicity has been implicated in driving phase selectivity. According to Bordovsky et al., strongly hydrophobic molecules (rhodamine) prefer interacting with the membrane rather than the bulk aqueous solution, thus driving them and their attached lipid into the L_d phases [381]. Indeed, it was demonstrated that a hydrophilic PEG spacer between the fluorescent label and lipid headgroup could "mute" the hydrophobic interactions between the fluorophore and lipid membrane, allowing it to enter the L_o phase from which it was previously excluded [381].

With a single fluorophore, the L_o phase can be identified by the absence of Rh-DPPE signal, as seen by the dark domains within the lipid patch boundary of Figure 6.2a. These regions were round in shape with smooth edges, which is typical of coexisting L_o/L_d phases, as the line tension acts to minimise the domain boundary between the two liquid phases, resulting in circular domains. To ensure that the L_o domains could be easily distinguished from pores and defects in the membrane, the

complementary fluorescent dye NaP was utilised. Although it produced a weak signal-to-noise ratio compared to Rh-DPPE, it still proved highly useful. NaP preferentially partitions into the L_o phase and has a distinctly different fluorescence emission and absorption to Rh-DPPE, allowing them to be used together. In doing so, a more robust interpretation of varying membrane behaviour could be acquired, with the evolution of membrane organisation clearly observable in both phases through the use of different labels. NaP is an accepted fluorescent label primarily used with ordered domains in DOPC/DPPC/Cholesterol systems, as only minor impacts on membrane miscibility of supported lipid systems are observed [85,187,189]. When the labelled GUVs fused to substrates, the resultant lipid patches demonstrated clear L_o/L_d domains (Figure 6.2a,e). Similarly to previous reports [85], the domain structure remained unchanged, with no lateral reorganisation over a time period of hours; indicating an inhibition of domain coalescence.

6.1.1 Cholesterol addition through the solution (soluble cholesterol)

Upon the addition of soluble cholesterol, the lipid patches begin to increase in area and spread across the substrate, as indicated by yellow arrows in Figure 6.2b. As the lipid patches continue to spread, the boundary between L_o and L_d domains becomes notably diffuse (Figure 6.2c) and eventually dissipates, leaving a uniform fluorescence signal across the patch (Figure 6.2d).

The observed loss of lipid domain structure is indicative of the composition crossing the phase boundary into a single miscible liquid phase. Looking at the DOPC:DPPC:Cholesterol phase diagram (Figure 6.1g), an infusion of > 20 mol% cholesterol would cause lipid patches of DOPC:DPPC:Cholesterol (40:40:20 mol%) to traverse from a phase region of coexisting L_o/L_d phase, into a single miscible liquid phase. Indeed, previous studies with equimolar DOPC:DPPC composition, containing a high cholesterol concentration (> 45 mol%) form single liquid phases with miscibility temperatures below 10 ^oC [59]. Although the addition of ~ 20 mol% cholesterol is a significant increase in cholesterol content, previous studies have shown the cholesterol content in lipid patches can be increased by ~ 60 mol%, indicating it is feasible [60].

Consistently, the fluorescence signal shows a drop in intensity concurrent with patch area increase. As Rh-DPPE is unaffected by the presence of soluble cholesterol [60], this indicates a decrease in intensity due to a drop in Rh-DPPE surface density, as it is redistributed across all areas of the patch.

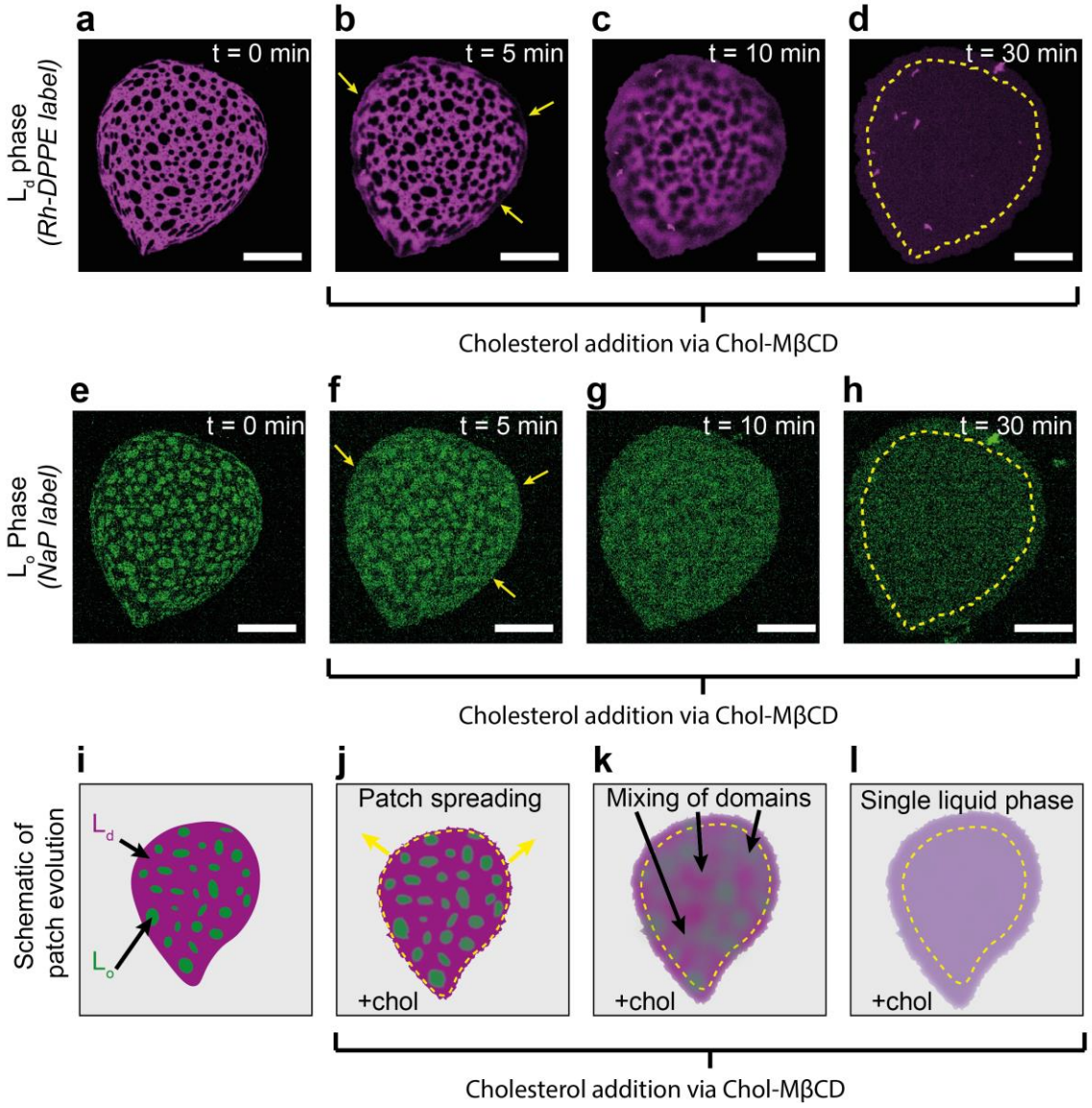

Figure 6.2: Doping of cholesterol into phase separated supported lipid bilayers. Fluorescence micrographs of lipid bilayer patches composed of DOPC:DPPC:Cholesterol (40:40:20 mol%) doped with 0.1 mol% Rh-DPPE and with 3 mol% NaP on a hydrophilic glass substrate at different time intervals after the exposure to 4.0 mg/mL soluble cholesterol (Chol-MβCD). The Rh-DPPE signal (a-d) identifies the L_d regions of the lipid patch, whereas the NaP signal (e-h) identifies the L_o regions. Cartoon schematic (i-l) demonstrating the transition to a single miscible liquid phase as cholesterol is infused into the phase separated lipid membrane. Yellow arrows indicate regions of initial spreading as cholesterol absorbs into the membrane. The dotted yellow outline indicates the initial patch area. Scale bars in (a-h) represent 50 µm.

A similar process is seen to occur in the L_o domains, with the regions increasing in area and becoming homogenously labelled (Figure 6.2e-h). Overall, this behaviour closely matches those described for free-floating vesicles systems undergoing cholesterol addition [59,82]. These results, although expected, demonstrate that at least some supported lipid bilayer behaviours remain consistent to those found in free-floating vesicle systems, but it is not the case for cholesterol depletion in this system.

6.1.2 Depletion of cholesterol through the solution (cyclodextrin)

To deplete the lipid bilayers of cholesterol, 1 mM methyl-β-cyclodextrin (MβCD) was injected into the buffer solution (see Chapter 2.4.2 for details on protocols). This induced an overall reduction in the patch area of ~15 - 20%, predominantly through the formation of pores in L_d regions, as indicated by the yellow arrows in Figure 6.3b-c. Although MβCD has been shown to extract PC lipids from membranes, this tends to occur over longer timescales [60,367,368,382], hence the large decrease in the patch area was attributed to a loss of cholesterol from lipid patches. Previous studies using MβCD to extract cholesterol from DOPC:Cholesterol lipid patches demonstrated no visible changes in lipid patch areas for low-cholesterol regimes (< 0.3 mole fraction) [199]. Therefore, the large decrease in patch area due to cholesterol loss was unexpected.

The preference for pore formation in the L_d regions could be related to their lower rigidity [156] and higher fluidity [383] compared to L_o regions, facilitating membrane reorganisation into pores after cholesterol extraction. Lateral diffusivity of the L_o phase is measured to be ~2 - 10 times smaller than the L_d phase in various studies [36,383–385]. This is expected, considering that pure DOPC bilayers have lateral diffusivities on the order of 1 $\mu m^2 s^{-1}$ [114,386], and pure DPPC bilayers have lateral diffusivities ~ 0.01 - 0.1 $\mu m^2 s^{-1}$ [113,386]; each being the predominant lipid species in L_d and L_o domains present in DOPC:DPPC:Cholesterol mixtures, respectively.

As DOPC and DPPC cannot easily redistribute between the L_o/L_d domains of lipid patches fixated to a substrate [85], cholesterol depletion of the L_o domains would likely leave the region with a high ratio of DPPC:DOPC. For this reason, depletion of cholesterol in the lipid patches was expected to form L_β phases in the regions that

were previously L_o regions. Simultaneously the surrounding fluid L_d regions would be depleted and left enriched in DOPC, hence remain fluid. This would leave the system in a coexisting L_β/L_d phase, if an equimolar composition of DOPC:DPPC was sufficiently depleted of cholesterol (Figure 6.1g), as expected from the phase diagram. Such behaviours are observed in the free GUV systems where cholesterol depletion promotes coexisting L_d and L_β domains; the latter characterised by their rough fractal edges, (as seen in Figure 6.1e, f).

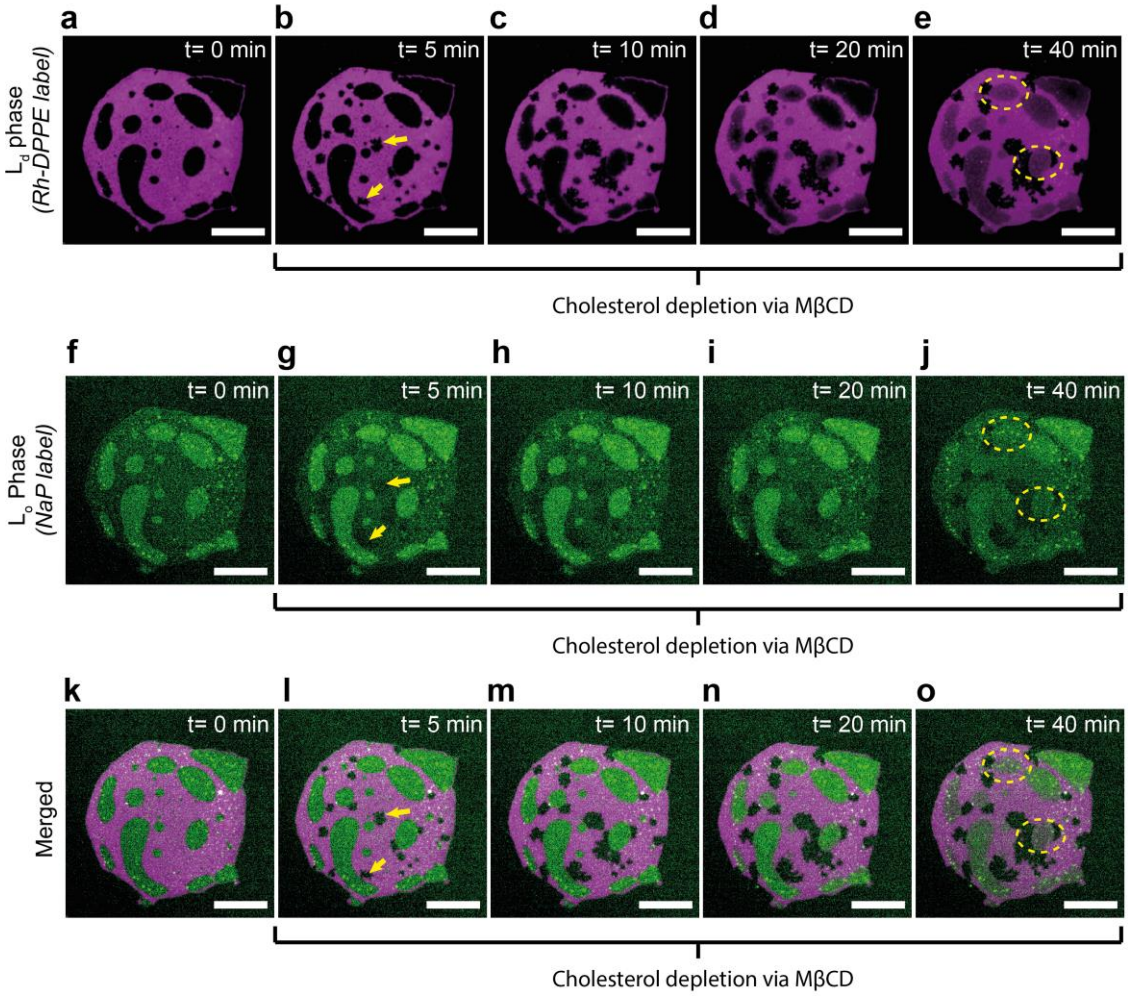

Figure 6.3: Depletion of cholesterol disrupting fluorophore partitioning for supported lipid membranes. Fluorescence micrographs of lipid bilayer patches composed of DOPC:DPPC:Cholesterol (40:40:20 mol%) doped with 0.1 mol% Rh-DPPE and with 3 mol% NaP on a hydrophilic glass substrate at different time intervals after the exposure to 1 mM methyl-β-cyclodextrin (MβCD). The Rh-DPPE signal (a-e) identifies the L_d regions of the lipid patch, whereas the NaP signal (f-j) identifies the regions the L_o region, with the merged (k-o) depicting both. Yellow arrows indicate regions where pores have formed due to cholesterol depletion, and dotted yellow outline indicates regions where Rh-DPPE has entered the L_o phase, from which it was previously excluded. Scale bars in (a-o) represent 50 µm.

The depletion of cholesterol from systems containing DOPC:DPPC:Cholesterol (40:40:20 mol%) would cause the system to cross the phase boundary into a three-phase coexistence of $L_\beta/L_o/L_d$, before arriving in a binary L_β/L_d phase. Other studies utilising AFM imaging on supported bilayer systems of DOPC:Sphingomyelin:Cholesterol, probed the nucleation of L_β domains in compositions possessing three-phase coexistence [74]. It was found that the formation of L_β domains could occur via both spinodal decomposition and nucleation, possibly forming a "disordered" or surface kinetically-trapped gel state within previous L_o regions of the supported lipid bilayer [74]. Although dark areas appear in the lipid patch during the initial stages of cholesterol depletion, the merged Rh-DPPE/NaP images reveal that these are most likely pore defects due to patch shrinkage (Figure 6.3k-o), and not the formation of small gel regions. The L_o domains themselves appear to retain their shape and structure initially, but after several minutes of MβCD exposure, Rh-DPPE begins to penetrate the regions (Figure 6.3d,e). The partitioning of Rh-DPPE into these regions is highly unusual due to it being sterically bulky and highly hydrophobic, making it unfavourable to sit within the more ordered regions [188,189,381].

Similarly, the NaP appears to dissipate into the surrounding L_d phase, as seen in Figure 6.3j. Unfortunately, such effects were harder to appreciate in the NaP channel, due to a diminishing fluorescence signal. It was concluded that loss of NaP intensity was partly due to its extraction from the bilayer by MβCD (Figure 6.4).

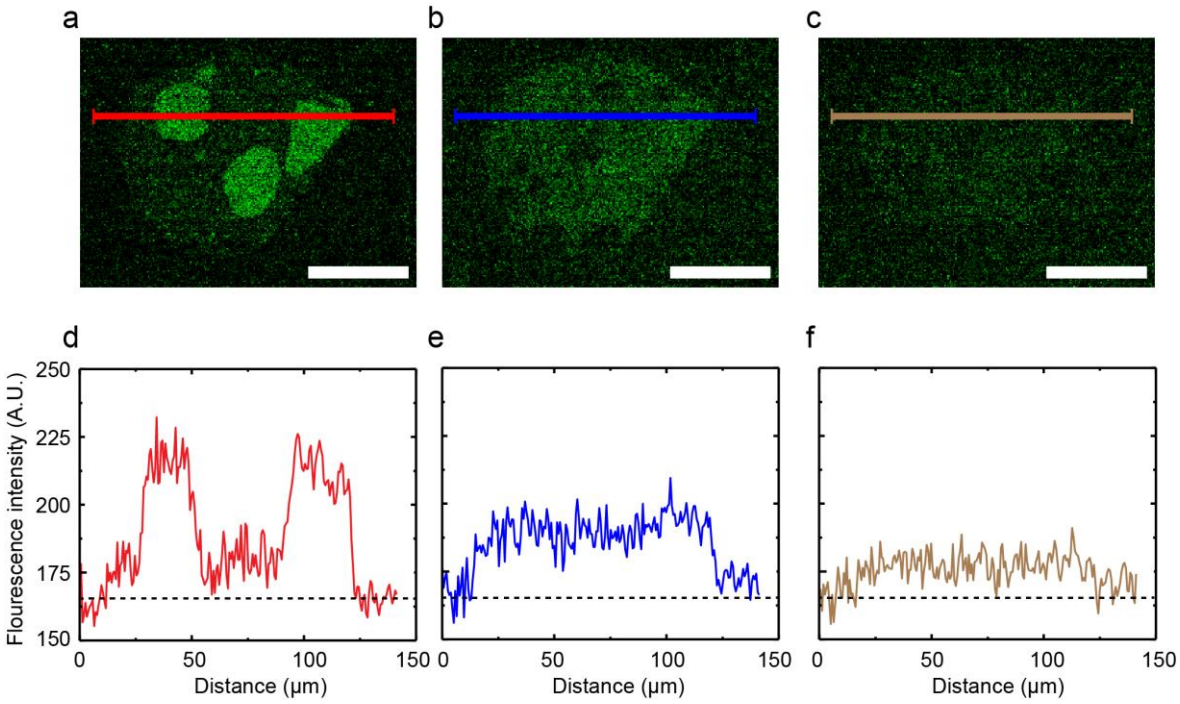

Figure 6.4: Homogenisation and loss of NaP signal during cholesterol depletion. Fluorescence micrographs of lipid bilayer patches composed of DOPC:DPPC:Cholesterol (40:40:20 mol%) doped with 0.1mol% Rh-DPPE and 3 mol% NaP. Micrographs show a lipid patch exposed to 1 mM methyl-β-cyclodextrin after 0 minutes (a), 20 minutes (b) and 40 minutes (c), with corresponding line profiles of fluorescence intensity from the NaP channel below (d-f). Scale bars represent 50 μm.

The diminishing fluorescence signal of the NaP can be attributed to three factors. Firstly, the reduced surface density of NaP as it penetrated the L_d regions of the lipid patch caused a drop in fluorescence intensity. This is best demonstrated in Figure 6.4b,e, where these regions are only just detectable above ambient noise. Secondly, the susceptibility of NaP to bleaching; causing a reduction in fluorescence intensity throughout imaging. Finally, it is here speculated that MβCD is depleting NaP from the lipid patch along with cholesterol, resulting in an almost complete loss of NaP fluorescence signal (Figure 6.4c,f). The first two factors are present in the cholesterol-addition experiments (Figure 6.2), but a complete loss in NaP signal is not observed. The ability of MβCD to deplete NaP from lipid bilayers is likely due to NaP sharing similar structural qualities to cholesterol; being a small hydrophobic molecule, made up of cyclic carbon compounds with attached functional groups. The shared chemical characteristics may make it similarly vulnerable to extraction via MβCD. For this reason, Rh-DPPE is predominantly used to quantify the redistribution of the fluorescent probe, as its signal was more resistant to bleaching and depletion.

Further measurements were required to characterise membrane phase behaviour after cholesterol depletion, as the drastic change in the composition clearly altered portioning properties of membrane species such as Rh-DPPE, likely disrupting the phase behaviour of initial L_o and L_d regions. To better characterise the effects observed in Figure 6.3, measurements were carried out to determine both the homogenisation of the Rh-DPPE between the initial L_o and L_d domains, and how domain lateral fluidity was altered after the redistributions of the fluorescent label.

6.2 Impact of cholesterol depletion on domain structure and membrane properties

As cholesterol is depleted, the bilayer structure is altered to allow Rh-DPPE to penetrate the initial L_o phase (Figure 6.5a-d). Although some of the L_o regions become homogenised (yellow dotted regions in Figure 6.5d) many domains are only partially infused with Rh-DPPE (green arrows in Figure 6.5a-d). Using the change in fluorescence intensity of the Rh-DPPE signal in each phase (Figure 6.5e), redistribution of the Rh-DPPE could be monitored. Here average fluorescence intensity is defined as the mean pixel intensity recorded within the L_o or L_d domains, normalised to the initial average fluorescence intensity measured in the L_d domains. When looking at the average change in Rh-DPPE signal of L_d and L_o domains, the increase in the intensity of L_o domains corresponds to a decrease in fluorescence intensity of the L_d domains (Figure 6.4e). This indicated that the Rh-DPPE is transferring from the L_d phase into the L_o phase. Interestingly, the ~60% increase in intensity in the L_o domains is much higher in magnitude than the ~5% decrease in intensity of the L_d phase from which the Rh-DPPE is migrating. This discrepancy in intensity changes between the two phases is likely due to alterations in the surface density of the Rh-DPPE.

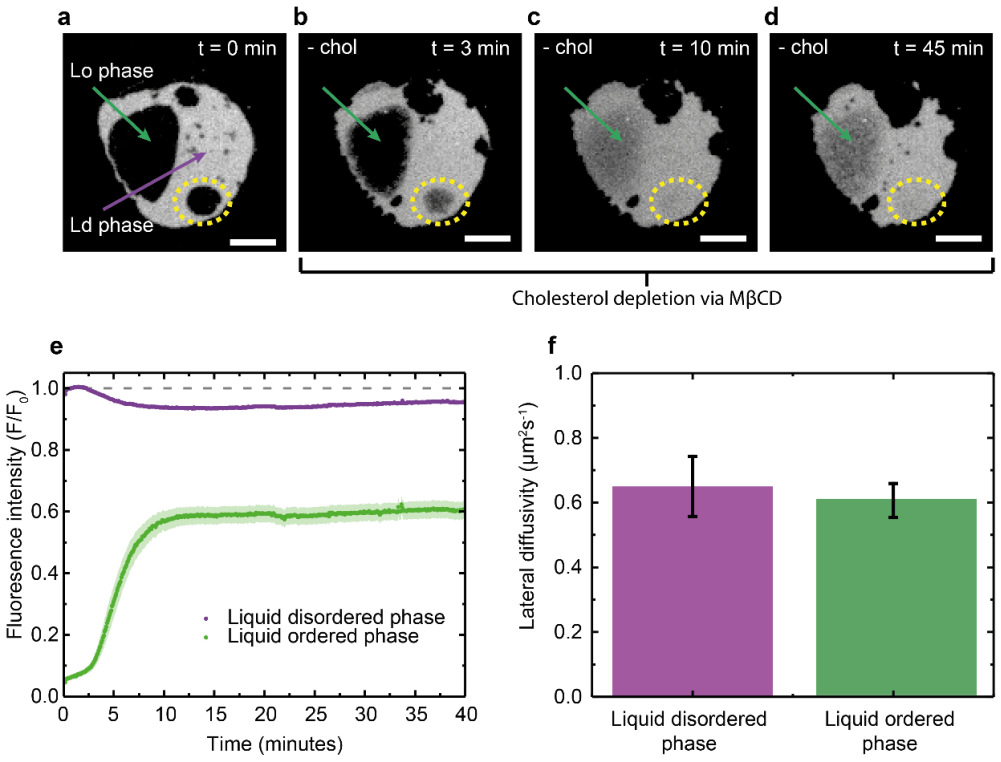

Figure 6.5: Depletion of cholesterol allows Rh-DPPE to penetrate the liquid-ordered phase. Fluorescence micrographs of lipid bilayer patches composed of DOPC:DPPC:Cholesterol (40:40:20 mol%) doped with 0.1 mol% Rh-DPPE on a hydrophilic glass substrate at different time intervals after the exposure to 1 mM methyl-β-cyclodextrin (MβCD) (a-d). The initial Rh-DPPE signal (a) identifies the L_d regions of the lipid patch, which begins to partition into the L_o phase (b-d), where it was previously excluded. Graph (e) shows the change in fluorescence intensity of the Rh-DPPE signal in the L_d and L_o regions during the cholesterol depletion of the lipid patch, normalised to their respective areas, with a graph (f) depicting the lateral diffusivities of the two phases after cholesterol has been depleted from the samples. Scale bars in (a-d) represent 20 μm.

As described in Figure 5.2e, the specific depletion of cholesterol from membranes causes an increase in fluorescence intensity for L_d regions, as the bilayer shrinks in area and the Rh-DPPE surface density increases.

Upon closer inspection, this effect is demonstrated by a slight increase in fluorescence intensity seen in the L_d domain curve of Figure 6.4e. As the L_d domains are depleted of cholesterol, the migration of Rh-DPPE into the L_o domains phase offsets a further increase in the fluorescence intensity of the L_d phase. The observation that Rh-DPPE diffuses into the L_o phase suggests, counter-intuitively, that L_o regions retain some degree of membrane fluidity after cholesterol depletion, despite the expectation that they will gel. The latter occurs in free vesicles following depletion of cholesterol (Figure 6.1d-f), with the fractal rough domain boundaries indicating a gel phase. As L_o domains possess a significant proportion of the

membrane's saturated lipids, they most likely transition into a more gel-like phase under depletion of cholesterol, hence causing a significant loss of lateral diffusivity. It has even been suggested that such regions already contain small gel domains within them [387], making L_o regions particularly favourable for further nucleation of gel domains. In Figure 6.4f, the average lateral diffusivity for L_d and L_o domains after cholesterol depletion is quantified using FRAP (see Chapter 2.5.2 for further details of protocols). The influx of Rh-DPPE into the initial L_o regions enables FRAP measurements to be conducted, and the lateral diffusivity of the region after cholesterol depletion to be measured. This was not possible with the original L_o/L_d domain structure as the Rh-DPPE was excluded from L_o regions, and the NaP was too susceptible to bleaching to acquire useful recovery curves. Surprisingly, FRAP results indicate that the L_o regions retain a significant degree of lateral diffusivity, with the magnitude of lateral diffusivity being similar to that of the L_d region, although literature suggests it should be appreciably lower [36,383–385]. It should be noted that these results only indicate Rh-DPPE's diffusivity within the bilayer, and thus cannot be used as a direct measure of overall membrane fluidity.

Even though the domains lateral diffusivity is preserved, the change in fluorophore partitioning suggests a drastic change in the membrane structure that allows the bulky Rh-DPPE to penetrate the liquid-ordered regions. Notably, this behaviour is distinctly different from the response of GUVs to cholesterol depletion, suggesting the substrate interactions are inducing this perturbation in the phase-separated bilayer in response to cholesterol extraction. Although partially infused with Rh-DPPE, the L_o domains appear to retain their general shape and location, suggesting that the regions had not been wholly disrupted, as was expected from previous studies [387–389]. This behaviour demonstrates that some lipid structures from the initial L_o domain persist even after cholesterol depletion had completed.

An assumption of the above discussions is that the domains remain in registry, with the observed effects occurring in both leaflets. This is not necessarily true, as no measurements were taken to confirm this assumption; although, previous literature indicates lipid domains to be rarely observed out of registry in free-floating GUVs [82,387,390]. This is in line with the predictions from theoretical models that indicate that fluctuations of L_d and L_o domains out of registry are on the nanometre length scale, explaining why they have not been observed by optical microscopy [89]. Other studies

have reported similar behaviours in supported lipid bilayers formed from vesicle fusion of GUVs, with domain structure being registered between leaflets after fusion [84,85] and remain so unless perturbed externally; for example, by significant shear flows of around ~ 20 Pa [87]. However, a study investigating non-equilibrium behaviour of supported lipid bilayers containing cholesterol did demonstrate that coexisting liquid-liquid domains could exist out of registry in between lipid leaflets [177]. Using Langmuir-Schafer and Langmuir-Blodgett deposition, phase-separated lipid monolayers of DOPC/DPPC/Cholesterol (40:40:20) were transferred onto a supported lipid monolayer of similar composition, adhered onto a glass substrate. It was found that domains of each monolayer were not in registration, and remained static over several hours [177]. With this in mind, the results presented in this chapter cannot conclusively confirm that domains remain in registry during cholesterol depletion by MβCD.

To further investigate the impact of L_o/L_d domains structure on membrane response to cholesterol depletion, the changes in the area of segregated and coalesced domain patterns were compared. Phase-separated GUVs used in vesicle fusion were heated to above the miscibility temperature during formation. See Chapter 2.4.2 for further details of protocols. The equilibration of such samples over several minutes lead to ripened, coalesced domains (Figure 6.6e), whereas the rapid cooling of such samples led to the formation of smaller L_o domains distributed in a continuous bulk L_d phase. The fusion of these GUVS formed lipid patches with a "segregated" L_o/L_d domain pattern, as seen in Figure 6.6a.

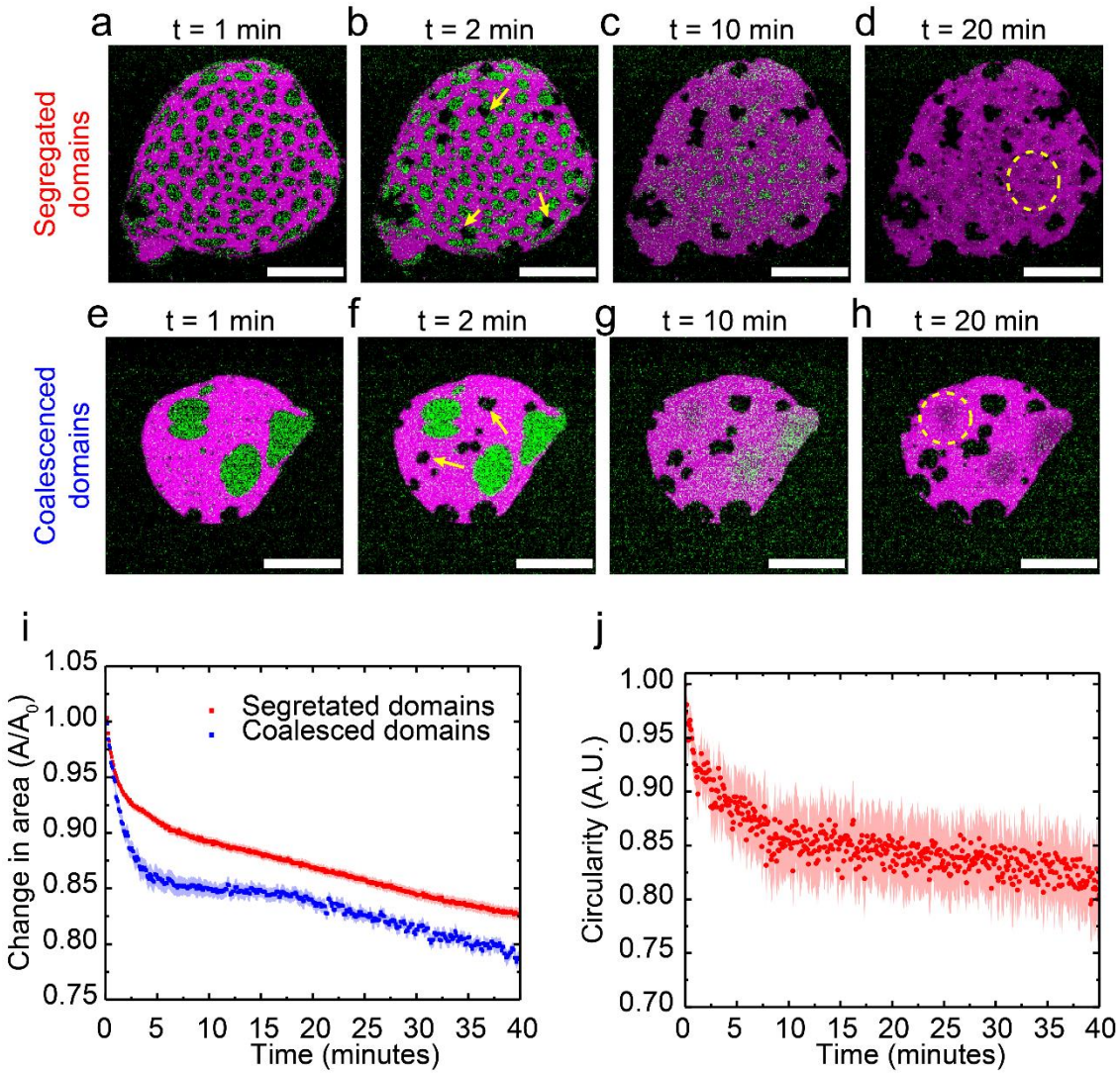

Figure 6.6: Change in patch morphology, pore formation, area shrinkage due to cholesterol depletion of phase separated supported bilayers. Fluorescence micrographs of lipid bilayer patches composed of DOPC:DPPC:Cholesterol (40:40:20 mol%) doped with 0.1mol% Rh-DPPE on a hydrophilic glass substrate at different time intervals after the exposure to 1 mM methyl-β-cyclodextrin (MβCD). The change in patch area during cholesterol depletion of lipid patches with smaller segregated domains (a-d) and larger coalesced domains (e-h). Graph (i) compares the change in patch area during cholesterol depletion for patches with segregated and coalesced domains. Graph (j) depicts the change in average circularity of pores formed preferentially in the L_d domain during cholesterol depletion. Scale bars in (a-h) represent 50 µm.

Comparing the effect of cholesterol depletion between segregated and coalesced domain patterns (Figure 6.6i), it can be seen that patches with multiple small domains had a slower reduction in the area, compared to patches with a few large domains.

A possible explanation is that the segregated systems obtained by temperature quenching exist far from equilibrium [82]. This may result in a higher degree of

saturated lipid remaining within the L_d phase, making such regions less prone to pore formation during cholesterol extraction. The latter could be verified by comparing the L_o:L_d domain area ratio, A_{L_o}/A, of coalesced and segregated lipid patches, to gain an indication of any difference in the lipid compositions between the two systems. The results show that both coalesced and segregated lipid patches displayed similar L_o:L_d domain area ratios, with coalesced and segregated patches having A_{L_o}/A values of 38.1 ± 2.5% and 37.8 ± 0.8% respectively. These L_o: L_d domain area ratios for DOPC:DPPC:Cholesterol (40:40:20 mol%) bilayers are consistent with previous studies, in which tie-line measurements were conducted on DOPC/DPPC/Cholesterol systems of similar composition to estimate L_o domain area fractions [384]. Thus, it is unlikely that L_o and L_d domains have much variation in composition between coalesced and segregated lipid patch systems, with a reasonable explanation for the difference in the rate of diffusion between coalesced and segregated lipid patches remaining elusive.

Interestingly, when observing the behaviour of pore formation in segregated and coalesced lipid patches, the pores once again had a strong preference for forming in the L_d phase, regardless of the confining geometry of the segregated patches (as indicated by yellow arrows in Figure 6.6b,f). When looking at the evolution of pores in the L_d regions, the average pore circularity decreases as the defect expands over time (Figure 6.6j). Circularity is defined by the following equation:

$$\text{Circularity} = 4\pi\left(\frac{Area}{Perimeter^2}\right) \qquad \text{Equation 6.1}$$

As the area and perimeter can be easily tracked using techniques described in Chapter 2.5.4, a change in pore circularity provides a simple and effective descriptor to characterise the evolution of pore morphology during cholesterol depletion. Initially, the pores are circular to minimise line tension in the membrane due to the opening of the defect. As depletion continues, the periphery of the pore is destabilised by drag forces, leading to rougher edges [290,391]. The origin of these drag forces is likely due to substrate interactions, with substrate adhesion and roughness known to impact lipid mobility [112,113,116]. Indeed, these same interactions are possibly the cause of the inhibited domain movement, with similar drag forces impeding large scale lateral reorganisation of L_o/L_d domains [87].

In both coalesced and segregated domain patterns, the L_o regions maintained their initial geometry, with few observable pores being formed during depletion. This can be rationalised by the L_o phase having an increased rigidity and low deformability, making such regions unfavourable to deformation compared to the L_d phase.

6.3 Increased resistance to cholesterol modulation conferred by saturated lipids

The previous sections evidence a significant substrate-induced impact on the behaviour of a model ternary membrane upon cholesterol depletion, but not cholesterol infusion. To verify that these effects are general and not unique to the specific composition of DOPC/DPPC/Cholesterol investigated so far, another composition of DOPC/DPPC/Cholesterol (64:16:20) was tested. This ternary mixture forms a predominant L_o phase, creating GUVs with an area fraction of 1:4 that favour the L_o domains [59]. This composition exists within a three-phase coexistence region on the phase diagram (Figure 6.1g), although the presence of L_β domains would be hard to distinguish due to their small size and thinness [59,392]. Using GUVs of this composition, lipid patches with a significantly higher content of saturated lipid were successfully made (Figure 6.7a) by comparison with those discussed earlier in the chapter. This alternative composition contained the same 0.2 cholesterol mole fraction, allowing the comparison between DOPC:DPPC:Cholesterol (40:40:20 mol%) systems, and provide an insight into how saturated lipid content impacted the response of the membrane to cholesterol depletion.

The addition of soluble cholesterol to the system induces a similar response to that described in Chapter 6.2, with cholesterol addition promoting the formation of a single miscible liquid phase (Figure 6.7a-e). Similarly, the higher but feasible infusion of ~ 30 mol% cholesterol into lipid patches of DOPC:DPPC:Cholesterol (16:64:20 mol%) would cause a movement across the phase diagram from a region of coexisting $L_\beta/L_o/L_d$ phases into a single miscible liquid phase. The patch displayed a significant increase in area and disruption of domain structure in accordance with crossing a phase boundary into a single miscible phase.

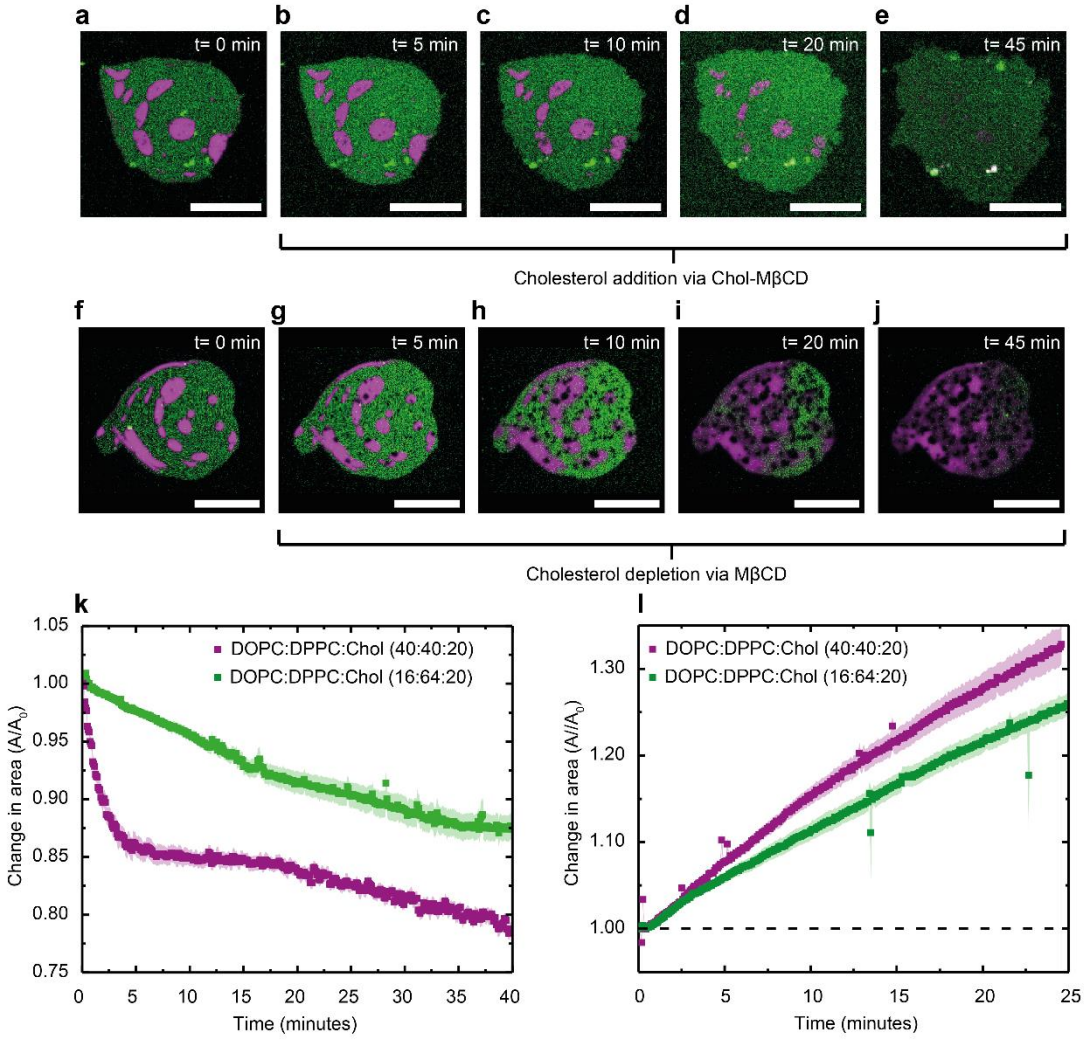

Figure 6.7: Effects of cholesterol depletion of supported lipid bilayers with a predominantly liquid-ordered phase. Fluorescence micrographs of lipid bilayer patches composed of DOPC:DPPC:Cholesterol (16:64:20 mol%) doped with 0.1 mol% Rh-DPPE and 3 mol% NaP on a hydrophilic glass substrate at different time intervals after the exposure to 4 mg/mL soluble cholesterol (Chol MβCD) (a-e) and 1 mM methyl-β-cyclodextrin (MβCD) (f-j), with graphs for average change in patch area during cholesterol depletion (k) and addition (l). Scale bars in (a-j) represent 50 µm.

Similarly, upon cholesterol depletion via the addition of MβCD, the patches shrank in area, formed pores and exhibited a redistribution of the fluorescence signal, with the Rh-DPPE visibly spreading and entering the L_o domains, and NaP into the L_d domains (Figure 6.7f-j). Depending on the level of cholesterol depletion, this could result in the final patch compositions passing through the three-phase coexistence region into a region of L_β/L_d coexistence, providing cholesterol levels are depleted below ~ 8 mol% cholesterol [59,378,379].

Although pores initially form in the L_d phase, pores can eventually be observed in the L_o phase. However, these pores are smaller in size, indicating that L_o regions are still less favourable to pore formation than the L_d domains. Notably, the samples enriched with saturated lipid show a slower rate of cholesterol addition and depletion compared to the samples enriched in unsaturated lipids (Figure 6.7k).

It should be noted that the composition containing more saturated lipid did have a smaller area fraction of L_d phase, with DOPC:DPPC:Cholesterol at 16:64:20 mol% having a value of A_{L_o}/A of ~ 85% [384], compared to DOPC:DPPC:Cholesterol at 40:40:20 mol% having a value of A_{L_o}/A of ~ 38%. It could be proposed that cholesterol extraction occurs solely from the L_d phase, and its reduced area fraction in the DOPC:DPPC:Cholesterol (16:64:20 mol%) composition led to slower depletion/absorption rates. But, even if the 20 mol% cholesterol present in the membrane was evenly distributed between the L_o and L_d domains, a complete depletion of cholesterol from solely L_d domains would only result in a crude estimation of a ~ 3 mol% loss of cholesterol (seeing as L_d only represented 15% of total patch area). Such a small change in composition would not shift the composition out of the three-phase coexistence region on the phase diagram (Figure 6.1g) and further, be unlikely to cause such drastic changes in the lipid patch morphology as demonstrated in Figure 6.7f-j. Considering that diffusion studies of isotopically labelled lipids in DOPC/DPPC/Cholesterol mixtures have identified that the cholesterol concentrations in the L_d are smaller than in the L_o phase [385], it is unlikely that cholesterol is solely depleted from L_d domains, but also from the L_o domains, albeit at a slower rate.

Interestingly the same behaviour is demonstrated for cholesterol addition, with the saturated composition showing slower adsorption timescales (Figure 6.7l). This suggests that not only is it more difficult to deplete heavily saturated mixtures of cholesterol, but also that it is more difficult to infuse them with cholesterol when compared to unsaturated compositions. The ability of saturated lipids to stabilise model membranes against cholesterol addition and depletion makes them a useful addition to model membrane systems, shedding light on their roles in fortifying biological compositions.

6.4 Substrate-induced cholesterol depletion disrupts domain behaviour

Many of the effects described in the previous sections have been linked to the depletion of cholesterol from the system, by the addition of a chemical agent to the system, MβCD, which could, in principle, also be affecting the membrane's behaviour. To verify that MβCD plays no significant role on the redistribution of Rh-DPPE into the L_o phase, and that cholesterol extraction is responsible for the observed effect, control experiments using another means of cholesterol extraction were conducted. As discussed in Chapter 5, partially plasma-treated PDMS substrates can stably support phospholipid membranes while specifically extracting cholesterol, providing an alternative method of cholesterol extraction to MβCD. The results presented in Figure 6.8a-h show that the ternary mixture of DOPC/DPPC/Cholesterol (40:40:20 mol%) behaves similarly, with a comparable change in area and fluorescence partitioning to that reported in Chapter 6.1. Several minutes after the initial lipid patch formation (Figure 6.8a) the pores appear (yellow arrows in Figure 6.8c), followed by the penetration of Rh-DPPE into the previous liquid-ordered phase (Figure 6.8d-h). Interestingly, the NaP signal quickly diminishes in the first few minutes, likely diffusing into the PDMS substrate. This is further validated by the presence of a diffuse NaP signal around the liquid-ordered regions, shortly after fusion (yellow dotted ring in Figure 6.8b). Indeed, the background signal for NaP notably increases after several minutes, as the fluorescent label penetrates the surrounding substrate (Figure 6.8c). This falls in line with current reports of PDMS being able to absorb small hydrophobic molecules from solution [265] and supported lipid bilayers [393] (as detailed in Chapter 5).

Another notable difference is that many of the liquid-ordered domains are not completely permeated by Rh-DPPE, with regions seemingly devoid of Rh-DPPE signal even after 120 minutes (Figure 6.8h). The regions exhibiting no Rh-DPPE penetration are located furthest from the domain boundary, and so have the longest diffusion pathway for the Rh-DPPE molecules.

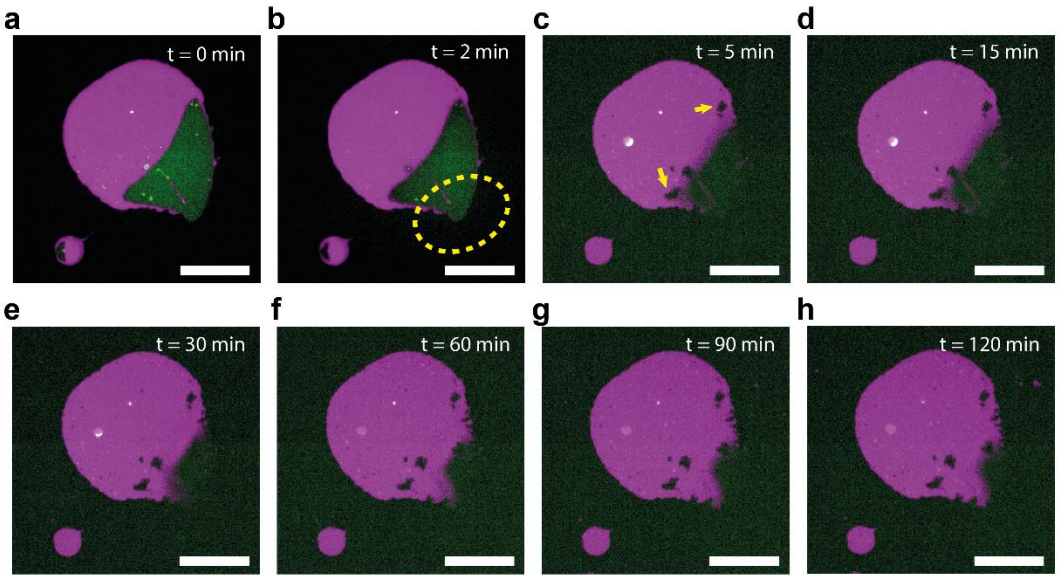

Figure 6.8: Disruption of fluorophore partitioning initiated by substrate-induced cholesterol depletion. Fluorescence micrographs of lipid bilayer patches composed of DOPC:DPPC:Cholesterol (40:40:20 mol%) doped with 0.1 mol% Rh-DPPE and with 3 mol% NaP at different time intervals after fusion to partially plasma-treated PDMS substrates. The combined Rh-DPPE and NaP signal (a-h) show changes in patch morphology and fluorescence partitioning. Yellow dotted ring indicates regions of NaP signal, which indicate the fluorophore dissipating into the PDMS substrate, accounting for the increased background signal in (c-h). Scale bars in (a-h) represent 50 µm.

The exact reason for this difference between substrate-induced and MβCD-induced cholesterol extraction remains unclear; but a possible explanation could be due to the increased roughness of the partially plasma-treated PDMS, which in turn would induce a greater drag effect on the L_o/L_d domains. Although local lipid diffusivity is maintained when lipid patches are formed on partially plasma-treated substrates (see Figure 4.1), the increased roughness likely induces more pinning and drag forces between the membrane and the substrate. This may hinder the migration of Rh-DPPE from the L_d phase into the L_o domain during cholesterol depletion, slowing the process down enough that Rh-DPPE can be kinetically trapped in the later stages of depletion.

Overall, it can be concluded that PDMS-led and MβCD-led cholesterol depletion both induced similar effects on the phase separate lipid patches, causing membrane pores to form, patch shrinkage to occur, and promote penetration of Rh-DPPE into initial L_o regions. These experiments also suggest the persistence of some domain structures after the majority of cholesterol has been depleted, as the Rh-DPPE distribution never fully homogenised across the patch, even after extended time

periods. In such a case, the reintroduction of cholesterol into a depleted membrane should restore initial domain structure and fluorophore partitioning.

6.5 Reversibility of lipid domain restructuring by cholesterol modulation

To test if the domain structure of the phase-separated lipid patches could be restored after cholesterol extraction, depleted lipid patches were exposed to soluble cholesterol. Such restoration of domains has been previously demonstrated with supported lipid monolayers and free GUVs [59,388,389], but little data is available when utilising supported lipid bilayers with micron-scale liquid-liquid coexisting domains. As seen in Figure 6.9a-e, the initial depletion of cholesterol from lipid membranes induces the expected area shrinkage and pore formation, with an example pore defect highlighted by a yellow arrow. The depleted membrane can be stabilised by washing the patch with TRIS buffer (Figure 6.9f), diluting the MßCD solution sufficiently to inhibit further depletion of cholesterol from the lipid patches. The patches are subsequently exposed to a buffer solution containing 4 mg/mL of soluble cholesterol, which reinfuses the membrane with cholesterol. Upon the reinsertion of cholesterol into the bilayer, patch areas increase, pore defects heal, and the initial fluorescent partitioning is regained, with Rh-DPPE being once again excluded from the L_o domains. The restoration of micron-scale domain structure with the addition of cholesterol further validates the hypothesis that cholesterol depletion does not fully destroy the lipid patch L_o/L_d domain structure. The continued exposure of the restored patches causes a slight increase in patch area and reduced contrast between L_o/L_d domains, as described in Figure 6.2. This once again can be halted by washing the membrane with TRIS buffer to dilute the soluble cholesterol concentration, and slow down the cholesterol addition (Figure 6.9k).

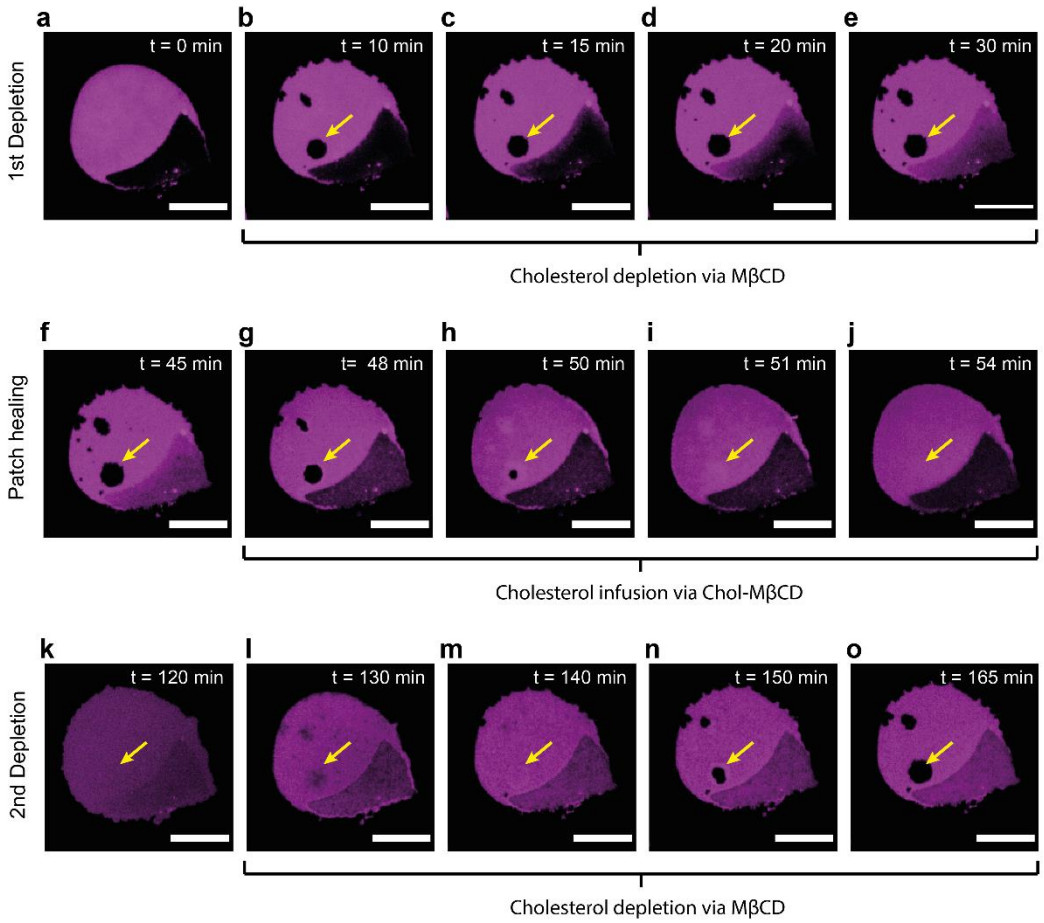

Figure 6.9: Cycling cholesterol extraction and addition to disrupt and heal phase-separated lipid patches. A sequence of fluorescence micrographs of lipid bilayer patches composed of DOPC:DPPC:Cholesterol (40:40:20 mol%) doped with 0.1 mol% Rh-DPPE and 3 mol% NaP on hydrophilic glass substrate being exposed to 1 mM methyl-β-cyclodextrin (MβCD) (a-e) , followed by 4 mg/mL soluble cholesterol (Chol MβCD) (f-j), and then once again with 1 mM methyl-β-cyclodextrin (MβCD) (k-o) depleting the patch of cholesterol. Yellow arrows indicate the position of pores formed during depletion, which heal and then reopen during the cycling of cholesterol extraction and doping into the membrane. Scale bars in (a-h) represent 50 µm.

Subsequent depletion of the healed lipid patch causes shrinkage in the patch area, characterised by the appearance of rough patch edges and the reappearance of pore defects, notably in the same regions where they initially appeared during the first depletion cycle (yellow arrow in Figure 6.9n). The reopening of previous pores suggests some form of scarring where initial pore defects existed, making such regions susceptible to future defect formation. A plausible explanation could be a preference for cholesterol to enrich specific areas. Pore edges are regions of high membrane curvature, and expose many local defects in the local lipid packing [394]. These defects are likely to make it easier for cholesterol to penetrate the membrane, hence becoming quickly enriched. The enrichment of these defect regions during

the period when cholesterol is being replenished would also render these areas more susceptible to subsequent depletion, as the increased local cholesterol mole fraction in these areas would also increase the ratio of cholesterol accessible to extraction [351,353,354].

Although the lipid patch integrity appeared to be fully restored (with pores and defects completely disappearing), some residual Rh-DPPE fluorophore remains in the L_o region. This suggests that the domain structure is only partially healed, with the overall process exhibiting some degree of residual Rh-DPPE remaining in the L_o phase. This effect seems accentuated when the domains are infused with cholesterol, as seen in Figure 6.9k.

This partial restoration of domain structure could have been due to shifts in lipid patch composition, due to the loss of DOPC and DPPC during exposure the to MβCD, which is able to extract PC lipids from membranes [60,367,368,382]. Unlike cholesterol, PC lipid loss would not be restored upon exposure to Chol-MβCD, permanently changing the initial DOPC/DPPC ratio and shifting the lipid composition left or right on the phase diagram (Figure 6.1g). A study using FRET and light scattering measurements to analyse lipid exchange and extraction via MβCD exposure demonstrated that DPPC had a greater resistance to solubilisation than DOPC [382]. This suggests that the lipid composition would tend to shift to the right with repeated MβCD exposure and could even shift the composition into the three-phase coexistence region.

To better investigate this hysteretic effect, a single miscible fluid phase was promoted by the addition of cholesterol (Figure 6.10a-f) and subsequently depleted of cholesterol (Figure 6.10g-i). Upon cholesterol depletion by MβCD, the initial domain structures and fluorescent partitioning is no longer restored. Instead, pores are formed uniformly across the patch with no apparent preference for regions that were initially in the L_o or L_d phase, as seen in Figure 6.2. Interestingly, area loss appears focused around the periphery of the lipid patch with the original patch perimeter remaining easily discernable after depletion (Figure 6.10i). According to Rahimi et al. this peripheral extraction is due to the lower adhesion of the newly spread regions of the lipid bilayer to the substrate [60].

As soluble cholesterol is added into the solution, it adheres to the glass substrate, mildly passivating the substrate surface. Hence, as the lipid bilayer is infused with cholesterol, the newly formed membrane spreads onto a layer of cholesterol water soluble, instead of on glass.

Taken together, these results provide insights into the depletion and healing of liquid-liquid coexisting membrane systems, and show how micron scale domain structures persist after cholesterol depletion and addition. Importantly, such behaviours hinge on the presence of substrate interactions, confirming that the substrate does not only locally modulate the movement of domains and coalescence, but also partially stabilises the domain structure when the cholesterol content is removed. From these experiments, a molecular mechanism can be proposed to explain the observed behaviour of supported phase-separated lipid patches. Initially, the lipid patch is stably supported on the substrate surface (Figure 6.11a). Once exposed to MβCD, cholesterol is depleted from the membrane causing area shrinkage and pore formation (Figure 6.11b). The depletion of cholesterol from the L_o regions could induce the formation of a gel mesh, perforated with local voids due to cholesterol depletion and the tight packing of the remaining saturated lipids. If present, the formation of small voids and pockets in the L_o region would cause a significant decrease in the lateral pressure at the phase boundary and provide space for the influx of species from the L_d phase to invaginate the remaining gel-mesh. It should be noted that this is likely concurrent with cholesterol depletion in the L_d phase. Although, in the L_d phase the effects of cholesterol depletion are more visible through the development of microscopic pores; the formation of which is likely facilitated by the phase's higher fluidity and deformability. The change in the structure of the cholesterol-depleted L_o regions leads to a redistribution of fluorescent probes (Figure 6.11c), most notably causing the migration of Rh-DPPE into L_o regions. This not only explains the penetration of Rh-DPPE into the previously L_o phase, but also the persisting fluidity of these regions after cholesterol depletion. Indeed, the idea of a gel mesh resonates with previously reported disordered solid states [395]; being a disrupted gel with a broken packing, unlike the regular tight packing commonly associated with gel phase. Such a state has been identified using techniques such as NMR spectroscopy [395] and AFM [74], with the resultant region displaying intermediate properties of the expected gel or

liquid-ordered phase. Alternatively, the depletion of cholesterol could result in the L_β phase being driven into a non-equilibrium state due to the reasonably rapid extraction of cholesterol not providing enough time for phase separation to fully advance, due to lipids eventually becoming kinetically trapped without previously L_o regions. This alternative was proposed by Aufderhorst-Roberts et al. [74], as it did not contradict their observations and those of broader literature, in that L_β phases are significantly disrupted by small alterations in cholesterol content. The formation of a non-equilibrium composition could also disrupt membrane packing interactions and hydrophobic interactions between rhodamine and the membrane; both of these factors have been demonstrated to strongly influence fluorophore phase selectivity [381].

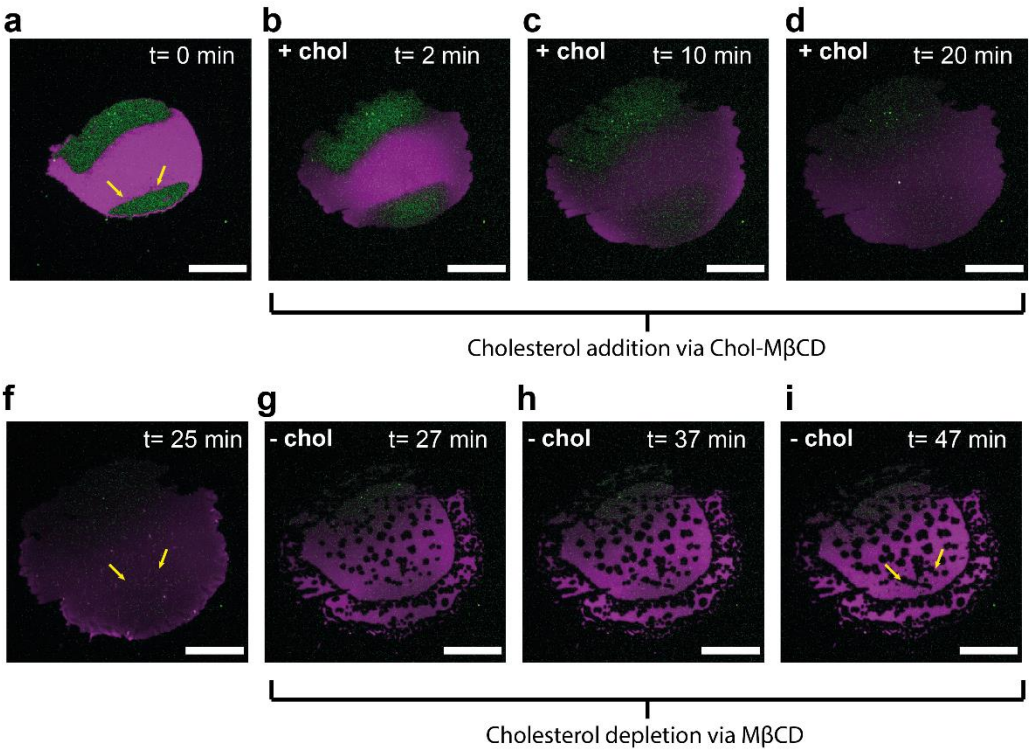

Figure 6.10: Effects of cholesterol depletion after phase separated lipid patches promoted into a single phase. Fluorescence micrographs of lipid bilayer patches composed of DOPC:DPPC:Cholesterol (40:40:20 mol%) doped with 0.1 mol% Rh-DPPE and 3 mol% NaP on hydrophilic glass substrate at different time intervals after the exposure to 4 mg/mL soluble cholesterol (Chol-MβCD) (a-d) promoting the patch into a single liquid phase. This is followed by subsequent exposure to 1 mM methyl-β-cyclodextrin (MβCD) (f-i), depleting the patch of cholesterol. Yellow arrows indicate the position of a liquid-ordered region (a) that has dissipated upon the addition of cholesterol (f) and does not return upon cholesterol extraction (i). Scale bars in (a-i) represent 50 µm.

The micron-scale size of the L_o domains formed by the fusion of phase separated lipid membranes is likely key to generating the disruption and recovery of the L_o/L_d

domain morphology upon cholesterol depletion, as the membrane cannot fully equilibrate across such macroscopic length scales due to local surface pinning [85]. The disruption of L_o/L_d domains by cholesterol depletion not only provides an insight into the behaviour of membranes under cholesterol modulation and how it impacts macroscale membrane responses, but also provides an insight into how the perturbation of substrate presence can have knock-on consequences and induce exotic membrane behaviours not accessible to free membranes.

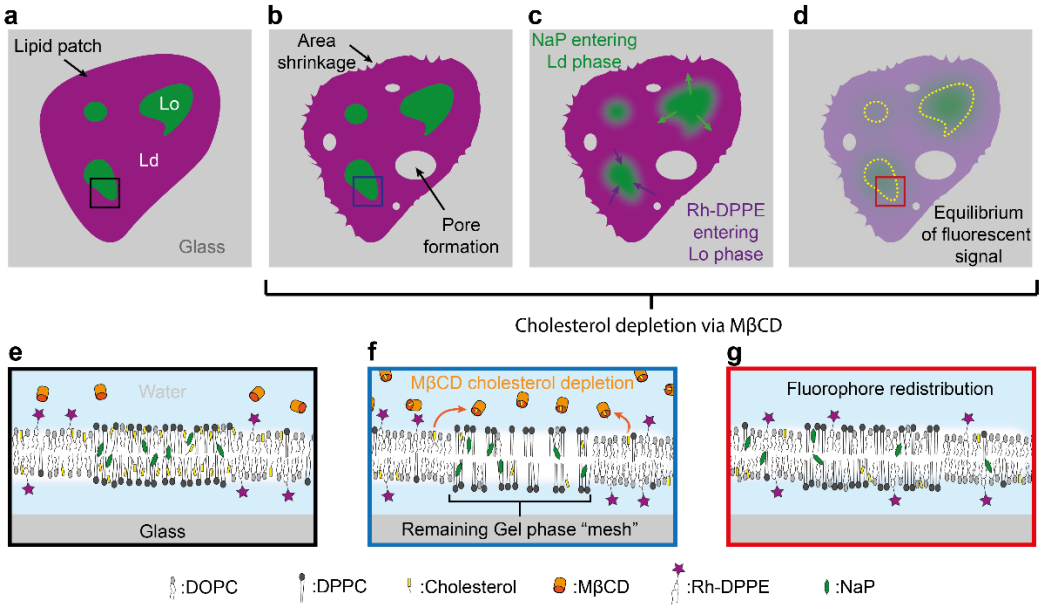

Figure 6.11: Change in patch morphology during cholesterol depletion. Illustrations of lipid bilayer patches composed of DOPC:DPPC:Cholesterol and doped with Rh-DPPE on a hydrophilic glass substrate at different time intervals after the exposure to methyl-β-cyclodextrin (MβCD). The change in patch area during cholesterol depletion of lipid patches with smaller segregated domains (a-d) and larger coalesced domains (e-g).

The stability of domain structures in lipid patches can be effectively disrupted by the promotion of a single miscible liquid phase through the addition of cholesterol into the lipid patches. The miscibility of different lipid phases can also increase by heating the lipid patches above the miscibility temperature. Such experiments, discussed in the following section, provide an alternative pathway to disrupting domain structure.

6.5.1 Preliminary investigations: Identifying sub-optical L_o/L_d domains formed by melting micron scale domain structure in lipid patches

The disruption of the lipid bilayer domain structure can also be induced by altering the temperature. The heating and cooling of the lipid membrane beyond the miscibility temperature causes significant lateral reorganisation in membrane structures. Substrate interactions are known to increase the miscibility temperature of supported lipid membranes in comparison to free-floating lipid systems [18,76,247]. The work of Gunderson et al. [86] demonstrated that phase-separated lipid patches formed on a glass substrate had a 5 ^{o} C increase in miscibility temperature compared to free-floating GUVs. Notably, if the lipid patches were not heated to sufficiently high temperatures, although domains lost contrast, the original domain patterns would reform on cooling. Patches that seemingly mixed thoroughly only partially regained the original domain structure upon cooling. This behaviour was postulated to be due to incomplete mixing of lipids in the leaflets and pinning of fractions of the lipid structure to the glass surface [86]. Such pinning was hypothesised to inhibit domain growth beyond the sub-optical length scale, causing them to effectively vanish in fluorescence microscopy images. To verify this hypothesis, lipid patches of DOPC/DPPC/Cholesterol (40:40:20 mol%), possessing micron scale L_o/L_d domains were imaged with both fluorescence microscopy and atomic force microscopy, before and after heat treatment. By raising the temperature of the samples to 40 ^{o}C, it was possible to go above the composition miscibility temperature (32 ^{o}C), whilst cooling back to 20 ^{o}C over 2 hours allowing the reformation of L_o/L_d domains.

The fusion of the phase separated lipid patches formed stable and distinct L_o/L_d domains, which could be easily visualised with fluorescence microscopy (Figure 6.12a) and atomic force microscopy (Figure 6.12b), exhibiting micron-scale domains in both. Similarly to the studies of Gunderson et al. [86], after heat treatment, much of the domain structure only partially recovered upon cooling, with many of the distinct domain structures no longer being resolvable with fluorescence microscopy (Figure 6.12c). When imaged with atomic force microscopy, it can be seen that liquid-ordered domains still exist within the lipid bilayer, even after heat treatment; although they are seemingly limited to a diameter of ~ 250 nm. The size of these

nanoscale domains approaches the diffraction limit of light, explaining why such domains appear to disappear with non-super resolution techniques.

The results depicted in Figure 6.12a-c are in line with reports found in the literature [85,118], which suggests that the substrate significantly inhibits coarsening beyond the nanometre scale, due to substrate roughness increasing membrane-substrate friction, local curvature and surface pinning. The measurements of Figure 6.12d-f confirm the proposed hypothesis of Gunderson et al. [86], that substrate interaction indeed inhibits the reformation of the original domain structure by impeding domain coarsening to sub-optical resolutions. The effects of passing through a miscibility phase transition on L_o/L_d domain structures are not completely reversible in supported lipid bilayers, in contrast to vesicles.

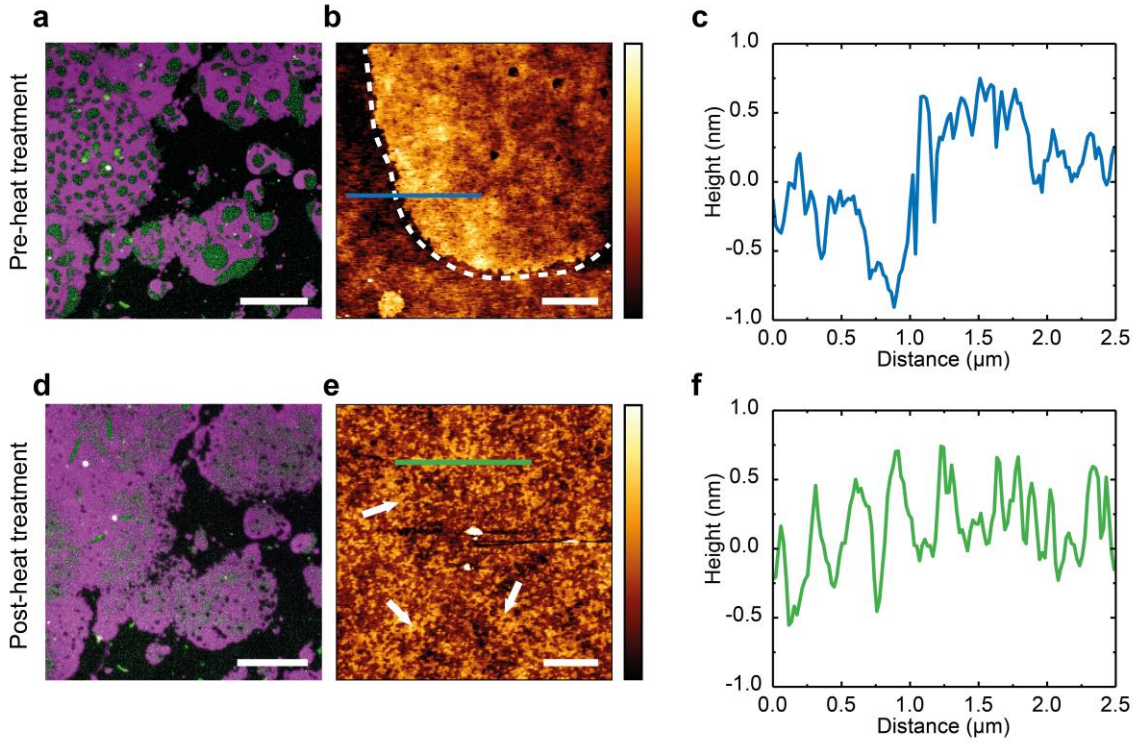

Figure 6.12: Disruption of liquid-ordered and disordered domain structure by heat treatment. Fluorescence micrographs and AFM scans of lipid bilayer patches composed of DOPC:DPPC:Cholesterol (40:40:20 mol%) doped with 0.1 mol% Rh-DPPE and with 3 mol% NaP on a hydrophilic glass substrate. Images (a,b) depict a phase-separated lipid patch before heat treatment, with accompanying line graph (c) from the line segment in AFM image, (b). Dotted white line in (b) shows outline of micron scale domain. Lipid patches from the same area imaged with fluorescence and AFM respectively (d,e) after heat treatment, with accompanying line graph (f) from the line segment in AFM image (e). White arrows in (e) indicate regions possessing nanoscale L_o domains. Scale bars in (a,d) represent 50 µm. Scale bars in (b,e) represent 500 nm, with a colour bar representing a range of 0 - 4 nm.

Interestingly, similarities can be drawn between the effects that miscibility phase transition and cholesterol modulation have on domain structure in supported lipid membranes. In both cases the substrate hinders domain movement, stabilising the shape and lateral distribution of micron scale domains, enabling them to be restored after cholesterol depletion, as shown above in Figure 6.9a-j, with the partial restoration of domain structure after a temperature cycle [86] .

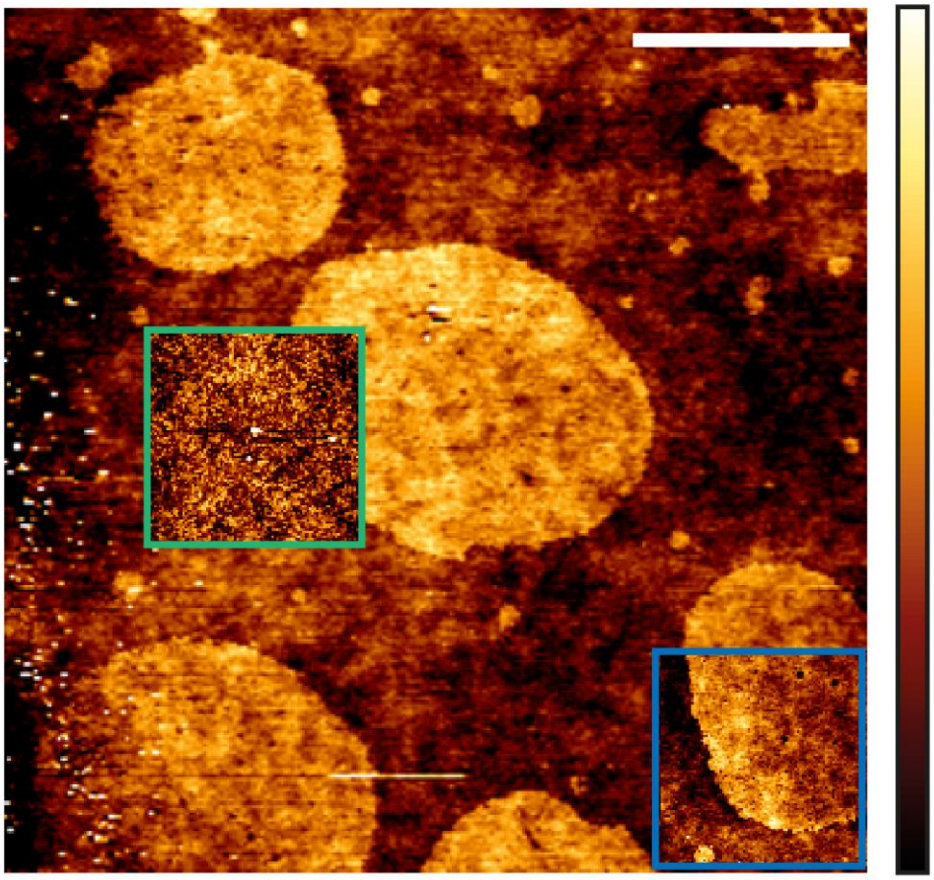

Figure 6.13: Image showing the relative positions of scans from Figure 6.12 (b,e). Scans most likely coincided within the 20 x 20 µm scan depicted here, indicating that previously large-scale phase separation of Figure 6.12b, shown in blue, has been replaced by non-optically resolvable domains of Figure 6.12e, shown in green. This figure simply shows the positions of the scans and that they are indeed from the same 20 μm^2 area that was previously inhabited by micron-sized L_o /L_d domain structures. Scale bar in the top right corner represents 5 µm and the colour bar represents a range of 0 - 2 nm.

Such reversible restructuring of un-coarsened domain patterns is absent in vesicle systems, in which liquid domains can freely move and coalesce to minimise their line tension. In both cases it seems that only the complete disruption of such structures by entering a single, miscible, fully homogenised liquid phase causes the utter disruption of L_o domains across micron length scales, thus prohibiting their

reformation and return to original domain patterns. These results indicate the persistence of a fraction of lipid structure, which can be exploited to reform domain structures after their partial disintegration.

6.5.2 Preliminary investigations: Using wrinkled substrates to investigate the influence of curvature on phase separation

An important factor in the lateral organisation of L_o/L_d domains of supported lipid bilayers is the local curvature of the substrate. The impact of substrate curvature on bilayer structure has been extensively investigated and characterised but tends to require bespoke substrate materials, which are often complex to synthesise. Many of the current experimental investigations utilise adhered nanoparticles [148,396,397], high-resolution surface etching [116,117,156] or preformed moulds; but such surface functionalisation techniques can be tricky to master and require various reagents. As eluded to earlier in Chapter 3.3, the wrinkled substrate surface can be easily made by controllably buckling the surface of PDMS, utilising the simple, cheap and effective protocols described in Chapter 2.4.1.

Additionally, wrinkled PDMS substrates can stably support lipid bilayers formed by vesicle fusion. Wrinkled PDMS substrates therefore offer a perfect support substrate for investigating the impact of curvature on the membrane structure. As part of a preliminary proof of concept, an example experiment using such wrinkled surfaces to supported phase separated lipid bilayers is discussed; demonstrating a facile method of creating curved surfaces to investigate their impact on membrane structure.

Figure 6.15 depicts a DOPC/DPPC (50:50 mol%) continuously supported lipid bilayer formed on a reasonably flat (Figure 6.14a) and wrinkled (Figure 6.14b) PDMS substrate. By heating the membranes to 60 ^{o}C, the bilayers were placed well above the composition miscibility temperature [398] and allowed to fully mix into a single miscible phase, before cooling to 20 ^{o}C over 4 hours; leaving a fully equilibrated supported lipid bilayer

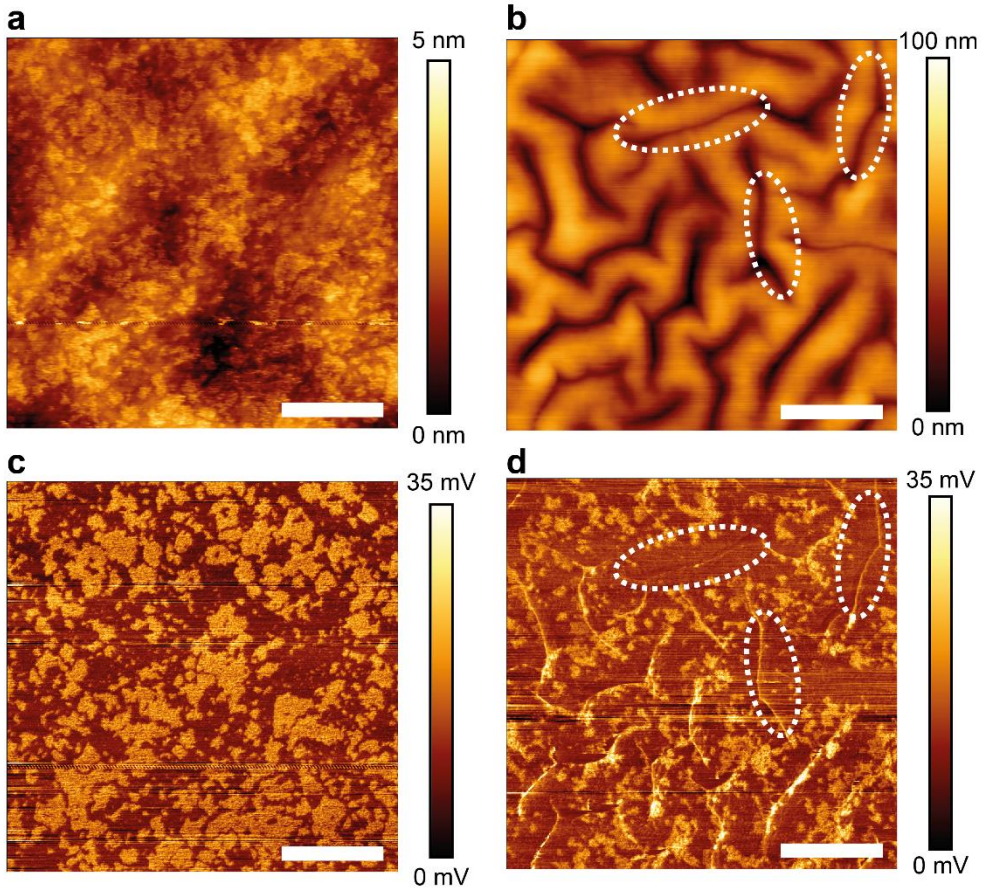

Figure 6.14: Impact of local curvature on gel domain formation. AFM images of continuously supported lipid bilayers composed of DOPC:DPPC (50:50 mol%) on PDMS substrate with a flat (a) and wrinkled (b) geometry. Below are accompanying lateral force microscopy images of the above lipid bilayers, emphasising the contrast between gel domains (bright regions) and liquid-disordered domains (dark region). Dotted white regions in (c,d) highlight the absence of liquid-ordered domains on folded regions. Scale bars in (a-d) represent 500 nm.

As the temperature is reduced, gel domains nucleate in the bilayer and can be easily distinguished as regions of increased height (~ 1.6 nm higher than the surrounding L_d phase) on the topographic images (Figure 6.14a). Although similar regions existed on the wrinkled substrate, they were obscured by the large height differences of the wrinkles. The poor imaging of these areas can be effectively corrected by processing AFM images with line flattening [399]; but alternatively, using the lateral force signal channel during imaging reveals the position of the L_β domains. As described in Chapter 2.6.3, this method of imaging is called lateral force microscopy and highlights differences in frictional interactions between the tip and the membrane. The stiffer gel domains cause more tip drag and create a contrast between the gel and liquid domains, allowing for their easy identification, as seen in Figure 6.14c with the brighter domains. Using this imaging method, lipid

domains could be easily located on the wrinkled topographies, and their noted absences from folded regions on the substrate surface (circled with white dotted lines of Figure 6.14b,d). These folds in the wrinkled substrate are regions of extreme curvature [301], hence are unfavourable regions for gel domain formation, due to them preferring flatter regions as a result of the higher bending rigidity of L_β domains [156,158].

Although preliminary, these results provide the initial steps to demonstrating how local substrate curvature of wrinkled PDMS substrates can be used to control the local membrane structure, favouring the formation of L_β domains in specified regions, effectively ordering membranes on the nanoscale.

6.6 Conclusion

The substrate's impact on supported lipid bilayers possessing L_o/L_d domains appears to go beyond increasing miscibility temperature and fixing domain movement. Cholesterol depletion of lipid patches containing L_o/L_d domains disrupts the partitioning behaviour of fluorescent dyes, while partially retaining domain structure. The addition of cholesterol into these systems can restore the original patch composition and distribution of lipid species.

The unexpected diffusion of Rh-DPPE from the L_d phase into the coexisting L_o phase after cholesterol depletion could have potential consequences for fluorescence microscopy studies utilising phase-separated supported lipid bilayers; especially considering that the interpretation of many fluorescence microscopy measurements relies on the preferential partitioning of fluorophores to identify lipid phases. Additionally, the observed effects were suggested to be due to the depletion of cholesterol, and not specific interactions with MβCD. However, lipid patches containing a high proportion of saturated lipids appeared to possess an increased resistance to cholesterol depletion (corroborating with previous literature), leading to the process occurring over longer timescales compared to unsaturated systems.

Phase separated supported lipid patches provide a unique model system that facilitates the investigation into how membrane species partitioning can dynamically

modulate with composition; all within a system affixed to a planar surface accessible to a variety of techniques. Also, such properties may be utilised by supporting structures in biology, with supporting substrates stabilising the lateral organisation of biomembranes without removing local fluidity.

Chapter 7: Conclusions and Future Outlook

This thesis explores the interplay between substrate surface properties and the behaviour of SLBs, and in particular, how surface properties such as roughness and hydrophilicity can be used to control and modified the SLB's behaviour. Commonly utilised substrates such as mica, glass and PDMS were demonstrated to impact the morphology, dynamics and composition of supported lipid bilayers formed by vesicle fusion, depending on the substrate's innate interfacial properties or its surface modification. The techniques of surface modification used in this thesis relied on simple and straightforward protocols, ensuring they could be easily applied to future studies that build on the presented work. Several distinct studies are presented in this thesis, detailing the impacts of the substrates interfacial properties on SLB behaviour, including changes in membrane formation, dynamics, morphology and composition. All of these results build on the same overarching strategy and highlight that appropriate consideration of substrate interactions is needed to understand and exploit SLB behaviour for biophysical investigations and to develop novel biointerfaces. To further expand on this global vision, the main results of the thesis and their implications are discussed together in the next section.

7.1 Thesis Summary

The ability to control and utilise membrane-substrate interactions is becoming prevalent in multiple fields of research and development. As briefly reviewed and discussed in Chapter 1, membrane-substrate interactions not only have important implications in developing our understanding of membrane behaviour in biological systems (for example the roles interfaces such as the cytoskeleton and extracellular matrix play in cellular response), but also in the future development of biotechnological interfaces; vital for technologies such as organ-on-chip devices.

Probing the impacts that substrate interactions have on the behaviour and morphology of supported biomembranes is difficult due to the wide range of length and time scales of the interactions at play. To help tackle this issue, Chapter 2 introduces a convenient minimal model system, SLBs, to explore the impact that

substrates have on the adhered membrane behaviour. Several techniques, namely AFM and epifluorescence microscopy, are used to investigate the extensive range of length and time scales required to characterise the substrates interfacial properties and their influence on SLB behaviour.

In Chapter 3, various means of PDMS substrate modification based on air plasma-treatment are demonstrated to control surface hydrophobicity, topography and response to mechanical stresses. Each described system can readily support lipid bilayers and was exploited in the investigations of later chapters; exemplifying the versatility of PDMS materials in the formation of functional biointerfaces, while exploring the consequences of described interfacial properties of functionalised PDMS on model membrane systems. Additionally, the outcomes of the studies presented in Chapter 3 highlighted the importance of full plasma-oxidation treatment of PDMS. A partial plasma-oxidation treatment of PDMS is shown to lead to significant differences in substrate hydrophilicity and roughness, compared to a fully plasma-treated PDMS substrate. SLBs readily form on both types of PDMS substrate when using GUV fusion, but their subsequent behaviour is very different, with partially plasma-treated PDMS later shown to induce the specific depletion of cholesterol from the SLBs. Without proper consideration, surface treatment can have unexpected effects with drastic consequences on the properties and behaviour of adhered membranes, such as those detailed in Chapters 4, 5 and 6 utilising partially plasma-treated PDMS.

Discussions in Chapter 3 also detailed techniques that are readily exploitable for future investigations exploring the effect of more exotic topographies on membrane behaviour; notably the impact of nanoscale wrinkles formed with PDMS. Although these techniques have been previously documented and discussed in the literature (especially in the work of Cabral et al. [299,300]), Chapter 3 highlights the chemical changes to the PDMS surface that accompany better understood topographical ones; these effects should not be overlooked. Additionally, the identification of nano-cracks on the surface of plasma-treated PDMS after stretching could have important implications for the use of these materials in flexible electronics and cell stretching devices; especially in conjunction with the work on specific cholesterol depletion effects covered in Chapter 5. PDMS substrates can be easily modified and adapted using simple techniques, with issues often considered caveats (such

as surface wrinkling, nanoscale cracking, and hydrophobic recovery) that can be beneficially employed in the development of new biotechnologies when applied with appropriate consideration.

The PDMS substrates developed in Chapter 3 are put to use in the investigations of subsequent chapters. In Chapter 4, it is shown that lipid patches formed by vesicle fusion on common substrates such as mica, glass and PDMS are not stable immediately after fusion. Clear changes in membrane structure, such as a "mottled" pattern in lipid patch fluorescence and the formation of lipid protrusions indicate significant membrane reorganisation after vesicle fusion has completed. The reorganisation of the membrane can even exist for extended periods of time, depending on lipid composition and interfacial properties such as substrate hydrophilicity. Interestingly, the mottling pattern observed immediately after vesicle fusion could be employed as a crude indicator of substrate hydrophilicity, with the effect visibly absent for lipid patches formed on partially hydrophilic surfaces. The mottling patterns and the formation of lipid protrusions discussed in Chapter 4 are still not fully understood. The most likely possibility is that they originate from a combination of membrane-substrate friction experienced during vesicle fusion inducing inhomogeneities in lipid density [336,337], and the incompressibility of the lipid bilayer during the rapid fusion process [56]. However, a definite answer as to the reasons behind these morphological changes, especially the fluctuation in patch area after vesicle fusion, remains to be obtained. The results of Chapter 4 clearly indicate that lipid patches are not fully equilibrated after vesicle fusion and, consequently, could impact on the subsequent membrane behaviour. These studies are relevant to the formation and use of lipid patches in biophysical investigation, especially considering the fact that lipid patches are an experimental tool that is growing in popularity [311]. This could have important consequence on how lipid patches are utilised, for example in bilayer-protein interaction studies. Indeed, although the current literature has already demonstrated that changes in substrate roughness, membrane tension and surface interactions during lipid patch formation can alter the pathways of SLB formation [108,110,111] and lipid distribution within the leaflets [110], the impact such differences have on subsequent protein-bilayer interactions remains unclear. For example, a recent study utilised lipid patches formed on flexible PDMS substrates to investigate the role of membrane

tension on the efficiency of incorporated fusion proteins syntaxin 1, synaptobrevin and SNAP 25 [318]; but the study made scarce mention of the substrate's impact on observed behaviours. In light of the results of Chapter 4, knowledge of the substrate's influence could alter how the results of this work are interpreted, as tension in lipid patches, and subsequently imposed on the proteins, is possibly not fully equilibrated after membrane fusion. Although the investigations of Chapter 4 are preliminary, the results presented provide novel insights into lipid membrane reorganisation after vesicle fusion by addressing a time frame overlooked by most experimental studies.

In Chapter 5, it is shown that plasma-modified PDMS substrates can specifically extract cholesterol directly from the adjacent supported lipid bilayer through simple physical contact. Importantly, PDMS substrates can leach small hydrophobic molecules directly out of an adhered lipid membrane, while leaving other membrane components stably supported; thereby significantly altering the supported biomembrane's composition and biophysical properties. A comprehensive review of the literature indicates this to be the first reported case where the composition of an adhered biomembrane is altered through membrane-substrate interactions. Previous reports have detailed the loss of small hydrophobic molecules from the surrounding solution, but not specifically at the membrane-substrate interface [265]. This finding has significant consequences for our understanding of the impact that PDMS materials have on bioassays and cell culture studies, as not only the incubation fluid but the biomembrane composition could be directly altered by the PDMS interface. A model describing the depletion of cholesterol from supported membranes derived by Litz et al. [199] was appropriately adapted to the present experimental data, relating the changes in lipid patch area fraction to the changing cholesterol mole fraction in lipid patches. It should be noted that the experimental observations of Litz et al. [199] were obtained with DOPC lipid patches exposed to the well-known MβCD cholesterol extraction method. In this thesis, the results of Litz et al. could be reasonably reproduced using the PDMS substrate-based cholesterol extraction method. The successful application of this model in Chapter 5 corroborates the growing evidence that two populations of cholesterol exist within lipid membranes, one being more accessible to depletion than the other. It is worth mentioning that an interesting parallel can be drawn between the MβCD and PDMS

cholesterol extraction methods: the MβCD molecules possess a hydrophilic surface and a sub-nanoscale hydrophobic cavity that can selectively remove cholesterol from bilayers. In this thesis, the experimental results suggest that similar features may exist on partially plasma-treated PDMS substrates with nanoscale hydrophobic and hydrophilic regions at the substrate interfaces potentially causing the depletion of cholesterol from adhered SLBs. Such combination of surface properties may go some way to explaining the poorly understood mechanisms utilised by nanoparticles and designed nanomaterials [138,400], HIV [36,37,401], and the surface of peptides [402,403] to disrupt and penetrate membranes with ease. The findings of Chapter 5 have hence significant implications not only for biotechnological developments relying on polymeric materials, but also to further our understanding of the impact supporting substrates have on biological materials; cells might utilise such mechanisms to modify biomembrane composition and behaviour.

Finally, Chapter 6 builds on the findings of Chapter 5 and exploits the unique properties of partially plasma-treated PDMS to investigate the effect of substrate-led cholesterol depletion on the phase behaviour of SLBs. Supported phase separated lipid bilayers were depleted of cholesterol, revealing how being adhered to a substrate influences transformations in L_o/L_d domain structure and morphology as the system's composition is altered. This unexpectedly resulted in the disruption of the partitioning behaviour of fluorescent dyes, while partially retaining domain structure. Upon cholesterol depletion, Rh-DPPE was able to penetrate the L_o region from which the fluorophore is usually strongly excluded. Upon the reinsertion of cholesterol into these systems, fluorescence partitioning was restored, and pore defects healed. This demonstrated that lipid patch composition, domain structure and lateral organisation could be recovered after cholesterol's extraction. Such effects are not clearly present in vesicle systems due to the domains being freely able to coarsen and coalesce over micron length scales. The results described in Chapter 6 hence also have wider implications regarding how the preferential partitioning of membrane species can be disrupted in supported lipid bilayer systems. The work demonstrates that shifts in membrane composition can drastically redistribute membrane species between domain structures, and likely facilitate the formation of non-equilibrium structures in supported lipid bilayers.

The development of micro/nanoengineered functional biomaterials facilitates the characterisation, manipulation and recreation of dynamical cell-microenvironments at cellular (micrometre) and subcellular (nanometre) length scales [404]. However, such development requires a great deal of consideration for the interfacial properties of the substrate materials, as they can significantly perturb the system's behaviour. The work of this thesis contributes to the development of such functional biomaterials by furthering current understanding of the substrate influence on SLB behaviour and presenting methods by which the interfacial properties of substrates can be used to manipulate model SLBs' morphology and behaviour. Notably, materials like PDMS are emerging as a popular platform for developing 3D tissue models and organ-on-chip devices. Indeed, many recent organ-on-chip studies have utilised PDMS as a base substrate to create, for example, patterned substrates that promote differentiation of stem cells [405], mechanically active "lung-on-a-chip" devices that simulate the stresses of breathing motions on supported lung cells and tissues [176], and the construction of complex multi-shaped, flexible scaffolding to host 3D tissue models [406]. The results presented in this thesis therefore add novel insights that will help guide the functionalisation of PDMS substrates and interpretation of results from SLB systems using PDMS as a substrate. The understanding of the nanoscale properties of substrate materials will also likely be key to the development of other novel biotechnological interfaces, by acting as a well-understood reference point. Overall, the work of this thesis contributes to these efforts by detailing and characterising simple and effective methods for manipulating substrate interactions to better exploit biological interfaces for scientific investigations utilising SLBs, as well as for developing new functional biointerfaces.

7.2 Outlook and Further Work

The work conducted in this thesis opens many possibilities for further studies, developments and novel research avenues. Some of the preliminary results in the thesis also merit further investigation. Presented here are several unresolved questions and proposed investigations, the exploration of which would complement the discussions of this thesis.

Further characterisation of partially plasma-treated PDMS

The partial plasma-treatment of PDMS substrates described in this thesis could be obtained and reproduced consistently (along with its influence on adhered membrane behaviour). However, the exact changes it induced in the PDMS surface chemistry was not accurately measured. Detailed knowledge of the silica-like surface layer's composition and distribution across the surface remains unclear, but likely key to achieving a full understanding of the impact of the functionalised substrate on the SLBs behaviour. This could be achieved using techniques such as X-ray photoelectron spectroscopy (XPS) which would provide more detailed information about changes in the chemical composition of PDMS during plasma-treatment. Current instruments can reach a lateral resolution below 10 nm [407], highly relevant here to identify the presence of a gradual chemical variation or discrete, patchy surface of hydrophilic/hydrophobic domains on the partially plasma-treated PDMS surface.

Alternatives to partially plasma-treated PDMS

Given the difficulty in fully controlling and understanding the chemical details of partially plasma-treated PDMS, it would be highly beneficial to recreate the effects demonstrated in Chapter 5 using materials other than PDMS. This would be useful both to expand research possibilities and to provide a point of comparison for PDMS experiments, thereby furthering our understanding of the PDMS ability to modulate the SLB's properties and behaviour. Hence, further investigations to recreate a partially hydrophilic surface using a more controlled means of surface functionalisation would be of significant interest. One example could be the deposition of thin, nanoscale hydrophobic features onto a porous hydrophilic surface, in an attempt to recreate the effects demonstrated with partially plasma-treated PDMS. Practically this could be achieved using hydrophobic flakes of graphene deposited onto a hydrophilic film of polyacrylamide (PAA) supported on glass. Such investigations would also help verify if there is a generality to behaviour described in Chapter 5, with polymeric substrates exhibiting partially hydrophilic interfaces being able to specifically deplete lipid species while leaving other membrane components stably supported. If successful, such measurements would stimulate and help guide further studies relying on surface hydrophilicity and

patterning in the specific extraction of molecules from lipid membranes without loss of overall membrane integrity.

Impact of osmotic stresses on lipid patch reorganisation in the absence of ionic effects

The preliminary experiments detailed in Chapter 4.4 rely on osmotic shocks to test whether the initial tension in the lipid vesicles has had an effect on the area instabilities observed following vesicle fusion. Although the results show a possible relationship between the two factors, a definitive conclusion could not be drawn because the influence of ionic effects was not accounted for. Changes in the NaCl concentration of the buffer solutions for osmotic shocking affected the ionic strength conditions between experiments, which could have an impact on vesicle adhesion, and subsequent rupture mechanics [142,243,333]. Further experiments using non-ionic sucrose to effectively modify osmotic stress in vesicles [108] could help clarify the issue and verify the link between the osmotic tension in vesicles and the area instabilities observed in lipid patches after fusion.

Precise identification of critical cholesterol mole fractions

The observation of a marked increase in cholesterol depletion above a 0.4 cholesterol mole fraction supports the current idea of a non-random organisation of cholesterol within the membrane and the presence of critical cholesterol mole fractions, at which sharp changes in membrane behaviour occur. Confirmation of such non-random organisation of cholesterol within membranes would be a significant step forward in our understanding of membrane structure and the role it plays in overall membrane dynamics and function. Indeed, cholesterol's organisation within bilayers not only facilitates lateral organisation of the membrane, but dictates its chemical activity [408,409], cholesterol solubility [351,410] and various membrane properties including thickness, bending rigidity and tail chain ordering [57,77,323,327,351]. A better understanding of cholesterol organisation within membranes would improve characterisation and predictions of the membrane behaviour. It would also help clarify the role of cholesterol in the formation and stabilisation of the more contentious lipid rafts. Experiments discussed in Chapter 5 provided a small contribution to this work, with indications of critical cholesterol mole fractions being

present in lipid patches losing cholesterol. This was achieved using a novel experimental approach for cholesterol depletion from SLBs.

Further investigation using a more extensive range of cholesterol mole fractions to precisely identify critical mole fractions would complement this work and provide a more comprehensive picture of the hypothesised two cholesterol populations. Additionally, investigations using a wider variety of sterols and lipids species to characterise the specificity of substrate-induced sterol depletion may be conducted. Such investigations could reveal whether the specificity regarding cholesterols depletion in lipid membranes is linked to the molecule's hydrophobicity, steric properties, presence of specific chemical groups, as well as the chemical structure of the surrounding lipid species.

Temperature controlled measurements of ternary lipid mixtures

Chapter 6 focuses on the effects relating changes in the lipid patch composition to the membrane phase behaviour. Quantitative measurements relating these two properties are however still sparse, with much room for additional data points. An obvious way forward would be a systematic approach to gather a more comprehensive analysis of the changes in the lipid patch phases behaviour during cholesterol depletion, hence allowing a more detailed and complete understanding of the link. One possibility would be to extend the investigations by using a temperature-controlled stage during epifluorescence measurements. This would allow the measurement of lipid patch miscibility temperature, including how this temperature is altered during cholesterol depletion. Importantly, it would help quantify the impact the Rh-DPPE redistribution can have on the membrane phase behaviour, particularly if the infusion of Rh-DPPE significantly changes the miscibility temperature of L_o regions due to its bulky steric groups disrupting tail chain packing and local lipid order.

Impact of substrate interactions on fluorophore and biomolecule partitioning in membranes

In general, the work of Chapter 6 while still open for improvement, provides thought-provoking results with respect to our current understanding of the changes in the partitioning properties of fluorophores (and possibly other membrane species) in SLBs undergoing compositional changes. An extension to these investigations

would expand on the selection of fluorophores used to label lipid patches. Utilising a range of fluorophores with various chemical structures and properties, a more comprehensive understanding and characterisation of the impact of substrate interactions influence fluorophore partitioning behaviour during a disruption in composition could be acquired. For example, more hydrophilic fluorophores such as fluorescein would provide a comparison of how fluorophore hydrophilicity impact the behaviour observed in Chapter 6. Such studies would complement the work of Bordovsky et al. [381], where hydrophobic interactions between fluorophores and the membrane were demonstrated to strongly influence partitioning selectivity.

There are numerous membranes biomolecules that are known to be excluded from the L_o phase in liquid-liquid coexisting systems; for example, human caveolin-3 and peripheral myelin protein-22 are known to preferentially partition into more ordered regions of lipid membranes [411]. Both of these proteins are directly related to several disorders including Alzheimer's disease [412] and Charcot-Marie-Tooth disease [413]. Therefore understanding why they have a preference for locating in more ordered regions of the membrane may illuminate the role of these proteins in the disease mechanisms and pathology. As highlighted in Chapter 6, the presence of a substrate can modify the partitioning behaviour of membrane-bound species. A PDMS substrate could provide a minimal model system for investigation on how protein-cytoskeletal interactions influence the partitioning of human caveolin-3 and peripheral myelin protein-22, and its implications on the development of subsequent pathologies. Although preliminary, repeating the investigations of Chapter 6 with these proteins could help elucidate how the segregation of these species can be manipulated through substrate interactions. More importantly, further understanding of how to disrupt the localisation of these proteins into more ordered regions of the membrane may inform the development of novel therapeutics.

Bibliography

1. Castellana, E. T. & Cremer, P. S. Solid supported lipid bilayers: From biophysical studies to sensor design. *Surf. Sci. Rep.* **61**, 429–444 (2006).
2. Tero, R. Substrate effects on the formation process, structure and physicochemical properties of supported lipid bilayers. *Materials (Basel).* **5**, 2658–2680 (2012).
3. Mazur, F., Bally, M., Städler, B. & Chandrawati, R. Liposomes and lipid bilayers in biosensors. *Adv. Colloid Interface Sci.* **249**, 88–99 (2017).
4. Szostak, J. W., Bartel, D. P. & Luisi, P. L. Synthesizing life. *Nature* **409**, 387–90 (2001).
5. Deamer, D. W. Origins of life: How leaky were primitive cells? *Nature* **454**, 37–8 (2008).
6. Thiam, A. R., Farese Jr, R. V. & Walther, T. C. The biophysics and cell biology of lipid droplets. *Nat. Rev. Mol. Cell Biol.* **14**, 775–786 (2013).
7. Welte, M. A. Expanding Roles for Lipid Droplets. *Curr. Biol.* **25**, 470–481 (2015).
8. Simons, K. & Toomre, D. Lipid rafts and signal transduction. *Nat. Rev. Mol. Cell Biol.* **1**, 31–39 (2000).
9. van Meer, G., Voelker, D. R. & Feigenson, G. W. Membrane lipids: where they are and how they behave. *Nat. Rev. Mol. Cell Biol.* **9**, 112–124 (2008).
10. Singer, S. J. & Nicolson, G. L. The fluid mosaic model of the structure of cell membranes. *Science* **175**, 720–31 (1972).
11. Lingwood, D. & Simons, K. Lipid Rafts As a Membrane-Organizing Principle. *Science* **327**, 46–50 (2010).
12. Yetukuri, L., Ekroos, K., Vidal-Puig, A. & Orešič, M. Informatics and computational strategies for the study of lipids. *Biochim. Biophys. Acta - Mol. Cell Biol. Lipids* **1811**, 991–999 (2011).
13. Sud, M. *et al.* LMSD: LIPID MAPS structure database. *Nucleic Acids Res.* **35**, D527-32 (2007).
14. Bogdanov, M., Sun, J., Kaback, H. R. & Dowhan, W. A phospholipid acts as a chaperone in assembly of a membrane transport protein. *J. Biol. Chem.* **271**, 11615–8 (1996).
15. Dowhan, W. MOLECULAR BASIS FOR MEMBRANE PHOSPHOLIPID DIVERSITY:Why Are There So Many Lipids? *Annu. Rev. Biochem.* **66**, 199–232 (1997).
16. Honerkamp-Smith, A. R., Veatch, S. L. & Keller, S. L. An introduction to critical points for biophysicists; observations of compositional heterogeneity in lipid membranes. *Biochim. Biophys. Acta* **1788**, 53–63 (2009).

17. Machta, B. B., Papanikolaou, S., Sethna, J. P. & Veatch, S. L. Minimal Model of Plasma Membrane Heterogeneity Requires Coupling Cortical Actin to Criticality. *Biophys. J.* **100**, 1668–1677 (2011).

18. Connell, S. D., Heath, G., Olmsted, P. D. & Kisil, A. Critical point fluctuations in supported lipid membranes. *Faraday Discuss.* **161**, 91–111; discussion 113-150 (2013).

19. Veatch, S. L. *et al.* Critical Fluctuations in Plasma Membrane Vesicles. *ACS Chem. Biol.* **3**, 287–293 (2008).

20. Simons, K. & Van Meer, G. Lipid sorting in epithelial cells. *Biochemistry* **27**, 6197–6202 (1988).

21. Brown, D. A. Lipid Rafts, Detergent-Resistant Membranes, and Raft Targeting Signals. *Physiology* **21**, 430–439 (2006).

22. Owen, D. M., Magenau, A., Majumdar, A. & Gaus, K. Imaging Membrane Lipid Order in Whole, Living Vertebrate Organisms. *Biophys. J.* **99**, L7–L9 (2010).

23. Gaus, K., Zech, T. & Harder, T. Visualizing membrane microdomains by Laurdan 2-photon microscopy (Review). *Mol. Membr. Biol.* **23**, 41–48 (2006).

24. Gaus, K. *et al.* Visualizing lipid structure and raft domains in living cells with two-photon microscopy. *Proc. Natl. Acad. Sci.* **100**, 15554–15559 (2003).

25. Edidin, M. The State of Lipid Rafts: From Model Membranes to Cells. *Annu. Rev. Biophys. Biomol. Struct.* **32**, 257–283 (2003).

26. Kenworthy, A. K. & Edidin, M. Distribution of a glycosylphosphatidylinositol-anchored protein at the apical surface of MDCK cells examined at a resolution of. *J. Cell Biol.* **142**, 69–84 (1998).

27. Carquin, M. *et al.* Recent progress on lipid lateral heterogeneity in plasma membranes: from rafts to submicrometric domains. *Prog. Lipid Res.* **62**, 1–24 (2015).

28. Mayor, S. & Rao, M. Rafts: Scale-Dependent, Active Lipid Organization at the Cell Surface. *Traffic* **5**, 231–240 (2004).

29. Gumí-Audenis, B. *et al.* Structure and Nanomechanics of Model Membranes by Atomic Force Microscopy and Spectroscopy: Insights into the Role of Cholesterol and Sphingolipids. *Membranes (Basel).* **6**, (2016).

30. Chiantia, S., Kahya, N. & Schwille, P. Raft Domain Reorganization Driven by Short- and Long-Chain Ceramide: A Combined AFM and FCS Study. *Langmuir* **23**, 7659–7665 (2007).

31. Brender, J. R., McHenry, A. J. & Ramamoorthy, A. Does cholesterol play a role in the bacterial selectivity of antimicrobial peptides? *Front. Immunol.* **3**, 195 (2012).

32. Losada-Pérez, P. *et al.* Melittin disruption of raft and non-raft-forming biomimetic membranes: A study by quartz crystal microbalance with dissipation monitoring. *Colloids Surfaces B Biointerfaces* **123**, 938–944 (2014).

33. Tsukamoto, M., Kuroda, K., Ramamoorthy, A. & Yasuhara, K. Modulation of raft domains in a lipid bilayer by boundary-active curcumin. *Chem. Commun.* **50**, 3427 (2014).

34. Kato, A. *et al.* Phase Separation on a Phospholipid Membrane Inducing a Characteristic Localization of DNA Accompanied by Its Structural Transition. *J. Phys. Chem. Lett.* **1**, 3391–3395 (2010).

35. Itzhaki, R. & Wozniak, M. Herpes simplex virus type 1, apolipoprotein E, and cholesterol: A dangerous liaison in Alzheimer's disease and other disorders. *Prog. Lipid Res.* **45**, 73–90 (2006).

36. Hardy, G. J. *et al.* HIV-1 antibodies and vaccine antigen selectively interact with lipid domains. *Biochim. Biophys. Acta - Biomembr.* **1838**, 2662–2669 (2014).

37. Schwarzer, R. *et al.* The cholesterol-binding motif of the HIV-1 glycoprotein gp41 regulates lateral sorting and oligomerization. *Cell. Microbiol.* **16**, 1565–1581 (2014).

38. Simons, K. & Ehehalt, R. Cholesterol, lipid rafts, and disease. *J. Clin. Invest.* **110**, 597–603 (2002).

39. Zimina, E. & Bruckner-Tuderman, L. Lipid Rafts and Bullous Diseases. *Open Dermatol. J.* **3**, 173–177 (2009).

40. Rios, F. J. O. *et al.* Uptake of oxLDL and IL-10 Production by Macrophages Requires PAFR and CD36 Recruitment into the Same Lipid Rafts. *PLoS One* **8**, e76893 (2013).

41. Allan Butterfield, D. Amyloid β-peptide (1-42)-induced Oxidative Stress and Neurotoxicity: Implications for Neurodegeneration in Alzheimer's Disease Brain. A Review. *Free Radic. Res.* **36**, 1307–1313 (2002).

42. Mizuno, T. *et al.* Cholesterol-dependent generation of a seeding amyloid beta-protein in cell culture. *J. Biol. Chem.* **274**, 15110–15114 (1999).

43. Gaus, K., Chklovskaia, E., Fazekas de St Groth, B., Jessup, W. & Harder, T. Condensation of the plasma membrane at the site of T lymphocyte activation. *J. Cell Biol.* **171**, 121–31 (2005).

44. Schörken, U. & Kempers, P. Lipid biotechnology: Industrially relevant production processes. *Eur. J. Lipid Sci. Technol.* **111**, 627–645 (2009).

45. Marsh, D. *Handbook of Lipid Bilayers*. (CRC Press, 2013).

46. Israelachvili, J. N. Intermolecular and Surface Forces. in *Intermolecular and Surface Forces* (Elsevier, 2011).

47. Dzieciol, A. J. & Mann, S. Designs for life: protocell models in the laboratory. *Chem. Soc. Rev.* **41**, 79–85 (2012).

48. Chen, I. A. & Walde, P. From self-assembled vesicles to protocells. *Cold Spring Harb. Perspect. Biol.* **2**, a002170 (2010).

49. Armstrong, R. Designing with protocells: applications of a novel technical platform. *Life (Basel, Switzerland)* **4**, 457–90 (2014).

50. Ma, W. & Feng, Y. Protocells: at the interface of life and non-life. *Life (Basel, Switzerland)* **5**, 447–58 (2015).

51. Sakuma, Y. & Imai, M. From vesicles to protocells: the roles of amphiphilic molecules. *Life (Basel, Switzerland)* **5**, 651–75 (2015).

52. Deamer, D., Dworkin, J. P., Sandford, S. A., Bernstein, M. P. & Allamandola, L. J. The first cell membranes. *Astrobiology* **2**, 371–381 (2002).

53. Frolov, V. A., Shnyrova, A. V & Zimmerberg, J. Lipid polymorphisms and membrane shape. *Cold Spring Harb. Perspect. Biol.* **3**, a004747 (2011).

54. Berg, J. M., Tymoczko, J. L. & Stryer, L. Fatty Acids Are Key Constituents of Lipids. (2002).

55. Kollmitzer, B., Heftberger, P., Rappolt, M. & Pabst, G. Monolayer spontaneous curvature of raft-forming membrane lipids. *Soft Matter* **9**, 10877 (2013).

56. Staykova, M., Arroyo, M., Rahimi, M. & Stone, H. A. Confined Bilayers Passively Regulate Shape and Stress. *Phys. Rev. Lett.* **110**, 028101 (2013).

57. Pan, J., Tristram-Nagle, S. & Nagle, J. F. Effect of cholesterol on structural and mechanical properties of membranes depends on lipid chain saturation. *Phys. Rev. E. Stat. Nonlin. Soft Matter Phys.* **80**, 021931 (2009).

58. Byfield, F. J., Aranda-Espinoza, H., Romanenko, V. G., Rothblat, G. H. & Levitan, I. Cholesterol Depletion Increases Membrane Stiffness of Aortic Endothelial Cells. *Biophys. J.* **87**, 3336–3343 (2004).

59. Veatch, S. L. & Keller, S. L. Separation of liquid phases in giant vesicles of ternary mixtures of phospholipids and cholesterol. *Biophys. J.* **85**, 3074–3083 (2003).

60. Rahimi, M. *et al.* Shape Transformations of Lipid Bilayers Following Rapid Cholesterol Uptake. *Biophys. J.* **111**, 2651–2657 (2016).

61. Ryu, Y.-S. *et al.* Reconstituting ring-rafts in bud-mimicking topography of model membranes. *Nat. Commun.* **5**, 4507 (2014).

62. Hafez, I. M. & Cullis, P. R. Roles of lipid polymorphism in intracellular delivery. *Adv. Drug Deliv. Rev.* **47**, 139–148 (2001).

63. Müller, R. H., Mäder, K. & Gohla, S. Solid lipid nanoparticles (SLN) for controlled drug delivery – a review of the state of the art. *Eur. J. Pharm. Biopharm.* **50**, 161–177 (2000).

64. Bender, J. *et al.* Lipid cubic phases for improved topical drug delivery in photodynamic therapy. *J. Control. Release* **106**, 350–360 (2005).

65. Madene, A., Jacquot, M., Scher, J. & Desobry, S. Flavour encapsulation and controlled release - a review. *Int. J. Food Sci. Technol.* **41**, 1–21 (2006).

66. Silvius, J. R. Thermotropic phase transitions of pure lipids in model membranes and their modifications by membrane proteins. *Lipid-protein Interact.* **2**, 239–281 (1982).

67. Jacobson, K. & Papahadjopoulos, D. Phase transitions and phase separations in phospholipid membranes induced by changes in temperature, pH, and concentration of bivalent cations. *Biochemistry* **14**, 152–161 (1975).

68. Burns, M., Wisser, K., Wu, J., Levental, I. & Veatch, S. L. Miscibility Transition Temperature Scales with Growth Temperature in a Zebrafish Cell Line. *Biophys. J.* **113**, 1212–1222 (2017).

69. Needham, D. & Nunn, R. S. Elastic deformation and failure of lipid bilayer membranes containing cholesterol. *Biophys. J.* **58**, 997–1009 (1990).

70. Staykova, M., Holmes, D. P., Read, C. & Stone, H. A. Mechanics of surface area regulation in cells examined with confined lipid membranes. *Proc. Natl. Acad. Sci. U. S. A.* **108**, 9084–9088 (2011).

71. Staykova, M. & Stone, H. a. The role of the membrane confinement in the surface area regulation of cells. *Commun. Integr. Biol.* **4**, 616–618 (2011).

72. Veatch, S. L. & Keller, S. L. Seeing spots: Complex phase behavior in simple membranes. *Biochim. Biophys. Acta - Mol. Cell Res.* **1746**, 172–185 (2005).

73. Connell, S. D. & Smith, D. A. The atomic force microscope as a tool for studying phase separation in lipid membranes (Review). *Mol. Membr. Biol.* **23**, 17–28 (2009).

74. Aufderhorst-Roberts, A., Chandra, U. & Connell, S. D. Three-Phase Coexistence in Lipid Membranes. *Biophys. J.* **112**, 313–324 (2017).

75. Johnston, L. J. Nanoscale Imaging of Domains in Supported Lipid Membranes. *Langmuir* **23**, 5886–5895 (2007).

76. Seeger, H. M., Marino, G., Alessandrini, A. & Facci, P. Effect of physical parameters on the main phase transition of supported lipid bilayers. *Biophys. J.* **97**, 1067–76 (2009).

77. Alwarawrah, M., Dai, J. & Huang, J. A Molecular View of the Cholesterol Condensing Effect in DOPC Lipid Bilayers. *J. Phys. Chem. B* **114**, 7516–23 (2010).

78. Vist, M. R. & Davis, J. H. Phase equilibria of cholesterol/dipalmitoylphosphatidylcholine mixtures: deuterium nuclear magnetic resonance and differential scanning calorimetry. *Biochemistry* **29**, 451–464 (1990).

79. Róg, T., Pasenkiewicz-Gierula, M., Vattulainen, I. & Karttunen, M. Ordering effects of cholesterol and its analogues. *Biochim. Biophys. Acta - Biomembr.* **1788**, 97–121 (2009).

80. Cicuta, P., Keller, S. L. & Veatch, S. L. Diffusion of Liquid Domains in Lipid Bilayer Membranes. *J. Phys. Chem. B* **111**, 3328–3331 (2007).

81. Veatch, S. L., Leung, S. S. W., Hancock, R. E. W. & Thewalt, J. L. Fluorescent Probes Alter Miscibility Phase Boundaries in Ternary Vesicles. *J. Phys. Chem. B* **111**, 502–504 (2007).

82. Veatch, S. L. & Keller, S. L. Organization in Lipid Membranes Containing

Cholesterol. *Phys. Rev. Lett.* **89**, 268101 (2002).

83. Bagatolli, L. A. & Gratton, E. A correlation between lipid domain shape and binary phospholipid mixture composition in free standing bilayers: A two-photon fluorescence microscopy study. *Biophys. J.* **79**, 434–47 (2000).

84. Bhatia, T., Cornelius, F. & Ipsen, J. H. Capturing suboptical dynamic structures in lipid bilayer patches formed from free-standing giant unilamellar vesicles. *Nat. Protoc.* **12**, 1563–1575 (2017).

85. Bhatia, T., Husen, P., Ipsen, J. H., Bagatolli, L. A. & Simonsen, A. C. Fluid domain patterns in free-standing membranes captured on a solid support. *Biochim. Biophys. Acta - Biomembr.* **1838**, 2503–2510 (2014).

86. Gunderson, R. S. & Honerkamp-Smith, A. R. Liquid-liquid phase transition temperatures increase when lipid bilayers are supported on glass. *Biochim. Biophys. Acta - Biomembr.* **1860**, 1965–1971 (2018).

87. Blosser, M. C. *et al.* Transbilayer Colocalization of Lipid Domains Explained via Measurement of Strong Coupling Parameters. *Biophys. J.* **109**, 2317–2327 (2015).

88. Appleyard, J.Y. & Yang, J. The Main Phase Transition of Mica-Supported Phosphatidylcholine Membranes. *J. Phys. Chem. B* **104**, 8097–8100 (2000).

89. Putzel, G. G., Uline, M. J., Szleifer, I. & Schick, M. Interleaflet Coupling and Domain Registry in Phase-Separated Lipid Bilayers. *Biophys. J.* **100**, 996–1004 (2011).

90. Fan, J., Sammalkorpi, M. & Haataja, M. Formation and regulation of lipid microdomains in cell membranes: Theory, modeling, and speculation. *FEBS Lett.* **584**, 1678–1684 (2010).

91. Fletcher, D. A. & Mullins, R. D. Cell mechanics and the cytoskeleton. *Nature* **463**, 485–492 (2010).

92. Hynes, R. O. The extracellular matrix: not just pretty fibrils. *Science* **326**, 1216–9 (2009).

93. Geiger, B., Bershadsky, A., Pankov, R. & Yamada, K. M. Transmembrane crosstalk between the extracellular matrix and the cytoskeleton. *Nat. Rev. Mol. Cell Biol.* **2**, 793–805 (2001).

94. Discher, D. E., Janmey, P. & Wang, Y.-L. Tissue cells feel and respond to the stiffness of their substrate. *Science* **310**, 1139–43 (2005).

95. Engler, A. J., Sen, S., Sweeney, H. L. & Discher, D. E. Matrix elasticity directs stem cell lineage specification. *Cell* **126**, 677–89 (2006).

96. Bezanilla, M., Gladfelter, A. S., Kovar, D. R. & Lee, W.-L. Cytoskeletal dynamics: a view from the membrane. *J. Cell Biol.* **209**, 329–37 (2015).

97. Suetsugu, S., Kurisu, S. & Takenawa, T. Dynamic Shaping of Cellular Membranes by Phospholipids and Membrane-Deforming Proteins. *Physiol. Rev.* **94**, 1219–1248 (2014).

98. Heinemann, F., Vogel, S. K. & Schwille, P. Lateral Membrane Diffusion

Modulated by a Minimal Actin Cortex. *Biophys. J.* **104**, 1465–1475 (2013).

99. Arumugam, S., Petrov, E. P. & Schwille, P. Cytoskeletal pinning controls phase separation in multicomponent lipid membranes. *Biophys. J.* **108**, 1104–13 (2015).

100. Honigmann, A. *et al.* A lipid bound actin meshwork organizes liquid phase separation in model membranes. *Elife* **3**, 1–16 (2014).

101. Fritzsche, M. *et al.* Self-organizing actin patterns shape membrane architecture but not cell mechanics. *Nat. Commun.* **8**, 14347 (2017).

102. Mulla, Y., Aufderhorst-Roberts, A. & Koenderink, G. H. Shaping up synthetic cells. *Phys. Biol.* **15**, 041001 (2018).

103. Tombari, E., Salvetti, G., Ferrari, C. & Johari, G. P. Thermodynamic functions of water and ice confined to 2nm radius pores. *J. Chem. Phys.* **122**, 104712 (2005).

104. Motegi, T., Yamazaki, K., Ogino, T. & Tero, R. Substrate-Induced Structure and Molecular Dynamics in a Lipid Bilayer Membrane. *Langmuir* **33**, 14748–14755 (2017).

105. Schoch, R. L., Barel, I., Brown, F. L. H. & Haran, G. Lipid diffusion in the distal and proximal leaflets of supported lipid bilayer membranes studied by single particle tracking. *J. Chem. Phys.* **148**, 123333 (2018).

106. Reichert, W. M., Bruckner, C. J. & Joseph, J. Langmuir-Blodgett films and black lipid membranes in biospecific surface-selective sensors. *Thin Solid Films* **152**, 345–376 (1987).

107. Wu, H.-L., Chen, P.-Y., Chi, C.-L., Tsao, H.-K. & Sheng, Y.-J. Vesicle deposition on hydrophilic solid surfaces. *Soft Matter* **9**, 1908–1919 (2013).

108. Hamai, C., Cremer, P. S. & Musser, S. M. Single Giant Vesicle Rupture Events Reveal Multiple Mechanisms of Glass-Supported Bilayer Formation. *Biophys. J.* **92**, 1988–1999 (2007).

109. Orozco-Alcaraz, R. & Kuhl, T. L. Interaction forces between DPPC bilayers on glass. *Langmuir* **29**, 337–343 (2013).

110. Fuhrmans, M. & Müller, M. Mechanisms of Vesicle Spreading on Surfaces: Coarse-Grained Simulations. *Langmuir* **29**, 4335–4349 (2013).

111. Kataoka-Hamai, C. & Yamazaki, T. Induced Rupture of Vesicles Adsorbed on Glass by Pore Formation at the Surface–Bilayer Interface. *Langmuir* **31**, 1312–1319 (2015).

112. Seeger, H. M., Cerbo, A. D. Di, Alessandrini, A. & Facci, P. Supported lipid bilayers on mica and silicon oxide: Comparison of the main phase transition behavior. *J. Phys. Chem. B* **114**, 8926–8933 (2010).

113. Scomparin, C., Lecuyer, S., Ferreira, M., Charitat, T. & Tinland, B. Diffusion in supported lipid bilayers: influence of substrate and preparation technique on the internal dynamics. *Eur. Phys. J. E. Soft Matter* **28**, 211–20 (2009).

114. Przybylo, M. *et al.* Lipid Diffusion in Giant Unilamellar Vesicles Is More than 2

Times Faster than in Supported Phospholipid Bilayers under Identical Conditions. *Langmuir* **22**, 9096–9099 (2006).

115. Contreras, F. X., Sánchez-Magraner, L., Alonso, A. & Goñi, F. M. Transbilayer (flip-flop) lipid motion and lipid scrambling in membranes. *FEBS Lett.* **584**, 1779–1786 (2010).

116. Blachon, F. *et al.* Nanoroughness Strongly Impacts Lipid Mobility in Supported Membranes. *Langmuir* **33**, 2444–2453 (2017).

117. Yoon, T.-Y. *et al.* Topographic control of lipid-raft reconstitution in model membranes. *Nat. Mater.* **5**, 281–285 (2006).

118. Goodchild, J. A., Walsh, D. L. & Connell, S. D. Substrate Roughness Significantly Affects Bilayer Phase Separation. (2019).

119. Krapf, D. Mechanisms Underlying Anomalous Diffusion in the Plasma Membrane. *Curr. Top. Membr.* **75**, 167–207 (2015).

120. Merkel, R., Sackmann, E. & Evans, E. Molecular friction and epitactic coupling between monolayers in supported bilayers. *J. Phys.* **50**, 1535–1555 (1989).

121. Israelachvili, J. & Wennerström, H. Role of hydration and water structure in biological and colloidal interactions. *Nature* **379**, 219–225 (1996).

122. Major, R. C., Houston, J. E., McGrath, M. J., Siepmann, J. I. & Zhu, X.-Y. Viscous Water Meniscus under Nanoconfinement. *Phys. Rev. Lett.* **96**, 177803 (2006).

123. Alba-Simionesco, C. *et al.* Effects of confinement on freezing and melting. *J. Phys. Condens. Matter* **18**, R15–R68 (2006).

124. Cafolla, C. & Voïtchovsky, K. Lubricating properties of single metal ions at interfaces. *Nanoscale* **10**, 11831–11840 (2018).

125. Piantanida, L., Bolt, H. L., Rozatian, N., Cobb, S. L. & Voïtchovsky, K. Ions Modulate Stress-Induced Nanotexture in Supported Fluid Lipid Bilayers. *Biophys. J.* **113**, 426–439 (2017).

126. Baumgart, T. *et al.* Large-scale fluid/fluid phase separation of proteins and lipids in giant plasma membrane vesicles. *Proc. Natl. Acad. Sci. U. S. A.* **104**, 3165–70 (2007).

127. Purrucker, O., Förtig, A., Jordan, R. & Tanaka, M. Supported Membranes with Well-Defined Polymer Tethers—Incorporation of Cell Receptors. *ChemPhysChem* **5**, 327–335 (2004).

128. Tanaka, M. & Sackmann, E. Polymer-supported membranes as models of the cell surface. *Nature* **437**, 656–663 (2005).

129. Smith, E. A. *et al.* Lipid bilayers on polyacrylamide brushes for inclusion of membrane proteins. *Langmuir* **21**, 9644–50 (2005).

130. Du, H., Chandaroy, P. & Hui, S. W. Grafted poly-(ethylene glycol) on lipid surfaces inhibits protein adsorption and cell adhesion. *Biochim. Biophys. Acta - Biomembr.* **1326**, 236–248 (1997).

131. Sterling, S. M. *et al.* Phospholipid diffusion coefficients of cushioned model membranes determined via z-scan fluorescence correlation spectroscopy. *Langmuir* **29**, 7966–74 (2013).

132. Tanaka, M., Kaufmann, S., Nissen, J. & Hochrein, M. Orientation selective immobilization of human erythrocyte membranes on ultrathin cellulose films. *Phys. Chem. Chem. Phys.* **3**, 4091–4095 (2001).

133. Wagner, M. L. & Tamm, L. K. Tethered polymer-supported planar lipid bilayers for reconstitution of integral membrane proteins: silane-polyethyleneglycol-lipid as a cushion and covalent linker. *Biophys. J.* **79**, 1400–14 (2000).

134. Zhang, L. & Granick, S. Slaved diffusion in phospholipid bilayers. *Proc. Natl. Acad. Sci. U. S. A.* **102**, 9118–21 (2005).

135. Hovis, J. S. & Boxer, S. G. Patterning and Composition Arrays of Supported Lipid Bilayers by Microcontact Printing. *Langmuir* **17**, 3400–3405 (2001).

136. Shahal, T., Melzak, K. A., Lowe, C. R. & Gizeli, E. Poly(dimethylsiloxane)-coated sensor devices for the formation of supported lipid bilayers and the subsequent study of membrane interactions. *Langmuir* **24**, 11268–75 (2008).

137. Buzea, C., Pacheco, I. I. & Robbie, K. Nanomaterials and nanoparticles: Sources and toxicity. *Biointerphases* **2**, MR17–MR71 (2007).

138. Beddoes, C. M., Case, C. P. & Briscoe, W. H. Understanding nanoparticle cellular entry: A physicochemical perspective. *Adv. Colloid Interface Sci.* **218**, 48–68 (2015).

139. Drews, J. Drug discovery: a historical perspective. *Science* **287**, 1960–4 (2000).

140. Neužil, P., Giselbrecht, S., Länge, K., Huang, T. J. & Manz, A. Revisiting lab-on-a-chip technology for drug discovery. *Nat. Rev. Drug Discov.* **11**, 620–632 (2012).

141. Huh, D., Hamilton, G. A. & Ingber, D. E. From 3D cell culture to organs-on-chips. *Trends Cell Biol.* **21**, 745–754 (2011).

142. Cremer, P. S. & Boxer, S. G. Formation and Spreading of Lipid Bilayers on Planar Glass Supports. *J. Phys. Chem. B* **103**, 2554–2559 (1999).

143. Groves, J. T., Ulman, N. & Boxer, S. G. Micropatterning fluid lipid bilayers on solid supports. *Science* **275**, 651–3 (1997).

144. Zhu, Y. & Moran-Mirabal, J. Micropatterning of Phase-Segregated Supported Lipid Bilayers and Binary Lipid Phases through Polymer Stencil Lift-Off. *Langmuir* **32**, 11021–11028 (2016).

145. Hovis, J. S. & Boxer, S. G. Patterning Barriers to Lateral Diffusion in Supported Lipid Bilayer Membranes by Blotting and Stamping. *Langmuir* **16**, 894–897 (2000).

146. Lenz, P., Ajo-Franklin, C. M. & Boxer, S. G. Patterned supported lipid bilayers and monolayers on poly(dimethylsiloxane). *Langmuir* **20**, 11092–9 (2004).

147. Gavutis, M., Navikas, V., Rakickas, T., Vaitekonis, Š. & Valiokas, R. Lipid dip-

pen nanolithography on self-assembled monolayers. *J. Micromechanics Microengineering* **26**, 025016 (2016).

148. Woodward, X., Stimpson, E. E. & Kelly, C. V. Single-lipid tracking on nanoscale membrane buds: The effects of curvature on lipid diffusion and sorting. *Biochim. Biophys. Acta - Biomembr.* **1860**, 2064–2075 (2018).

149. Kabbani, A. M., Woodward, X. & Kelly, C. V. Resolving the effects of nanoscale membrane curvature on lipid mobility. (2017).

150. Sanii, B., Smith, A. M., Butti, R., Brozell, A. M. & Parikh, A. N. Bending membranes on demand: fluid phospholipid bilayers on topographically deformable substrates. *Nano Lett.* **8**, 866–871 (2008).

151. Roiter, Y. *et al.* Interaction of nanoparticles with lipid membrane. *Nano Lett.* **8**, 941–4 (2008).

152. Roiter, Y. *et al.* Interaction of lipid membrane with nanostructured surfaces. *Langmuir* **25**, 6287–99 (2009).

153. Sundh, M., Svedhem, S. & Sutherland, D. S. Formation of Supported Lipid Bilayers at Surfaces with Controlled Curvatures: Influence of Lipid Charge. *J. Phys. Chem. B* **115**, 7838–7848 (2011).

154. McMahon, H. T. & Gallop, J. L. Membrane curvature and mechanisms of dynamic cell membrane remodelling. *Nature* **438**, 590–596 (2005).

155. Parthasarathy, R. & Groves, J. T. Curvature and spatial organization in biological membranes. *Soft Matter* **3**, 24–33 (2007).

156. Parthasarathy, R., Yu, C. & Groves, J. T. Curvature-Modulated Phase Separation in Lipid Bilayer Membranes. *Langmuir* **22**, 5095–5099 (2006).

157. Schütte, O. M. *et al.* Size and mobility of lipid domains tuned by geometrical constraints. *Proc. Natl. Acad. Sci. U. S. A.* **114**, E6064–E6071 (2017).

158. Orth, A., Johannes, L., Römer, W. & Steinem, C. Creating and Modulating Microdomains in Pore-Spanning Membranes. *ChemPhysChem* **13**, 108–114 (2012).

159. Steltenkamp, S. *et al.* Mechanical Properties of Pore-Spanning Lipid Bilayers Probed by Atomic Force Microscopy. *Biophys. J.* **91**, 217–226 (2006).

160. Quaglino, A., Salierno, M., Pellegrotti, J., Rubinstein, N. & Kordon, E. C. Mechanical strain induces involution-associated events in mammary epithelial cells. *BMC Cell Biol.* **10**, 55 (2009).

161. Tremblay, D., Chagnon-Lessard, S., Mirzaei, M., Pelling, A. E. & Godin, M. A microscale anisotropic biaxial cell stretching device for applications in mechanobiology. *Biotechnol. Lett.* **36**, 657–65 (2014).

162. Janmey, P. A. & McCulloch, C. A. Cell Mechanics: Integrating Cell Responses to Mechanical Stimuli. *Annu. Rev. Biomed. Eng.* **9**, 1–34 (2007).

163. Rodal, S. K. *et al.* Extraction of cholesterol with methyl-beta-cyclodextrin perturbs formation of clathrin-coated endocytic vesicles. *Mol. Biol. Cell* **10**, 961–74 (1999).

164. Ren, B. *et al.* HP-β-cyclodextrin as an inhibitor of amyloid-β aggregation and toxicity. *Phys. Chem. Chem. Phys.* **18**, 20476–20485 (2016).

165. Tsai, F.-C. & Koenderink, G. H. Shape control of lipid bilayer membranes by confined actin bundles. *Soft Matter* **11**, 8834–8847 (2015).

166. Hu, S.-K., Huang, L.-T. & Chao, L. Membrane species mobility under in-lipid-membrane forced convection. *Soft Matter* **12**, 6954–6963 (2016).

167. Benz, R., Beckers, F. & Zimmermann, U. Reversible electrical breakdown of lipid bilayer membranes: A charge-pulse relaxation study. *J. Membr. Biol.* **48**, 181–204 (1979).

168. Kotnik, T. *et al.* Electroporation-based applications in biotechnology. *Trends Biotechnol.* **33**, 480–488 (2015).

169. Dimitrov, D. S. & Angelova, M. I. Lipid swelling and liposome formation mediated by electric fields. *Bioelectrochemistry Bioenerg.* **19**, 323–336 (1988).

170. Moscho, A., Orwar, O., Chiu, D. T., Modi, B. P. & Zare, R. N. Rapid preparation of giant unilamellar vesicles. *Proc. Natl. Acad. Sci. U. S. A.* **93**, 11443–7 (1996).

171. Bi, H., Fu, D., Wang, L. & Han, X. Lipid Nanotube Formation Using Space-Regulated Electric Field above Interdigitated Electrodes. *ACS Nano* **8**, 3961–3969 (2014).

172. Daniel, S. *et al.* Separation of Membrane-Bound Compounds by Solid-Supported Bilayer Electrophoresis. *J. Am. Chem. Soc.* **129**, 8072–8073 (2007).

173. Lozano, M. M., Hovis, J. S., Moss, F. R. & Boxer, S. G. Dynamic Reorganization and Correlation among Lipid Raft Components. *J. Am. Chem. Soc.* **138**, 9996–10001 (2016).

174. Lim, C. T., Zhou, E. H. & Quek, S. T. Mechanical models for living cells—a review. *J. Biomech.* **39**, 195–216 (2006).

175. Stubbington, L., Arroyo, M. & Staykova, M. Sticking and sliding of lipid bilayers on deformable substrates. *Soft Matter* **13**, 181–186 (2017).

176. Huh, D. *et al.* Reconstituting organ-level lung functions on a chip. *Science* **328**, 1662–8 (2010).

177. Stottrup, B. L., Veatch, S. L. & Keller, S. L. Nonequilibrium behavior in supported lipid membranes containing cholesterol. *Biophys. J.* **86**, 2942–50 (2004).

178. Stottrup, B. L., Stevens, D. S. & Keller, S. L. Miscibility of ternary mixtures of phospholipids and cholesterol in monolayers, and application to bilayer systems. *Biophys. J.* **88**, 269–76 (2005).

179. Koynova, R., Koumanov, A. & Tenchov, B. Metastable rippled gel phase in saturated phosphatidylcholines: calorimetric and densitometric characterization. *Biochim. Biophys. Acta - Biomembr.* **1285**, 101–108 (1996).

180. Rappolt, M. & Rapp, G. Structure of the stable and metastable ripple phase of dipalmitoylphosphatidylcholine. *Eur. Biophys. J.* **24**, 381–386 (1996).

181. Kaasgaard, T., Leidy, C., Crowe, J. H., Mouritsen, O. G. & Jørgensen, K. Temperature-controlled structure and kinetics of ripple phases in one- and two-component supported lipid bilayers. *Biophys. J.* **85**, 350–360 (2003).

182. Stevens, M. M., Honerkamp-Smith, A. R. & Keller, S. L. Solubility limits of cholesterol, lanosterol, ergosterol, stigmasterol, and β-sitosterol in electroformed lipid vesicles. *Soft Matter* **6**, 5882 (2010).

183. Huang, J., Buboltz, J. T. & Feigenson, G. W. Maximum solubility of cholesterol in phosphatidylcholine and phosphatidylethanolamine bilayers. *Biochim. Biophys. Acta - Biomembr.* **1417**, 89–100 (1999).

184. Bouvrais, H., Pott, T., Bagatolli, L. A., Ipsen, J. H. & Méléard, P. Impact of membrane-anchored fluorescent probes on the mechanical properties of lipid bilayers. *Biochim. Biophys. Acta - Biomembr.* **1798**, 1333–1337 (2010).

185. Skaug, M. J., Longo, M. L. & Faller, R. The Impact of Texas Red on Lipid Bilayer Properties. *J. Phys. Chem. B* **115**, 8500–8505 (2011).

186. Waters, J. C. Accuracy and precision in quantitative fluorescence microscopy. *J. Cell Biol.* **185**, 1135–48 (2009).

187. Baumgart, T., Hunt, G., Farkas, E. R., Webb, W. W. & Feigenson, G. W. Fluorescence probe partitioning between Lo/Ld phases in lipid membranes. *Biochim. Biophys. Acta - Biomembr.* **1768**, 2182–2194 (2007).

188. Klymchenko, A. S. & Kreder, R. Fluorescent Probes for Lipid Rafts: From Model Membranes to Living Cells. *Chem. Biol.* **21**, 97–113 (2014).

189. Leung, S. S. W. & Thewalt, J. Link between Fluorescent Probe Partitioning and Molecular Order of Liquid Ordered-Liquid Disordered Membranes. *J. Phys. Chem. B* **121**, 1176–1185 (2017).

190. Wen, Y., Dick, R. A., Feigenson, G. W. & Vogt, V. M. Effects of Membrane Charge and Order on Membrane Binding of the Retroviral Structural Protein Gag. *J. Virol.* **90**, 9518–32 (2016).

191. Beneš, M. *et al.* Surface-Dependent Transitions during Self-Assembly of Phospholipid Membranes on Mica, Silica, and Glass. *Langmuir* **20**, 10129–10137 (2004).

192. Lobovkina, T. *et al.* Protrusive growth and periodic contractile motion in surface-adhered vesicles induced by Ca2+-gradients. *Soft Matter* **6**, 268–272 (2010).

193. Richter, R., Mukhopadhyay, A. & Brisson, A. Pathways of lipid vesicle deposition on solid surfaces: a combined QCM-D and AFM study. *Biophys. J.* **85**, 3035–47 (2003).

194. Trewby, W., Livesey, D. & Voïtchovsky, K. Buffering agents modify the hydration landscape at charged interfaces. *Soft Matter* **12**, 2642–51 (2016).

195. Henke, L., Nagy, N. & Krull, U. J. An AFM determination of the effects on

surface roughness caused by cleaning of fused silica and glass substrates in the process of optical biosensor preparation. *Biosens. Bioelectron.* **17**, 547–555 (2002).

196. Fujii, T. PDMS-based microfluidic devices for biomedical applications. *Microelectron. Eng.* **61**–**62**, 907–914 (2002).

197. Koschwanez, J. H., Carlson, R. H. & Meldrum, D. R. Thin PDMS Films Using Long Spin Times or Tert-Butyl Alcohol as a Solvent. *PLoS One* **4**, e4572 (2009).

198. Chau, K. *et al.* Dependence of the quality of adhesion between poly(dimethylsiloxane) and glass surfaces on the composition of the oxidizing plasma. *Microfluid. Nanofluidics* **10**, 907–917 (2011).

199. Litz, J. P., Thakkar, N., Portet, T. & Keller, S. L. Depletion with Cyclodextrin Reveals Two Populations of Cholesterol in Model Lipid Membranes. *Biophys. J.* **110**, 635–645 (2016).

200. Groves, J. T., Parthasarathy, R. & Forstner, M. B. Fluorescence imaging of membrane dynamics. *Annu. Rev. Biomed. Eng.* **10**, 311–338 (2008).

201. Lakowicz, J. R. *Principles of Fluorescence Spectroscopy*. (Springer Science & Business Media, 2007).

202. Rust, M. J., Bates, M. & Zhuang, X. Sub-diffraction-limit imaging by stochastic optical reconstruction microscopy (STORM). *Nat. Methods* **3**, 793–5 (2006).

203. Eggeling, C. *et al.* Direct observation of the nanoscale dynamics of membrane lipids in a living cell. *Nature* **457**, 1159–62 (2009).

204. Hess, S. T. *et al.* Dynamic clustered distribution of hemagglutinin resolved at 40 nm in living cell membranes discriminates between raft theories. *Proc. Natl. Acad. Sci. U. S. A.* **104**, 17370–5 (2007).

205. Galush, W. J., Nye, J. A. & Groves, J. T. Quantitative fluorescence microscopy using supported lipid bilayer standards. *Biophys. J.* **95**, 2512–9 (2008).

206. Reits, E. A. J. & Neefjes, J. J. From fixed to FRAP: measuring protein mobility and activity in living cells. *Nat. Cell Biol.* **3**, E145–E147 (2001).

207. Pincet, F. *et al.* FRAP to characterize molecular diffusion and interaction in various membrane environments. *PLoS One* **11**, 1–19 (2016).

208. Tero, R., Sazaki, G., Ujihara, T. & Urisu, T. Anomalous Diffusion in Supported Lipid Bilayers Induced by Oxide Surface Nanostructures. *Langmuir* **27**, 9662–9665 (2011).

209. Schindelin, J. *et al.* Fiji: an open-source platform for biological-image analysis. *Nat. Methods* **9**, 676–682 (2012).

210. Blumenthal, D., Goldstien, L., Edidin, M. & Gheber, L. A. Universal Approach to FRAP Analysis of Arbitrary Bleaching Patterns. *Sci. Rep.* **5**, 11655 (2015).

211. Sullivan, K. D., Majewska, A. K. & Brown, E. B. Single and Multiphoton Fluorescence Recovery after Photobleaching. *Cold Spring Harb. Protoc.* **2015**, pdb.top083519 (2015).

212. Limozin, L. & Sengupta, K. Quantitative Reflection Interference Contrast Microscopy (RICM) in Soft Matter and Cell Adhesion. *ChemPhysChem* **10**, 2752–2768 (2009).

213. Johnson, J. Not seeing is not believing: improving the visibility of your fluorescence images. *Mol. Biol. Cell* **23**, 754–7 (2012).

214. N. Holambe, P. S. & G. Kumbhar, P. Comparison between Otsu's Image Thresholding Technique and Iterative Triclass. *Int. J. Comput. Trends Technol.* **33**, 80–82 (2016).

215. Binnig, G. & Quate, C. F. Atomic Force Microscope. *Phys. Rev. Lett.* **56**, 930–933 (1986).

216. Voïtchovsky, K. *et al.* In Situ Mapping of the Molecular Arrangement of Amphiphilic Dye Molecules at the TiO_2 Surface of Dye-Sensitized Solar Cells. *ACS Appl. Mater. Interfaces* **7**, 10834–42 (2015).

217. Segura, J. J. *et al.* Adsorbed and near surface structure of ionic liquids at a solid interface. *Phys. Chem. Chem. Phys.* **15**, 3320–3328 (2013).

218. Hayes, R., Warr, G. G. & Atkin, R. Structure and Nanostructure in Ionic Liquids. *Chem. Rev.* **115**, 150601082109009 (2015).

219. Kumaki, J. Observation of polymer chain structures in two-dimensional films by atomic force microscopy. *Polym. J.* **48**, 3–14 (2015).

220. Schmidt, S., Biegel, E. & Müller, V. The ins and outs of Na(+) bioenergetics in Acetobacterium woodii. *Biochim. Biophys. Acta* **1787**, 691–696 (2009).

221. Bippes, C. A. & Muller, D. J. High-resolution atomic force microscopy and spectroscopy of native membrane proteins. *Reports Prog. Phys.* **74**, 086601 (2011).

222. Chada, N. *et al.* Glass is a Viable Substrate for Precision Force Microscopy of Membrane Proteins. *Sci. Rep.* **5**, 12550 (2015).

223. Möller, C., Allen, M., Elings, V., Engel, A. & Müller, D. J. Tapping-mode atomic force microscopy produces faithful high-resolution images of protein surfaces. *Biophys. J.* **77**, 1150–1158 (1999).

224. Antoranz Contera, S., Voïtchovsky, K. & Ryan, J. F. Controlled ionic condensation at the surface of a native extremophile membrane. *Nanoscale* **2**, 222–9 (2010).

225. Haugstad, G. *Atomic Force Microscopy*. (John Wiley & Sons, Inc., 2012).

226. Oliver, R. A. Advances in AFM for the electrical characterization of semiconductors. *Reports Prog. Phys.* **71**, 076501 (2008).

227. Giessibl, F. J. Subatomic Features on the Silicon (111)-(7x7) Surface Observed by Atomic Force Microscopy. *Science (80-.).* **289**, 422–425 (2000).

228. Moreno-Herrero, F., Colchero, J., Gómez-Herrero, J. & Baró, A. M. Atomic force microscopy contact, tapping, and jumping modes for imaging biological samples in liquids. *Phys. Rev. E. Stat. Nonlin. Soft Matter Phys.* **69**, 031915 (2004).

229. Gan, Y. Atomic and subnanometer resolution in ambient conditions by atomic force microscopy. *Surf. Sci. Rep.* **64**, 99–121 (2009).

230. Patil, S. V. & Hoffmann, P. M. Small-Amplitude Atomic Force Microscopy. *Adv. Eng. Mater.* **7**, 707–712 (2005).

231. Fukuma, T. & Jarvis, S. P. Development of liquid-environment frequency modulation atomic force microscope with low noise deflection sensor for cantilevers of various dimensions. *Rev. Sci. Instrum.* **77**, 043701 (2006).

232. García, R. & San Paulo, A. Attractive and repulsive tip-sample interaction regimes in tapping-mode atomic force microscopy. *Phys. Rev. B* **60**, 4961–4967 (1999).

233. García, R. *Amplitude Modulation Atomic Force Microscopy*. (Wiley-VCH Verlag GmbH & Co. KGaA, 2010).

234. Bharat, B. *Encyclopedia of Nanotechnology*. (Springer Netherlands, 2012).

235. Kiracofe, D. & Raman, A. On eigenmodes, stiffness, and sensitivity of atomic force microscope cantilevers in air versus liquids. *J. Appl. Phys.* **107**, 033506 (2010).

236. Voïtchovsky, K., Kuna, J. J., Contera, S. A., Tosatti, E. & Stellacci, F. Direct mapping of the solid-liquid adhesion energy with subnanometre resolution. *Nat. Nanotechnol.* **5**, 401–405 (2010).

237. Voïtchovsky, K. Anharmonicity, solvation forces, and resolution in atomic force microscopy at the solid-liquid interface. *Phys. Rev. E. Stat. Nonlin. Soft Matter Phys.* **88**, 022407 (2013).

238. Fukuma, T., Higgins, M. J. & Jarvis, S. P. Direct imaging of individual intrinsic hydration layers on lipid bilayers at Angstrom resolution. *Biophys. J.* **92**, 3603–3609 (2007).

239. San Paulo, A. & García, R. High-resolution imaging of antibodies by tapping-mode atomic force microscopy: attractive and repulsive tip-sample interaction regimes. *Biophys. J.* **78**, 1599–1605 (2000).

240. Miller, E. J. *et al.* Sub-nanometer Resolution Imaging with Amplitude-modulation Atomic Force Microscopy in Liquid. *J. Vis. Exp.* e54924 (2016).

241. Gnecco, E., Bennewitz, R., Gyalog, T. & Meyer, E. Friction experiments on the nanometre scale. *J. Phys. Condens. Matter* **13**, 202 (2001).

242. Nanosurf. AFM Theory — Contact Modes - Nanosurf. 1 Available at: https://www.nanosurf.com/en/how-afm-works/contact-modes. (Accessed: 1st October 2018)

243. Jackman, J. A., Choi, J.-H., Zhdanov, V. P. & Cho, N.-J. Influence of Osmotic Pressure on Adhesion of Lipid Vesicles to Solid Supports. *Langmuir* **29**, 11375–11384 (2013).

244. Parsegian, V. A. & Zemb, T. Hydration forces: Observations, explanations, expectations, questions. *Curr. Opin. Colloid Interface Sci.* **16**, 618–624 (2011).

245. Garcia-Manyes, S. & Sanz, F. Nanomechanics of lipid bilayers by force spectroscopy with AFM: a perspective. *Biochim. Biophys. Acta* **1798**, 741–9 (2010).

246. Chiantia, S., Ries, J., Kahya, N. & Schwille, P. Combined AFM and Two-Focus SFCS Study of Raft-Exhibiting Model Membranes. *ChemPhysChem* **7**, 2409–2418 (2006).

247. Facci, P. & Alessandrini, A. Phase transitions in Supported Lipid Bilayers studied by AFM. *Soft Matter* **10**, 7145-7164 (2014).

248. Alessandrini, A., Seeger, H. M., Caramaschi, T. & Facci, P. Dynamic Force Spectroscopy on Supported Lipid Bilayers: Effect of Temperature and Sample Preparation. *Biophys. J.* **103**, 38–47 (2012).

249. Alessandrini, A., Seeger, H. M., Di Cerbo, A., Caramaschi, T. & Facci, P. What do we really measure in AFM punch-through experiments on supported lipid bilayers? *Soft Matter* **7**, 7054 (2011).

250. Lee, C.-K., Wang, Y.-M., Huang, L.-S. & Lin, S. Atomic force microscopy: Determination of unbinding force, off rate and energy barrier for protein–ligand interaction. *Micron* **38**, 446–461 (2007).

251. Craig, V. S. J. & Neto, C. In Situ Calibration of Colloid Probe Cantilevers in Force Microscopy: Hydrodynamic Drag on a Sphere Approaching a Wall. *Langmuir* **17**, 6018–6022 (2001).

252. Hilner, E. *et al.* The effect of ionic strength on oil adhesion in sandstone--the search for the low salinity mechanism. *Sci. Rep.* **5**, 9933 (2015).

253. Xie, L. *et al.* Mapping the Nanoscale Heterogeneity of Surface Hydrophobicity on the Sphalerite Mineral. *J. Phys. Chem. C* **121**, 5620–5628 (2017).

254. Henrik Hillborg, Nikodem Tomczak, Attila Olàh, Holger Schönherr, A. & Vancso, G. J. Nanoscale Hydrophobic Recovery: A Chemical Force Microscopy Study of UV/Ozone-Treated Cross-Linked Poly(dimethylsiloxane). *Langmuir* **20**, 785–794 (2003).

255. Xu, X. Modified Wenzel and Cassie Equations for Wetting on Rough Surfaces. *SIAM J. Appl. Math.* **76**, 2353–2374 (2016).

256. A. F. Stalder, G. Kulik, D. Sage, L. Barbieri, and P. H. A snake-based approach to accurate determination of both contact points and contact angles. *Colloids Surfaces A Physicochem. Eng. Asp.* **286**, 92–103 (2006).

257. Schwartz, J. *et al.* The Nikon Perfect Focus System (PFS). Available at: https://www.microscopyu.com/tutorials/the-nikon-perfect-focus-system-pfs. (Accessed: 27th November 2018)

258. Tsao, C.-W. & Chia-Wen. Polymer Microfluidics: Simple, Low-Cost Fabrication Process Bridging Academic Lab Research to Commercialized Production. *Micromachines* **7**, 225 (2016).

259. Rogers, J. A., Someya, T. & Huang, Y. Materials and mechanics for stretchable electronics. *Science* **327**, 1603–7 (2010).

260. Pennisi, C. P., Zachar, V., Gurevich, L., Patriciu, A. & Struijk, J. J. The influence of surface properties of plasma-etched polydimethylsiloxane (PDMS) on cell growth and morphology. *Conf. Proc. ... Annu. Int. Conf. IEEE Eng. Med. Biol. Soc. IEEE Eng. Med. Biol. Soc. Annu. Conf.* **2010**, 3804–7 (2010).

261. Trichet, L. *et al.* Evidence of a large-scale mechanosensing mechanism for cellular adaptation to substrate stiffness. *Proc. Natl. Acad. Sci. U. S. A.* **109**, 6933–8 (2012).

262. Hardelauf, H. *et al.* Micropatterning neuronal networks. *Analyst* **139**, 3256–3264 (2014).

263. Wang, L., Sun, B., Ziemer, K. S., Barabino, G. A. & Carrier, R. L. Chemical and physical modifications to poly(dimethylsiloxane) surfaces affect adhesion of Caco-2 cells. *J. Biomed. Mater. Res. A* **93**, 1260–71 (2010).

264. Kim, J., Chaudhury, M. K. & Owen, M. J. Hydrophobic Recovery of Polydimethylsiloxane Elastomer Exposed to Partial Electrical Discharge. *J. Colloid Interface Sci.* **226**, 231–236 (2000).

265. Toepke, M. W. & Beebe, D. J. PDMS absorption of small molecules and consequences in microfluidic applications. *Lab Chip* **6**, 1484 (2006).

266. Swanson, J. W. & Lebeau, J. E. The effect of implantation on the physical properties of silicone rubber. *J. Biomed. Mater. Res.* **8**, 357–367 (1974).

267. Kala, S. V, Lykissa, E. D., Neely, M. W. & Lieberman, M. W. Low molecular weight silicones are widely distributed after a single subcutaneous injection in mice. *Am. J. Pathol.* **152**, 645–9 (1998).

268. Carmen, R. & Mutha, S. C. Lipid absorption by silicone heart valve poppets: in-vivo and in-vitro results. *J. Biomed. Mater. Res.* **6**, 327–346 (1972).

269. Vondráček, P. & Doležel, B. Biostability of medical elastomers: a review. *Biomaterials* **5**, 209–214 (1984).

270. Deshpande, S. & Dekker, C. On-chip microfluidic production of cell-sized liposomes. *Nat. Protoc.* **13**, 856–874 (2018).

271. Liu, C.-F., Wang, M.-H. & Jang, L.-S. Microfluidics-based hairpin resonator biosensor for biological cell detection. *Sensors Actuators B Chem.* **263**, 129–136 (2018).

272. Li, G. & Lee, D.-W. An advanced selective liquid-metal plating technique for stretchable biosensor applications. *Lab Chip* **17**, 3415–3421 (2017).

273. Alberti, M. *et al.* Multi-chamber microfluidic platform for high-precision skin permeation testing. *Lab Chip* **17**, 1625–1634 (2017).

274. Zeng, S. *et al.* Bio-inspired sensitive and reversible mechanochromisms via strain-dependent cracks and folds. *Nat. Commun.* **7**, 11802 (2016).

275. van Meer, B. J. *et al.* Small molecule absorption by PDMS in the context of drug response bioassays. *Biochem. Biophys. Res. Commun.* **482**, 323–328 (2017).

276. Trantidou, T., Elani, Y., Parsons, E. & Ces, O. Hydrophilic surface modification of PDMS for droplet microfluidics using a simple, quick, and robust method via PVA deposition. *Microsystems Nanoeng.* **3**, 16091 (2017).

277. Abate, A. R., Lee, D., Do, T., Holtze, C. & Weitz, D. A. Glass coating for PDMS microfluidic channels by sol–gel methods. *Lab Chip* **8**, 516 (2008).

278. Bauer, W.-A. C., Fischlechner, M., Abell, C. & Huck, W. T. S. Hydrophilic PDMS microchannels for high-throughput formation of oil-in-water microdroplets and water-in-oil-in-water double emulsions. *Lab Chip* **10**, 1814 (2010).

279. Séguin, C., McLachlan, J. M., Norton, P. R. & Lagugné-Labarthet, F. Surface modification of poly(dimethylsiloxane) for microfluidic assay applications. *Appl. Surf. Sci.* **256**, 2524–2531 (2010).

280. van Midwoud, P. M., Janse, A., Merema, M. T., Groothuis, G. M. M. & Verpoorte, E. Comparison of biocompatibility and adsorption properties of different plastics for advanced microfluidic cell and tissue culture models. *Anal. Chem.* **84**, 3938–44 (2012).

281. Mortazavi, M. & Nosonovsky, M. A model for diffusion-driven hydrophobic recovery in plasma treated polymers. *Appl. Surf. Sci.* **258**, 6876–6883 (2012).

282. Hillborg, H. *et al.* Crosslinked polydimethylsiloxane exposed to oxygen plasma studied by neutron reflectometry and other surface specific techniques. *Polymer (Guildf).* **41**, 6851–6863 (2000).

283. Tóth, A. *et al.* Oxidative damage and recovery of silicone rubber surfaces. I. X-ray photoelectron spectroscopic study. *J. Appl. Polym. Sci.* **52**, 1293–1307 (1994).

284. Owen, M. J. & Smith, P. J. Plasma treatment of polydimethylsiloxane. *J. Adhes. Sci. Technol.* **8**, 1063–1075 (1994).

285. Bodas, D. & Khan-Malek, C. Hydrophilization and hydrophobic recovery of PDMS by oxygen plasma and chemical treatment-An SEM investigation. *Sensors Actuators, B Chem.* **123**, 368–373 (2007).

286. Wang, Z., Volinsky, A. A. & Gallant, N. D. Crosslinking effect on polydimethylsiloxane elastic modulus measured by custom-built compression instrument. *J. Appl. Polym. Sci.* **131**, n/a-n/a (2014).

287. Béfahy, S. *et al.* Thickness and Elastic Modulus of Plasma Treated PDMS Silica-like Surface Layer. *Langmuir* **26**, 3372–3375 (2010).

288. Hillborg, H., Sandelin, M. & Gedde, U. W. Hydrophobic recovery of polydimethylsiloxane after exposure to partial discharges as a function of crosslink density. *Polymer (Guildf).* **42**, 7349–7362 (2001).

289. Alam, A. U., Howlader, M. M. R. & Deen, M. J. The effects of oxygen plasma and humidity on surface roughness, water contact angle and hardness of silicon, silicon dioxide and glass. *J. Micromechanics Microengineering* **24**, 035010 (2014).

290. Stubbington, L. Lipid bilayers on deformable elastic substrates. *PhD Thesis*.

Durham University. (2018).

291. Lee, D. & Yang, S. Surface modification of PDMS by atmospheric-pressure plasma-enhanced chemical vapor deposition and analysis of long-lasting surface hydrophilicity. *Sensors Actuators B Chem.* **162**, 425–434 (2012).

292. Regehr, K. J. *et al.* Biological implications of polydimethylsiloxane-based microfluidic cell culture. *Lab Chip* **9**, 2132–9 (2009).

293. Eddington, D. T., Puccinelli, J. P. & Beebe, D. J. Thermal aging and reduced hydrophobic recovery of polydimethylsiloxane. *Sensors Actuators B Chem.* **114**, 170–172 (2006).

294. Wen, J. H. *et al.* Interplay of matrix stiffness and protein tethering in stem cell differentiation. *Nat. Mater.* **13**, 979–987 (2014).

295. Bormashenko, E., Chaniel, G. & Grynyov, R. Towards understanding hydrophobic recovery of plasma treated polymers: Storing in high polarity liquids suppresses hydrophobic recovery. *Appl. Surf. Sci.* **273**, 549–553 (2013).

296. Lee, J.-B., Yoon, S.-S. & Khang, D.-Y. The importance of interfacial adhesion in the buckling-based mechanical characterization of materials. *RSC Adv.* **3**, 17364 (2013).

297. Kaczorowski, W., Szymanski, W., Batory, D. & Niedzielski, P. Effect of plasma treatment on the surface properties of polydimethylsiloxane. *J. Appl. Polym. Sci.* **132**, 41635 (2015).

298. Park, H.-G., Jeong, H.-C., Jung, Y. H. & Seo, D.-S. Control of the wrinkle structure on surface-reformed poly(dimethylsiloxane) via ion-beam bombardment. *Sci. Rep.* **5**, 12356 (2015).

299. Chiche, A., Stafford, C. M. & Cabral, J. T. Complex micropatterning of periodic structures on elastomeric surfaces. *Soft Matter* **4**, 2360 (2008).

300. Nania, M., Foglia, F., Matar, O. K. & Cabral, J. T. Sub-100 nm wrinkling of polydimethylsiloxane by double frontal oxidation. *Nanoscale* **9**, 2030–2037 (2017).

301. Kim, P., Abkarian, M. & Stone, H. A. Hierarchical folding of elastic membranes under biaxial compressive stress. *Nat. Mater.* **10**, 952–7 (2011).

302. Sadeghi, S., Müller, M. & Vink, R. L. C. Raft formation in lipid bilayers coupled to curvature. *Biophys. J.* **107**, 1591–600 (2014).

303. Semrau, S. & Schmidt, T. Membrane heterogeneity – from lipid domains to curvature effects. *Soft Matter* **5**, 3174 (2009).

304. Baumgart, T., Hess, S. T. & Webb, W. W. Imaging coexisting fluid domains in biomembrane models coupling curvature and line tension. *Nature* **425**, 821–824 (2003).

305. Jin, L., Auguste, A., Hayward, R. C. & Suo, Z. Bifurcation Diagrams for the Formation of Wrinkles or Creases in Soft Bilayers. *J. Appl. Mech.* **82**, 061008 (2015).

306. Huang, Y. & Nguyen, N.-T. A polymeric cell stretching device for real-time imaging with optical microscopy. *Biomed. Microdevices* **15**, 1043–54 (2013).

307. Mills, K. L., Zhu, X., Takayama, S. & Thouless, M. D. The mechanical properties of a surface-modified layer on polydimethylsiloxane. *J. Mater. Res.* **23**, 37–48 (2008).

308. Huh, D. *et al.* Tuneable elastomeric nanochannels for nanofluidic manipulation. *Nat. Mater.* **6**, 424–428 (2007).

309. Peng, R. & Li, D. Fabrication of polydimethylsiloxane (PDMS) nanofluidic chips with controllable channel size and spacing. *Lab Chip* **16**, 3767–3776 (2016).

310. Zhu, X. *et al.* Fabrication of reconfigurable protein matrices by cracking. *Nat. Mater.* **4**, 403–406 (2005).

311. Miller, E., Stubbington, L., Dinet, C. & Staykova, M. Biophysical insights from supported lipid patches. *Adv. Biomembr. Lipid Self-Assembly* **29**, 23–48 (2019).

312. Jiang, F. Y., Bouret, Y. & Kindt, J. T. Molecular Dynamics Simulations of the Lipid Bilayer Edge. *Biophys. J.* **87**, 182–192 (2004).

313. May, S. A molecular model for the line tension of lipid membranes. *Eur. Phys. J. E* **3**, 37–44 (2000).

314. Henderson, J. M., Waring, A. J., Separovic, F. & Lee, K. Y. C. Antimicrobial Peptides Share a Common Interaction Driven by Membrane Line Tension Reduction. *Biophys. J.* **111**, 2176–2189 (2016).

315. Lam, K. L. H. *et al.* Mechanism of structural transformations induced by antimicrobial peptides in lipid membranes. *Biochim. Biophys. Acta - Biomembr.* **1818**, 194–204 (2012).

316. Lam, K. L. H. *et al.* Mechanism of Supported Membrane Disruption by Antimicrobial Peptide Protegrin-1. *J Phys Chem B* **110**, 21282-21286 (2006)

317. Puech, P. H., Borghi, N., Karatekin, E. & Brochard-Wyart, F. Line Thermodynamics: Adsorption at a Membrane Edge. *Phys. Rev. Lett.* **90**, 128304 (2003).

318. Kliesch, T. T. *et al.* Membrane tension increases fusion efficiency of model membranes in the presence of SNAREs. *Sci. Rep.* **7**, 12070 (2017).

319. Morris, C. E., Wang, J. A. & Markin, V. S. The Invagination of Excess Surface Area by Shrinking Neurons. *Biophys. J.* **85**, 223–235 (2003).

320. Morris, C. E. & Homann, U. Cell Surface Area Regulation and Membrane Tension. *J. Membr. Biol.* **179**, 79–102 (2001).

321. Shindell, O., Mica, N., Cheng, K. H., Wang, E. & Gordon, V. D. Dynamic Fingering in Adhered Lipid Membranes. *Langmuir* **34**, 4673–4680 (2018).

322. Coderch, L. *et al.* Influence of cholesterol on liposome fluidity by EPR. Relationship with percutaneous absorption. *J. Control. Release* **68**, 85–95 (2000).

323. Ohvo-Rekilä, H., Ramstedt, B., Leppimäki, P. & Peter Slotte, J. Cholesterol interactions with phospholipids in membranes. *Prog. Lipid Res.* **41**, 66–97 (2002).

324. Bronner, F. & Kleinzeller, A. *Current Topics in Membranes and Transport,* **10**. (Academic Press, 1978).

325. Knorr, R., Staykova, M., Gracià, R. & Dimova, R. Wrinkling and electroporation of giant vesicles in the gel phase. *Soft Matter* **6**, 1990 (2010).

326. Lipowsky, R. Spontaneous tubulation of membranes and vesicles reveals membrane tension generated by spontaneous curvature. *Faraday Discuss.* **161**, 305–331 (2013).

327. Hung, W.-C., Lee, M.-T., Chen, F.-Y. & Huang, H. W. The Condensing Effect of Cholesterol in Lipid Bilayers. *Biophys. J.* **92**, 3960–3967 (2007).

328. Sorre, B. *et al.* Curvature-driven lipid sorting needs proximity to a demixing point and is aided by proteins. *Proc. Natl. Acad. Sci.* **106**, 5622–5626 (2009).

329. Smaby, J. M., Momsen, M. M., Brockman, H. L. & Brown, R. E. Phosphatidylcholine acyl unsaturation modulates the decrease in interfacial elasticity induced by cholesterol. *Biophys. J.* **73**, 1492–1505 (1997).

330. Reimhult, E. , Höök, F., & Kasemo, B. Intact Vesicle Adsorption and Supported Biomembrane Formation from Vesicles in Solution: Influence of Surface Chemistry, Vesicle Size, Temperature, and Osmotic Pressure. *Langmuir* **19**, 1681-1691 (2002)

331. Reimhult, E., Kasemo, B. & Höök, F. Rupture pathway of phosphatidylcholine liposomes on silicon dioxide. *Int. J. Mol. Sci.* **10**, 1683–96 (2009).

332. Hauser, H., Oldani, D. & Phillips, M. C. Mechanism of ion escape from phosphatidylcholine and phosphatidylserine single bilayer vesicles. *Biochemistry* **12**, 4507–4517 (1973).

333. Anderson, T. H. *et al.* Formation of Supported Bilayers on Silica Substrates. *Langmuir* **25**, 6997–7005 (2009).

334. Zhang, Y. *et al.* Lipid membrane formation on chemical gradient modified surfaces. *RSC Adv.* **6**, 11325–11328 (2016).

335. Cho, N.-J., Jackman, J. A., Liu, M. & Frank, C. W. pH-Driven Assembly of Various Supported Lipid Platforms: A Comparative Study on Silicon Oxide and Titanium Oxide. *Langmuir* **27**, 3739–3748 (2011).

336. Nissen, J., Jacobs, K. & Rädler, J. O. Interface Dynamics of Lipid Membrane Spreading on Solid Surfaces. *Phys. Rev. Lett.* **86**, 1904–1907 (2001).

337. Nissen, J., Gritsch, S., Wiegand, G. & Rädler, J. O. Wetting of phospholipid membranes on hydrophilic surfaces - Concepts towards self-healing membranes. *Eur. Phys. J. B* **10**, 335–344 (1999).

338. Martiniere, A. *et al.* Cell wall constrains lateral diffusion of plant plasma-membrane proteins. *Proc. Natl. Acad. Sci.* **109**, 12805–12810 (2012).

339. Spillane, K. M. M. *et al.* High-speed single-particle tracking of gm1 in model

membranes reveals anomalous diffusion due to interleaflet coupling and molecular pinning. *Nano Lett.* **14**, 5390–5397 (2014).

340. Faysal, K. M. R., Park, J. S., Nguyen, J., Garcia, L. & Subramaniam, A. B. Lipid bilayers are long-lived on solvent cleaned plasma-oxidized poly(dimethyl) siloxane (ox-PDMS). *PLoS One* **12**, 1–16 (2017).

341. MacDonald, R. I. Characteristics of self-quenching of the fluorescence of lipid-conjugated rhodamine in membranes. *J. Biol. Chem.* **265**, 13533–9 (1990).

342. Aroeti, B. & Henis, Y. I. Fusion of native Sendai virions with human erythrocytes: Quantitation by fluorescence photobleaching recovery. *Exp. Cell Res.* **170**, 322–337 (1987).

343. Hoekstra, D., De Boer, T., Klappe, K. & Wilschut, J. Fluorescence method for measuring the kinetics of fusion between biological membranes. *Biochemistry* **23**, 5675–5681 (1984).

344. Ham. Fast flip-flop of cholesterol and fatty acids in membranes: implications for membrane transport proteins. *Curr. Opin. Lipidol.* **14**, 263–271 (2003).

345. Bruckner, R. J., Mansy, S. S., Ricardo, A., Mahadevan, L. & Szostak, J. W. Flip-Flop-Induced Relaxation of Bending Energy: Implications for Membrane Remodeling. *Biophys. J.* **97**, 3113–3122 (2009).

346. Jo, S., Rui, H., Lim, J. B., Klauda, J. B. & Im, W. Cholesterol Flip-Flop: Insights from Free Energy Simulation Studies. *J. Phys. Chem. B* **114**, 13342–13348 (2010).

347. Yang, Z. P., Engquist, I., Kauffmann, J.-M. & Liedberg, B. Thiocholesterol on Gold: A Nanoporous Molecular Assembly. *Langmuir* **12**, 1704–1707 (1996).

348. Stetter, F. W. S., Cwiklik, L., Jungwirth, P. & Hugel, T. Single Lipid Extraction: The Anchoring Strength of Cholesterol in Liquid-Ordered and Liquid-Disordered Phases. *Biophys. J.* **107**, 1167–1175 (2014).

349. Guzmán, E., Liggieri, L., Santini, E., Ferrari, M. & Ravera, F. Mixed DPPC–cholesterol Langmuir monolayers in presence of hydrophilic silica nanoparticles. *Colloids Surfaces B Biointerfaces* **105**, 284–293 (2013).

350. Steiner, T. The Hydrogen Bond in the Solid State. *Angew. Chemie Int. Ed.* **41**, 48–76 (2002).

351. Ali, M. R., Cheng, K. H. & Huang, J. Assess the nature of cholesterol-lipid interactions through the chemical potential of cholesterol in phosphatidylcholine bilayers. *Proc. Natl. Acad. Sci. U. S. A.* **104**, 5372–7 (2007).

352. Beseničar, M. P., Bavdek, A., Kladnik, A., Maček, P. & Anderluh, G. Kinetics of cholesterol extraction from lipid membranes by methyl-β-cyclodextrin—A surface plasmon resonance approach. *Biochim. Biophys. Acta - Biomembr.* **1778**, 175–184 (2008).

353. Olsen, B. N. *et al.* The structural basis of cholesterol accessibility in membranes. *Biophys. J.* **105**, 1838–47 (2013).

354. Parker, A., Miles, K., Cheng, K. H. & Huang, J. Lateral distribution of cholesterol in dioleoylphosphatidylcholine lipid bilayers: cholesterol-phospholipid interactions at high cholesterol limit. *Biophys. J.* **86**, 1532–44 (2004).

355. Somerharju, P., Virtanen, J. A. & Hon Cheng, K. Lateral organisation of membrane lipids: The superlattice view. *Biochim. Biophys. Acta* **1440**, 32-48 (1999).

356. Mandal, P. *et al.* Cholesterol Depletion from a Ceramide/Cholesterol Mixed Monolayer: A Brewster Angle Microscope Study. *Sci. Rep.* **6**, 26907 (2016).

357. Silvius, J. R. Role of cholesterol in lipid raft formation: lessons from lipid model systems. *Biochim. Biophys. Acta - Biomembr.* **1610**, 174–183 (2003).

358. Lund-Katz, S., Laboda, H. M., McLean, L. R. & Phillips, M. C. Influence of molecular packing and phospholipid type on rates of cholesterol exchange. *Biochemistry* **27**, 3416–23 (1988).

359. Fugler, L., Clejan, S. & Bittman, R. Movement of cholesterol between vesicles prepared with different phospholipids or sizes. *J. Biol. Chem.* **260**, 4098–102 (1985).

360. van Blitterswijk, W. J., van der Meer, B. W. & Hilkmann, H. Quantitative contributions of cholesterol and the individual classes of phospholipids and their degree of fatty acyl (un)saturation to membrane fluidity measured by fluorescence polarization. *Biochemistry* **26**, 1746–56 (1987).

361. McMullen, T. P. W. & McElhaney, R. N. Differential Scanning Calorimetric Studies of the Interaction of Cholesterol with Distearoyl and Dielaidoyl Molecular Species of Phosphatidylcholine, Phosphatidylethanolamine, and Phosphatidylserine †. *Biochemistry* **36**, 4979–4986 (1997).

362. McMullen, T. P. W., Lewis, R. N. A. H. & McElhaney, R. N. Cholesterol–phospholipid interactions, the liquid-ordered phase and lipid rafts in model and biological membranes. *Curr. Opin. Colloid Interface Sci.* **8**, 459–468 (2004).

363. Ramstedt, B. & Slotte, J. P. Interaction of Cholesterol with Sphingomyelins and Acyl-Chain-Matched Phosphatidylcholines: A Comparative Study of the Effect of the Chain Length. *Biophys. J.* **76**, 908–915 (1999).

364. Tierney, K. J., Block, D. E. & Longo, M. L. Elasticity and phase behavior of DPPC membrane modulated by cholesterol, ergosterol, and ethanol. *Biophys. J.* **89**, 2481–2493 (2005).

365. Rubenstein, J. L. R., Smith, B. A. & Mcconnell, H. M. Lateral diffusion in binary mixtures of cholesterol and phosphatidylcholines (lipid bilayer/photobleaching/phase equilibria/model membrane). *Chemistry (Easton).* **76**, 15–18 (1979).

366. Feng, Z. V., Spurlin, T. A. & Gewirth, A. A. Direct Visualization of Asymmetric Behavior in Supported Lipid Bilayers at the Gel-Fluid Phase Transition. *Biophys. J.* **88**, 2154-2164 (2005).

367. Zidovetzki, R. & Levitan, I. Use of cyclodextrins to manipulate plasma membrane cholesterol content: Evidence, misconceptions and control

strategies. *Biochim. Biophys. Acta - Biomembr.* **1768**, 1311–1324 (2007).

368. Giocondi, M.-C. *et al.* Use of Cyclodextrin for AFM Monitoring of Model Raft Formation. *Biophys. J.* **86**, 861–869 (2004).

369. Gracià, R. S., Bezlyepkina, N., Knorr, R. L., Lipowsky, R. & Dimova, R. Effect of cholesterol on the rigidity of saturated and unsaturated membranes: fluctuation and electrodeformation analysis of giant vesicles. *Soft Matter* **6**, 1472 (2010).

370. Hao, M., Mukherjee, S. & Maxfield, F. R. Cholesterol depletion induces large scale domain segregation in living cell membranes. *Proc. Natl. Acad. Sci. U. S. A.* **98**, 13072–7 (2001).

371. Qi, M., Liu, Y., Freeman, M. R. & Solomon, K. R. Cholesterol-regulated stress fiber formation. *J. Cell. Biochem.* **106**, 1031–1040 (2009).

372. van Deurs, B., Roepstorff, K., Hommelgaard, A. M. & Sandvig, K. Caveolae: anchored, multifunctional platforms in the lipid ocean. *Trends Cell Biol.* **13**, 92–100 (2003).

373. di Cagno, M. & Pio, M. The Potential of Cyclodextrins as Novel Active Pharmaceutical Ingredients: A Short Overview. *Molecules* **22**, 1 (2016).

374. Lentz, B. R., Barenholz, Y. & Thompson, T. E. Fluorescence depolarization studies of phase transitions and fluidity in phospholipid bilayers. 2 Two-component phosphatidylcholine liposomes. *Biochemistry* **15**, 4529–37 (1976).

375. Elliott, R., Katsov, K., Schick, M. & Szleifer, I. Phase separation of saturated and mono-unsaturated lipids as determined from a microscopic model. *J. Chem. Phys.* **122**, 044904 (2005).

376. Sezgin, E., Levental, I., Mayor, S. & Eggeling, C. The mystery of membrane organization: composition, regulation and roles of lipid rafts. *Nat. Rev. Mol. Cell Biol.* **18**, 361–374 (2017).

377. Grecco, H. E., Schmick, M. & Bastiaens, P. I. H. Signaling from the living plasma membrane. *Cell* **144**, 897–909 (2011).

378. de Almeida, R. F. M. & Joly, E. Crystallization around solid-like nanosized docks can explain the specificity, diversity, and stability of membrane microdomains. *Front. Plant Sci.* **5**, 72 (2014).

379. de Almeida, R. F. M., Borst, J., Fedorov, A., Prieto, M. & Visser, A. J. W. G. Complexity of Lipid Domains and Rafts in Giant Unilamellar Vesicles Revealed by Combining Imaging and Microscopic and Macroscopic Time-Resolved Fluorescence. *Biophys. J.* **93**, 539–553 (2007).

380. Jensen, M. H., Morris, E. J. & Simonsen, A. C. Domain Shapes, Coarsening, and Random Patterns in Ternary Membranes. *Langmuir* **23**, 8135–8141 (2007).

381. Bordovsky, S. S., Wong, C. S., Bachand, G. D., Stachowiak, J. C. & Sasaki, D. Y. Engineering Lipid Structure for Recognition of the Liquid Ordered Membrane Phase. *Langmuir* **32**, 12527–12533 (2016).

382. Huang, Z. & London, E. Effect of Cyclodextrin and Membrane Lipid Structure upon Cyclodextrin–Lipid Interaction. *Langmuir* **29**, 14631–14638 (2013).

383. Kahya, N., Scherfeld, D., Bacia, K., Poolman, B. & Schwille, P. Probing lipid mobility of raft-exhibiting model membranes by fluorescence correlation spectroscopy. *J. Biol. Chem.* **278**, 28109–15 (2003).

384. Husen, P., Arriaga, L. R., Monroy, F., Ipsen, J. H. & Bagatolli, L. A. Morphometric Image Analysis of Giant Vesicles: A New Tool for Quantitative Thermodynamics Studies of Phase Separation in Lipid Membranes. *Biophys. J.* **103**, 2304–2310 (2012).

385. Lindblom, G., Orädd, G. & Filippov, A. Lipid lateral diffusion in bilayers with phosphatidylcholine, sphingomyelin and cholesterol: An NMR study of dynamics and lateral phase separation. *Chem. Phys. Lipids* **141**, 179–184 (2006).

386. Tamm, L. K. & McConnell, H. M. Supported phospholipid bilayers. *Biophys. J.* **47**, 105–13 (1985).

387. Samsonov, A. V., Mihalyov, I. & Cohen, F. S. Characterization of Cholesterol-Sphingomyelin Domains and Their Dynamics in Bilayer Membranes. *Biophys. J.* **81**, (Cell Press, 2001).

388. Dietrich, C., Volovyk, Z. N., Levi, M., Thompson, N. L. & Jacobson, K. Partitioning of Thy-1, GM1, and cross-linked phospholipid analogs into lipid rafts reconstituted in supported model membrane monolayers. *Proc. Natl. Acad. Sci. U. S. A.* **98**, 10642–7 (2001).

389. Lawrence, J. C., Saslowsky, D. E., Michael Edwardson, J. & Henderson, R. M. Real-Time Analysis of the Effects of Cholesterol on Lipid Raft Behavior Using Atomic Force Microscopy. *Biophys. J.* **84**, 1827–1832 (2003).

390. Dietrich, C. *et al.* Lipid rafts reconstituted in model membranes. *Biophys. J.* **80**, 1417–28 (2001).

391. Verma, P., Mager, M. D. & Melosh, N. A. Rough-smooth-rough dynamic interface growth in supported lipid bilayers. *Phys. Rev. E* **89**, 012404 (2014).

392. Korlach, J., Schwille, P., Webb, W. W. & Feigenson, G. W. Characterization of lipid bilayer phases by confocal microscopy and fluorescence correlation spectroscopy. *Proc. Natl. Acad. Sci. U. S. A.* **96**, 8461–6 (1999).

393. Miller, E. J., Voïtchovsky, K. & Staykova, M. Substrate-led cholesterol extraction from supported lipid membranes. *Nanoscale* **10**, 16332-16342, (2018).

394. Vanni, S., Hirose, H., Barelli, H., Antonny, B. & Gautier, R. A sub-nanometre view of how membrane curvature and composition modulate lipid packing and protein recruitment. *Nat. Commun.* **5**, 4916 (2014).

395. Clarke, J. A., Seddon, J. M. & Law, R. V. Cholesterol containing model membranes studied by multinuclear solid state NMR spectroscopy. *Soft Matter* **5**, 369–378 (2009).

396. Black, J. C., Cheney, P. P., Campbell, T. & Knowles, M. K. Membrane

curvature based lipid sorting using a nanoparticle patterned substrate. *Soft Matter* **10**, 2016–23 (2014).

397. Mornet, S., Lambert, O., Duguet, E. & Brisson, A. The formation of supported lipid bilayers on silica nanoparticles revealed by cryoelectron microscopy. *Nano Lett.* **5**, 281–5 (2005).

398. Attwood, S. J., Choi, Y. & Leonenko, Z. Preparation of DOPC and DPPC Supported Planar Lipid Bilayers for Atomic Force Microscopy and Atomic Force Spectroscopy. *Int. J. Mol. Sci.* **14**, 3514–39 (2013).

399. Connell, S. D., Heath, G. R. & Goodchild, J. A. Quantitative Analysis of Structure and Dynamics in AFM Images of Lipid Membranes. in *Atomic Force Microscopy: Methods and Protocols*, *Methods Mol Biol* **1886**, 29–44 (2019).

400. Yang, K. *et al.* Partitioning of nanoscale particles on a heterogeneous multicomponent lipid bilayer. *Phys. Chem. Chem. Phys.* **20**, 28241–28248 (2018).

401. Aloia, R. C., Tian, H., Jensen, F. C. & Vogt, V. M. Lipid composition and fluidity of the human immunodeficiency virus envelope and host cell plasma membranes. *Proc. Natl. Acad. Sci.* **90**, 5181–5185 (1993).

402. Nir, S. & Nieva, J. L. Interactions of peptides with liposomes: pore formation and fusion. *Prog. Lipid Res.* **39**, 181–206 (2000).

403. Shai, Y. Mechanism of the binding, insertion and destabilization of phospholipid bilayer membranes by α-helical antimicrobial and cell non-selective membrane-lytic peptides. *Biochim. Biophys. Acta - Biomembr.* **1462**, 55–70 (1999).

404. Shao, Y. & Fu, J. Integrated micro/nanoengineered functional biomaterials for cell mechanics and mechanobiology: a materials perspective. *Adv. Mater.* **26**, 1494–533 (2014).

405. Guilak, F. *et al.* Control of Stem Cell Fate by Physical Interactions with the Extracellular Matrix. *Cell Stem Cell* **5**, 17–26 (2009).

406. Chumtong, P. *et al.* On-chip Flexible Scaffold for Construction of Multishaped Tissues. *2014 IEEE/RSJ Int. Conf. Intell. Robot. Syst. (IROS 2014)* 4692–4697

407. Unger, W. E. S., Senoner, M., Wirth, T., Bütefisch, S. & Busch, I. Lateral Resolution of Imaging Surface-Analytical Instruments as SIMS, AES and XPS: Application of the BAM-L200 Certified Reference Material and Related ISO Standards. *J. Surf. Anal.* **24**, 123–128 (2017).

408. Radhakrishnan, A. & McConnell, H. M. Chemical Activity of Cholesterol in Membranes. *Biochemistry* **39**, 8119–8124 (2000).

409. Radhakrishnan, A. & McConnell, H. M. Condensed complexes of cholesterol and phospholipids. *Biophys. J.* **77**, 1507–17 (1999).

410. Garg, S. *et al.* Cholesterol Solubility Limit in Lipid Membranes probed by Small Angle Neutron Scattering and MD simulations. *Soft Matter* **10**, 9313-9317 (2014).

411. Schlebach, J. P. *et al.* Topologically Diverse Human Membrane Proteins Partition to Liquid-Disordered Domains in Phase-Separated Lipid Vesicles. *Biochemistry* **55**, 985–988 (2016).

412. Wolfe, M. S. Processive proteolysis by γ-secretase and the mechanism of Alzheimer's disease. *Biol. Chem.* **393**, 899–905 (2012).

413. Li, J., Parker, B., Martyn, C., Natarajan, C. & Guo, J. The PMP22 Gene and Its Related Diseases. *Mol. Neurobiol.* **47**, 673–698 (2013).